GEOLOGICA ULTRAIECTINA

Mededelingen van de
Faculteit Aardwetenschappen
Universiteit Utrecht

no. 199

Thermal evolution of high-pressure metamorphic rocks in the Alps

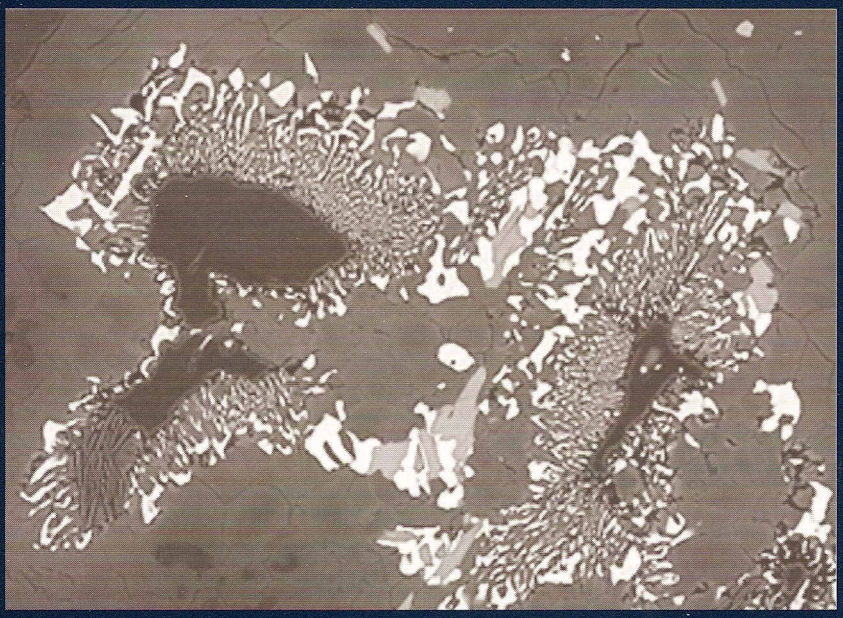

Fraukje M. Brouwer

GEOLOGICA ULTRAIECTINA

Mededelingen van de

Faculteit Aardwetenschappen

Universiteit Utrecht

No. 199

Thermal evolution of high-pressure metamorphic rocks in the Alps

Fraukje M. Brouwer

Cover illustration: Spinel-corundum-plagioclase symplectite surrounding kyanite in a metabasic rock from the Lepontine gneisses near Bellinzona, Switzerland. SEM backscatter electron image.

Thermal evolution of high-pressure metamorphic rocks in the Alps

Thermische evolutie van hoge druk metamorfe gesteenten in de Alpen

(met een samenvatting in het Nederlands)

PROEFSCHRIFT

ter verkrijging van de graad van Doctor aan de Universiteit Utrecht

op gezag van de Rector Magnificus Prof. Dr. H.O. Voorma

ingevolge het besluit van het College voor Promoties in het openbaar te verdedigen

op 20 november 2000, des namiddags te 16.15 uur

door

Fraukje Myriam Brouwer

Geboren op 24 mei 1973, te Uden

Supervisors:

Prof. Dr. R.L.M. Vissers
Prof. Dr. M.J.R. Wortel

Members of the dissertation committee:

Prof. Dr. R. Compagnoni
Dipartimento di Scienze Mineralogiche e Petrologiche
Università degli Studi di Torino, Italy

Prof. Dr. M. Engi
Mineralogisch-Petrographisches Institut
Universität Bern, Switzerland

Prof. Dr. S.M. Schmid
Geologisch-Paläontologisches Institut
Universität Basel, Switzerland

Prof. Dr. J.L.R. Touret
Faculteit Aardwetenschappen
Vrije Universiteit Amsterdam, The Netherlands

ISBN 90-5744-056-3

Voor mijn ouders

NWO

The research described in this thesis was conducted at the Faculty of Earth Sciences, Utrecht University, under the programme of the Vening Meinesz Research School of Geodynamics (VMSG). The author acknowledges financial support from the Geosciences Foundation (GOA, currently ALW) of the Netherlands Organisation for Scientific Research (NWO), project number 750-196-15.

Contents

Samenvatting (Abstract in Dutch) 11
Riassunto (Abstract n Italian) 15
Abstract 19

Chapter 1 Introduction 21
1.1 Scope of this study 21
1.2 Approach 22
1.3 Outline of this thesis 22

Chapter 2 Introduction to Alpine geology 25
2.1 Plate tectonic setting 25
2.2 Geometry of the Alps 25
2.3 Structure of the central and western Alps 28
2.3.1 The central Alps 28
2.3.2 The western Alps 29
2.3.3 The Ligurian Alps 31

Chapter 3 Metamorphic history of the Lepontine gneisses around Alpe Arami, southern Switzerland 33
3.1 Abstract 33
3.2 Introduction 33
3.2.1 Geology of the Lepontine Alps 33
3.2.2 The origin and history of the Alpe Arami peridotite 36
3.2.3 The study area 37
3.3 Structural history of the Lepontine gneisses 38
3.3.1 Structures of the gneisses 38
3.3.2 Comparison with regional studies 44
3.4 Lithologies and mineral chemistry 45
3.4.1 Petrography 45
3.4.2 Eclogites and eclogite-amphibolites 46
3.4.2.1 Petrography of eclogites and eclogite-amphibolites 46
3.4.2.2 Symplectitic transformations 47
3.4.2.3 Mineral chemistry of eclogites and eclogite-amphibolites 49
3.4.3 Cima Lunga metapelitic lens 52
3.4.3.1 Petrography of metapelites 53
3.4.3.2 Mineral chemistry of metapelites 56
3.4.4 Thermobarometry 56
3.4.5 Compilation of the PTt trajectory 63

3.5 Geodynamic implications 66
3.5.1 Juxtaposition of the Cima Lunga nappe and the Arbedo zone 66
3.5.2 Three possible scenarios for Alpe Arami and the Lepontine gneisses 67
3.5.3 Implications for orogenic processes 68
3.6 Conclusions 70

Chapter 4 Structure and metamorphism of the Gran Paradiso massif, western Alps, Italy 73
4.1 Abstract 73
4.2 Introduction 73
4.2.1 Geology of the western Alps 73
4.2.2 Gran Paradiso massif 75
4.3 Structure of the Gran Paradiso basement 77
4.3.1 Pre-Alpine deformation 77
4.3.2 Alpine deformation 77
4.4 Metamorphism of the Gran Paradiso basement 80
4.4.1 Petrography 80
4.4.2 Mineral chemistry 85
4.4.3 Thermobarometry 89
4.4.4 Compilation of the PTt trajectory 94
4.5 Geodynamic implications 98
4.6 Conclusions 99

Chapter 5 Metamorphic history of eclogitic metagabbro blocks from a tectonic mélange in the Voltri massif, Ligurian Alps, Italy 101
5.1 Abstract 101
5.2 Introduction 101
5.2.1 Geology of the Voltri massif 101
5.2.2 Tectonic mélange in the northern Voltri massif 102
5.3 Metagabbros of the Voltri mélange 105
5.3.1 Petrography 105
5.3.2 Mineral chemistry 107
5.4 Metamorphic history 109
5.4.1 Thermobarometry 109
5.4.2 Compilation of the PTt trajectory 113
5.5 Discussion 116
5.5.1 Comparison with previous studies 116
5.5.2 Tectonic implications 116
5.6 Conclusions 118

Chapter 6 The thermal evolution of convergent margins: a numerical modelling study applied to the Alps 119
6.1 Abstract 119
6.2 Introduction 119
6.3 Possible causes for heating 122
6.3.1 Processes in the upper mantle 122
6.3.2 Radiogenic heating within the deformed crust 124
6.3.3 Selection of possibly viable hypotheses 126
6.4 Numerical investigations 126
6.4.1 Slab detachment 126
6.4.2 Tectonically Accreted Radiogenic Material (TARM) 129
6.4.3 Comparison of model results for the two hypotheses 131
6.5 Comparison of model results with observations: a test of the hypotheses 133
6.5.1 Geodynamic setting and PTt trajectories of selected areas 133
6.5.2 Comparison of model results with observations 136
6.6 Exhumation of high-pressure rocks in the Alps 138
6.7 Conclusions 141

Chapter 7 Conclusions and future research 143

References 146

Appendix 1 Thermobarometry 157
A1.1 Introduction 157
A1.2 Garnet-omphacite thermobarometry 157
A1.2.1 Krogh (1988) 157
A1.2.2 Holland (1983) 157
A1.2.3 Powell (1985) 159
A1.3 Garnet-phengite thermometry 160
A1.4 Phengite barometry 161
A1.5 Garnet-clinopyroxene-phengite barometry 162
A1.6 Garnet-amphibole thermometry 163
A1.7 Garnet-amphibole barometry 164
A1.8 Amphibole-plagioclase thermometry 167
A1.9 GASP barometry 169
A1.10 Garnet-biotite thermometry 170
A1.10.1 Ferry and Spear (1978) 170
A1.10.2 Hodges and Spear (1982) 170
A1.10.3 Kleemann and Reinhardt (1994) 171
A1.11 Simultaneous solution of GASP and garnet-biotite 171
A1.11.1 GASP and Ferry and Spear (1978) 172
A1.11.2 GASP and Kleemann and Reinhardt (1994) 172

Appendix 2 **Representative electron microprobe analyses from the Lepontine gneisses** 173

Appendix 3 **Representative electron microprobe analyses from Gran Paradiso** 191

Appendix 4 **Representative electron microprobe analyses from the Voltri mélange** 207

Dankwoord, Acknowledgements 217

Curriculum Vitae 221

Samenvatting

Eén van de belangrijke onderwerpen in de geologie, de studie van de aarde, is de vorming van gebergten. De grootschalige processen die gebergtevorming veroorzaken worden redelijk begrepen: de aardkorst bestaat uit lithosfeerplaten en waar deze tegen elkaar botsen of onder elkaar schuiven ontstaan gebergten, als een soort kreukelzones. Verschillende kleinschaliger processen die een rol spelen in gebergtevorming zijn echter nog niet verklaard. Deze processen zijn het onderwerp van dit proefschrift. Een belangrijk instrument van geologen bij de bestudering van gebergtevorming is de petrologie: de studie van mineralen en mineraal-assemblages in gesteenten. In stenen vormen zich bij bepaalde temperatuur en druk nieuwe mineralen (metamorfose). In de aarde nemen de druk en de temperatuur toe met de diepte; de samenstelling en combinatie van mineralen in gesteentemonsters geven dus aan hoe diep de steen was en hoe warm het daar was toen deze mineralen groeiden. Een deel van die informatie blijft bewaard en zo maakt de steen een soort bandopname van zijn weg naar het oppervlak, vergelijkbaar met de zwarte doos van een vliegtuig. Het ontcijferen van de bewaarde gegevens levert waardevolle informatie op over de gang van de steen naar het aardoppervlak.
De Alpen zijn ongetwijfeld het meest bestudeerde gebergte op aarde. Het ontstaan van de Alpen is het een gevolg van de botsing van Italië met de rest van Europa, ongeveer 50 miljoen jaar geleden. Ondanks de enorme hoeveelheid geologische en geofysische gegevens die in de afgelopen twee eeuwen is vergaard, begrijpen aardwetenschappers de ontwikkeling van het gebergte maar tot een bepaald niveau en bestaan er nog steeds veel meningsverschillen. Twee vraagstukken over de geologie van de Alpen hebben te maken met de metamorfe geschiedenis van stenen in de interne zones van de Alpen in Noordwest-Italië en Zuid-Zwitserland. Ten eerste zijn er aanwijzingen dat stenen, op geologische tijdschaal kort geleden, meer dan vijftig of zelfs honderd kilometer diep in de aarde zaten, terwijl ze nu aan het aardoppervlak liggen. Aangezien de Alpen maximaal zo'n 250 kilometer breed zijn, moeten de processen waardoor de stenen meer dan 100 kilometer naar boven komen effect hebben op het hele gebergte. Ten tweede bevatten sommige van deze hoge druk metamorfe stenen aanwijzingen, dat ze op hun weg naar boven eerst afkoelden en daarna weer opgewarmd zijn, terwijl normaal gesproken de temperatuur afneemt naarmate het aardoppervlak genaderd wordt. Het weer opwarmen van de stenen in een laat stadium van de gebergtevorming wordt in de Alpen Lepontiene metamorfose genoemd.
In dit proefschrift wordt geologisch bewijs verzameld voor hoge druk metamorfose, snel transport naar het oppervlak, afkoeling die soms wordt gevolgd door opwarming tijdens dit transport en worden mogelijke oorzaken onderzocht. De gegevens worden verzameld in een combinatie van veldgeoriënteerd onderzoek, met name het reconstrueren van de druk-temperatuur geschiedenis door de tijd (PTt-paden) van stenen uit de Alpen, en computermodellen van processen die de opwarming kunnen verklaren. In deze computermodellen worden mogelijke verklaringen uitgewerkt. De ontwikkeling van de geometrie van de botsingszone van de twee platen wordt nagebootst, waarbij de

temperatuurverdeling in het systeem door de tijd verandert. Op deze manier kunnen de modellen grenzen aangeven aan de mogelijke afkoeling en opwarming van stenen voor de gekozen geometrie. PTt-paden worden gebruikt als randvoorwaarden voor de computermodellen en maken het mogelijk verklaringen voor de opwarming van de hoge druk metamorfe stenen op hun weg naar het oppervlak te testen.
In de metamorfe Penninische Zone van de Alpen zijn drie gebieden geselecteerd voor gedetailleerde studie van hun metamorfe (PT) geschiedenis (kaartje zie figuur 2.2). De gebieden liggen respectievelijk in de zogenaamde Lepontiene Gneissen in de centrale Alpen van Zuid-Zwitserland, in de metamorfe ondergrond van het Gran Paradiso massief in de westelijke Alpen in Noordwest-Italië en in het Voltri Massief in de Ligurische Alpen bij Genua. Ze zijn gekozen vanwege hun verspreiding langs de boog van de Alpen, steeds op ongeveer 150 kilometer van elkaar, om zo op de schaal van het hele gebergte inzicht te krijgen in de overeenkomsten en verschillen in de metamorfe ontwikkeling van de stenen in de interne zones van de Alpen.
Bij het reconstrueren van de metamorfe geschiedenis van de Lepontiene Gneissen die het Alpe Arami granaatperidotietlichaam omringen (hoofdstuk 3 – zie ook samenvattend figuur 6.8) ligt de nadruk op de thermische geschiedenis. De gebruikte informatie is vooral vergaard uit een lens van pelitische (meta-sedimentaire) gesteenten en uit meta-basische gesteenten (gemetamorfoseerde stenen van vulkanische oorsprong) uit de omliggende Arbedo Zone. De stenen sluiten relicten in van hoge druk metamorfose bij een druk van 21 kilobar, wat overeen komt met een diepte van ongeveer 70 kilometer. De temperatuur was ongeveer 900 °C. Volgens recente dateringsstudies vond deze hoge druk metamorfose ongeveer 37 tot 40 miljoen jaar geleden plaats. Hierna begonnen de stenen aan hun weg richting het aardoppervlak, met een snelheid van ongeveer 7 millimeter per jaar, waarbij ze eerst afkoelden tot onder ongeveer 650 °C. Rond 32 miljoen jaar geleden werden de stenen, op een diepte van ongeveer 20 kilometer, weer zo'n 110 °C warmer, waardoor mineralen groeiden die wijzen op metamorfose bij matige druk en hoge temperatuur, zoals bijvoorbeeld cordiëriet en sillimaniet. De informatie uit de stenen wijst op een temperatuur van 760 °C, bij een druk van 4 tot 6 kilobar. Na deze opwarming koelden de stenen af tijdens hun verdere weg naar boven. Rond 18 miljoen jaar geleden waren ze nog maar 200 °C en 7 miljoen jaar geleden waren ze afgekoeld tot onder 100 °C. Het laatste deel van het transport naar het aardoppervlak ging met een snelheid van ongeveer 0.8 millimeter per jaar, veel langzamer dan in het begin.
De metamorfe geschiedenis van het Gran Paradiso massief in de Italiaanse westelijke Alpen (hoofdstuk 4) lijkt een beetje op die van de Lepontiene Gneissen. De stenen ondergingen hoge druk metamorfose bij ongeveer 525 °C en 12 tot 14 kilobar, wat overeenkomt met een diepte van ongeveer 50 kilometer. Dit gebeurde ongeveer 43 miljoen jaar geleden. In het begin bewogen de stenen, met een snelheid van ongeveer 3.3 millimeter per jaar, snel richting het aardoppervlak waarbij ze afkoelden. Op een diepte van ongeveer 20 kilometer werden de stenen weer enkele tientallen graden opgewarmd, waardoor matige druk-, matige temperatuur-metamorfose plaatsvond bij 6 kilobar en 550 °C. Op basis van dateringsstudies van andere aardwetenschappers vond het opwarmen naar schatting kort voor 34 miljoen jaar geleden plaats. Na de opwarming

koelden de stenen af op hun verdere weg naar het oppervlak, waarbij ze rond 30 miljoen jaar geleden onder 200 °C kwamen en tussen 24 en 20 miljoen jaar geleden onder 100 °C. Na de opwarmfase bewogen de stenen met een gemiddelde snelheid van 0.6 millimeter per jaar naar het oppervlak.
In een tektonische melange in het Voltri Massief in de Ligurische Alpen bij Genua drijven grote blokken eclogiet (basische stenen met sporen van hoge druk metamorfose) in een fijnkorrelige massa (hoofdstuk 5). Door middel van thermobarometrische studie van de hoge druk mineralen is bepaald dat de hoogste druk die deze stenen hebben geregistreerd ongeveer 18 kilobar is, wat overeen komt met een diepte van ongeveer 65 kilometer. De temperatuur op deze diepte was ongeveer 525 °C. Op hun weg omhoog werden deze stenen steeds verder afgekoeld, waarbij eerst de temperatuur langzaam daalde en de druk snel, terwijl later de temperatuur sneller afnam. Er zijn geen dateringsstudies beschikbaar van deze stenen, dus de ouderdom van de hoge druk metamorfose is onbekend. Hierdoor kunnen ook de snelheid waarmee de stenen naar het oppervlak hebben bewogen en hun afkoelingssnelheid niet worden bepaald. Het Voltri Massief lag 34 miljoen jaar geleden op de zeebodem tussen Italië en Frankrijk, waarna er sedimenten zijn afgezet.
Samenvattend kan worden vastgesteld dat de stenen in alledrie de gebieden hoge druk metamorfose hebben ondergaan. In de centrale en westelijke Alpen koelden de stenen eerst af op hun weg omhoog, waarna zij werden opgewarmd op een diepte van ongeveer 20 kilometer (met respectievelijk 110 en 40 °C in ongeveer 7 miljoen jaar), terwijl de stenen in het Voltri Massief tijdens hun gang naar het aardoppervlak alleen afkoelden.
Het vervolg op het veldonderzoek bestaat uit het zoeken van een verklaring voor de opwarming die is geregistreerd in de centrale en westelijke Alpen. De klassieke verklaring voor opwarming tijdens gebergtevorming is opwarming door het verval van radioactieve mineralen die in relatief grote hoeveelheden aanwezig zijn in de aardkorst. Dit effect kan eventueel versterkt worden door ophoping van radioactief materiaal in de zone waar de ene lithosfeerplaat onder een andere schuift. Een alternatieve verklaring voor de opwarming is het afbreken van de onderschuivende plaat. Het afgebroken deel zinkt weg in de mantel en de vrijgekomen ruimte wordt opgevuld met warm mantelmateriaal. Deze twee hypotheses zijn vergeleken met behulp van computermodellen, zoals hiervoor al kort is beschreven (zie hoofdstuk 6).
In eerste instantie hebben we de computermodellen toegepast op de centrale Alpen, omdat in dit gebied de botsing tussen de platen min of meer frontaal was, waardoor het proces beschreven kan worden met een tweedimensionaal model. De resultaten van de computermodellen geven aan, dat beide mechanismen voldoende opwarming kunnen veroorzaken. Het verschil tussen de twee is echter dat radiogene opwarming veel langer duurt, terwijl er niet voldoende tijd is om een wig van korstmateriaal te accumuleren waarin het verwarmende effect van de radioactieve mineralen wordt versterkt. De opwarming in de centrale Alpen kan verklaard worden door het afbreken van de onderschuivende plaat.
In de westelijke Alpen is de geometrie veel ingewikkelder. Omdat de Alpen de vorm

van een boog hebben, is de onderschuivende beweging in het westen niet loodrecht, maar schuin ten opzichte van het contact tussen de twee platen. Het lijkt het meest waarschijnlijk dat de gesteenten in de westelijke Alpen zijn opgewarmd door het afbreken van de plaat in de centrale Alpen, en dat ze tijdens het omhoog komen zich niet alleen verticaal hebben verplaatst, maar ook horizontaal: weg van de stenen die nu in de centrale Alpen aan het oppervlak liggen.
Hoe de stenen in de Alpen precies naar het oppervlak gebracht zijn is nog niet helemaal duidelijk, maar het is wel zeker dat dit met (geologisch) hoge snelheid gebeurd is. Een mogelijk scenario, dat past bij de informatie die bekend is over de Alpen en hun geschiedenis, is het volgende: door dichtheidsverschillen veroorzaakte opwaartse druk "duwt" de stenen van hun diepste positie naar de onderkant van de korst. Van daaraf worden ze verder omhoog gebracht door een proces van corner flow, of wigstroming. Aan de onderkant van het, in verticale doorsnede, wigvormige gebergte worden steeds stukken gesteente toegevoegd die de bovenliggende gesteenten omhoog duwen. Ter compensatie van het steeds steiler worden van de wig, bewegen de stenen boven in de wig zijwaarts, waardoor diepere gesteenten het aardoppervlak bereiken. Het afbreken van de onderschuivende plaat zou een rol kunnen spelen in het omhoog brengen van de gesteenten, maar die rol is niet helemaal duidelijk. Het is wel duidelijk dat dit proces hoogstwaarschijnlijk een belangrijke bijdrage heeft geleverd aan de thermische geschiedenis van de onderzochte gesteenten uit de Alpen.

Riassunto

Uno degli argomenti più avvincenti della geologia, che si occupa dello studio della Terra, è la formazione delle catene montuose (orogenesi). I processi a grande scala che causano la formazione delle montagne sono stati capiti abbastanza bene. La croste della terra è formata da "placche litosferiche" e le catene montuose si formano ove queste placche si scontrano o dove una placca scorre al di sotto di un'altra. Molti processi a più piccola scala correlati alla costruzione delle catene montuose non sono invece ancora stati compresi. Lo studio di alcuni di questi processi costituisce l'argomento di questa tesi di dottorato.

La petrologia, o studio dei minerali e delle associazioni mineralogiche delle rocce, è uno strumento importante utilizzato dai geologi nello studio delle catene montuose. A determinate temperature e pressioni nelle rocce si formano infatti nuovi minerali (metamorfismo). Pressione e temperatura crescono all'aumentare della profondità, e così la composizione ed il tipo di minerali di una roccia riflettono la temperatura e pressione locali del momento in cui questi minerali si sono formati. Parte delle informazioni così registrate nelle rocce viene preservata, e la roccia registra in tal modo informazioni sul percorso che compie nel suo viaggio verso la superficie, in maniera analoga a quella di una "scatola nera" di un aeroplano. Decifrare le informazioni registrate dalle rocce può dare informazioni utili sul loro percorso verso la superficie terrestre.

Senza dubbio le Alpi sono la catena montuosa più studiata della terra. Si sono formate grazie alla collisione dell'Italia con il resto dell'Europa circa 50 milioni di anni fa. Nonostante l'abbondanza di dati geologici e geofisici che sono stati raccolti negli ultimi due secoli, l'evoluzione delle Alpi è capita solo parzialmente e molti punti sono ancora dibattuti. Vi sono due principali argomenti ancora irrisolti nella geologia alpina che riguardano l'evoluzione metamorfica delle rocce delle zone interne delle Alpi. Primo, rocce che mostrano l'evidenza di un recente metamorfismo di alta o ultra-alta pressione sono oggi affioranti in superficie, implicando quindi l'esumazione da profondità fino a 100 km in una catena meno ampia di 250 km di larghezza. Questo implica che i processi coinvolti nell' esumazione fino in superficie agiscono alla scala dell'intera catena. Secondo, queste rocce di alta pressione talora mostrano segni di un riscaldamento significativo durante la loro risalita, un fenomeno conosciuto nelle Alpi Centrali come metamorfismo Lepontino. Di solito invece la temperatura decresce avvicinandosi alla superficie.

Questa tesi studia alcune evidenze geologiche di queste due caratteristiche in rocce Alpine ed investiga alcune delle possibili cause. Ciò è stato fatto tramite la combinazione di dettagliati studi di terreno che hanno condotto alla ricostruzione delle traiettorie Pressione–Temperatura-tempo (PTt) di alcune rocce delle Alpi, con una modellizzazione al computer dei processi che possono spiegare un riscaldamento durante l'esumazione. Lo sviluppo della geometria di una zona di collisione tra due placche è stato simulato in due dimensioni, facendo cambiare la distribuzione delle temperature nel tempo. I modelli forniscono informazioni sui valori limite di riscaldamento e raffreddamento per

le rocce per ogni data geometria delle placche. I percorsi PTt servono come limiti di verifica per i risultati ottenuti con la modellizaazione numerica, e permettono di testare le ipotesi contrastanti che riguardano le possibili cause del riscaldamento durante l'esumazione delle rocce di alta pressione nelle Alpi.
Sono state selezionate tre aree nella Zona Penninica delle Alpi per compiere un dettagliato studio della loro evoluzione metamorfica (PT), si veda la carta in figura 2.2. le aree di studio, rispettivamente negli gneiss Lepontini vicino all'Alpe Arami, nelle Alpi centrali della Svizzera meridionale, nel basamento del Gran Paradiso nelle Alpi occidentali dell'Italia centro-occidentale e nel Massiccio di Voltri, nelle Alpi liguri vicino a Genova, sono state scelte a distanze tra loro di circa 150 km lungo l'arco alpino, in modo da poter avere un'indicazione sulle somiglianze e differenze dell'evoluzione metamorfica delle rocce a scala della catena.
Lo studio degli gneiss Lepontini, che circondano il corpo di peridotiti a granato di Alpe Arami, nelle Alpi Centrali, si è concentrato sull'evoluzione termica (capitolo 3 e figura 6.8) determinata grazie allo studio di una scaglia di rocce pelitiche (meta-sedimenti) dell'Unità di Cima Lunga e di metabasiti (rocce di natura magmatica metamorfosate) provenienti dalla Zona di Arbedo. Le rocce hanno subìto un metamorfismo di alta pressione con pressioni di picco fino a 21 kbar, equivalenti a profondità maggiori di 70 km, e temperature intorno ai 900 °C. Recenti studi geocronologici suggeriscono un'età, per questo metamorfismo, tra 37 e 40 milioni di anni. Successivamente le rocce si sono raffreddate a temperature inferiori a 650 °C durante un primo episodio di trasporto verso la superficie (esumazione) a velocità di almeno 7 mm/anno. Intorno a 32 milioni di anni le rocce sono state riscaldate di circa 110 °C, con un metamorfismo di media pressione ed alta temperatura a pressioni di 4-6 kbar, equivalenti a profondità intorno ai 20 km, e temperature massime fino a 760 °C. L'esumazione finale fino alla superficie terrestre è avvenuta a velocità inferiori, di circa 0.8 mm/anno.
L'evoluzione metamorfica del massiccio del Gran Paradiso è abbastanza simile a quella descritta per gli gneiss Lepontini. Il metamorfismo di alta pressione ha avuto luogo in condizioni di 525 °C e 12-14 kbar, equivalenti a profondità di una cinquantina di chilometri circa 43 milioni di anni fa. La prima decompressione è stata veloce, con velocità stimate intorno ai 3.3 mm/anno, ed è stata contemporanea ad un raffreddamento. A circa 20 km di profondità le rocce hanno quindi subito un riscaldamento di qualche decina di gradi, con un metamorfismo di media pressione e media temperatura a 6 kbar e 550 °C. Sulla base di studi geocronologici di altri autori si ritiene che questo riscaldamento sia avvenuto poco prima di 34 milioni di anni fa. L'esumazione finale è poi avvenuta con velocità medie basse, intorno a 0.6 mm/anno.
Nel Gruppo di Voltri, nelle Alpi Liguri italiane è presente un mélange tettonico che contiene blocchi di metagabbri eclogitici (rocce basiche con tracce di metamorfismo di alta pressione) compresi in una matrice a grana fine. Studi termobarometrici effettuati sui blocchi eclogitici indicano che il metamorfismo culminò a pressioni di 18 kbar, equivalenti a profondità di 65 km, e temperature intorno a 525 °C. Per il momento non esistono dati geocronologici per questo metamorfismo di alta pressione. Le condizioni di picco metamorfico sono state seguite da un raffreddamento continuo fino

all'esumazione in superficie, all'inizio con rapporti P/T relativamente alti, ovvero lungo un gradiente geotermico basso, seguito da un'esumazione finale lungo un gradiente geotermico decisamente maggiore. A causa della mancanza di dati sull'età, le velocità di raffreddamento e trasporto verso la superficie non possono essere stimate. Comunque la deposizione di sedimenti continentali sulle rocce di alta pressione esumate nel Massiccio di Voltri indica che il Massiccio di Voltri era esposto in superficie a partire da 34 milioni di anni fa.

Riassumendo i risultati dello studio di terreno è chiaro che le rocce di tutte e tre le aree campione hanno subìto un metamorfismo di alta pressione. Nelle Alpi centrali ed occidentali le rocce hanno subìto un raffreddamento iniziale durante l'esumazione, dopodichè sono state riscaldate rispettivamente di 110 e 40 °C a profondità di circa 20 chilometri per circa 7 milioni di anni. Le rocce del Massiccio di Voltri si sono invece raffreddate con continuità durante il loro percorso verso la superficie terrestre.

Successivamente a questi studi di terreno si è cercata una spiegazione al riscaldamento osservato nelle Alpi centrali ed occidentali. La spiegazione classica per il riscaldamento durante la formazione di una catena montuosa è che il calore sia generato dal decadimento degli isotopi dei minerali radioattivi, presenti in quantità relativamente grandi nella crosta terrestre. Questo effetto può essere aumentato dall'accumulo di materiale radioattivo in una zona di subduzione, ove una placca litosferica scorre sotto ad un'altra. Una spiegazione alternativa per la produzione di calore è la rotture della placca inferiore in una zona di subduzione (slab breakoff). La parte distaccata della placca affonderebbe nel mantello lasciando un vuoto riempito da un flusso di materiale mantellico caldo. Tramite modellizzazioni fatte utilizzando il computer queste due ipotesi sono state confrontate, come sopra brevemente descritto (si veda il cap. 6).

In un primo momento i modelli sono stati applicati al caso delle Alpi centrali perché in questa regione la collisione tra le due placche è avvenuta ortogonalmente, il che ci permette di utilizzare una geometria bidimensionale per il modello. I risultati della modellizzazione indicano che entrambi i meccanismi possono generare abbastanza calore. La differenza tra i due processi è che il riscaldamento per decadimento radioattivo richiede un tempo maggiore che la rotture della placca sottostante (breakoff), mentre non c'è abbastanza tempo per accumulare un cuneo di materiale radioattivo sufficiente da permettere il riscaldamento per decadimento. L'episodio di riscaldamento osservato nelle Alpi Centrali può essere pertanto spiegato meglio attraverso un meccanismo di breakoff della placca inferiore.

Nelle Alpi occidentali la geometria della zona di collisione è più complessa. A causa della forma arcuata delle Alpi, la placca discendente si muove obliquamente, e non perpendicolarmente, rispetto al contatto tra le due placche litosferiche. Sembra molto probabile che le rocce nelle Alpi Occidentali si siano riscaldate a causa del breakoff della placca litosferica nelle Alpi Centrali. Le rocce del Gran Paradiso, in seguito a tale rottura, si mossero orizzontalmente e verticalmente allontanandosi sempre più dalle rocce che sono oggi esposte nelle Alpi Centrali rispetto a quelle cui erano vicine al momento del riscaldamento.

Come esattamente le rocce siano state trasportate in superficie rimane ancora oscuro,

ma questo "trasporto" è sicuramente avvenuto a velocità (geologicamente parlando) elevate. Uno scenario possibile, ottenuto combinando informazioni diverse sulle Alpi, la loro storia e la loro evoluzione, è qui delineato: forze di galleggiamento dovute alle differenze di densità "spingono" le rocce dalle più grandi profondità, fino alla base della crosta. In seguito le rocce sarebbero trasportate in superficie da cosiddetti fenomeni di "corner flow" (flusso laterale) o "wedge flow" (flusso all'interno di un cuneo orogenico). Alla base del cuneo, in sezione verticale, porzioni di materiale crostale continuano ad aggiungersi e spingono le rocce sovrastanti verso l'alto. Per compensare l'aumento di pendenza del cuneo dovuto alla continua aggiunta di materiale le rocce delle porzioni superiori fluiscono di lato, permettendo la risalita delle rocce profonde fino alla superficie. La rottura della placca al di sotto del cuneo orogenico può anch'essa giocare un ruolo nel trasporto verso la superficie di queste rocce, ma questo ruolo non è ancora stato capito. E' tuttavia chiaro che questi processi hanno contribuito in maniera significativa all'evoluzione termica delle aree studiate.

Abstract

There are two major and currently unresolved issues in Alpine geology concerning the metamorphic evolution of the rocks in the internal zones of the Alps. First, rocks showing evidence for geologically young, high-pressure to very high-pressure metamorphism are now exposed at the Earth's surface, implying exhumation from depths as much as 100 km in a belt less than 250 km wide. Secondly, these high-pressure rocks, in places, show evidence for significant re-heating during their ascent, a phenomenon known in the central Alps as the Lepontine metamorphism.

This thesis addresses geological evidence for these two features in rocks from the Alps, and investigates possible causes. This is done by a combination of detailed field-based studies involving reconstruction of pressure-temperature-time (PTt) trajectories of pertinent rocks, and numerical modelling of processes that may explain a re-heating during exhumation. The PTt paths serve as constraints on numerical modelling results, and allow testing of contending hypotheses regarding possible causes for heating during exhumation of the high-pressure rocks in the Alps.

Three areas in the metamorphic Pennine Zone of the Alps were selected for a detailed study of their metamorphic (PT) histories. These areas, in the Lepontine gneisses near Alpe Arami in the central Alps, the Gran Paradiso basement in the western Alps, and the Voltri massif in the Ligurian Alps, respectively, were chosen at spatial intervals of the order of 150 kilometres measured along the Alpine arc, in order to obtain an orogen-scale insight in similarities and differences in metamorphic evolution of the rocks in question.

The present study of the Lepontine gneisses surrounding the Alpe Arami garnet peridotite body in the central Alps focuses on thermal information, obtained from a sliver of pelitic rocks from the Cima Lunga nappe as well as from metabasic rocks in the surrounding Arbedo zone. The rocks underwent high-pressure metamorphism at peak pressures of up to 21 kbar[1], equivalent to depths in excess of 70 km, and temperatures of around 900 °C. Recent geochronological studies suggest an age of this stage of metamorphism around 37 to 40 Ma. The rocks subsequently cooled below about 650 °C during initial exhumation at rates of at least 7 mm/yr. The rocks were re-heated by about 110 °C around 32 Ma ago, leading to medium-pressure, high-temperature metamorphism at pressures of 4 to 6 kbar equivalent to depths around 20 km, and climax temperatures up to 760 °C. Final exhumation to the Earth's surface occurred at slower rates of about 0.8 mm/yr.

The metamorphic history of the Gran Paradiso massif in the Italian western Alps is somewhat similar. High-pressure metamorphism took place at conditions of 525 °C and 12 to 14 kbar, equivalent with depths of some 50 km, around 43 million years ago. Initial decompression was fast, at an estimated average rate of 3.3 mm/yr, and was accompanied by cooling. At around 20 kilometres depth the rocks were re-heated by a few tens of degrees, reflected by medium-pressure, medium-temperature

[1] *1 kbar = $1 \cdot 10^8$ Pa = 100 MPa. Although the kilobar is not an S.I. unit it is used in this thesis, because it is customarily used in the geological literature.*

metamorphism at 6 kbar and 550 °C. On the basis of geochronological studies by other workers this re-heating is inferred to have occurred shortly before 34 Ma. Final exhumation occurred at a slow rate of 0.6 mm/yr.
A tectonic mélange in the Voltri massif in the Ligurian Alps of Italy contains blocks of eclogitic metagabbro. Thermobarometric studies of these rocks indicates that metamorphism culminated at pressures of about 18 kbar, equivalent with depths of 65 km, and temperatures of around 525 °C. There are no geochronological data available to constrain the age of this high-pressure metamorphism. Peak metamorphic conditions were followed by continuous cooling during decompression, initially at relatively high P/T ratios, i.e. along a low thermal gradient, followed by eventual exhumation along a distinctly higher thermal gradient. The lack of age data, however, precludes quantification of the cooling and exhumation rates involved. Deposition of continental sediments on exhumed high-pressure rocks in the Voltri massif indicates that the Voltri massif was exposed at the Earth's surface by 34 Ma.
Plausible causes for the re-heating observed in the central and western Alps are explored, and two hypotheses are selected that, at least qualitatively, seem capable to provide the heat explaining the observed thermal evolutions during exhumation: detachment or breakoff of the subducted slab, and heating by accreted radiogenic material (TARM). Thermomechanical numerical modelling of these two hypotheses allows comparison of their thermal implications with the PTt trajectories reconstructed for the metamorphic rocks in the study areas selected. Modelling results show that re-heating in the central Alps may have been caused by slab detachment, whilst the timescale implied by the geochronological data precludes the observed re-heating to be caused by radiogenic heating due to the presence of a TARM wedge. Due to oblique convergence, block rotations and out-of-section transport, conclusions cannot be drawn in a straightforward manner for the case of the western Alps. Again, the available age data preclude re-heating in the western Alps in response to the presence of a TARM wedge, but a possible role of slab detachment is difficult to confirm or discard. On the basis of existing evidence for large-scale transpression, and changes in convergence direction I propose as a possible explanation that the Gran Paradiso rocks experienced their moderate re-heating in a position much closer to the Lepontine gneisses of the central Alps, prior to tectonic transport toward their present-day position in the western Alps.
This study does not provide constraints regarding the precise kinematics or dynamics underlying the exhumation of the high-pressure to very high-pressure rocks. Inasmuch as these rocks reached subcrustal depths, a tentative scenario involves buoyancy-driven exhumation to the base of the crust, followed by further exhumation via corner flow in the orogenic wedge driven by continuous underplating of subducting material at the base of the wedge (Platt, 1986). Changes in exhumation rates along the pressure-temperature-time trajectories in both the central and western Alps may point to a combination of exhumation mechanisms. Slab detachment, inferred to have taken place in the central Alps, with implications for the thermal evolution of rocks presently exposed in the western Alps, can explain the re-heating observed in these areas, but its role in the exhumation of the high-pressure rocks is, as yet, unclear.

Chapter 1

Introduction

1.1 Scope of this study

The Alps of southern Europe are without doubt the most extensively studied mountain chain on Earth. However, despite the wealth of geological and geophysical data on the Alps accumulated over the last two centuries, its evolution is still not completely understood and many debates remain.

One key issue of current interest and focus of many recent studies concerns the occurrence of high-pressure and very high-pressure metamorphic rocks in the internal zones of the Alps. Some of these rocks, now exposed at the Earth's surface, are thought to have been metamorphosed at depths of more than 100 kilometres around 35 millions years ago, i.e. relatively recently in the geological history of the Alps. In view of the maximum width of the mountain belt of some 250 kilometres the exhumation of these very high-pressure rocks must be related to orogen-scale geodynamic processes. Both the kinematics and the dynamics of the processes involved in their exhumation are as yet poorly understood, while insight in these processes is of major importance to the understanding of mountain building.

The way in which high-pressure metamorphic rocks return to the Earth's surface is reflected by their pressure-temperature-time (PTt) trajectory. Documented PTt trajectories of metamorphic rocks from the Alps are often complicated, and may for instance reflect subduction or, in some cases, a deep origin, but also heating during exhumation or changes in exhumation rates. In this respect a well-known feature of the thermal history of the Alps is the Tertiary Lepontine stage of medium-pressure, high-temperature metamorphism in the central Alps, superimposed on earlier metamorphic assemblages (Niggli and Niggli, 1965; Todd and Engi, 1997; Wenk, 1956). In addition, details of PTt paths of metamorphic rocks documented in the Alps vary with position along the length of the orogen. Marked temperature increases during exhumation are currently reported from several units in the internal western Alps (Borghi et al., 1996; Rolland et al., 2000), indicating that Lepontine metamorphism may have affected the rocks in the internal Alps on a much wider scale than previously thought. As metamorphic pressures and the thermal evolution during decompression reflect orogen-scale geodynamic processes, such features of metamorphic PTt trajectories may help to discriminate between different geodynamic hypotheses. This emphasises the need for detailed study of the pressure and temperature evolution of metamorphic rocks during their exhumation, rather than assessment of peak pressure or temperature conditions alone.

Against this background, the primary aims of this study are to assess the nature, distribution and cause of the Lepontine metamorphism via careful structural and metamorphic study of rocks from the internal zones, and a subsequent quantitative modelling of hypotheses regarding Lepontine metamorphism, in which the regional context of the study areas is taken into account.

1.2 Approach

A twofold approach was taken in this study. Three study areas in the metamorphic Pennine Zone of the Alps (fig. 2.1) were selected for a detailed study of their metamorphic (PT) history. These areas, located in the Lepontine gneisses near Alpe Arami in the central Alps, the Gran Paradiso basement in the western Alps, and the Voltri massif in the Ligurian Alps, were chosen at spatial intervals of the order of 150 kilometres measured along the Alpine arc, in order to obtain an orogen-scale insight in similarities and differences in the metamorphic evolutions of the rocks in question. Each of these areas was known to contain high-pressure metamorphic rocks, while peak temperatures during decompression were known to be variable.
The area in the central Alps was chosen first because it may be held representative for the metamorphic history of Lepontine area in the central Alps, and secondly because of recent interest in evidence for ultra-high pressures recorded in the Alpe Arami peridotite body. The study area in the Gran Paradiso basement of the western Alps was selected because the massif occupies a tectonic position similar to that of the southerly Dora Maira massif where mineralogical and metamorphic studies in the early eighties have documented very-high pressure assemblages in continental rocks (Chopin, 1984; Hirajima and Compagnoni, 1995). In addition, the recent ECORS-CROP deep seismic section crosses the Gran Paradiso massif (Roure et al., 1996; Roure et al., 1990), and potentially provides additional data on the orogen scale geometry in that region. The eclogitic metagabbro blocks of the Voltri tectonic mélange were principally selected to search for possible very-high pressure metamorphic assemblages, as well as to extend present insight in similarities and differences in pressure-temperature evolutions at the scale of the Alpine arc.
Finally, the PTt trajectories instigate an inventory of possible causes for metamorphic history, with particular reference to heat sources. Results of quantitative modelling of potentially viable mechanisms are confronted with our observations and discussed within their regional tectonic context.

1.3 Outline of this thesis

Chapter 2 of this thesis provides a brief introduction to the plate tectonic setting and geometry of the Alps. The core of the thesis is made up of two parts: Chapters 3 to 5 report results of the field-based studies, while Chapter 6 is concerned with numerical modelling.
Chapter 3 documents the structural and metamorphic evolution of the country rock gneisses and schists surrounding the Alpe Arami garnet peridotite body, which form part of the Lepontine gneisses in the central Alps. Chapter 4 reports on the structural and metamorphic history of the Gran Paradiso massif in the western Alps. Chapter 5 concerns the metamorphic evolution of eclogitic metagabbro blocks from a tectonic mélange in the Voltri massif of the Ligurian Alps. Thermobarometric methods applied

in Chapters 3, 4 and 5 are outlined in Appendix 1, and Appendices 2, 3 and 4 list mineral assemblages of the studied samples and representative electron microprobe analyses of most of the observed minerals, as well as all analyses used to reconstruct the pertinent PTt trajectories.

Chapter 6 is concerned with numerical models of the thermal evolution of convergent continental plate margins. The modelling results are confronted with the PTt trajectories obtained in the previous three chapters, and with geochronological and kinematic data documented in the literature. Chapter 7 presents the main conclusions of this study, and suggestions for future research.

Chapters 3, 4, 5 and 6 were written as self-standing entities, intended to be published as separate papers. As a result some repetition was inevitable.

Chapter 2

Introduction to Alpine geology

2.1 Plate tectonic setting

The Alps are part of the Alpine-Himalayan mountain chain, formed from the Cretaceous onward in response to convergence of the African and Indian subcontinents to the south and Eurasia to the north. These continental masses became separated during Mesozoic breakup of the Pangean supercontinent, the late-Variscan assembly of all six present-day continents formed by previous convergence and collision of Gondwana and Laurasia in Paleozoic times (Ricou, 1994). Breakup of Pangea led to the formation of the Neotethys ocean between Eurasia to the north and Africa to the south which, during the Jurassic, became connected with the gradually widening Atlantic in between the Americas to the west and Africa and Eurasia to the east (fig. 2.1; Frisch, 1981; Ricou, 1994).

Paleogeographical reconstructions of the Tethys ocean on smaller and larger scales have been widely discussed (e.g. Dercourt et al., 1993; Ricou, 1994; Stampfli, 1993; Stampfli and Marchant, 1997). The geometry of the Mediterranean Tethys was not that of a single oceanic basin between two plates of continental lithosphere, but was complicated by the presence of several continental fragments, of which Adria, the northern part of Apulia, played a major role in the formation of the Alps. Apulia can be considered as an African promontory (Ricou, 1994), although there is evidence that it rotated independently between 130 and 80 Ma (Westphal et al., 1986) as well as since 35 Ma (e.g. Thomas et al., 1999). The part of the Neotethys in between Adria and the southern margin of Eurasia is generally called the Piemonte-Ligurian ocean. The Alps formed as the direct result of subduction of the Piemonte-Ligurian ocean and eventual collision of the southern margin of Eurasia and the northern margin of Adria, while the arcuate shape of the belt became accentuated by westward movement of the indenting continental fragments (e.g. Vialon et al., 1989). The geometry of the Piemonte-Ligurian ocean is commonly thought to be further complicated by the presence of the Briançonnais ribbon continent south of the Eurasian margin, separated from the Eurasion continent by the possibly oceanic Valais basin. The Briançonnais is considered to have been connected to Europe to the south-west (e.g. Stampfli and Marchant, 1997).

2.2 Geometry of the Alps

Geologists have studied the Alps for about two centuries now. The existence of large-scale thrust slices in the Alps was first identified by Arnold Escher von der Linth (1841) in the Glarner Alps. The large-scale structure of the Alps became only gradually clear by systematic mapping of the Alps until the early twentieth century, when Emile Argand summarised the structure of the Alps in orogen-scale structural cross-sections (e.g. Argand, 1916). Insight in the present-day geometry of the Alps has been strongly

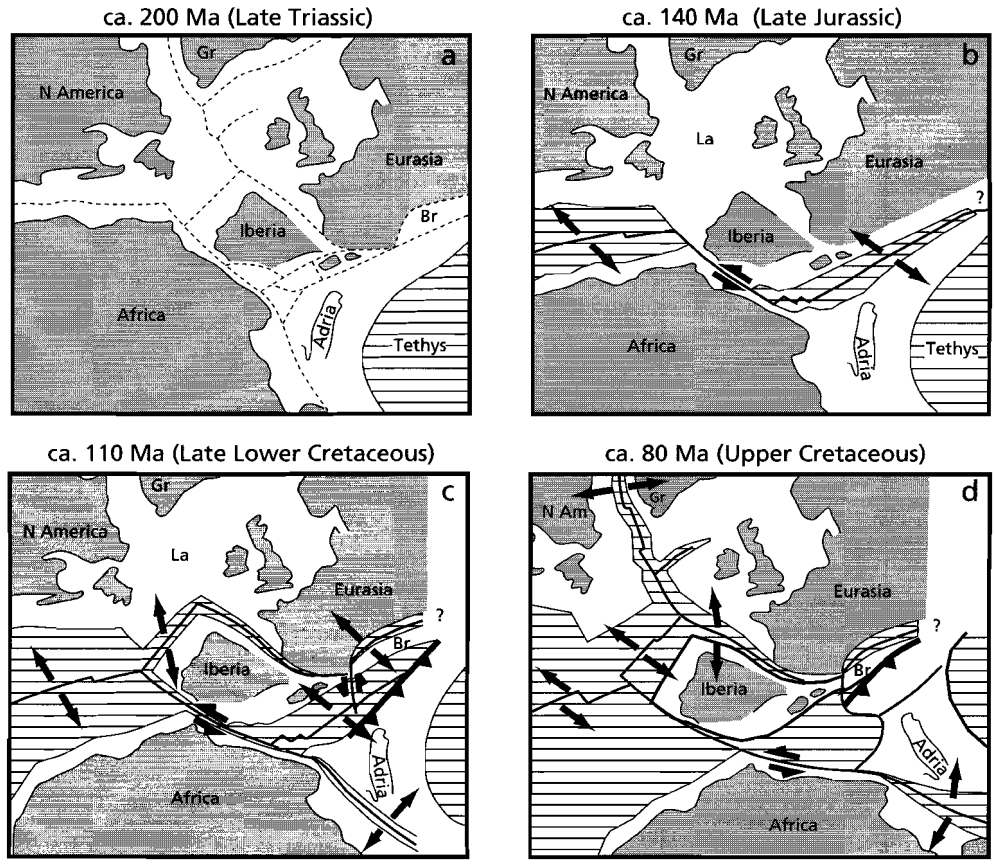

Figure 2.1: Simplified paleogeography of the Tethys and early Atlantic oceans. Time slices at **a.** 200 Ma, **b.** 140 Ma, **c.** 110 Ma and **d.** 80 Ma. Modified after Frisch (1981). Br = Briançonnais, Gr = Greenland, La = Laurasia.

enhanced by large-scale deep seismic sounding of the western (Roure et al., 1996; Roure et al., 1990) and central Alps (Pfiffner et al., 1997). In map view, the geometry of the Alps seems at first inspection relatively simple (fig 2.2), being characterised by three essentially concentric domains made up of the Helvetic, Penninic and Austro-Alpine nappe complexes. Each of these domains contains a basement made up of rocks affected by Variscan deformation, metamorphism and mainly granitic intrusion, separated by an unconformity from a cover sequence of Mesozoic and Tertiary sediments. Aside this roughly concentric arrangement, there is also a systematic vertical relationship in that rocks of the Penninic Zone tectonically overly those of the Helvetic domain, while Austro-Alpine rocks in turn overly rocks of the Penninic zone.

The western and central Alps are largely made up of Helvetic and Penninic basement and cover nappes, while the Austro-Alpine units in this part of the chain are limited to the Dent-Blanche and Monte Emilius klippen and the relatively small Sesia-Lanzo slice

in the internal part of the arc. In the eastern Alps, the Austro-Alpine units form an orogenic lid thrust over the Penninic rocks that are exposed in the tectonic windows of the Engadine Alps and the Hohe Tauern massif.
The Helvetic and Penninic units are believed to represent the shelf and slope to oceanic domains of the Eurasian continental margin, respectively (e.g. Hsü, 1989). The Austro-Alpine nappes and the southern Alps represent the margin of Adria (fig 2.1), separated in Jurassic times from the Eurasian continent by the Piemonte-Ligurian ocean, relics of which are now exposed in ophiolitic rocks preserved in the structurally highest, presumably most internal parts of the Penninic zone (e.g. Schmid et al., 1996). As indicated above, a relatively narrow basin, the Valais basin, separated the Briançonnais ribbon continent from the southern Eurasian margin (Stampfli, 1993). This basin was underlain by thinned continental and possibly incipient oceanic crust (e.g. Florineth and Froitzheim, 1994). To the south, the Periadriatic fault system separates the Alps from the Southern Alps, which represent portions of the Adrian margin that were only affected by late-orogenic brittle thrusting during the Miocene (e.g. Schönborn, 1992).
Rocks of the Penninic basement underwent Eoalpine high-pressure (between 30 and 90 km depth; e.g. Compagnoni and Lombardo, 1974) or ultra-high pressure (over 100 km

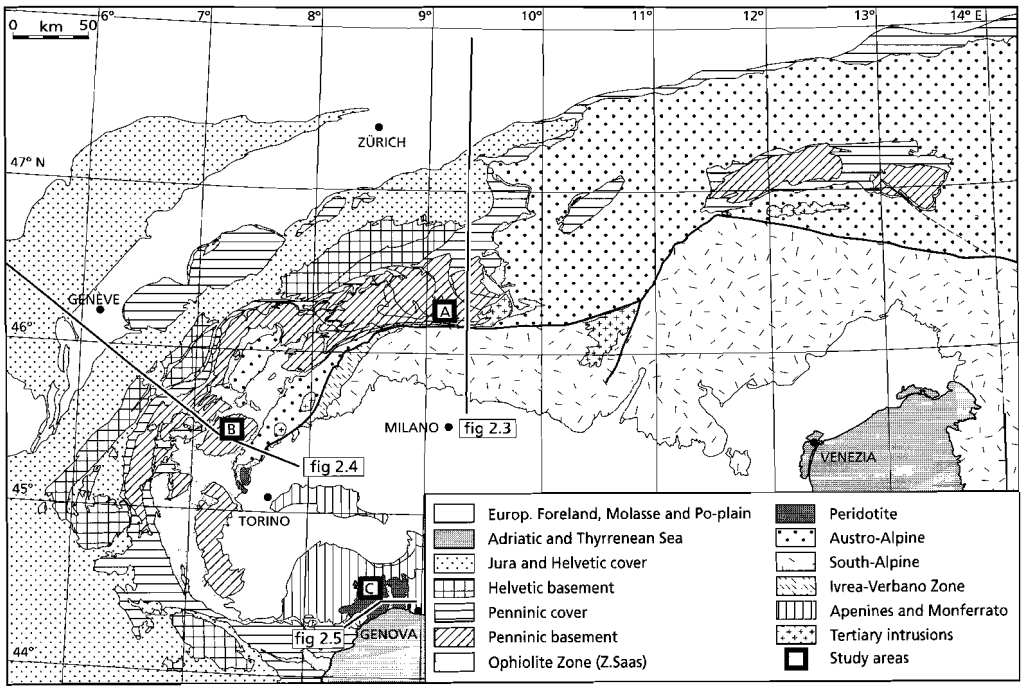

Figure 2.2: Tectonic map of the Alps, modified after Bigi et al. (1983), indicating the locations of the cross sections shown in figures 2.3 to 2.5, and locations of the three areas selected for detailed study: A = Lepontine gneisses (Chapter 3), B = Gran Paradiso (Chapter 4), C = Voltri mélange (Chapter 5).

depth; Chopin, 1984) metamorphism during Alpine convergence, while the rocks of the ophiolite zone were also metamorphosed at high (e.g. Messiga and Scambelluri, 1991) to ultra-high (Reinecke, 1991) pressures. Rocks presently exposed in the Alps were metamorphosed at high pressures from possibly as early as the Late Cretaceous, until some 40 Ma. Large volumes of these high pressure metamorphic rocks subsequently became subject to exhumation and, in the central Alps, were overprinted by Lepontine medium-pressure, high-temperature metamorphism during the Eocene before eventual exhumation to the Earth's surface.

2.3 Structure of the central and western Alps

Although, or possibly because the Alps are by far the most intensively studied mountain belt, there are still many questions and associated debates regarding its origin and evolution. This includes issues such as the number of oceanic basins involved in Alpine subduction (e.g. Channell and Kozur, 1997; Froitzheim et al., 1996), the age of the (very) high-pressure metamorphism (e.g. Desmons et al., 1999; Rubatto and Gebauer, 1999), the origin and significance of some of the ultramafic fragments in the Penninic zone (Green et al., 2000; Trommsdorff et al., 2000), and the mechanism(s) by which high-pressure metamorphic rocks were exhumed (e.g. Avigad, 1996; Michard et al., 1993; Von Blanckenburg and Davies, 1995). The present study is focussed on the thermal history of rocks from the Penninic zone during their exhumation from the deep levels associated with high-temperature, low-pressure metamorphism, and the possible geodynamic significance of this thermal history. This involved detailed study of the structure and metamorphism of rocks of the Penninic zone exposed in three study areas in different parts of the Alps arc, namely, the central, western and Ligurian Alps (fig. 2.2). The large-scale structural geometry of the Alps in these different areas is summarised in some detail below.

2.3.1 The central Alps

A simplified representation of the results of the NRP-20 East, a recent large-scale geophysical study of the central Alps (Pfiffner et al., 1997), is shown in the cross-section of figure 2.3. A wedge of Adriatic mantle is indented in between the European upper and lower crust, facilitating southward (back)thrusting of both European and Adriatic upper crustal basement and cover nappes. The Piemonte-Ligurian oceanic realm is represented to a limited extent in this section. Middle Penninic nappes like the Adula and Simano units underwent Alpine high-pressure metamorphism. More external units were affected by greenschist metamorphism, but in an area up to about 40 kilometres north from the Insubric line, high pressure rocks were overprinted by amphibolite to granulite facies metamorphism (e.g. Engi et al., 1995; Todd and Engi, 1997), before being exhumed in late Tertiary times (Hunziker et al., 1989). Comprehensive reviews of the evolution of the central Alps have been published by Schmid et al. (1996) and Steck and Hunziker (1994), among others.

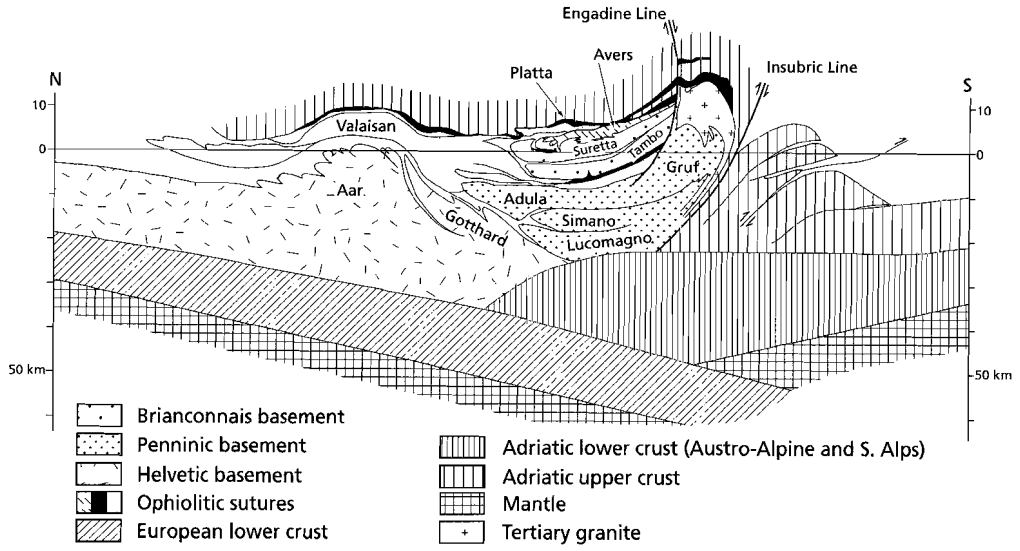

Figure 2.3: Simplified structural cross section along the NRP-20 East, and the EGT geophysical profiles in central southern Switzerland. Location in figure 2.2; modified after Schmid and Kissling (2000).

2.3.2 The western Alps

A cross-section through the western Alps, along the WNW-ESE oriented ECORS-CROP geophysical profile (Roure et al., 1996; Roure et al., 1990) shows that the geometry is markedly different from that in the central Alps (fig 2.4). In the western Alps the Ivrea body represents a slice of Adriatic mantle material, that acted as a rigid buttress with respect to the advancing European lithosphere. Wedging of the European lower crust caused NW-ward thrusting of the internal units. The core of the western Alps is made up of the Internal Penninic Nappes nappes (IPN; i.e. from north to south, the Monte Rosa, Gran Paradiso and Dora Maira massifs). Some workers have argued that the Internal Penninic Nappes of the western Alps originate from the Briançonnais ribbon continent off the Eurasian margin (e.g. Radelli and Desmons, 1987; Stampfli, 1993) or even that they were derived from the northern margin of Adria (e.g. Hunziker et al., 1989; Stampfli and Marchant, 1997), such that the provenance of the Internal Penninic is currently a matter of debate. Units to the north-west of the IPN are considered to be derived from the Valais oceanic basin and the European margin, while the units on top and east of the IPN are generally believed to originate from the Piemonte-Ligurian ocean and Adria. A detailed discussion of the large-scale tectonics of the western Alps was recently published by Schmid and Kissling (2000). These authors emphasise that the western and Ligurian Alps show significant rotation, oblique convergence and out-of
section movements (e.g. Schmid and Kissling, 2000; Thomas et al., 1999). During the early stages of collision of Adria with the European plate (50-35 Ma), the NNE-SSW

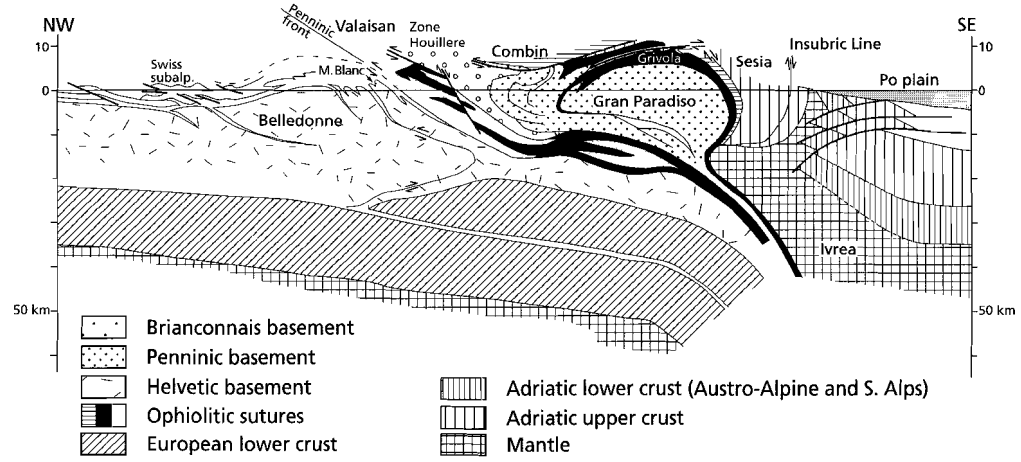

Figure 2.4: Simplified structural cross section along the ECORS-CROP geophysical profile across the Franco-Italian border in the western Alps. Location in figure 2.2; modified after Schmid and Kissling (2000).

segment of the plate margin formed a zone of sinistral transpression (e.g. Schmid and Kissling, 2000; Stampfli and Marchant, 1997), to accommodate the northward movement of Adria. After 35 Ma ago, the movement of Adria with respect to the European plate is inferred to have shifted to a north-westerly direction, leading to another 100 kilometres of shortening along the ECORS-CROP seismic section (Schmid and Kissling, 2000).

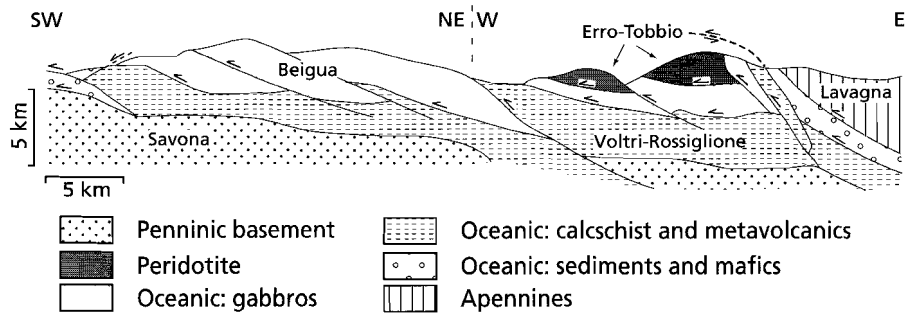

Figure 2.5: Simplified structural cross section across the Voltri Massif in the Ligurian Alps of Italy. Location in figure 2.2; modified after Hoogerduijn Strating (1994).

2.3.3 The Ligurian Alps

There are, unfortunately, no large-scale deep seismic data documenting the crustal-scale structure of the Ligurian Alps. The profile in figure 2.5 shows a diagrammatic cross-section across the Voltri Massif, a large ophiolite massif situated near the transition between the Alps and the Apennines containing ubiquitous evidence of Alpine high-pressure metamorphism. The rocks of the Voltri Massif are currently thought to represent part of a wedge that formed on top of a Paleocene, intra-oceanic subduction zone (Hoogerduijn Strating, 1994), thrusted onto the European margin, represented in this part of the Alps by the Savona unit to the west. No deep crustal rocks of the margin of Adria are exposed in the area, and the location of the Voltri massif near the transition from the Alps to the Apennines renders paleogeographic interpretations difficult.

Chapter 3

Metamorphic history of the Lepontine gneisses around Alpe Arami, southern Switzerland

3.1 Abstract

The metamorphic history of the gneisses, metapelites and eclogites surrounding the Alpe Arami garnet peridotite body (central Alps, Switzerland) has been characterised with the aim to place constraints on the geodynamic processes underlying the tectonothermal history of the area. This involved small-scale mapping of structures and lithologies, as well as a detailed study of the petrography, mineral chemistry and thermobarometry of selected samples.

The rocks studied are commonly grouped into the Cima Lunga nappe and Arbedo zone. My results indicate that the Lepontine gneisses of the Cima Lunga nappe as well as those from the Arbedo zone underwent high-pressure metamorphism ($P \geq 21$ kbar[1]), and that these units may have been juxtaposed at depth. After cooling during initial decompression the rocks were heated by about 110 °C during Lepontine metamorphism. Spectacular symplectitic microstructures in amphibolites of eclogitic origin, as well as the occurrence of cordierite in a metapelite from the Cima Lunga nappe indicate that the temperature during the peak of the Lepontine overprint became as high as 740 °C at pressures of 4-6 kbar, which is higher than previously estimated. Initial exhumation after the peak of high-pressure metamorphism was very fast, but the underlying mechanism is poorly understood. In contrast, final exhumation following Lepontine metamorphism was relatively slow and was probably accommodated by tectonic uplift related to dextral transpressive movements and development of the steep root zone along the Insubric Line, and concomitant erosion.

3.2 Introduction

3.2.1 Geology of the Lepontine Alps

The Lepontine gneiss dome of the central Swiss Alps has been subject of numerous regional and detailed studies of its structure and regional metamorphism. However, the extent of the high-pressure metamorphism, the origin and history of peridotite bodies enclosed in the gneisses, and the nature and cause of the Lepontine amphibolite facies metamorphism are still matters of debate. The rocks investigated in this study belong to a sequence of high-grade gneisses, migmatites and pelitic schists enclosing lenses and bands of mafic eclogites. The gneisses enclose the Alpe Arami garnet peridotite body (outcrop about 1 km long and 400 m wide) in the southern part of the Lower Penninic

[1] *1 kbar = $1 \cdot 10^8$ Pa = 100 MPa. Although the kilobar is not an S.I. unit it is used in this thesis, because it is customarily used in the geological literature.*

Cima Lunga nappe (fig 3.1, 3.2). The origin and significance of the 100 m scale Alpe Arami peridotite is subject of debate as discussed below. The gneisses bordering the Cima Lunga nappe to the SE are part of the Mergoscia Arbedo zone (henceforth Arbedo zone), which itself is supposedly part of the lower Penninic Antigorio nappe (Fischer, 1974).

Prior to Alpine orogeny the lower Penninic nappes were part of the basement of the southern margin of the European plate (Pfiffner and Trommsdorff, 1998; Schmid et al., 1997). Like the structurally equivalent Adula nappe (fig 3.1), the Cima Lunga nappe underwent high-pressure metamorphism (e.g. Heinrich, 1986; Meyre et al., 1999) indicating that these units were deeply subducted. Likewise, rocks from the Arbedo zone contain relics of eclogite facies assemblages (Bocchio et al., 1985; Möckel, 1969). Eclogites surrounding the Alpe Arami garnet peridotite body have yielded a 37.5 Ma age for high-pressure metamorphism (Becker, 1993), and similar ages have been obtained from within the peridotite body (Gebauer, 1996; Gebauer, 1999). These results are at variance with earlier geochronological studies indicating that high-pressure metamorphism occurred during Cretaceous times (e.g. Hunziker et al., 1989). The validity of these Cretaceous ages for the high-pressure metamorphism has been questioned by several groups (Engi et al., 1995; Frey and

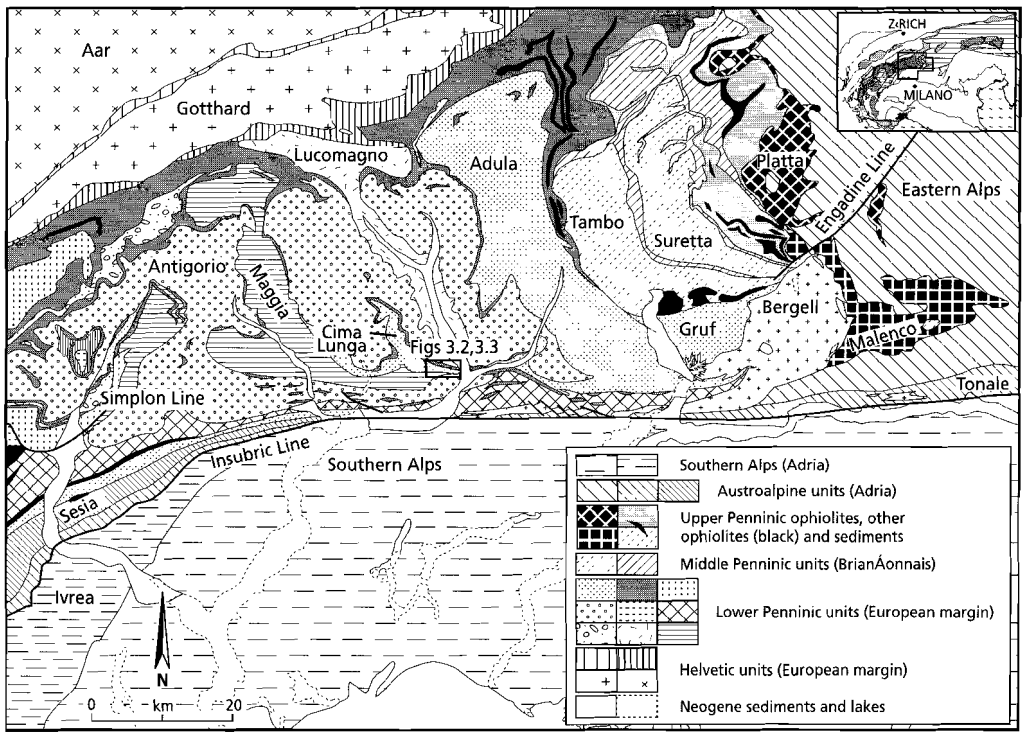

Figure 3.1: Tectonic map of the Central Alps. After Spicher (1980) and Pfiffner and Trommsdorff (1998).

Ferreiro Mählmann, 1999; Schmid et al., 1997), and there is growing evidence that high-pressure metamorphic conditions in the Alps prevailed well into the Eocene (e.g. Amato et al., 1999; Duchêne et al., 1997).
After collision of the European and African margins and the related high-pressure metamorphism, the lower Penninic nappes were exhumed. Hypotheses proposed for the process driving exhumation include buoyant rise caused by slab-breakoff (Davies and Von Blanckenburg, 1995) as well as several extensional models (e.g. Merle, 1994), generally in combination with unroofing by erosion. This aspect of the history of the Central Alps is poorly understood, and the hypotheses proposed so far are still subject of scientific scrutiny (Schmid et al., 1997).
It is clear, however, that after exhumation to relatively shallow levels the lower Penninic nappes were subjected to high-temperature metamorphism. In the central part of the so-called Lepontine gneiss dome (Wenk, 1956) peak metamorphic temperatures became as high as 675 °C at pressures of 6 to 8 kilobars (e.g. Engi et al., 1995; Frey et al., 1980; Frey and Ferreiro Mählmann, 1999; Todd and Engi, 1997). This episode in the metamorphic history is generally referred to as the Lepontine metamorphism. Metamorphic isograds related to this stage of metamorphism cut across nappe contacts, indicating that the nappe stack had essentially acquired its present-day sequence prior to peak-Lepontine metamorphism. There is no evidence of any appreciable compression or extension of the isograds by faulting sub-parallel to the nappe boundaries (Engi et al., 1995).
The peak of Lepontine metamorphism has been dated around 33 Ma (Gebauer, 1996), and cooling ages have been obtained using several methods: Rb-Sr on white mica (cooling below 500 °C) yields around 24 Ma, Rb-Sr on biotite (below 300 °C) yields about 10 Ma, zircon fission track (below 225 °C) about 18 Ma and apatite fission track indicates cooling below 100 °C at 6.9 Ma (Hunziker et al., 1992; Hunziker et al., 1997; Hurford, 1986; Hurford et al., 1989; Wagner et al., 1977). The cause of Lepontine metamorphism is not well understood. Radiogenic self-heating of the thick nappe pile was thought to be the most plausible mechanism (Hunziker et al., 1989; Vance and O'Nions, 1992), but with the growing amount of Eocene ages for high-pressure metamorphism this hypothesis has become untenable: the short time-span of the order of about 5 Ma between high-pressure metamorphism and the peak of the Lepontine event seems too short to allow any significant radiogenic heating at a regional scale. There is growing agreement that a process in the upper mantle below the developing orogen may have caused regional advection of heat (Frey and Ferreiro Mählmann, 1999; Schmid et al., 1997) Detachment of the subducted continental lithosphere as proposed by Wortel and Spakman (1992) and Von Blanckenburg and Davies (1995) is currently thought to be a viable mechanism to explain the Eocene Lepontine metamorphism and magmatism.
Unroofing of the Lepontine Alps is commonly ascribed to collisional and post-collisional backfolding and subsequent erosion of the nappe pile, and to sinistral oblique slip on the Insubric Line (Pfiffner and Trommsdorff, 1998; Schmid et al., 1997). The curvature of the nappes into the root zone (fig 3.1) and the change in orientation of lineations and foliation trends, from about NS in the north to approximately EW in the south (e.g.

Merle et al., 1989; Ring, 1992) are thought to be related to such movement along the Insubric Line.

3.2.2 The origin and history of the Alpe Arami peridotite

The Alpe Arami garnet peridotite is a lenticular body, almost a kilometre long and about 400 metres wide, enclosed in gneisses of the Cima Lunga nappe in the alpine root zone E of Bellinzona. The peridotite was first described by Grubenmann (1908) as a garnet-olivine rock. Extensive studies of the petrography (Dal Vesco, 1953) and microstructures (Buiskool Toxopeus, 1976; Möckel, 1969) of the peridotite body led to the conclusion that the peridotite was of metamorphic origin. On chemical grounds, however, a mantle origin for the peridotite body had been proposed (O'Hara and Mercy, 1966), and Den Tex (1971) showed that the petrofabrics described from the peridotite could only have been formed at pressures prevailing at mantle depths. Ernst (1977; 1981) came to similar conclusions on petrological grounds.

In the 1990's a vigorous debate was initiated by Dobrzhinetskaya et al. (1996) who reported on the presence of $FeTiO_3$ needles in olivine in an Alpe Arami sample. The orientation of these needles with respect to the host olivine, as well as the reported extremely high TiO_2 concentration (>0.6 wt%) lead the authors to propose a depth of origin in excess of 400 kilometres for the peridotite. Further work from the same group (Bozhilov et al., 1999; Dobrzhinetskaya et al., 1999; Green et al., 1997; Green et al., 2000) provided additional support to these conclusions. It was suggested that the Alpe Arami peridotite was brought to crustal depths within a lens of deeply subducted gneisses, although no further evidence was presented to support this hypothesis. Independent support for the hypothesis of a very deep origin of the Alpe Arami peridotite was provided by the thermobarometric results of Brenker and Brey (1997). These workers inferred the highest recorded metamorphic conditions of the peridotite to be around 1120 ± 50 °C and 5.0 ± 0.2 GPa. This pressure is equivalent to a depth of origin of at least 150 kilometers.

The paper by Dobrzhinetskaya et al. (1996) provoked spirited discussion. The techniques used to determine the high TiO_2 concentration were questioned (e.g. Hacker et al., 1997; Risold et al., 1997), and the solubility of TiO_2 in olivine and its high-pressure equivalents was studied experimentally (Ulmer and Trommsdorff, 1997). All of these workers argued that the features reported by Dobrzhinetskaya et al. could well have formed during decompression from about 3.0 GPa (Risold et al., 1997). Revised thermobarometry of the Alpe Arami peridotite by this group yielded maximum metamorphic conditions of 833 ± 34 °C, and 3.2 ± 0.3 GPa, equivalent to depths of about 110 kilometres (Nimis et al., 1999). The trace element geochemistry of the Alpe Arami peridotite suggests that the garnet bearing assemblage was in geochemical equilibrium (Rampone et al., 1999), supporting the equilibrium thermobarometry of Nimis et al. (1999) rather than the results of Brenker and Brey (1997), which were based on the assumption of disequilibrium. These lower maximum recorded metamorphic pressures would fit a scenario in which the Alpe Arami peridotite body initially formed part of the European continental upper mantle and was subducted during Alpine convergence (Pfiffner and Trommsdorff, 1998). The peridotite would then be trapped in a lithospheric

mélange in the subduction zone, followed by juxtaposition with its present-day country rocks during the later stages of Alpine orogenesis (Trommsdorff et al., 2000).
To date, the above debate has not been settled, which forms an additional motivation to focus this study on the rocks immediately surrounding the Alpe Arami peridotite.

3.2.3 The study area

The study area is situated in the steep root zone of the Lepontine Alps (e.g. Schmid et al., 1996) and comprises rocks from several nappes (fig 3.2; adapted from Fischer (1974) and Spicher (1980)). Below I focus on the rocks from the Arbedo zone along the road from Gorduno to Bedretto and the track leading to Alpe Arami. Much of the structural and metamorphic information described here was obtained from a lens of Cima Lunga metapelitic material enclosed in the migmatitic gneisses of the Arbedo zone. In addition, I lend special attention to metabasic lenses of both the Cima Lunga nappe and the Arbedo zone. The locations of the relevant outcrops and samples are indicated in figure

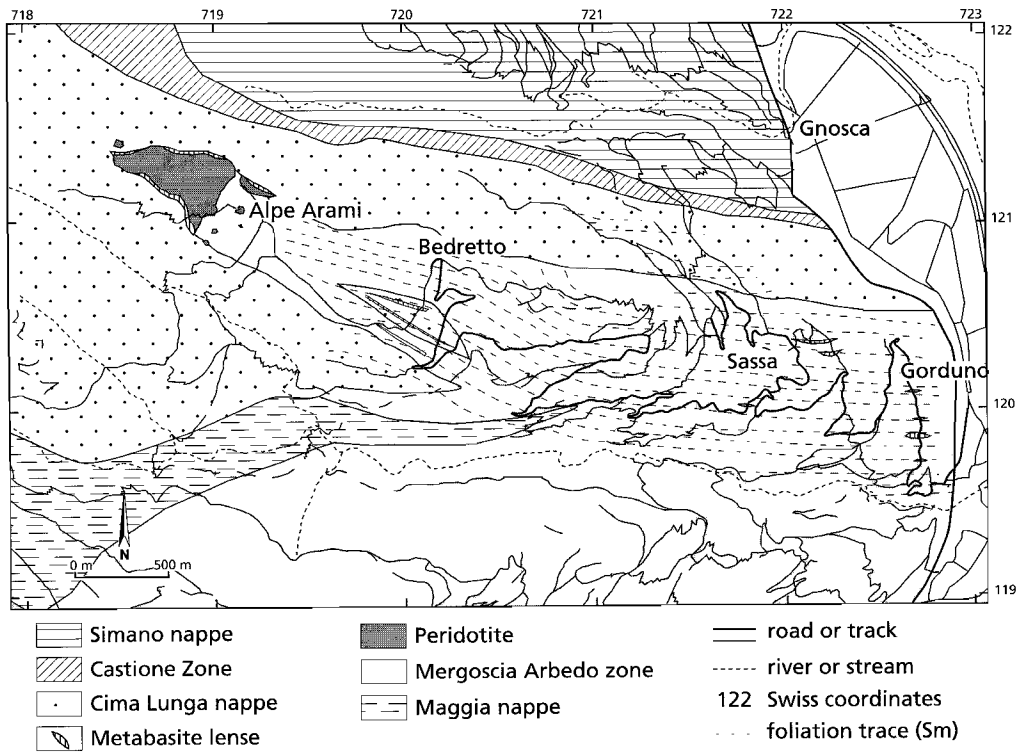

Figure 3.2: Tectonic map of the study area, after Fischer (1974) and Spicher (1980). Traces of the main-phase foliation from the present study.

3.3. The local names of the lithologies used in figure 3.3 follow the Geological Atlas of Switzerland (sheet 1313, Bellinzona; Fischer, 1980).
The Cima Lunga nappe is similar to other Penninic nappes in the Central Alps, in that it comprises an association of granitic and metapelitic gneisses including lenses of metabasites and layers of calcsilicate rock. In addition, the Cima Lunga nappe contains few lenses of garnet peridotite, including the Alpe Arami body. The Arbedo zone consists mainly of migmatitic granitic gneisses that enclose lenses of mafic eclogite as well as some layers of calcsilicate rock. The calcsilicate rocks contain variable amounts of carbonates and amphiboles. In the present study, the amphibole-bearing rocks without carbonates will be termed amphibolites. In addition, I use the term eclogite-amphibolites to denote amphibolites containing relics of an eclogitic mineral assemblage.

3.3 Structural history of the Lepontine gneisses

The structural history of the Lepontine gneisses around the Alpe Arami garnet peridotite body was only briefly described by Möckel (1969). More recent studies into the Alpine deformation focussed on the northern part of the Cima Lunga nappe (Grond et al., 1995) or even further north, on the northern parts of the Maggia and Simano nappes (Grujic and Mancktelow, 1996) and the northern parts of the Adula, Tambo and Suretta nappes (Ring, 1992). In addition, Nagel and Frey (1999) have published a preliminary report of a study into the structures of the southern Adula nappe, to which the Cima Lunga nappe is commonly considered to be equivalent.
The southern part of the Lepontine gneiss dome is dominated by a steep foliation parallel to the axial planes of tight to isoclinal folds seen in all lithologies. The strike is roughly EW. Within the study area, traces have been mapped of the main foliation and the result is shown in figures 3.2 and 3.3. Because of its dominant nature I describe this foliation as the main-phase foliation Sm, related to the main deformation phase Dm. Deformational structures developed prior to Dm are termed Dm-1, etc., whilst structures post-dating Dm are labelled Dm+1, etc. Folds related to Dm are labelled Fm, fold axes Fa_m, and foliation planes and lineations are denoted Sm and Lm, respectively.

3.3.1 Structures of the gneisses

A geological map of the study area is presented in figure 3.3. The traces of the dominant foliation (Sm, fig 3.2) show a coherent pattern of EW trending steep planes. This coherence is illustrated in figs. 3.4a and 3.4b showing stereographic projections of foliations and stretching lineations. Foliations gradually rotate towards a NW-SE strike as one approaches the garnet peridotite body. This pattern fits existing lineation maps of the Lepontine Alps. These maps show that lineations are roughly NS on the northern edge of the area and turn through NW-SE towards an EW trend near the Insubric Line, while cutting across nappe contacts (Möckel, 1969, fig 1; Ring, 1992).
The deformation history of the area is marked by the development of at least three generations of structures. This multiphase nature of the deformation is very obvious in

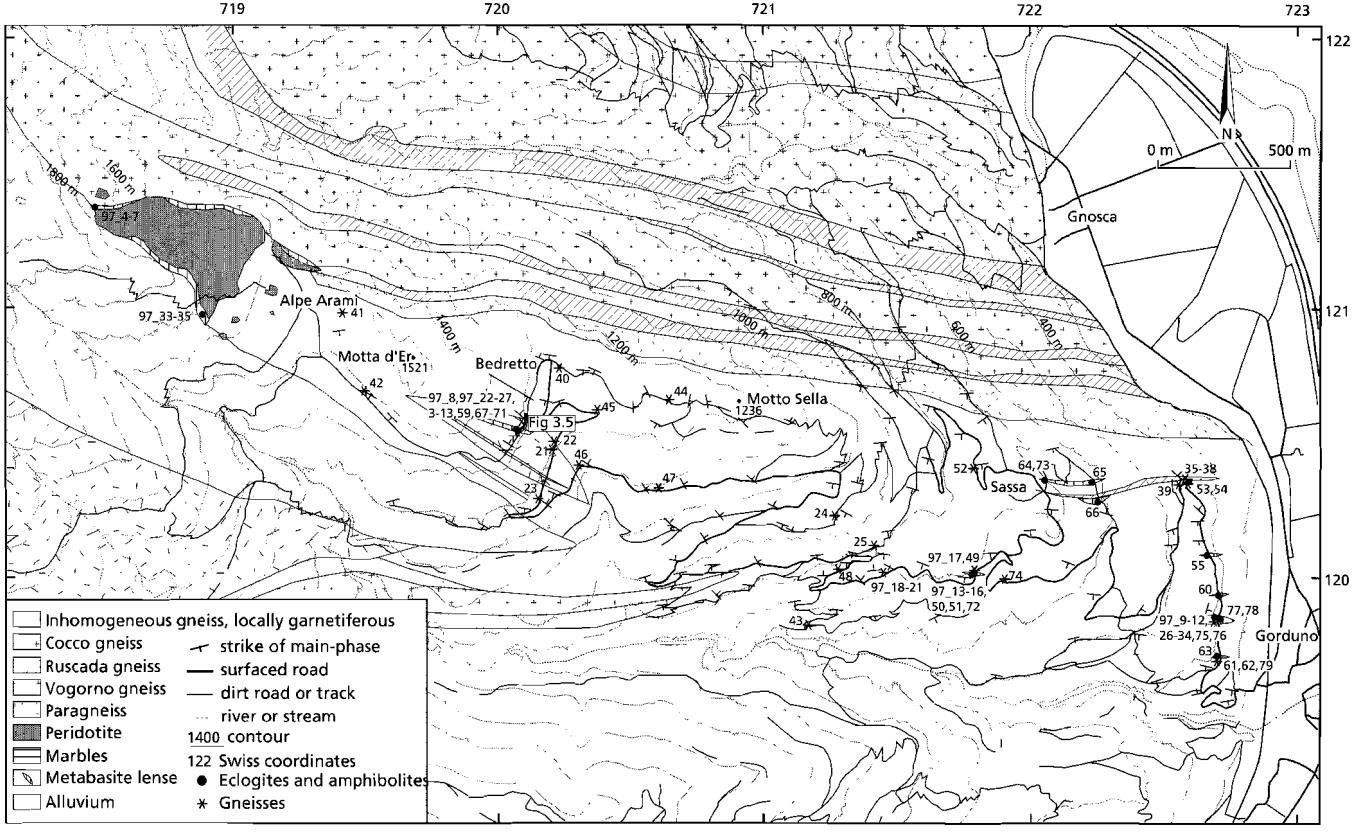

Figure 3.3: Geological map of the study area, after Fischer (1974). Strike and dip of the main foliation are indicated, as well as the locations of samples and figures.

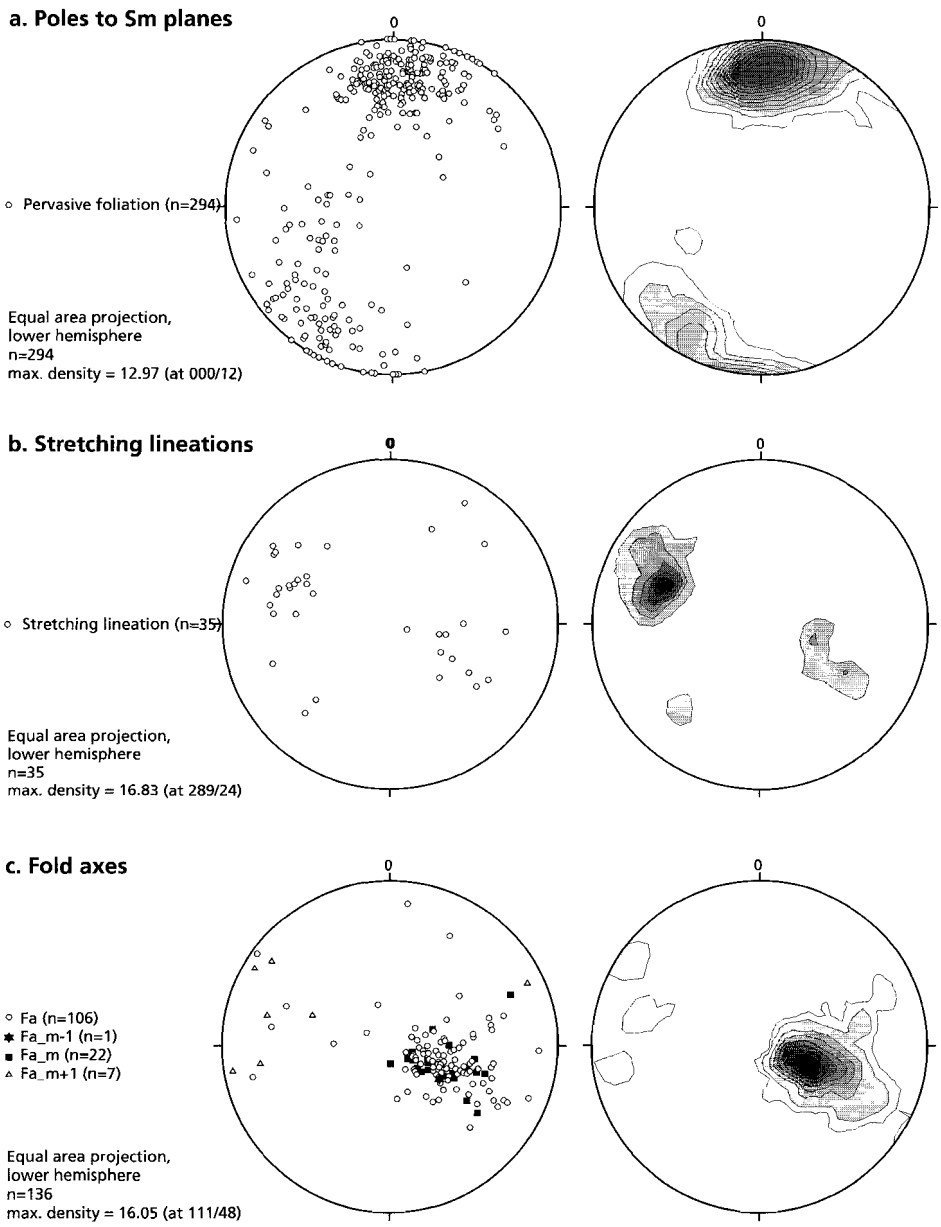

Figure 3.4: Equal area lower hemisphere projections of structural data. **a.** Poles to the main-phase foliation (Sm), all lithologies. **b.** Stretching lineations, all lithologies. **c.** Fold axes, all lithologies.

an outcrop of the Cima Lunga metapelite lens enclosed in the migmatitic gneisses of the Arbedo zone just south of Bedretto (fig 3.3, 3.5). This outcrop is remarkable in the ubiquitous presence of folds predating the main phase of deformation whilst a variable lithology accentuates the structures. In addition, the outcrop includes the contact between the Cima Lunga metapelites and Arbedo migmatites, which is marked by a gouge zone in the northern part of the outcrop.

Similar to most localities in the area, Dm folds in this exposure are generally steep and tight to isoclinal (figs. 3.5a, 3.5c). The axial planes strike roughly EW and dip slightly to the south, with fold axes plunging gently towards the east (fig 3.4c). The dips of the axial planes of main-phase folds become progressively shallower towards the northern part of the exposure, in the Arbedo migmatites. The axial planar foliation related to Dm is the dominant foliation (Sm) in all lithologies in the area. The dominant foliation and Sm-1 are roughly parallel to the various lithological contacts, because of the tight to isoclinal nature of the main-phase folds. This parallelism of the early structures with the main phase shows up very clearly on the map (fig 3.2), and is reflected by a point concentration of poles to the main phase foliation Sm (fig 3.4a).

In most of the samples studied the pervasive foliation is mainly defined by oriented biotite. Biotite locally grows on edges of flakes of white mica microstructurally related to earlier deformation. Occasionally, white mica recrystallised to fibrous sillimanite in places where nearby biotite crystals were available to participate in this transformation (fig 3.7a, sample AA98-26L). In sample AA98-13, from the Cima Lunga metapelite lens near Bedretto, the main fabric Sm is made up of sillimanite that locally includes remnants of white mica. Arcuate sillimanite trails suggest that the sillimanite is pseudomorphic after a crenulated white mica fabric (fig 3.7b). The growth of sillimanite clearly indicates that the structures related to Dm developed at high temperatures.

Isoclinal folds related to a Dm-1 phase are seen at several localities in the exposure of figure 3.5. The associated fold axes are difficult to measure but appear to plunge gently towards the SE. The outcrop of figure 3.5a shows a refolded Fm-1 fold with a layer of amphibolite in its core. A biotite bearing differentiated layering is folded in the Fm-1 hinges (Sm-2 in fig 3.5c), so Dm-1 must have been preceded by an earlier phase of deformation, only reflected by the differentiated, hence deformational fabric folded by Fm-1. A refolded tight Fm-1 fold is shown in fig 3.6a. The folded layering is made up of an alternation of biotite and amphibole bearing layers that show a weak earlier fabric.

The gneisses of the Arbedo zone dominantly show steep foliations and isoclinal folds related to main-phase deformation. A further indication for the high-temperature nature of the main-phase deformation in the Arbedo zone is observed in an outcrop showing a leucosome escaping from the hinge of a Dm fold (fig 3.6b). This feature suggests that the rocks partially melted during Dm folding. Apart from the presence of differentiated layering folded by Dm isoclinal folds, there is little evidence in the gneisses of the Arbedo zone for earlier stages of deformation.

Brittle-ductile kinks of both the pervasive foliation and the banding of the migmatitic gneisses (fig 3.6c) reflect deformation that post-dates the development of the main-phase structures. The associated Dm+1 fold axes plunge gently to the E, and the axial planes

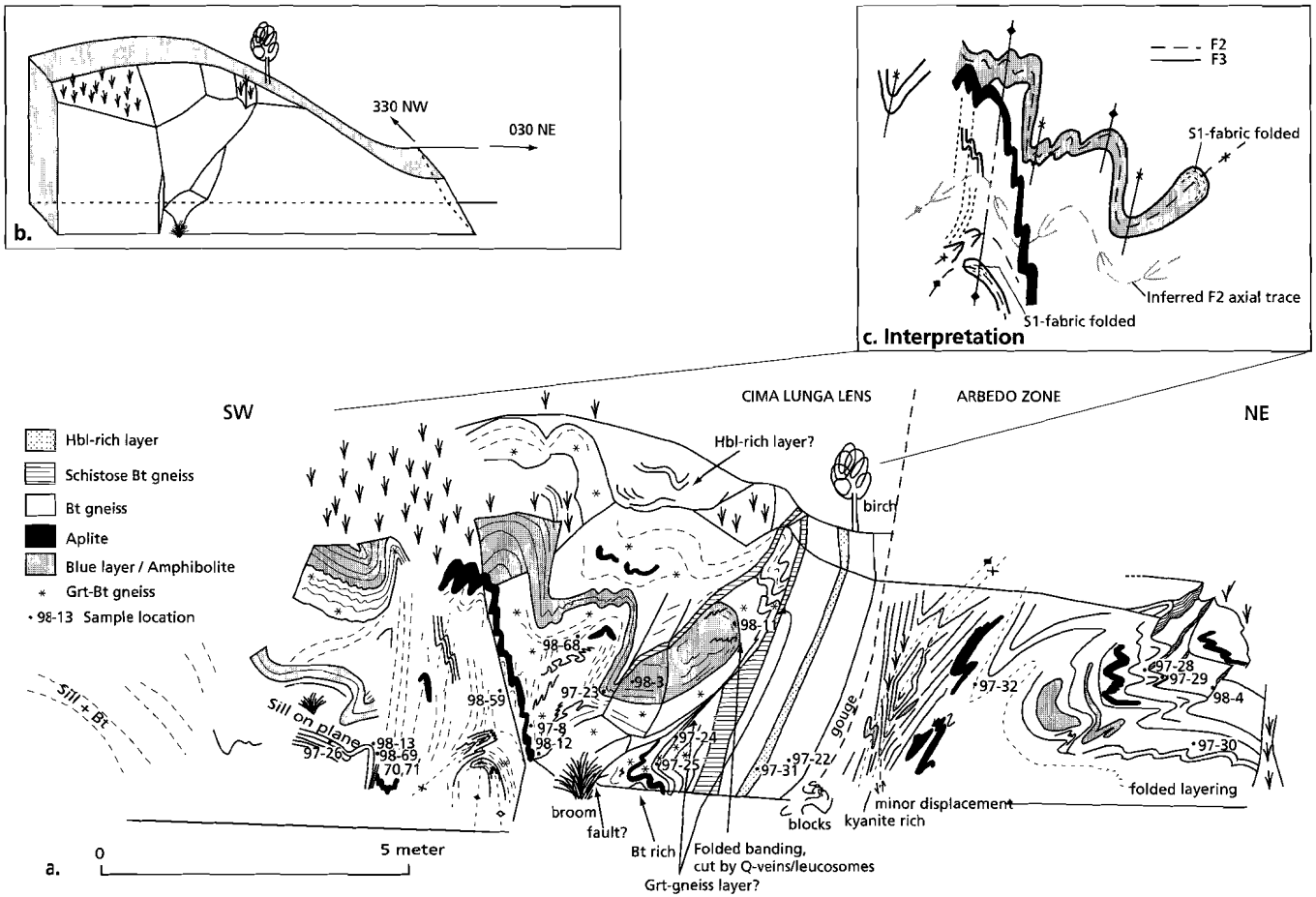

Figure 3.5: Outcrop of a lens of Cima Lunga metapelitic and amphibolitic rocks, included in the Arbedo zone. **a.** Sketch of the outcrop. **b.** Schematic drawing of the geometry of the outcrop. **c.** Interpretative sketch of the observed structures.

Figure 3.6: Field slides. **a.** Refolded Dm-1 fold, just south of figure 3.5 (see fig 3.3). **b.** Leucosome escaping from a Dm fold. **c.** Dm+1 kinkfold; hammer for scale.

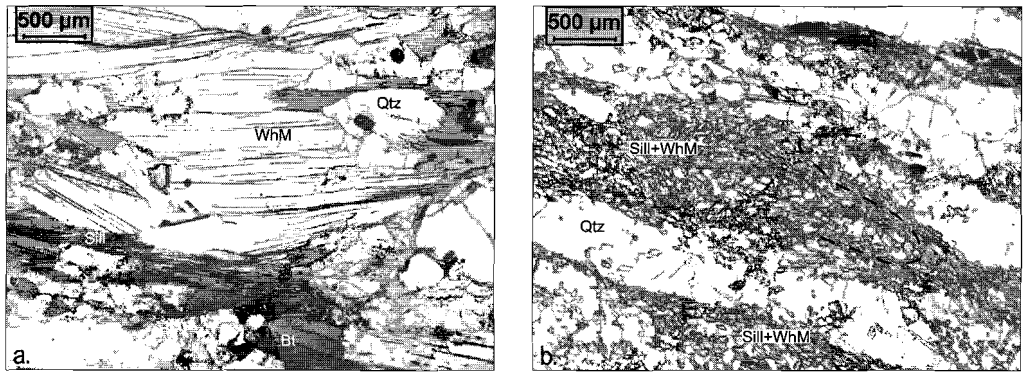

Figure 3.7: Microstructural evidence from thin sections. a. White mica is transformed to biotite and sillimanite during later deformation (AA98-26L). b. Arcuate sillimanite after white mica crenulation (AA98-13).

of very open Fm+1 folds are sub-horizontal. Immediately west of Gorduno subvertical pegmatite dikes cut all structures, and are themselves undeformed, indicating that the dikes post-date Dm+1. These pegmatites are thought to be related to the Novate granite intrusion (Gebauer, 1996), i.e. the latest stage of granitic intrusion in the central Alps.

3.3.2 Comparison with regional studies

The structural history described above essentially confirms the results of an earlier structural study in the Alpe Arami country rock gneisses (Möckel, 1969). Unfortunately, Möckel's (1969) structural interpretation of the gneisses was largely based on the analysis of a key outcrop that has since become inaccessible due to the construction of a house. The present results can be tentatively correlated with the structures identified by Grond et al. (1995) in the northern section of the Cima Lunga nappe. Their reported D1 isoclinal folds with a NS fold axes seem equivalent to my Dm-1. The difference in orientation of the pertinent fold axes is most probably related to the aforementioned gradual change in orientation of all structures towards the Insubric Line. Grond et al. (1995) relate this deformation to the development of the present-day nappe stack. Their D2 comprises a penetrative axial planar foliation related to tight and isoclinal folds, and is presumably equivalent to my Dm. Their D2 and D3 are both associated with metamorphic mineral assemblages indicating high temperatures (600-660 °C) and intermediate to low pressures (6-8 kbar). In my study area, Dm is much steeper but this is again probably related to the development of the steep root zone structure and associated movement on the Insubric Line. The D3 steep open folds and allied microscopic axial planar fabrics reported by Grond et al. (1995) do not seem to have an equivalent in my study area. The fourth deformation phase of brittle ductile kinking of the pervasive foliation has clearly affected both study areas.

Comparison of my results with the preliminary results of Nagel and Frey (1999) suggests that the D1 folds documented by these authors in the northern part of their study area in the southern Adula nappe are not present near Alpe Arami. Their D2 folds, however,

seem equivalent to Dm-1 at Alpe Arami, while the steep D3 folds correlate well with Dm in my study area, especially because the D3 axial planes strike NNW-SSE in the North and turn into an EW strike in the south of their area.
The obvious consistency between the structural histories documented in the Cima Lunga and Adula nappes and the structures described here from the Arbedo zone and the enclosed Cima Lunga metapelite lense suggests that during all of the recorded deformation phases the rocks in the area were closely associated. This conclusion is supported by the notion that the nappe stack in the Lepontine gneiss dome predates the peak of Lepontine metamorphism (e.g. Engi et al., 1995).

3.4 Lithologies and mineral chemistry

The study area contains a variety of lithologies inviting detailed study of the metamorphic mineral assemblages developed in these different compositions. The Alpe Arami garnet peridotite has been studied in great detail (e.g. Dal Vesco, 1953; Dobrzhinetskaya et al., 1996; Möckel, 1969; Risold et al., 1997), which allows me to focus on the Lepontine gneisses and on the eclogites that surround the peridotite body. Several previous studies have described the eclogites and eclogitic amphibolites in variable detail (e.g. Bocchio et al., 1985; Bocchio et al., 1978; Dal Vesco, 1953; Möckel, 1969). These rocks contain relics of the high-pressure mineral assemblage modified by metamorphic reactions producing complicated symplectite microstructures, and are described below in a separate section (3.4.2). The metapelitic rocks of the Cima Lunga lens south of Bedretto were only briefly mentioned by Möckel (1969) and have hitherto not been studied by other workers. The mineralogy of these rocks will be described in some detail below.
The mineral abbreviations used in the following sections are all taken from Kretz (1983). In addition, WhM is used to denote unspecified white mica, As to denote unspecified aluminium silicate (andalusite, kyanite or sillimanite), while Carb refers to unspecified carbonate minerals, and Op to opaques.

3.4.1 Petrography

The Lepontine gneisses of the Arbedo zone area are a composite of migmatites, locally including some metapelitic rocks, and layers of amphibolite, calcsilicate rocks and eclogite-amphibolites. The migmatites were probably formed by partial melting of orthogneisses and/or metapelitic rocks. The term amphibolite is used here to denote amphibole-bearing rocks carrying no relics of any eclogite facies assemblage. Eclogite-amphibolites show symplectites around relics of garnet and sometimes omphacite or kyanite and thus preserved relics of an eclogite facies high-pressure metamorphism. Eclogites with only minor evidence of retrogression only occur in a layer, up to about 20 metres wide (Möckel, 1969), surrounding the peridotite body. These eclogites are commonly considered to be part of the Cima Lunga nappe.
The mineral assemblage of the migmatites is Qtz + Pl + Bt ± Grt ± Sill ± Ms ± Czo ±

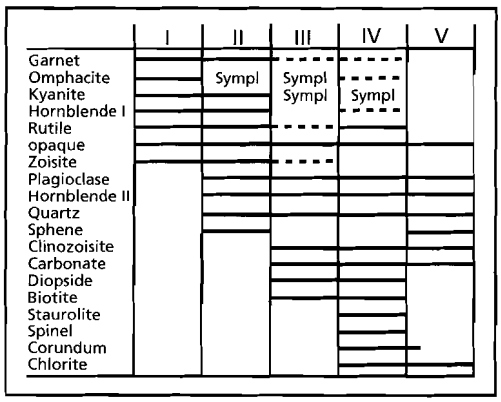

Figure 3.8: Mineral assemblages of the eclogites and eclogite-amphibolites. Dashed lines: relics.

late Chl around biotite and garnet. Accessory minerals are Tml, Czo, Ep, Ilm, Ttn, Carb. Centimetre-size hornblende crystals sometimes occur in aplitic patches and veins. The amphibolites generally show the assemblage Pl + Qtz + Hbl ±Grt ± Bt ± Ep ± Ilm ± late Chl. Rt, Ttn, Ep occur as accessory minerals. Layers of calcsilicate rocks commonly bear the assemblage Pl + Hbl + Carb + Qtz ± Scp ± Di ± Ep. Accessory minerals in these rocks are Grt, Ilm, Ttn and Bt. The mineralogy of the eclogites, eclogite-amphibolites and metapelites is described below.

3.4.2 Eclogites and eclogite-amphibolites

The Gorduno amphibolites were extensively studied by Bocchio et al. (1975; 1977; 1985; 1978). These studies focussed on the bulk and mineral chemistry of these rocks, but included few microprobe analyses. Considering only trace elements insensitive to secondary processes (like metamorphism), bulk trace element analyses of eclogites as well as eclogite-amphibolites indicate a tholeiitic affinity (Bocchio et al., 1985). The eclogites and eclogite-amphibolites are therefore considered to represent one single group of geochemically related rocks.

3.4.2.1 Petrography of eclogites and eclogite-amphibolites

The eclogites and eclogite-amphibolites show a range of mineral assemblages, reflecting

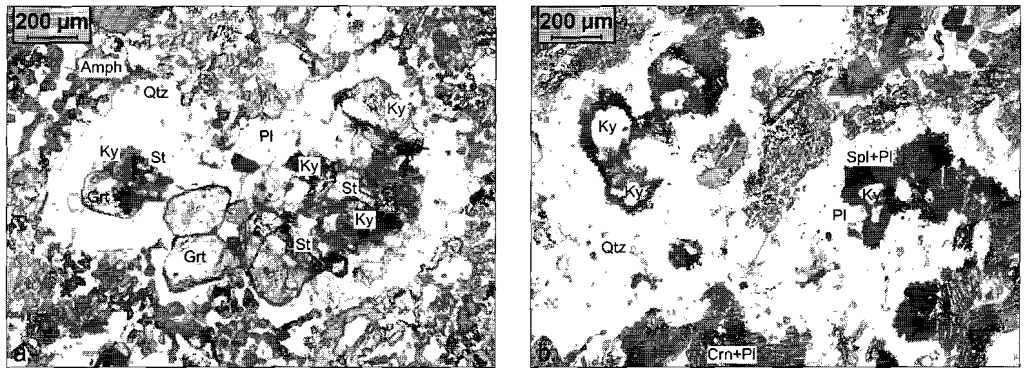

Figure 3.9: Photomicrographs. **a.** Intergrowth of staurolite and kyanite (AA97-16(2)). **b.** Optically nearly opaque symplectite surrounding kyanite.

various stages of retrogression (fig. 3.8). Most samples preserve various stages of retrogression affecting the primary high-pressure assemblage, such that these samples contain mineral assemblages pertaining to two or more stages of metamorphism in the diagram. The subdivision shown, with mineral assemblages labelled in Roman numerals I to V, has been adapted from Bocchio et al. (1985).
Eclogites s.s. (i.e. fresh, unaltered eclogites with type I primary eclogitic assemblages, fig 3.8) are only found in the rim of eclogites surrounding the Alpe Arami peridotite. These eclogites show small quantities of kyanite and hornblende in addition to garnet and omphacite. Besides hornblende, accessory zoisite is the only other hydrous phase in the eclogite assemblage. In garnet-bearing symplectitic amphibolites (type II) omphacites show rims of Pl + Di or Pl + Hbl symplectite. Garnet-bearing amphibolites (type III) contain only few relics of omphacite, and the symplectites derived from omphacite often contain a core of diopside. Garnet is surrounded by symplectites of hornblende and plagioclase. Hornblende crystals are also present in the matrix.
The most spectacular stage of retrogression is shown in the quartz-amphibolites with relics of garnet (type IV). Only few relics are preserved of the original eclogitic mineral assemblage, which is largely replaced by amphiboles and plagioclase. Tiny relics of kyanite are occasionally intergrown with staurolite (fig 3.9a) and, optically, symplectites after kyanite are practically opaque (fig 3.9b). Scanning electron microscopy and energy dispersive qualitative analyses (EDA) reveal the presence of complex intergrowths of either spinel and plagioclase or corundum and plagioclase. These transformations are discussed in more detail below.
Epidosites (type V) are rich in Pl, Czo, Carb and Qtz and represent the last stage of retrogression.

3.4.2.2 Symplectitic transformations

Several of the eclogite-amphibolites show spectacular symplectite transformations. Optically nearly opaque symplectites are observed around corroded relics of kyanite. The constituent components of these symplectites have been identified in the scanning electron microscope by EDA (fig. 3.10). In the core of the symplectite a relic of kyanite is sometimes present (fig 3.10a). Outward from the core, a first rim zone contains strings of very fine Fe-Mg-spinel intergrown with plagioclase of almost pure anorthite composition (fig 3.10b). The spinels show a gradual increase in magnesium content with distance away from the symplectite core. Further outward, the spinel is coarser grained, and a coarse symplectite rim of corundum and plagioclase may have developed. The outer ring of the symplectite is a plagioclase of intermediate composition with decreasing anorthite contents towards the outer edge.
Locally, a corundum symplectite with intermediate plagioclase is found to grow within spinel symplectite (fig 3.10c). In other instances, nests of corundum needles and grains are found in a matrix of intermediate plagioclase (fig 3.10d). These nests seem to replace a previous symplectite after kyanite.
The presence of corundum and spinel in the eclogite-amphibolites of Gorduno has been mentioned in the literature (Bocchio et al., 1985; Dal Vesco, 1953; Möckel, 1969),

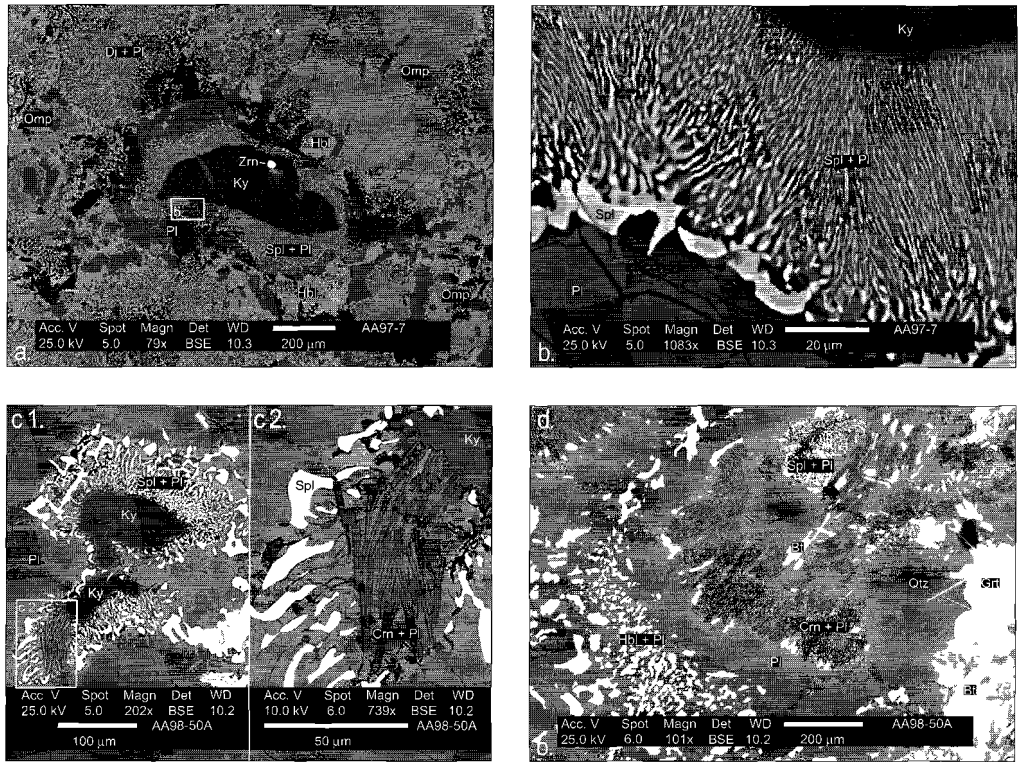

Figure 3.10: Backscattered electron SEM images of symplectites. **a.** Overview of a symplectite around kyanite (AA98-50A). **b.** Kyanite broke down to spinel and plagioclase (AA97-7). **c.** Kyanite surrounded by spinel, plagioclase and corundum (AA98-50a). **d.** Nest of plagioclase and corundum, probably after kyanite (AA98-50a).

but the associated transformations have never been described in detail. Microstructures very similar to those shown here from the eclogite-amphibolites were previously reported from the Alpine Rhodope of Greece (Liati and Seidel, 1994; Liati and Seidel, 1996) and from the Hercynian Armorican Massif in France (Godard and Mabit, 1998). In both areas symplectitisation was attributed to a granulite facies metamorphic overprint affecting dry eclogite facies mineral assemblages. The associated temperatures were inferred to have been as high as 800 °C at pressures of over 15 kbar (Liati and Seidel, 1996). However, in both of these occurrences the authors describe the presence of sapphirine in the outer margins of the symplectites. There is no evidence of any sapphirine in the Alpe Arami eclogite-amphibolites, indicating that conditions were probably different, with temperatures below 1050 °C, i.e. below the lower stability limit of sapphirine in mafic granulites (Spear, 1993, p. 384). Another striking difference is the growth, in the Swiss eclogite-amphibolites, of corundum after spinel, while both in the Rhodope and in the Armorican massif corundum is inferred to have developed first. Unfortunately, investigation of the symplectite-forming reactions using the

TWQ2.02 internally consistent thermodynamic database (Berman, 1991; Berman and Aranovich, 1996) yields no additional constraints regarding the metamorphic conditions at which these transformations took place.
Some of the reactions inferred to be involved in the formation of the symplectites in the Armorican massif seem to have operated in the Swiss eclogite-amphibolites as well. For the formation of spinel and after kyanite, additional Fe, Mg and Ca are needed. Godard and Mabit (1998) suggest that these elements might be derived from the breakdown of omphacitic pyroxene to diopside or hornblende. Possible reactions between various endmember pyroxenes and kyanite to form corundum, another pyroxene, and plagioclase include:

$$Jd + Ky = Crn + Ab$$
$$Ts + Ky = Crn + An$$
$$Di + Ky = En + An$$

(Johansson and Möller, 1986). Sodium from omphacite seems to be a slowly diffusing element as it stays in the outer rim of the kyanite symplectite, to form intermediate plagioclase, whereas plagioclase in the inner rim is almost pure anorthite. A change in hornblende composition in my eclogite-amphibolites, reflected by its colour zoning from green to brown, suggests that hornblende may have been involved in the transformations as well.

3.4.2.3 Mineral chemistry of eclogites and eclogite-amphibolites

Microchemical analyses were carried out using the automated JEOL 8600 electron microprobe at the EU Geochemical Facility in the University of Bristol, UK. The accelerating voltage during the analyses was 15 kV at a beam current of 15 nA, the spot size was 1–5 microns, with the larger spot size used for Na-

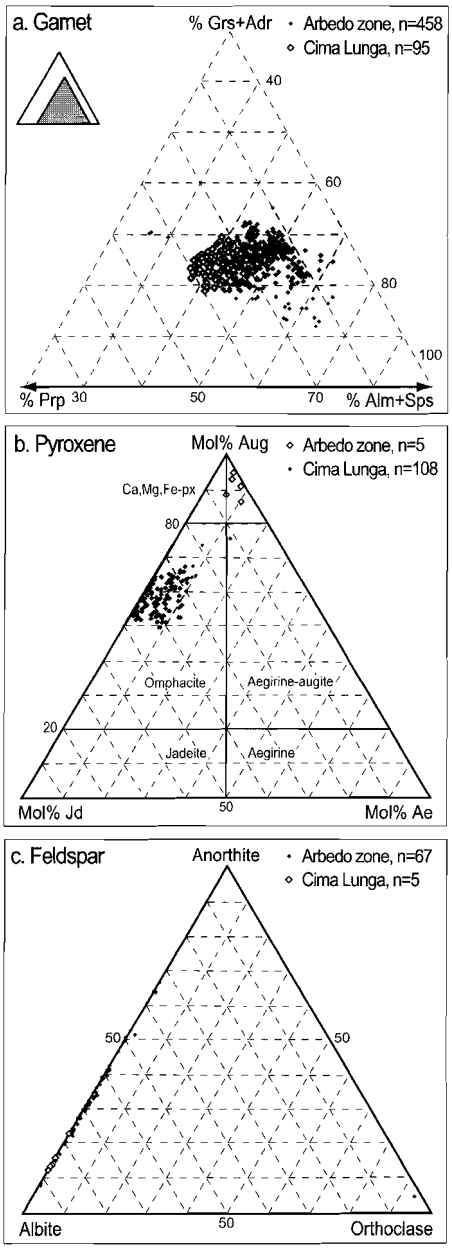

Figure 3.11: Ternary plots for eclogites and eclogite–amphibolites. **a.** Garnet compositions. **b.** Clinopyroxene compositions (cf. Morimoto et al., 1988) **c.** Plagioclase compositions.

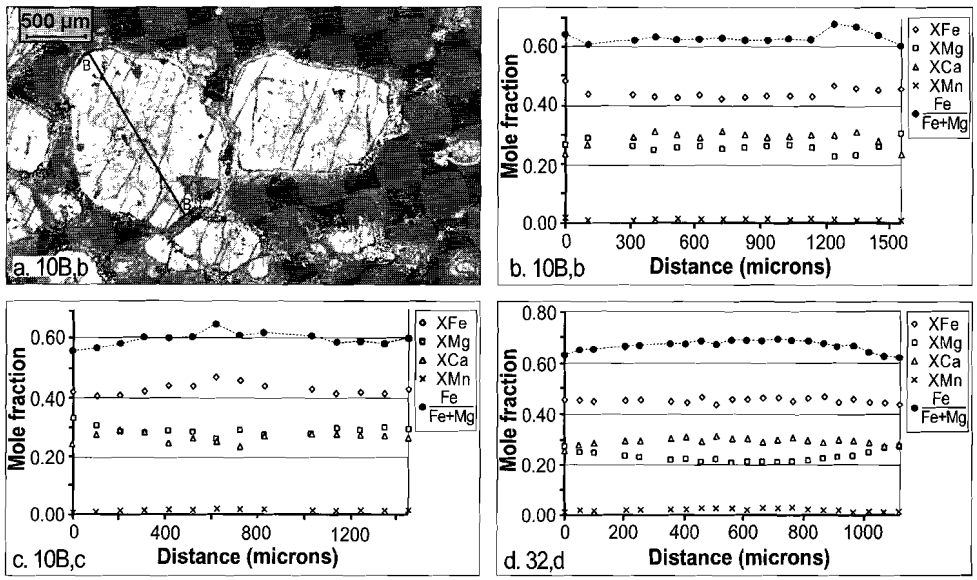

Figure 3.12: Garnet zoning in eclogites. **a.** Photomicrograph of a zoned eclogite garnet from the Cima Lunga nappe. **b.** Compositional variation across a zoned eclogite garnet from the Cima Lunga nappe. **c.** Id. **d.** Id.

bearing phases in order to minimise alkali volatilisation. Peak counting times ranged between 15 and 20 seconds. The following standards were used: albite for Na, olivine for Mg, spinel for Al, diopside for Si, K-feldspar for K, wollastonite for Ca, $SrTiO_3$ for Ti, hematite for Fe, MnO for Mn, Cr_2O_3 for Cr and nickel (metal) for Ni. Representative analyses of Grt, Omp, amphiboles, Zo, Pl, Ky and Czo are presented in Appendix 2.

Ferric iron estimation

The relative proportions of ferric (trivalent) and ferrous (divalent) iron cannot be determined directly by microprobe analysis. Various workers have therefore proposed recalculation schemes to estimate the ferric iron content of silicate minerals. Most of these schemes are based on a stoichiometric charge balance (e.g. Droop, 1987; Neumann, 1976; Schumacher, 1991). This approach assumes, that if the number of cations of the recalculated mineral formula taking all iron as ferrous is less than stoichiometric, this is caused by the presence of ferric iron. Alternatively, for the case of clinopyroxene, recalculation schemes have been proposed that only allocate ferric iron if there is an excess of Na over Al (Cawthorn and Collerson, 1974).

Following earlier work, a mixed approach has been adopted here for recalculation of mineral analyses to estimate the amounts of trivalent iron (Carswell et al., 1997). Ferric iron in garnet is estimated using Droop's (1987) charge balance equation, while for clinopyroxene I applied the method of Cawthorn and Collerson (1974). Amphiboles were recalculated according to charge

balance as described by Holland and Blundy (1994), and the ferric iron content in biotite was estimated from the hematite content of coexisting ilmenite (Williams and Grambling, 1990). The latter calculation was done for a few pairs and all other biotites were assumed to contain similar amounts of Fe^{3+}. Other minerals have been assumed to contain ferrous iron only, either because they contain only minor amounts of iron (e.g. feldspars) or because estimation by means of charge balance would be very inaccurate, as in the case of white mica, where the water content is unknown.

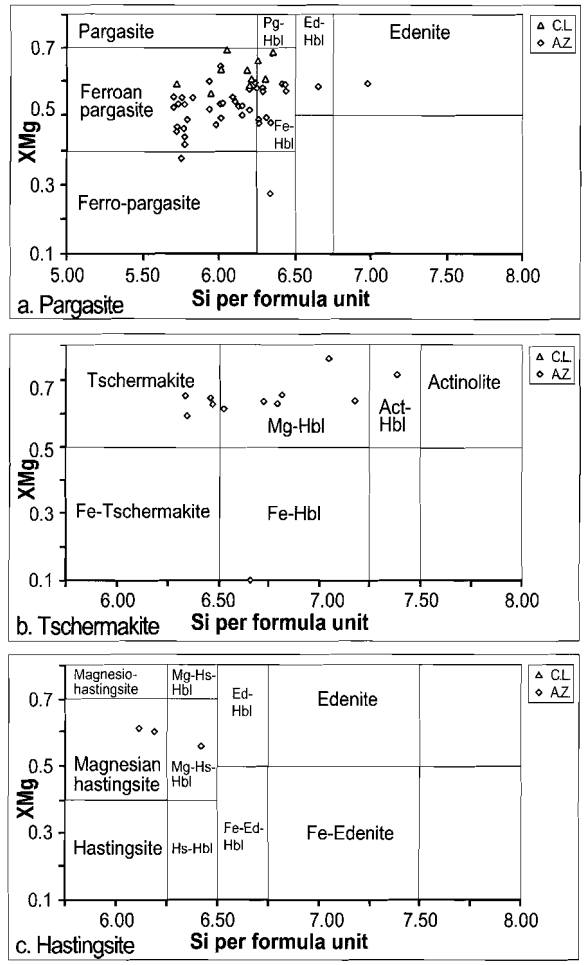

Figure 3.13: Amphibole compositions (cf. Leake, 1978). **a.** Calcic amphiboles, pargasite series. **b.** Calcic amphiboles, tschermakite series. **c.** Calcic amphiboles, hastingsite series.

Garnet

Garnet compositions are fairly similar for all eclogites and eclogite-amphibolites (fig 3.11a). Garnet from the Cima Lunga eclogites surrounding the Alpe Arami garnet peridotite body are slightly enriched in magnesium with respect to the eclogite-amphibolites from the Arbedo zone. Garnets in the eclogites have an average composition of $Alm_{39}And_4Grs_{21}Prp_{35}Sps_1$, while the eclogite-amphibolites garnets show average compositions of $Alm_{46}And_6Grs_{19}Prp_{27}Sps_2$. Both in the eclogites and in the eclogite-amphibolites garnets are often zoned (fig 3.12a-d). The relative proportions of iron and magnesium are indicative of the temperature during garnet formation (e.g. Råheim and Green, 1974). A decrease of $Fe^{2+}/(Fe^{2+}+Mg)$ indicates an increase in metamorphic temperature (e.g. Spear, 1993, p. 370), such that the garnet zoning generally indicates a temperature increase during garnet growth.

Clinopyroxene
The composition of pyroxenes in the eclogites and eclogite-amphibolites is shown in the ternary diagram of figure 3.11b. The nomenclature used for sodic-calcic pyroxenes is adapted from Morimoto et al. (1988). Jadeite contents were calculated as the sodium content minus the amount of acmite (ferric iron). Most pyroxene analyses are from the Cima Lunga eclogites adjacent to the peridotite body, and they plot well within the omphacite field. In the eclogite-amphibolites of the Arbedo zone pyroxene is scarce. The analyses in the top of the ternary plot represent diopsides grown during retrograde metamorphism.

Amphibole
All amphiboles analysed are rich in calcium. Following the nomenclature of Leake (1978) they are subdivided in three different groups. The pargasitic amphiboles are mostly ferroan pargasites (fig 3.13a), tschermakitic amphiboles are tschermakite or magnesium-hornblende (fig 3.13b), and the remaining amphiboles are magnesium-rich varieties of the hastingsite group (fig 3.13c). Pargasitic amphiboles from the Cima Lunga eclogites are slightly richer in magnesium than those from the Arbedo zone. The variety of amphiboles found in my samples probably reflects their formation as reaction products derived from different source minerals, like garnet or pyroxene. Locally, highly aluminous pargasite is part of the eclogitic assemblage, which is later replaced by pargasite with a lower aluminium content (Bocchio, 1977).

Feldspar
Feldspars in the eclogites and eclogite-amphibolites have a general composition of $Ab_{34-94}An_{6-66}Or_{0-4}$, although one K-feldspar was analysed that was enclosed in garnet (fig 3.11c). The Cima Lunga eclogites all have plagioclase compositions near that of the albite endmember. This suggests that the large range of compositions found in the more retrogressed samples is due to the growth of more anorthite-rich varieties during the symplectitic transformations described above.

3.4.3 Cima Lunga metapelitic lens
So far, very few workers have aimed their studies on the Lepontine gneisses that surround the spectacular peridotite and eclogite occurrences in the Adula-Cima Lunga nappe system. Moreover, most of these studies have focussed on the structural rather than the metamorphic history of the gneisses (e.g. Grond et al., 1995; Grujic and Mancktelow, 1996), although a preliminary report by Nagel and Frey (1999) indicates similar work on the metamorphic history of the southern Adula nappe is in progress. In view of my general aim, focussed on the thermal history of the Lepontine gneisses surrounding the Alpe Arami peridotite during their exhumation, I consider the metamorphic evolution of the metapelites in some detail.

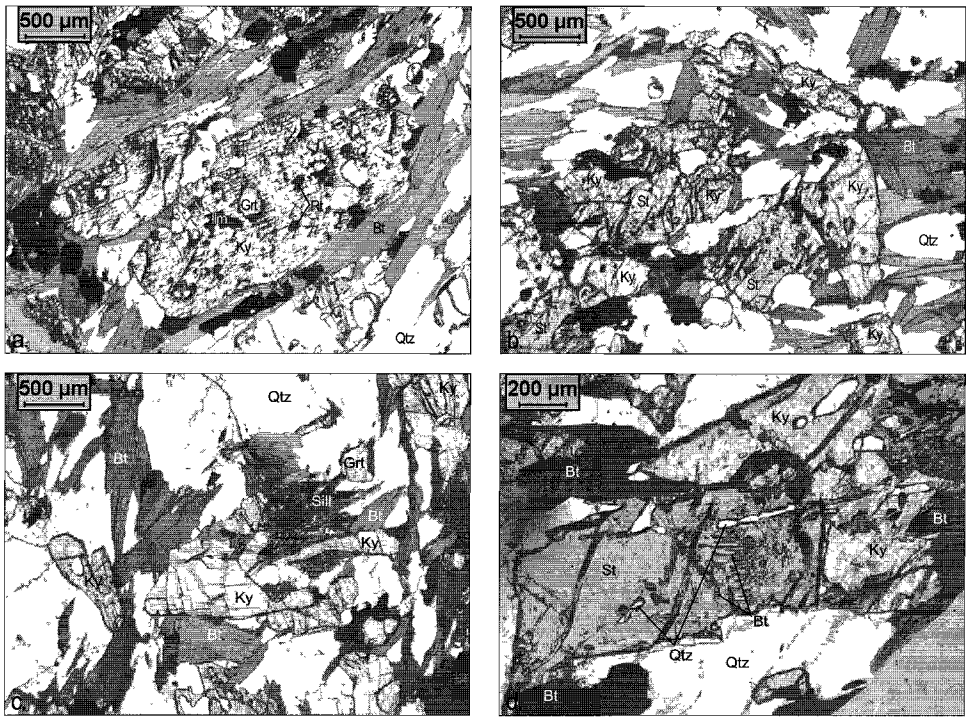

Figure 3.14: Petrography of pelites from the Cima Lunga lens (AA97-8). **a.** Garnet, rutile and opaques enclosed in kyanite. **b.** Intergrowths of staurolite and kyanite. **c.** Kyanite and biotite are together transformed to sillimanite. **d.** Exsolutions of quartz and biotite from staurolite.

3.4.3.1 Petrography of metapelites

The Lepontine gneisses of the Cima Lunga nappe include metapelitic layers and lenses. One of these lenses of mainly metapelitic material from the Cima Lunga nappe is enclosed in the Arbedo gneisses in my study area (figs 3.2, 3.3) and provides an excellent structural context to study the metamorphic evolution of the pertinent rocks. The mineral assemblages of the metapelites reflect part of the metamorphic evolution of the region. The rocks contain the assemblage Grt + Ky + St + Bt + Pl + Qtz ± Kf ± Sill (after Ky+Bt) ± Crd ± late Chl (after Bt and Grt). Accessory minerals are WhM, Rt, Ilm and Ctd included in Grt. In order to illustrate the various reactions involved, the mineral transformations in two of my samples are described below.

Sample AA97-8: Kyanite-staurolite schist

Sample AA97-8, collected from the outcrop shown in figure 3.5, contains the mineral assemblage Grt + Ky + St + Bt + Pl + Kf + Qtz + Ilm + Sill (after Ky + Bt). Rutile, zircon and apatite are accessory constituents. Inclusion relationships are as follows: kyanite includes Grt, Rt and Op (fig 3.14a), biotite carries inclusions of Grt, Ky, St, Pl and Op,

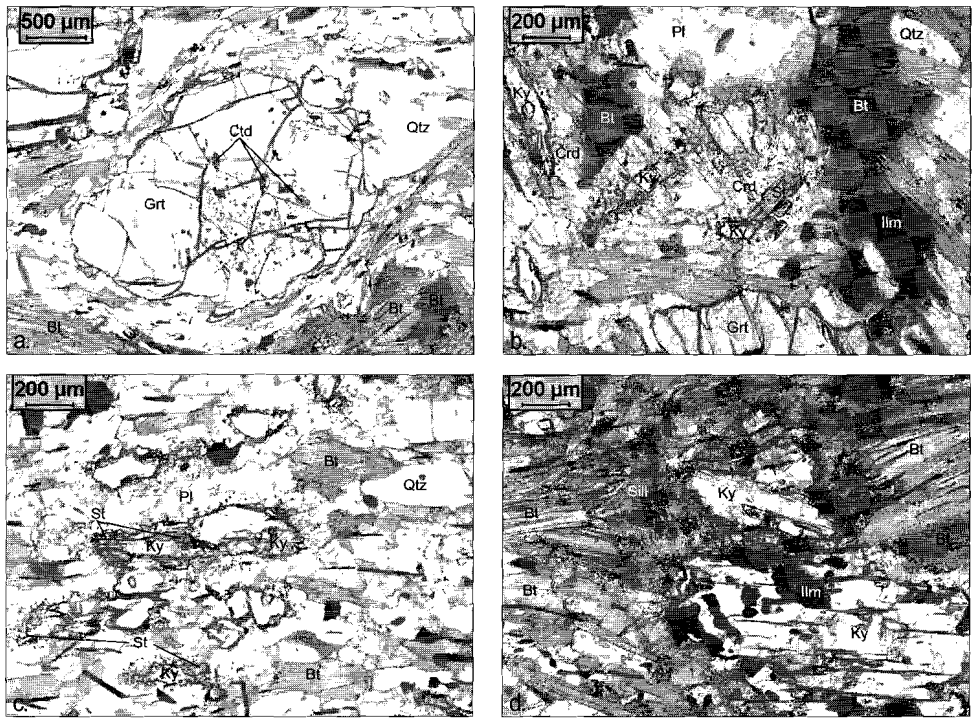

Figure 3.15: Petrography of pelites from the Cima Lunga lens (AA98-8A). **a.** Chloritoid inclusions in garnet. **b.** Cordierite enclosing kyanite and staurolite. **c.** Kyanite and staurolite intergrowths. Staurolite grows at the expense of kyanite. **d.** Kyanite and biotite are together transformed to fibrolitic sillimanite.

staurolite includes only opaque minerals and small matrix garnets include Rt and Ilm. Kyanite, staurolite, garnet, biotite, plagioclase and quartz appear to have formed a stable mineral assemblage. Intergrowths of kyanite and staurolite occur (fig 3.14b). Fibrolitic sillimanite grew, possibly together with K-feldspar, at the expense of kyanite and biotite (fig 3.14c). Locally, corroded relics of staurolite are associated with kyanite and biotite relics, suggesting that staurolite was also involved in this reaction. Unless biotite is present, breakdown of kyanite to sillimanite does not occur, which suggests that the presence of this hydrous mineral enhanced the kinetics of the breakdown reaction. The presence of a corroded garnet relict at the rim of staurolite suggests that garnet was involved in the staurolite forming reaction. Exsolutions of quartz from staurolite indicate that staurolite became unstable during the later stages of metamorphism (fig 3.14d).

Sample AA98-8A: Cordierite-bearing kyanite-staurolite schist

Sample AA98-8A was collected a few metres SW of the outcrop shown in figure 3.5. The rock is mainly a black flaky aggregate of biotite, amphibole and plagioclase, in which some of the biotite shows transformations to sillimanite. In addition, this sample contains some

chlorite grown at the expense of biotite. Accessory minerals are ilmenite and rutile. The black biotite-amphibole rock locally includes garnet bearing lenses (a few centimetres wide and about 10 centimetres long), which upon microscopic inspection are found to have a metapelitic mineral assemblage of Grt + Ky + St + Bt + Crd + Pl + Kf + Qtz + Sill (after Ky+Bt) + late Chl (after Bt and Grt). Accessory minerals are Rt, Zrn, Ap, and Op (ilmenite, and possibly others). The following conspicuous inclusion populations are found. Garnet includes small crystals of chloritoid (fig 3.15a), which in one case was found to have partly reacted to staurolite, rutile and an opaque mineral. In other cases, Ctd inclusions may have reacted to Chl. Other inclusions in garnet are Bt, Rt and Op. Kyanite includes Rt and opaques, biotite includes Grt, Ky, St and Op and cordierite includes Ky, St and Op (fig 3.15b). Biotite grains are aligned, and make up the foliation in the rock.
One of the reactions that probably occurred is:

$$Ctd = Grt + Bt + As$$

consistent with the presence of partially corroded chloritoid inclusions in garnet. Staurolite locally grew at the expense of kyanite, yielding mimetic intergrowths, presumably because of the similar crystal structure of the two minerals (fig 3.15c). Kyanite and biotite together break down to fibrolitic sillimanite (fig 3.15d). Kyanite, biotite and quartz are involved in the formation of cordierite, some K-feldspar, and opaques (fig 3.15b). Occasionally, small biotite crystals are formed. Locally, garnet, sillimanite and possibly staurolite are involved in cordierite formation. Chlorite formed at a late stage at the expense of biotite.
Cordierite has been reported in the Lepontine gneiss dome, but only in the Simano and Gruf nappes (Frey and Ferreiro Mählmann, 1999, and references therein). The latter occurrence is related to contact metamorphism around the Bergell granite complex. This first report of cordierite in the Adula-Cima Lunga nappe system may be related to partial melting of a pelitic precursor, because extraction of a granitic partial melt may leave a bulk composition appropriate to the crystallisation of cordierite (Deer et al., 1992, p. 129). This

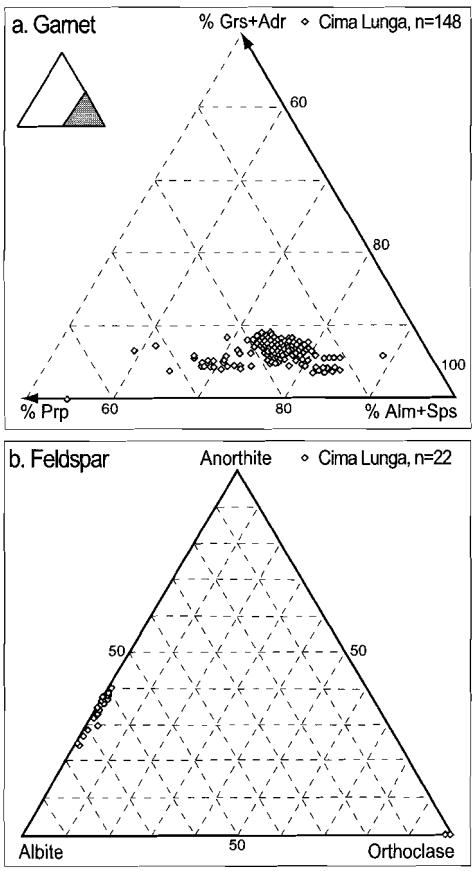

Figure 3.16: Ternary plots for pelitic rocks. **a.** Garnet compositions. **b.** Plagioclase compositions.

inference is supported by the fact that cordierite only occurs in a single, 2 by 10 centimetre, pelitic lens within a melanosome surrounded by ubiquitous migmatites. The conditions of cordierite formation will be discussed below (section 3.4.4).

3.4.3.2 Mineral chemistry of metapelites

Procedures for the study of the mineral chemistry of the metapelites were the same as those outlined above, in section 3.3.2.3. Representative analyses of Grt, Ky, St, Bt, Crd and feldspars are listed in Appendix 2.

Garnet

Garnet analyses from the metapelitic samples show that this mineral is very rich in iron and magnesium and poor in calcium, as expected for garnets in pelitic rocks (fig 3.16a). Their average composition is $Alm_{71}And_5Grs_2Prp_{18}Sps_4$. Pyrope contents may increase up to a mole fraction of 0.42. The garnets analysed do not show any appreciable zoning.

Staurolite and cordierite

Both staurolite and cordierite in the present metapelitic rocks are Fe-Mg solid solutions (Tables A2.9 and A2.10 in Appendix 2). Totals of the electron microprobe analyses do not add up to 100, however, indicating the presence of H, H_2O, or another element that was not analysed. Both observations imply that reactions involving the pertinent mineral phases are divariant. The presence of Mg in staurolite enlarges its stability field to somewhat higher temperatures (e.g. Spear and Cheney, 1989), whereas the presence of Mg in cordierite increases its stability at higher pressures (e.g. Martignole and Sisi, 1981).

Feldspar

Most feldspars analysed are plagioclase feldspars, although some K-feldspar occurs (fig 3.16b). The composition of the plagioclase ranges from An_{25} to An_{41}. Because plagioclase takes up most of the Ca present, this variation in An-content of plagioclase probably reflects variations bulk Ca contents of the rocks. The absence of muscovite in most of my samples suggests that K-feldspar may have grown as a reaction product of the muscovite-breakdown reaction, whereby muscovite and quartz react to form sillimanite and K-feldspar. This interpretation is supported by the occasional preservation of corroded relics of white mica amidst aggregates of fibrolitic sillimanite (see section 3.3.1).

3.4.4 Thermobarometry

The rocks from my study area in the lower Penninic nappes in the core of the Lepontine gneiss dome contain several generations of metamorphic minerals, implying that they preserve at least a partial record of evolving pressure-temperature conditions. Deciphering the pressure-temperature record is challenging because of the difficulty in demonstrating that a given assemblage has preserved equilibrium mineral compositions during changing pressure-temperature conditions. The preservation of partial retrogression

and mineral zonation demonstrate the need for caution when attempting to quantify metamorphic temperatures and pressures using the compositions of co-existing minerals. However, careful examination of pertinent textures and microstructures permits selection of mineral pairs most suitable for geothermobarometry. The exact formulations of thermobarometric calibrations used in this study are summarised in Appendix 1. Assuming the analysed minerals were in equilibrium, the errors on thermobarometric techniques like those applied here are generally of the order of ± 25-50 °C and ± 0.5-2 kbar (Spear, 1989). The microprobe analyses used for thermobarometry and representative analyses for other minerals are tabulated in Appendix 2. The locations of the samples studied are indicated in figure 3.3 and 3.5.

Garnet-omphacite pairs

The temperature dependence of iron-magnesium partitioning between garnet and clinopyroxene has long been established (e.g. Råheim and Green, 1974). In this study I follow the approach of Carswell et al. (1997) and use Powell's (1985) calibration, because all analysed garnets from garnet-omphacite pairs show $X_{Ca}<0.35$. The distribution coefficient (K_D, for definitions see Appendix 1) has been calculated for pairs of garnet and omphacite. The reaction

$$Ab = Jd + Qtz$$

is pressure dependent with respect to the jadeite content of omphacite (Holland, 1983). This barometer was reformulated by Carswell and Harley (1990) and is applied to several metabasic samples in this study. Because omphacite does not occur in equilibrium with plagioclase, the pressures obtained represent minimum estimates only. Table 3.1 shows the results of simultaneous solution of the garnet-clinopyroxene thermometer and the jadeite barometer with the highest PT conditions for core-and-rim pairs of each sample. The results are thus a mathematical solution of the barometer for the Omp analysis with the highest jadeite content of the sample, and the thermometer applied to analyses of neighbouring pairs of Grt and Omp showing apparent (microstructural) equilibrium.

Unit	Sample	Grt	Omp	Omp max Jd	core / rim	X_{Ca}	X_{Jd}	K_D	T (°C)	P (kbar)
CLE	AA97-4	4.1	4.4	4.7	core	0.459	0.459	4.780	927	20.0
CLE	AA97-4	4.2	4.12	4.7	rim	0.459	0.459	5.009	897	19.4
CLE	AA97-5	3.50	3.53	3.43	core	0.468	0.468	5.179	876	19.1
CLE	AA97-6	1.9	1.8	1.61	rim	0.483	0.483	3.675	957	20.8
CLE	AA97-6	1.15	1.18	1.61	core	0.483	0.483	5.198	860	18.9
CLE	AA97-7	4.26	4.27	4.47	rim	0.394	0.394	4.451	923	19.2
CLE	AA97-7	4.34	4.29	4.47	core	0.394	0.394	4.798	896	18.7
CLE	AA97-33	1.18	1.19	1.13	rim	0.263	0.263	5.182	821	15.6
CLE	AA97-33	1.31	1.28	1.13	core	0.263	0.263	4.781	855	16.1

Table 3.1: Garnet-omphacite equilibrium pressures and temperatures. Combined solution of Holland (1983) and Powell (1985). Exact formulations are in Appendix 1, complete microprobe analyses are in Appendix 2. In this and the following tables CLE denotes Cima Lunga eclogites, CLL refers to the Cima Lunga metapelitic lens and Arb refers to samples from the Arbedo zone.

Garnet-omphacite thermobarometry has been performed on five samples from the eclogite rim surrounding the Alpe Arami peridotite body (fig 3.3), because only in those samples relatively unaltered garnet-clinopyroxene pairs have survived retrograde metamorphism. For each sample the maximum PT conditions obtained for core and rim pairs are listed in table 3.1. Core pairs of samples AA97-4 to 7 equilibrated around 860-927 °C and 18.7-20.0 kbar, whereas rim pairs yield 897 to 957 °C and 19.2-20.8 kbar. The pressure estimates represent minimum, rather than exact metamorphic pressures, whilst differences between conditions obtained from core and rim pairs are very small. For this reason, no inferences are made on the basis of garnet-omphacite thermobarometry about possible changes in metamorphic conditions during garnet and clinopyroxene growth.
Sample AA97-33, taken in a different location in the eclogite rim (fig 3.3), yields significantly lower peak temperatures and pressures. The core pair equilibrated at 855 °C and 16.1 kbar, and for the rim pair values of 821 °C and 15.6 kbar were obtained. The lower conditions from the rim pair suggest that these minerals grew during retrograde metamorphism, but it is emphasised that the value obtained for the metamorphic pressure is again a minimum estimate.

Garnet-hornblende pairs and garnet-amphibole-quartz-plagioclase barometry
Iron-magnesium partitioning between coexisting garnet en amphibole is temperature dependent. For the case of hornblende it may be represented by the reaction:

ferro-pargasite + pyrope = pargasite + almandine

(Graham and Powell, 1984). The temperatures obtained with this thermometer were used as input in the garnet-amphibole-quartz-plagioclase barometer (henceforth referred to as the garnet-amphibole barometer) as well as in the applied mixing models for garnet, amphibole and plagioclase (Kohn and Spear, 1990). The PT values obtained for garnet-hornblende-plagioclase-quartz quartets from eight different samples are listed in table 3.2. Sample AA97-16(2) was taken from a kyanite-bearing eclogite-amphibolite lens in the Arbedo zone, the other samples pertain to amphibolitic layers in the metapelitic Cima Lunga lens described above. Pressures obtained with the iron barometer are 0.6 to 1.0 kbar higher than those of the magnesium barometer. Garnet-hornblende thermometry in combination with the Mg garnet-amphibole barometer yields values of 610-675 °C and 6.0-8.5 kbar for the Cima Lunga samples and 733 °C and 9.3 kbar for the Arbedo eclogite-amphibolite.
Kohn and Spear (1990) explicitly state that the results of the garnet-amphibole barometer are only valid if applied to minerals with compositions within the range of those on which the calibration was based. Strikingly, for mineral quartets in which only the amphibole was outside the recommended range of compositions (Na > 0.6 cations per 23 oxygens) I obtained results that were consistent with Grt-Cpx thermobarometry, as can be checked for sample AA97-7 from the Cima Lunga eclogites around the peridotite. I also applied this method to samples from smaller eclogite-amphibolite lenses that are distributed

Unit	Sample	Grt	Amph	Plag	Keq(Mg)	Keq(Fe)	P (Mg, kbar)	P (Fe, kbar)	T (°C,G&P84)	Note
CLL	AA97-22	4.84	4.89	4.94	0.016	1.304	6.8	7.4	632	
Arb	AA97-16(2)	2.19	2.24	2.23	0.431	39.650	9.3	10.3	733	
CLL	AA97-31A	3.40	3.43	3.41	0.006	0.430	6.1	6.7	637	
CLL	AA97-31A	3.44	3.45	3.48	0.171	14.311	8.5	9.2	675	
CLL	AA97-31A	3.50	3.51	3.52	0.137	10.375	8.3	8.9	656	
CLL	AA97-31A	3.50	3.54	3.52	0.109	8.255	8.1	8.7	647	
CLL	AA98-11	2.63	2.68	2.64	0.004	0.557	6.0	6.8	610	
CLL	AA98-11	2.67	2.68	2.65	0.009	0.693	6.4	7.0	628	
CLE	AA97-7	4.49	4.50	4.39	5977.709	184884.743	18.0	18.3	892	High Na
Arb	AA97-10B	3.2	3.5	3.1	297.041	3284.287	14.8	14.2	807	High Na
Arb	AA97-10B	2.146	3.7	3.1	139.580	1970.429	13.9	13.4	771	High Na
Arb	AA97-10B	2.165	3.14	3.12	45.130	1718.781	12.4	12.2	657	High Na
Arb	AA97-16(2)	2.19	2.25	2.23	0.376	20.320	9.2	9.8	731	High Na
Arb	AA98-32	1.58	1.63	1.62	9.129	82.255	11.8	11.2	778	High Na
Arb	AA98-32	1.66	1.64	1.65	2.636	34.337	10.7	10.3	749	High Na
Arb	AA98-32	1.67	1.64	1.65	9.458	76.243	12.0	11.5	825	High Na
Arb	AA98-33B	2.150	2.189	2.188	22.210	302.543	12.2	11.6	725	High Na
Arb	AA98-33B	2.150	2.190	2.188	9.493	147.675	11.5	11.0	711	High Na

Table 3.2: Garnet-amphibole equilibrium pressures for reactions involving Fe and Mg respectively (Kohn and Spear, 1990). Temperatures from garnet-hornblende thermometry (Graham and Powell, 1984). Exact formulations are in Appendix 1, complete microprobe analyses are in Appendix 2.

throughout the study area in the Arbedo zone (fig 3.3). These results, listed separately in table 3.2, range between 657 and 892 °C and 9.2 and 18.0 kbar for the Mg-barometer. The higher pressure at which sodium bearing amphiboles are stable explains the fact that all of these pressures and temperatures are higher. The pressure estimates for sodium rich amphiboles should be viewed with caution, because the wide pressure range obtained from the sodium-rich amphiboles may be related to the difficulties of applying a barometer outside the recommended compositional range. On the other hand, the coincidence with garnet-omphacite thermobarometry for sample AA97-7, and the fluent transition from the PT-estimates for Na-rich amphiboles to the estimates for suitable amphiboles suggest that the obtained pressure range represents a real range in equilibration pressures.

GASP barometry and garnet-biotite thermometry

The GASP geobarometer is based on the pressure dependence of the reaction:

$$\text{anorthite} = \text{grossular} + \text{kyanite} + \text{quartz}$$

which describes the upper pressure stability of anorthite. Koziol and Newton (1988) published new experimental results and a new calibration using the activity models described by Newton and Haselton (1981). The GASP barometer was solved simultaneously with two different calibrations of the garnet-biotite geothermometer (Ferry and Spear, 1978; Kleemann and Reinhardt, 1994), which is based on the Fe-Mg exchange between garnet and biotite. FS78 yields temperatures and pressures between 100 and 130 °C and about 2 kbar higher than the KR94 calibration. It should be noted, that both garnet and

Lithology	Sample	Grt	Bt	Plag	AlSil	X_{Grs}	X_{Py}	X_{Alm}	X_{An}	$X_{Al,Bt}$	$X_{Ti,Bt}$
CLL	AA97-8	2.18	2.22	2.21	2.23	0.075	0.189	0.757	0.360	0.114	0.040
CLL	AA97-26	2.96	2.94	2.93	2.92	0.052	0.243	0.653	0.362	0.128	0.044
CLL	AA97-26	2.96	2.95	2.93	2.92	0.052	0.243	0.653	0.362	0.134	0.034
CLL	AA97-32P	1.85	1.81	1.83	1.84	0.045	0.173	0.755	0.245	0.141	0.050
CLL	AA97-32P	1.85	1.82	1.83	1.84	0.045	0.173	0.755	0.245	0.139	0.055
CLL	AA97-32P	1.87	1.88	1.86	1.84	0.053	0.147	0.767	0.289	0.135	0.048
CLL	AA98-8A	2.221	2.223	2.225	2.226	0.076	0.309	0.614	0.377	0.113	0.018

								GASP+KR94		GASP+FS78	
Lithology	Sample	Grt	Bt	Plag	AlSil	K (GrtBt)	K (GASP)	P (kbar)	T (°C)	P (kbar)	T (°C)
CLL	AA97-8	2.18	2.22	2.21	2.23	0.2330	0.4508	7.4	577	9.6	701
CLL	AA97-26	2.96	2.94	2.93	2.92	0.2251	0.3098	6.4	565	8.3	681
CLL	AA97-26	2.96	2.95	2.93	2.92	0.2133	0.3098	6.3	557	7.9	657
CLL	AA97-32P	1.85	1.81	1.83	1.84	0.2269	0.4760	6.6	566	8.9	687
CLL	AA97-32P	1.85	1.82	1.83	1.84	0.2200	0.4760	6.5	559	8.6	673
CLL	AA97-32P	1.87	1.88	1.86	1.84	0.2015	0.4421	5.8	542	7.5	633
CLL	AA98-8A	2.221	2.223	2.225	2.226	0.2231	0.4229	8.5	580	10.3	686

Table 3.3: Equilibrium pressures and temperatures of combined solution of the GASP geobarometer (Koziol and Newton, 1988; Newton and Haselton, 1981) with two different calibrations of the garnet-biotite geothermometer. FS78 denotes Ferry and Spear (1978), KR94 denotes Kleemann and Reinhardt (1994). Exact formulations are in Appendix 1; complete microprobe analyses are in Appendix 2.

plagioclase analyses used as input for the GASP barometer have very low Ca contents, which renders the barometer imprecise, with uncertainties over 3 kbar (Todd, 1998). Obtained equilibrium conditions are 542-580 °C and 5.8-8.5 kbar for GASP in combination with the KR94 thermometer, and 633-701 °C and 7.5-10.3 kbar for GASP in combination with the FS78 thermometer.

Mineral	Grt	Bt	Crd	Ky	Grt	Bt	Crd	Fspar	Ky
Analysis	2.216	2.217	2.219	2.220	2.222	2.223	2.224	2.225	2.226
Thin section	AA98-8A	AA98-8A	AA98-8A	AA98-8A	AA98-8A	AA98-8A	AA98-8A	AA98-8A	AA98-8A
Na2O	0.03	0.69	0.19	0.00	0.03	0.64	0.28	7.30	0.00
MgO	5.91	15.42	10.36	0.00	5.58	15.67	10.09	0.00	0.00
SiO2	37.54	36.72	48.48	36.35	37.40	37.97	48.14	58.27	36.37
Al2O3	21.55	17.17	32.94	62.83	21.36	17.40	32.93	26.15	62.55
K2O	0.00	7.76	0.01	0.02	0.01	7.97	0.01	0.03	0.00
CaO	2.17	0.09	0.00	0.01	2.31	0.02	0.00	8.02	0.01
TiO2	0.00	1.45	0.03	0.00	0.00	0.94	0.00	0.00	0.00
FeO	31.11	14.58	5.21	0.70	31.30	13.97	5.52	0.04	0.51
MnO	2.67	0.09	0.15	0.01	2.45	0.00	0.21	0.01	0.00
Cr2O3	0.00	0.11	0.00	0.04	0.00	0.00	0.01	0.00	0.06
Total	100.94	94.09	97.34	99.88	100.40	94.55	97.17	99.77	99.43
Additional	Sil,Qtz,Op				Qtz, Op				
Notes	Sil seems later				Plag not in equilibrium				
TWQ results	**630-660°C**	**5.5-6.0 kbar**			**630-665°C**	**5.5 kbar**			

Table 3.4: Microprobe analyses used as input for TWQ2.02 programme (Berman, 1990), using the Berman and Aranovich (1996) internally consistent thermodynamic dataset. PT estimates for intersections of the following equilibria: (1) 4 Sill + 5 αQtz + 2 Alm = 3 FeCrd; (2) 4 Sill + 5 αQtz + 2 Py + 2 Ann = 3 Crd + 2Phl; (3) 4 Sill + 5 αQtz + 2 Py = 3 Crd; (4) Alm + Phl = Py + Ann; (5) 3 Crd + 2 Alm = 3 FeCrd + 2 Py

TWQ analysis of cordierite-forming reactions

In most cases cordierite was formed at the expense of biotite and kyanite, although in some cases garnet, sillimanite and possibly staurolite are involved as well. Secondary products of cordierite formation are minor quantities of K-feldspar, biotite and opaques (probably ilmenite; fig 3.15b). Cordierite-forming reactions were investigated using the programme TWQ2.02 (Berman, 1991) with the internally consistent thermodynamic dataset of Berman and Aranovich (1996). The analysed cordierites are in direct contact with biotite and kyanite. There are no contacts with garnet, but in other cases garnet seems to be involved in a cordierite forming reaction. Two input files were generated, with the assumption that the analysed cordierites are in equilibrium with garnet, biotite, kyanite and quartz (table 3.4). All the obtained reactions for both input files intersect within 35 °C and 500 bars. This suggests that conditions obtained for the formation of cordierite, i.e. 630-665 °C and 5.5-6.0 kbar, represent equilibrium between the minerals. It should be noted that in most cases cordierite seems to grow at the expense of biotite and kyanite, rather than garnet, and that no garnet was formed in conjunction with cordierite. This may indicate that cordierite growth also took place at somewhat higher pressures.

Amphibole-plagioclase pairs

The exchange of Na and Ca between coexisting amphibole and plagioclase is temperature dependent (Holland and Blundy, 1994). Of two calibrated thermometers, one concerns a Si–saturated system, while the other can be applied to assemblages without free quartz. Holland and Blundy (1994) emphasise that the reactions must not be combined in order to obtain an estimate of equilibrium pressure, because the pressure residuals were not minimised. They note, however, that the simultaneous use of both thermometers does allow assessment of the validity of the resulting K_D lines.

Plagioclase-hornblende pairs have been analysed in fifteen samples from the different units. The obtained temperatures vary between 3 and 158 °C within samples. For four samples, the temperature estimates within the sample varies by more than 50 °C, in which cases the pertinent PT estimates have been discarded for reasons of possible disequilibrium. The highest temperature estimate of each of the remaining samples is listed in table 3.5. The temperatures have been calculated for pressures of 5 and 10 kbar, consistent with the pressure range obtained from garnet-amphibole barometry.

Unit	Sample	Amph	Plag	T_B (°C, 5 kbar)	T_B (°C, 10 kbar)
CLE	AA97-7	4.40	4.39	623	687
Arb	AA97-11	3.24	3.21	718	757
Arb	AA97-16(1)	1.99	1.100	724	760
Arb	AA97-16(2)	2.24	2.23	746	777
CLL	AA97-22	4.89	4.94	706	758
CLL	AA97-31A	3.45	3.48	693	748
CLL	AA98-11	2.68	2.64	730	791
Arb	AA98-21BL	3.58	3.57	717	750
Arb	AA98-23	1.181	1.182	659	701
Arb	AA98-35	2.50	2.52	707	734
Arb	AA98-37	3.127	3.124	717	757

Table 3.5: Amphibole-plagioclase equilibrium temperatures calculated with Holland and Blundy (1994). Exact formulations are in Appendix 1, complete microprobe analyses are in Appendix 2.

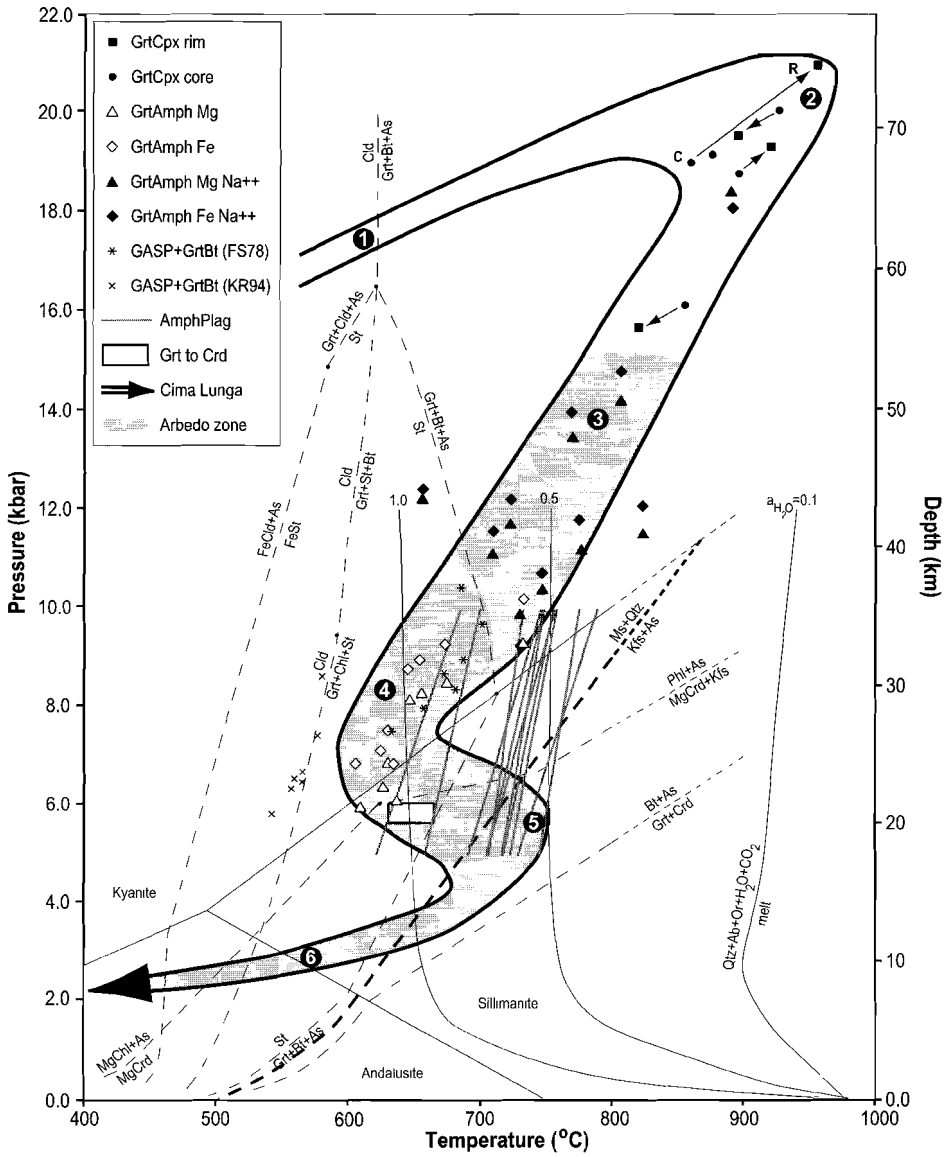

Figure 3.17: Compilation and interpretation of thermobarometric results. Abbreviations: C = core, R = rim. The arrow delimited by thin black lines refers to the eclogites and metapelites of the Cima Lunga nappe, whereas the grey shading refers to data obtained from metabasites and metapelites from the Arbedo zone.
Thermobarometric results were obtained using different calibrations. GrtCpx = garnet-clinopyroxene thermometry (Krogh, 1988); or (Powell, 1985) combined with jadeite barometry (Holland, 1983), see table 3.1. Garnet-amphibole Fe = the iron endmember of the garnet-amphibole barometer (Kohn, 1990) combined with the garnet-hornblende thermometer (Graham, 1984), see table 3.2. Garnet-amphibole Mg = idem, but now the magnesium endmember. When Na++ is added, the amphibole is too rich in Na to fit the compositional criteria, however, the pertinent results seem useful

3.4.5 Compilation of the PTt trajectory

The PT path

Figure 3.17 shows a compilation of the thermobarometric results described above. In addition, reactions are included that, based on petrographical observations, constrain the evolving PT conditions. A path is constructed through the results obtained for the Arbedo zone and the southern part of the Cima Lunga nappe. Possible alternative scenarios will be discussed below. For reasons of clarity, the segments of the inferred PT trajectory are labelled (1) through (6). These labels are indicated in figure 3.17.

(1) The path starts on the low temperature side of the reaction:

$$Ctd = Grt + Bt + As$$

because of the presence of Ctd inclusions in the absence of staurolite in Cima Lunga metapelite garnets. This reaction may be divariant and shift in temperature, due to Fe-Mg exchange and the presence of hydrous phases. The observation that garnet contains ubiquitous Ctd inclusions, whereas St inclusions are absent, in combination with the absence of Ctd inclusions in staurolite, suggest that breakdown of chloritoid did not involve staurolite. Hence, it seems most likely that the PT conditions evolved at pressures above the St stability limit of 16 kbar at 620 °C. The actual metamorphic pressure may have been substantially higher. The implication is that the Lepontine gneisses of the Cima Lunga nappe underwent Alpine high-pressure metamorphism, although the conditions are, admittedly, poorly constrained.

(2) Pressures and temperatures then increased towards the peak of high-pressure metamorphism around 950 °C and 21 kbar estimated for the eclogites surrounding the Alpe Arami peridotite body. Because garnet and clinopyroxene did not coexist with plagioclase, the pressure obtained is a minimum estimate. Further results of Grt-Cpx thermobarometry indicate that after peak pressure metamorphism the rocks cooled through 800-850 °C at pressures of 15-16 kbar.

Despite intense search for petrographical evidence such as radial cracks around quartz inclusions in garnet, no indications have been found for the presence of coesite or any other ultrahigh-pressure phase in either the Lepontine gneisses or the eclogites. Hence, I infer that the lower stability limit of coesite (about 28 kbar at 800 °C) may be taken as an upper limit for the Alpine metamorphic pressures. On the other hand, any relics of such very high pressures may have completely disappeared during later transformations or recrystallisation.

(see text for discussion). GASP+GrtBt denotes the combined solution of the GASP barometer (Koziol, 1988) and two garnet-biotite thermometers, see table 3.3. FS78 = Ferry and Spear (1978); KR94 is Kleemann and Reinhardt (1994). The white box labelled Grt to Crd represents the results of investigation of cordierite-forming reactions using the TWQ2.02 programme (Berman, 1991); (Berman, 1996), (see table 3.4). AmphPlag = amphibole-plagioclase thermometry using the calibration of Holland and Blundy (1994), see table 3.5. The thin solid and dashed lines are reactions that constrain the metamorphic conditions. The bent solid lines indicate melting curves for rocks of granitic composition for different water pressures (taken from Uohannes, 1990). All other reactions were taken from the KFMASH petrogenetic grid of Spear and Cheney (1989).

(3) The results of combined garnet-hornblende thermometry and garnet-amphibole barometry on rocks with Na-rich pyroxenes, referred to as GrtAmph in figure 3.17, indicate a straight cooling and decompression trajectory following the pressure peak, well into the staurolite stability field. More importantly, values as high as 14-15 kbar at 810 °C were obtained for eclogite-amphibolite lenses included in the migmatitic gneisses and metapelites of the Arbedo zone, supporting the notion that the Arbedo zone and the included eclogite-amphibolites underwent high-pressure metamorphism.
It is important to note that eclogite-amphibolites from the Arbedo zone contain relics of kyanite (e.g. AA98-50A, fig 3.10a), indicating that the metamorphic pressure must have exceeded 12-14 kbar at 800-900 °C (Godard and Mabit, 1998). Although garnet-clinopyroxene thermobarometry is not possible in these rocks because they lack fresh pyroxene, they thus contain clear evidence of high-pressure metamorphism, coinciding with those obtained by garnet-amphibole thermobarometry on Na-rich assemblages. There is no evidence for any shear deformation along the contacts between the eclogite-amphibolite lenses and the migmatitic gneisses of the Arbedo zone.
(4) The stability of staurolite in the absence of chloritoid after high-pressure metamorphism indicates that the PT trajectory passes into the stability field of staurolite in metapelitic rocks. Staurolite in these rocks contains minor amounts of Mg, increasing its stability towards higher temperatures, with respect to the pure iron endmember. Temperatures remain above the upper stability limit of chloritoid. Pressures and temperatures subsequently decreased towards conditions between 6.0 and 9.0 kbar and 600-680 °C, as indicated by the results of garnet-amphibole thermobarometry on amphibole-bearing layers in the Cima Lunga lens. The results of GASP barometry combined with the FS78 garnet-biotite thermometer are in line with the inferred temperature decrease. It seems that the KR94 calibration is less appropriate, because those results plot well within the chloritoid stability field, while chloritoid is absent.
(5) My samples show a variety of features indicating that, after cooling during initial decompression, the rocks were heated again. The growth of cordierite at the expense of kyanite, took place within the sillimanite stability field (table 3.4, fig 3.17), and in another sample muscovite was almost completely consumed by sillimanite growth. These observations, combined with the results from amphibole-plagioclase thermometry, indicate that re-heating by about 110 °C occurred after cooling during initial decompression, culminating in peak temperatures of 710-760 °C at pressures of 4 to 6 kbar. The PT trajectory nearly crosses the solidus for rocks of granitic bulk composition with a water activity of 0.5 (taken from Johannes and Holtz (1990)), which is consistent with the widespread occurrence of migmatitic gneisses in the study area. This high-temperature stage at relatively low pressures is also supported by the development of Spl + Pl en Crn + Pl symplectites after kyanite in eclogites and eclogite-amphibolites. As indicated above, the ambient conditions prevailing during these transformations are poorly constrained, but the breakdown of kyanite to spinel and corundum bearing symplectites certainly indicates high temperatures, at relatively low pressures. Cordierite and garnet were not found to crystallise together, despite the ubiquitous presence of kyanite, sillimanite and biotite, indicating that the PT trajectory stays at pressures above and temperatures below the reaction:

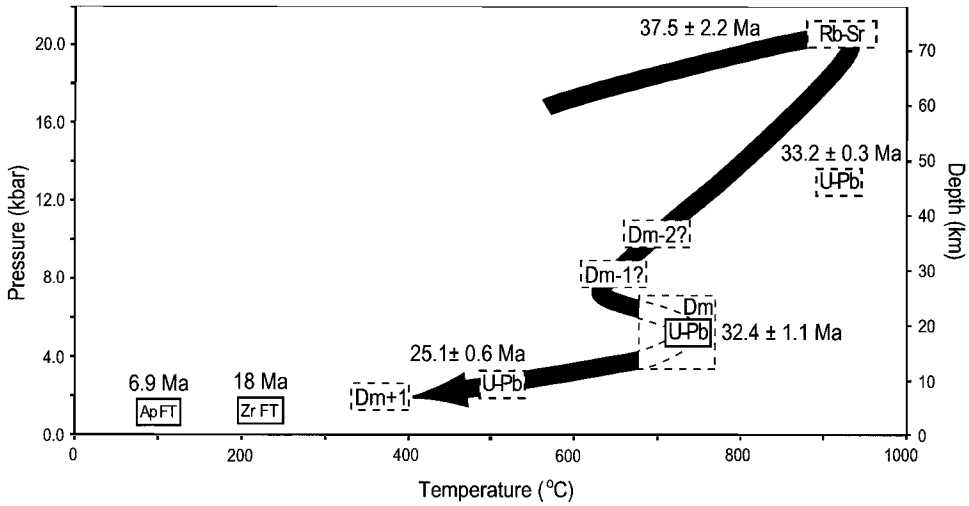

Figure 3.18: Relative and absolute timing of structural and metamorphic events. Rb-Sr dating from Becker (1993), U-Pb SHRIMP ages from Gebauer (1996), zircon fission track estimated (based on Hunziker, 1992; Hunziker, 1997; Schlunegger, 1999), and apatite fission track age from Wagner et al. (1977).

$$Bt + As = Crd + Grt.$$

(6) After the thermal peak the rocks cooled, as indicated by the growth of chlorite rims around biotite in all lithologies. Chlorite growth marks the latest stage in the metamorphic history. The conditions at which this transformation takes place are, unfortunately, poorly constrained.

Relative timing of structures and metamorphism

There are no constraints on the age of Dm-2 and Dm-1 structures, other than that they predate structures related to Dm (fig 3.18). It turned out to be impossible to relate the biotite and amphibole bearing fabrics with confidence to any specific part of the PT-path. The timing of the Dm folds is quite well constrained, because it is coeval with the growth of sillimanite and the development of leucosomes in the migmatitic gneisses. This interpretation fits the conclusion of Grond et al. (1995) that the pervasive fabric and its related isoclinal folds developed during peak metamorphism. The local folding of leucosomes demonstrates the progressive nature of the deformation producing the Dm folds. Dm is continuous across the Cima Lunga metapelite lens included in the migmatites of the Arbedo zone, which lends further support to the notion that the Arbedo zone and the Cima Lunga nappe were juxtaposed by the time they were affected by peak Lepontine metamorphism.

Dm+1 structures have a brittle-ductile nature and must have developed at much lower temperatures, during final cooling.

Structures and metamorphism related to radiometric dating
The age of the high-pressure metamorphic assemblage of the eclogites surrounding the Alpe Arami garnet peridotite body was estimated at 37.5 ± 2.2 Ma by Sm-Nd dating (fig 3.18, Becker, 1993). This age was obtained using an isochron for garnet, clinopyroxene and the whole rock chemistry, which is assumed to reflect cooling below 600 °C, but on petrological grounds was taken to be very close to the age of high-pressure metamorphism (Becker, 1993).
U-Pb SHRIMP dating of zircons from pyroxenites and a peridotite from the Alpe Arami body itself yielded an age of 33.2 ± 0.3 Ma for granulite facies retrogression (Gebauer, 1996). Unfortunately, these granulite facies conditions are not specified in any detail. Hence, this age does not refer to a well-documented set of PT-conditions, and is only roughly indicated in a PT-diagram.
A more useful U-Pb SHRIMP age was obtained by the same author from a leucosome in the migmatites (32.4 ± 1.1 Ma). This age is taken to reflect the peak of the late-stage heating. Zircons from a pegmatite that crosscuts the steep structures yield 25.1 ± 0.6 Ma. This age was interpreted to be related to the latest stage of intrusions in the Bergell region.
There are no zircon fission track ages available for the present study area, but results from the nearby Maggia valley (Hurford, 1986) as well as those from regional compilations (Hunziker et al., 1992; Hunziker et al., 1997; Schlunegger and Willet, 1999) suggest that likely ages are around 18 Ma for zircons cooling below 225 ± 25 °C. The only available apatite fission track age, obtained a few kilometres east of the present study area, is 6.9 Ma (Wagner et al., 1977), indicating cooling below 100 ± 20 °C (fig 3.18).

3.5 Geodynamic implications

3.5.1 Juxtaposition of the Cima Lunga nappe and the Arbedo zone
The pressure-temperature-time-deformation (PTtD) path reconstructed above has implications for the tectonic history of the Penninic Alps. My results indicate that the Arbedo zone and probably also the metapelites of the Cima Lunga nappe underwent high-pressure metamorphism and that they have since followed similar PT paths. This result challenges the conclusion by other workers (e.g. Grond et al., 1995; Pfiffner and Trommsdorff, 1998; Trommsdorff, 1990) that the Lepontine gneisses have not undergone high-pressure metamorphism and that mafic and ultramafic lenses with an early high-pressure history were incorporated in the country rock gneisses at a later stage, at low pressures and intermediate to high temperatures.
Although the timing of metamorphism in the Arbedo zone is not well constrained, this study suggests suggests that the Arbedo zone and the Cima Lunga nappe were juxtaposed at pressures of around 15 kbar (fig 3.17), equivalent to a depth of about 50 kilometres. Since exhumation of such large units may be problematic, it is also possible that both units moved as nearby individual slices, along essentially the same path. The very limited time available between high-pressure metamorphism of the Cima Lunga eclogites and the peak

of Lepontine metamorphism lends indirect support to this interpretation (fig 3.18). Around the peak of Lepontine metamorphism, the steep structures of the main phase of deformation developed that cut across nappe contacts (e.g. Möckel, 1969; Pfiffner and Trommsdorff, 1998). The hypothesis that the Cima Lunga nappe was emplaced between the other lower Penninic nappes during a late stage of Lepontine metamorphism (Engi et al., 1995) does not seem to be valid, unless the Arbedo gneisses of the present study area are part of the Adula-Cima Lunga nappe system and not of the Antigorio nappe, to which it has classically been attributed (Fischer, 1974; Spicher, 1980).

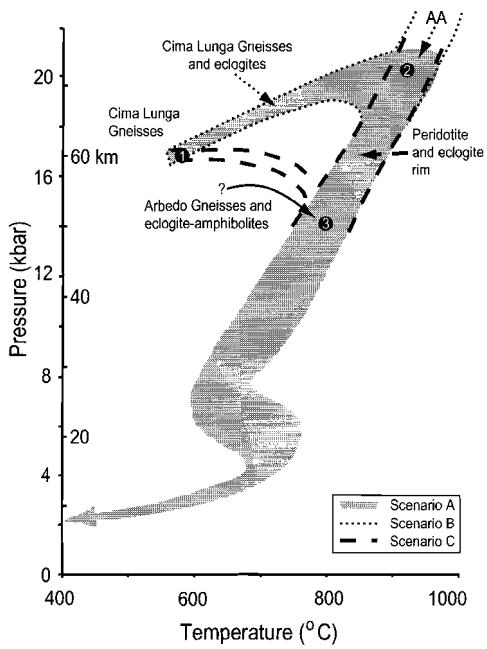

Figure 3.19: Three possible scenarios for the juxtaposition of the Alpe Arami garnet peridotite and its country rocks. Letters indicate the three scenarios, numbers label the critical observations.
Observation **1** is the presence of ctd inclusions in garnet in the Cima Lunga metapelite lens; **2** refers to the peak metamorphic pressure in the eclogites surrounding the peridotite body; **3** pertains to the highest recorded pressures in the eclogite-amphibolites of the Arbedo zone. See text for discussion.

3.5.2 Three possible scenarios for Alpe Arami and the Lepontine gneisses

The present analysis of the PTtD history of rocks from the Cima Lunga nappe and the Arbedo zone leaves three possible scenarios for the juxtaposition of the lithologies in the study area. The observations most pertinent to this discussion are labeled as follows on the PT-path of figure 3.19: (1) represents the presence of chloritoid inclusions within garnet in metapelites from the Cima Lunga nappe, (2) denotes the highest pressure and temperature recorded by the eclogites in the rim surrounding the Alpe Arami garnet peridotite body, and (3) marks the highest pressure and temperature recorded by the eclogites-amphibolites of the Arbedo zone. In each scenario the rocks from the Cima Lunga nappe and the Arbedo zone were juxtaposed at depth, for reasons argued above.

Scenario A: Alpe Arami subducted with Lepontine gneisses

In this scenario the Alpe Arami garnet peridotite body, the surrounding eclogites, and the Cima Lunga gneisses and metapelites were subducted during Alpine convergence. They may have originated from mid-crustal depths, as, for instance, suggested by Pfiffner and Trommsdorff (1998) and Trommsdorff et al. (2000). In that case, and supposing that the microstructures in the peridotite indeed reflect an ultra-deep origin (Dobrzhinetskaya et al., 1996), these microstructures must have formed during a

previous orogenic cycle. Consequently, they must have survived both earlier transport to crustal depths and the subsequent Alpine orogeny. My results have no bearing on the origin of the aforementioned microstructures and are inconclusive as to the depth of their formation, because these depths exceed the depth recorded by the country rocks addressed in this study.

Scenario B: Alpe Arami included in Cima Lunga gneisses and eclogites at great depth
In this scenario I assume that during the Alpine orogenic cycle the Alpe Arami peridotite body has been exhumed from a depth greater than about 70 kilometres, as suggested by Dobrzhinetskaya et al. (1999) and Green et al. (1997; 2000). In this case the gneisses and eclogites of the Cima Lunga nappe were subducted and incorporated the peridotite body at depth, possibly at depths reflected by the highest recorded pressures, or deeper, in which case no record of such higher conditions was preserved in the gneisses nor in the metabasites. This scenario does not seem very likely, however, because the rim of eclogites surrounding the peridotite body suggests that the eclogites and the peridotite body are genetically related. The systematic variations in garnet major element composition between the Arbedo and Cima Lunga metabasites also indicate that the eclogites surrounding the peridotite underwent a different Alpine metamorphic history compared to those of the Arbedo zone. On the other hand, the present scenario is supported by the identical trace element signature of the metabasic lenses from the Arbedo zone, of metabasites elsewhere in the Cima Lunga nappe, and of the eclogites surrounding the peridotite (Bocchio, 1975; Bocchio et al., 1985), indicating that all of these rocks have a tholeitic affinity.

Scenario C: Alpe Arami and eclogites included in Cima Lunga gneisses at intermediate depth
In the third scenario it is assumed that the Cima Lunga gneisses and metapelites did not reach pressures higher than the maximum recorded pressure in these rocks of about 16 kbar, which is equivalent to a depth of about 55 kilometres. In this scenario the Alpe Arami peridotite body and the surrounding eclogites were incorporated in the gneisses near the depth at which the Cima Lunga nappe and the Arbedo zone were juxtaposed, a hypothesis that would fit a lithospheric mélange origin for the Cima Lunga nappe (Trommsdorff, 1990). In this case however, the identical trace element signature of all eclogites and eclogite-amphibolites mentioned above remains difficult to explain.

As each of these three scenarios is consistent with the results of my study, as well as with data from the literature, this study cannot discriminate between these scenarios.

3.5.3 Implications for orogenic processes
The thermal history inferred here for the Alpe Arami country rock gneisses and eclogites shows during their exhumation two striking features (fig 3.18). Firstly, peak pressure metamorphism was followed by a very high rate of exhumation, prior to the Lepontine thermal overprint. The rocks were brought from a depth of at least 60 kilometres to about 18 kilometres in 5.1 million years, implying exhumation rates in excess of

7 mm/year (fig 3.18). The exhumation rate after the peak of Lepontine metamorphism was much lower, i.e. about 0.8 mm/yr.
The marked difference in exhumation rates prior to and after the peak of Lepontine metamorphism suggests that different processes have been active. The nature of the tectonic process that was responsible for the high initial exhumation rates is as yet poorly understood. The most popular hypothesis currently envisaged to be responsible for initial exhumation involves the squeezing of slices of subducted material northward, back up the subduction zone by an unspecified mechanism (e.g. Platt, 1993; Schmid et al., 1997). I note that top-to-the-south kinematics, expected in such a scenario, have not been reported, although this could also be due to later rotation of structures, or to reactivation.
The later stages of exhumation may have been caused by tectonic uplift along the Insubric Line due to continuous underplating of subducted material at the base of the orogenic wedge, forcing material at the back of the wedge to move upwards against the overriding plate (e.g. Platt, 1986). Numerical experiments concerning the tectonothermal history of the central Alps indicate that the exhumation rates during the later stages of the Alpine history are compatible with erosion without a significant contribution of extensional faulting (Schlunegger and Willet, 1999), although interplay of both processes is likely, because the later stages of folding indicate vertical shortening, hence horizontal extension (e.g. Grujic and Mancktelow, 1996).
The second striking feature of the retrograde history concerns the thermal evolution after high-pressure metamorphism, involving a stage of cooling during initial decompression, after which the rocks were re-heated by some 110 °C to about 740 °C at pressures of 4 to 6 kbar, before final exhumation. This thermal peak has long been recognised as the Lepontine metamorphism (e.g. Frey et al., 1980; Niggli and Niggli, 1965; Wenk, 1956). My study of the Alpe Arami country rock gneisses has yielded evidence that peak temperatures were higher than previously reported (e.g. Engi et al., 1995; Todd and Engi, 1997).
Classical explanations of the Lepontine amphibolite facies metamorphism involve radiogenic self-heating of the thickened crustal pile (e.g. Hunziker et al., 1989; Vance and O'Nions, 1992, and references therein). However, recent geochronological studies (e.g. Becker, 1993; Gebauer, 1996) have shown that the time span between high-pressure metamorphism of the Cima Lunga eclogites and the peak of Lepontine metamorphism is of the order of 5 Ma, precluding any significant regional rise of metamorphic temperatures due to such a process. Contact metamorphism is not a likely cause either, because of the regional nature of the Lepontine metamorphism, and because the underlying magmatism would still need explanation.
It has been suggested that slab detachment (Wortel and Spakman, 1992) of the subducted continental lithosphere may allow for an influx of hot material near the base of the orogen (Von Blanckenburg and Davies, 1995). This process potentially explains the sudden increase of the metamorphic temperature during exhumation, as well as the widespread occurrence of Eocene plutons along the Insubric Line in the central Alps (Von Blanckenburg et al., 1998). It is, as yet, unclear how slab detachment, or breakoff,

may have contributed to the mechanics of the exhumation process. Decrease of the slab pull force may increase the buoyancy of the remaining slab and cause vertical movement in the orogen (Buiter et al., 1998), but the role of such a process in forcing slivers of subducted material upward along the subduction zone, as suggested by Davies and Von Blanckenburg (1995) is unclear. The mechanism by which deeply subducted slivers are transported towards the base of the orogenic wedge thus remains enigmatic.

3.6 Conclusions

The present study of the country rock gneisses and eclogites near Alpe Arami yields new details on the metamorphic evolution of these rocks. The occurrence of chloritoid inclusions in garnet in the metapelites of the Cima Lunga nappe led me to infer that these rocks underwent high-pressure metamorphism before the onset of Lepontine amphibolite facies metamorphism. The presence of relics of high-pressure metamorphism in eclogite-amphibolites distributed in the Arbedo zone suggests that the Cima Lunga nappe and the migmatitic gneisses of the Arbedo zone were juxtaposed before Lepontine re-heating, possibly at depths as much as 50 kilometres below the Earth's surface. Since deep juxtaposition would hamper fast early exhumation, I envisage that both units were exhumed as nearby but tectonically separate entities, along essentially the same trajectory.

Spectacular spinel and corundum-bearing symplectites developed in the eclogite-amphibolites of the Arbedo zone and in the Cima Lunga eclogites during Lepontine high-temperature metamorphism. This observation, the presence of cordierite, and the breakdown of muscovite to sillimanite in metapelites from the Cima Lunga nappe support results from amphibole-plagioclase thermometry, which indicate that temperatures were as high as 740 °C at pressures of 4-6 kbar. These temperatures are significantly higher than previously inferred. In view of the rapidly growing evidence for a Tertiary age of the high-pressure metamorphism, leaving very limited time between peak pressure metamorphism and the Lepontine high-temperature peak, I suggest that breakoff of subducted continental lithosphere is the most likely cause of Lepontine metamorphism in the central Alps.

I envisage the following three possible scenarios for the evolution of the Alpe Arami peridotite body and its incorporation into the surrounding country rock gneisses: (1) the Alpe Arami peridotite body may owe its ultra-high pressure microstructures and assemblages to a previous orogenic cycle, and have become subducted during the Alpine orogeny together with the Lepontine country rocks; (2) the peridotite may have been included in the country rocks at great depth, or (3) the peridotites and eclogites may have become juxtaposed with the country rock gneisses at intermediate depths. The structure and metamorphism of the country rocks addressed in this study are inconclusive as to these three scenarios.

The exhumation rate between the high-pressure peak and the climax of high-temperature metamorphism is extremely high. The mechanism by which subducted material is

transported to mid-crustal depth at such high velocities is poorly understood, although transport back up the subduction zone at present seems to be the only viable possibility to explain the return of high-pressure rocks to shallower levels. Exhumation rates after the Lepontine metamorphism are much slower. This part of the exhumation history may have been achieved by interplay of tectonic uplift along the Insubric Line, and erosion.

Chapter 4

Structure and metamorphism of the Gran Paradiso massif, western Alps, Italy

4.1 Abstract

The processes involved in the exhumation of high-pressure metamorphic rocks in the Alps have long been subject of debate. Moreover, the discovery of ultrahigh-pressure metamorphic rocks in the western and central Alps has led to enhanced interest regarding possible exhumation mechanisms, in particular because of accumulating evidence for an Eocene age of the high-pressure metamorphism. It follows that pertinent exhumation mechanisms should be capable not only of carrying the high-pressure rocks from sub-crustal levels to the Earth's surface, but also to achieving this exhumation in geologically very short time spans.

This study aims to improve constraints on the pressure-temperature evolution of high-pressure rocks presently exposed in the Gran Paradiso massif in western Alps. The pressure-temperature-time trajectory and structural history of the studied rocks provides constraints on the processes that cause the thermal evolution and exhumation of the pertinent rocks.

High-pressure metamorphism in the rocks of the Gran Paradiso massif is found to have culminated at temperatures around 525 °C and pressures of 12 to 14 kbar. After high-pressure metamorphism, the rocks cooled by about 40 °C during initial decompression, while undergoing top-to-the-west shear on chlorite bearing shear bands and larger scale shear zones. Biotite bearing shear bands and larger shear zones related to top-to-the-east deformation affected the Gran Paradiso massif during reheating to temperatures of around 550 °C at 6 to 7 kbar. Further exhumation occurred at relatively high temperatures via conditions of about 400 °C and 2 to 3 kbar. It follows, that the exhumation history of the Gran Paradiso rocks involved a stage of re-heating by several tens of degrees before final cooling and exhumation. A potentially viable explanation of this re-heating may be breakoff of a subducting slab in the upper mantle, allowing advective heat transfer from upwelling asthenospheric mantle to the base of the crust.

4.2 Introduction

4.2.1 Geology of the western Alps

The Alps are generally considered to have formed during southward subduction of the Alpine Tethys underneath the African plate (e.g. Droop et al., 1990), related to the approach and eventual collision of the African and European margins. The Internal Penninic nappes (IPN), i.e. the Monte Rosa, Gran Paradiso and Dora Maira units, are the tectonically lowermost units exposed in the Western Alps (fig 4.1). As indicated by their composition dominated by metamorphosed granites and metasediments, these

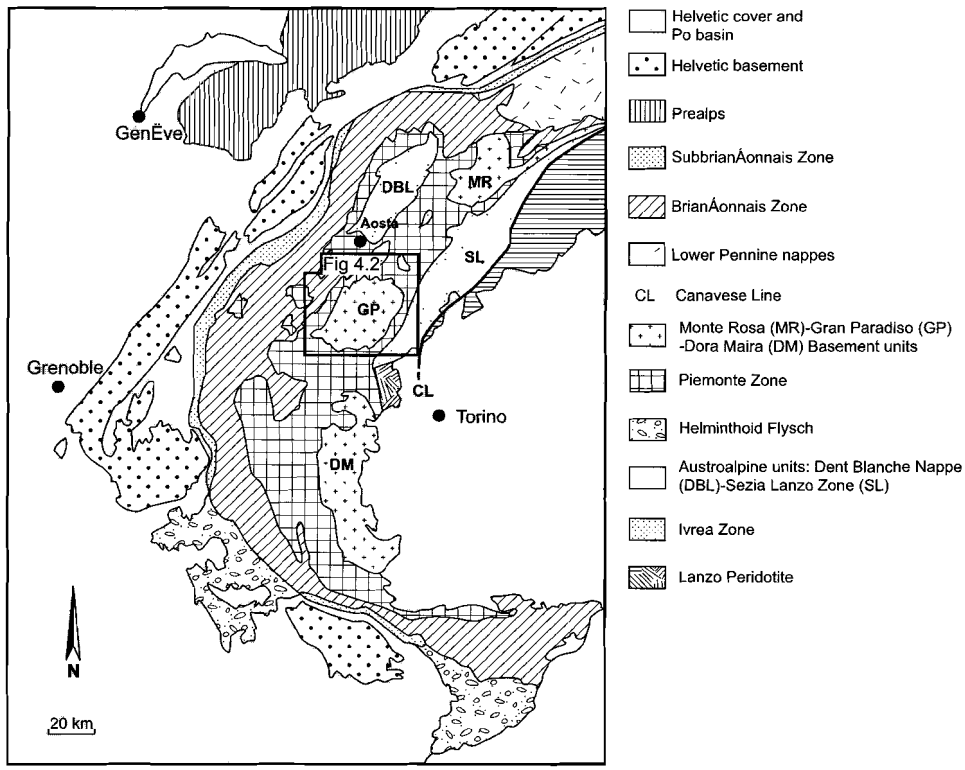

Figure 4.1: Tectonic map of the Western Alps.

rocks are clearly derived from continental crust, but their provenance is debated. There is no agreement to date on whether the IPN originate from the northern margin of Adria, an African promontory (e.g. Hunziker et al., 1989; Stampfli and Marchant, 1997), from the Briançonnais ribbon continent along the southern margin of Europe (e.g. Platt, 1986; Radelli and Desmons, 1987), or from the European margin itself (e.g. Hsü, 1989; Rubatto and Gebauer, 1999). On the basis of poorly dated sedimentary deposits and selected radiometric age determinations, it has been suggested that the Gran Paradiso massif originates from the northwestern margin of Adria (Stampfli et al., 1998). An Adriatic origin, however, does not fit recent age determinations of high-pressure metamorphism in Gran Paradiso (Meffan-Main, pers. comm.), Dora Maira (Gebauer et al., 1993; Tilton et al., 1989) and Monte Rosa (Rubatto and Gebauer, 1999). A related question concerns the number of oceanic basins subducted during Alpine convergence (e.g. Mattauer et al., 1987; Rubatto, 1998).

Despite these different interpretations, many workers believe that the IPN represent basement fragments of the Briançonnais ribbon continent, located paleogeographically in between the Piemonte-Ligurian ocean and the possibly oceanic Valais basin (e.g. Schmid

and Kissling, 2000; Stampfli, 1993). The Briançonnais ribbon continent was subducted underneath Adria from about 65 Ma at a rate of about 1 cm/yr (Schmid and Kissling, 2000). The geometry of convergence and collision in the western Alps is complicated, however, because of existing evidence for significant rotation, oblique convergence and out-of-section movements (e.g. Schmid and Kissling, 2000; Thomas et al., 1999). During the early stages of collision of Adria with the European plate (50-35 Ma), the NNE-SSW segment of the plate margin served as a zone of sinistral transpression (e.g. Schmid and Kissling, 2000; Stampfli and Marchant, 1997), to accommodate the northward movement of Adria. After 35 Ma ago, the movement of Adria with respect to the European plate is inferred to have shifted to a northwesterly direction, leading to another 100 kilometres of shortening along the WNW-ESE oriented ECORS-CROP seismic section that crosses the Gran Paradiso massif (Schmid and Kissling, 2000).
During subduction, the Internal Penninic nappes underwent high-pressure, low-temperature metamorphism and were subsequently exhumed. The exhumation history of the IPN has been a matter of debate, especially since the first reports of coesite from the Dora Maira massif (Chopin, 1984) indicating that crustal material, subducted to depths in excess of 90 kilometres, had returned to the Earth's surface during the Alpine orogeny. For several decades, high-pressure metamorphism has been considered to have occurred between 140 and 85 Ma (Bocquet et al., 1974; Chopin and Maluski, 1980; Hunziker et al., 1992, and references therein), but recent geochronological studies provide accumulating evidence for an Eocene age of peak pressure metamorphism (e.g. Amato et al., 1999; Gebauer et al., 1993; Meffan-Main, pers. comm., 1999; Tilton et al., 1989; Tilton et al., 1991). Both the high peak metamorphic pressures and the fast exhumation of the IPN implied by recent the geochronological data have reinforced the need for detailed reconstruction of the metamorphic history of these units during their exhumation. Many authors focus on either the structural (e.g. Butler and Freeman, 1996), or the metamorphic history (e.g. Borghi et al., 1996; Borghi and Sandrone, 1995), but few attempt to combine information from both fields.
The present work aims to elucidate the pressure-temperature evolution of the Gran Paradiso basement rocks through a combination of structural and metamorphic study, with focus on the thermal evolution during decompression. Results are reported from detailed lithological mapping in the Valle Piantonetto as a structural cross section across the northern half of the massif, and from thermobarometric investigation of samples from these areas and from the Vallone del Roc (fig. 4.2). The new data are tied in with radiometric dating documented in the literature, and implications for the geodynamic processes that took place in this part of the Western Alps are discussed.

4.2.2 Gran Paradiso massif

The oldest lithological unit identified in the Gran Paradiso basement is the Gneiss Minuti. The Gneiss Minuti (GM) largely consist of a polymetamorphic unit of probable sedimentary origin (GM s.s.), which overlies the monometamorphic Money or Erfaulet unit (fig 4.2, 4.6) made up of quartzite conglomerate and felsic meta-igneous rocks (Compagnoni et al., 1974).

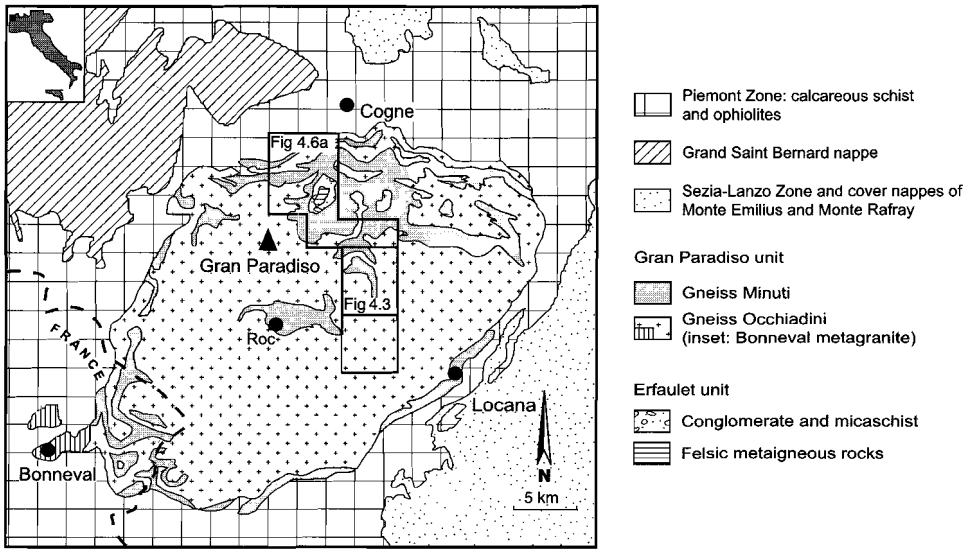

Figure 4.2: Geological map of Gran Paradiso, indicating sample location in Vallone del Roc, and locations of figures 4.3 and 4.6a. After Compagnoni et al. (1974).

The Gneiss Minuti (s.s.) include lenses and bands of mafic rock. The largest exposed mafic body is about 2.5 kilometres long and some 100 m wide, and occurs in the Vallone del Roc (Dal Piaz and Lombardo, 1986). A smaller, 10 metre scale, outcrop occurs at Lago di Telessio (figs 4.4a, 4.6). These, and abundant smaller mafic pods occur as boudinaged layers subparallel to the metasedimentary layering. The metabasites (M) are important for metamorphic studies, because they often contain relics of an eclogite facies mineral assemblage. A body of gabbroic rocks with a continental affinity has been described near the southern edge of the Gran Paradiso massif (Biino and Pognante, 1989). Other metabasites have a basaltic or ferro-basaltic bulk composition, and locally occurring Ca-rich assemblages in the Vallone del Roc point towards a volcaniclastic origin (Dal Piaz and Lombardo, 1986).

The composite of Gneiss Minuti and metabasites was intruded by a porphyritic granite during late Variscan times. Total Pb zircon dates range between 301 and 350 Ma and reflect crystallisation of the granite (Buchs et al., 1962; Chessex et al., 1964; Pangaud et al., 1957). The magmatic age of similar granites in the Dora Maira massif, commonly considered structurally and paleogeographically equivalent to the Gran Paradiso massif, has recently been determined at 275 Ma by SHRIMP U-Pb zircon dating (Gebauer et al., 1997).

During Alpine times the granitic rocks were transformed into augengneisses, often referred to as the Gneiss Occhiadini (GO) by Italian geologists (fig 4.2). Intrusive contacts have been reported between the augengneisses and the Gneiss Minuti (Callegari et al., 1969; Compagnoni and Prato, 1969) as well as between the augengneisses and metabasites (Compagnoni and Lombardo, 1974), which confines the age of the metabasites

to the upper Carboniferous or lower Permian and demonstrates that the high-pressure assemblages found in the metabasic rocks must be related to Alpine metamorphism. The Bonneval metagranite in the SW part of the Gran Paradiso massif (fig 4.2) is separated from the augengneisses by a fault, but structural studies suggest that this granite was part of the Gran Paradiso nappe during Alpine orogenesis (Vearncombe, 1985).

4.3 Structures of the Gran Paradiso basement

The structure and lithology of the central Gran Paradiso massif have been mapped in detail (1:10,000) in the upper Valle Piantonetto (figs 4.3, 4.6b). This mapping was used as a basis to assess the structural history of the massif and to select structurally controlled samples appropriate for geothermobarometry.
The rocks of the Gran Paradiso massif commonly show a dominant planar fabric which, in the Gneiss Minuti is parallel to the axial planes of tight to isoclinal folds of a compositional layering. This fabric can be traced into the gneissic layering of the augengneisses, and is here referred to as the main-phase foliation Sm related to the main phase of deformation (Dm). The Sm fabric serves as a reference in unravelling and relative timing of different generations of deformational structures that either predate (Dm-2, Dm-1) or postdate (Dm+1) the main structure.

4.3.1 Pre-Alpine deformation

The earliest deformational structures in the Gran Paradiso basement are found in the Gneiss Minuti. Xenoliths of Gneiss Minuti enclosed in the augengneisses or Gneiss Occhiadini show a Dm-2 folded fabric (fig 4.4b) indicating that the Gneiss Minuti were deformed before they were intruded by multiple generations of porphyritic granites (fig 4.4c). In larger bodies of the Gneiss Minuti, Dm-2 folds are locally cut by cm to dm thick aplites and pegmatites that are thought to be related to intrusion of the aforementioned granites. The folded fabric may either be a sedimentary layering or a differentiated layering, which indicates at least one, or even two phases of pre-Alpine deformation.

4.3.2 Alpine deformation

The earliest Alpine structure is a Dm-1 chloritoid bearing foliation seen in both the Gneiss Minuti and the augengneisses (fig 4.5a). The chloritoid is usually intergrown with white mica, and coexists with garnet and quartz. Locally, some aluminosilicate (sillimanite or kyanite) is observed in this fabric. The chloritoid bearing foliation (Sm-1) clearly predates the main phase deformation because Sm-1 is demonstrably folded by main-phase folds. Intense stretching and boudinage of pegmatites that intruded the Gneiss Minuti also predates the main-phase and may be related to Dm-1 (fig 4.4d).
Features related to the main phase of deformation (Dm) dominate in the Gran Paradiso massif (fig 4.6). Dm is characterised by a chlorite and occasionally biotite bearing foliation in both the Gneiss Minuti and in the augengneisses. The main-phase foliation is continuous across intrusive contacts of the gneisses with the adjacent Gneiss Minuti. In

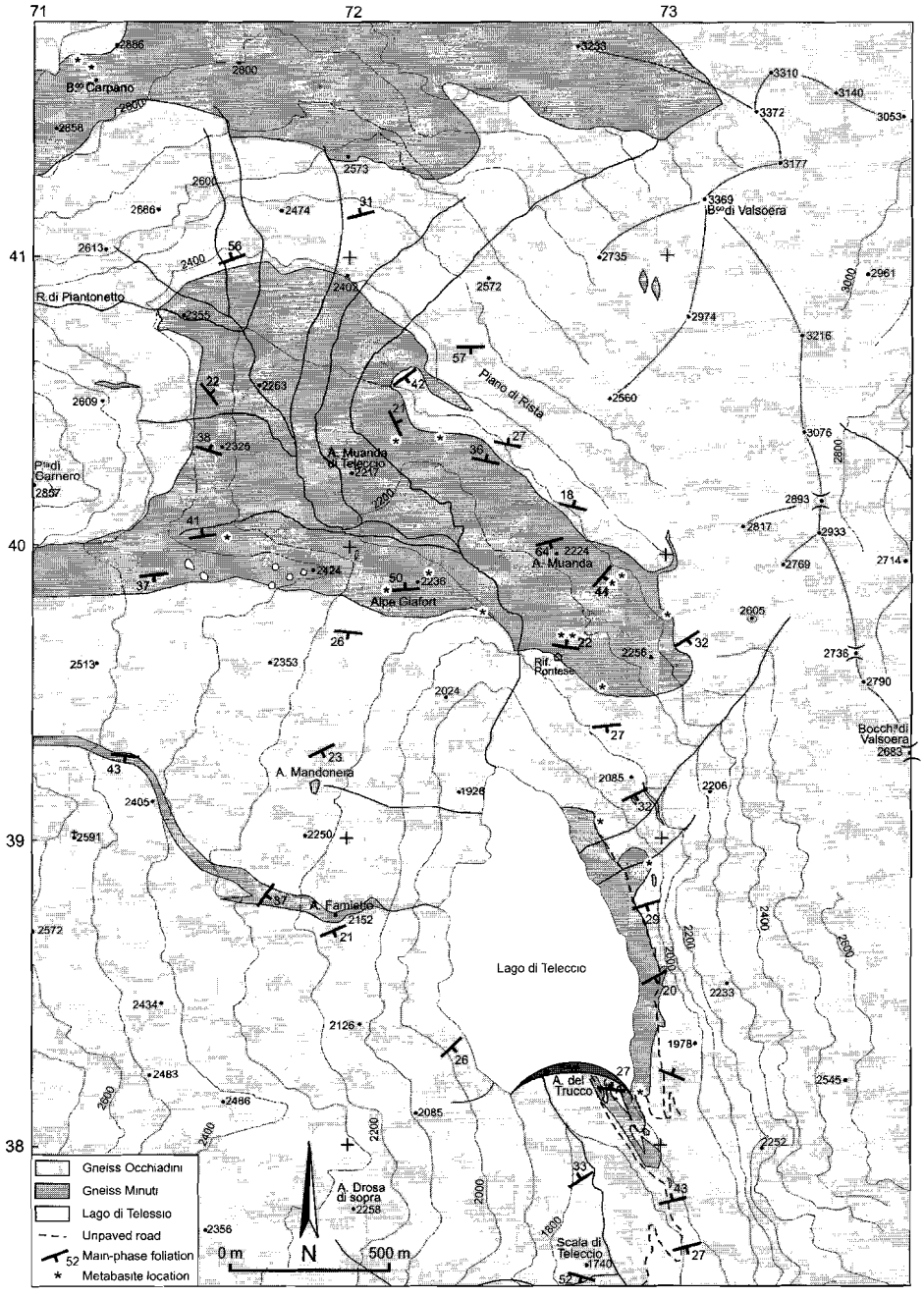

Figure 4.3: Geological map of the upper Piantonetto Valley indicating the trend of the mainphase foliation and metabasite locations.

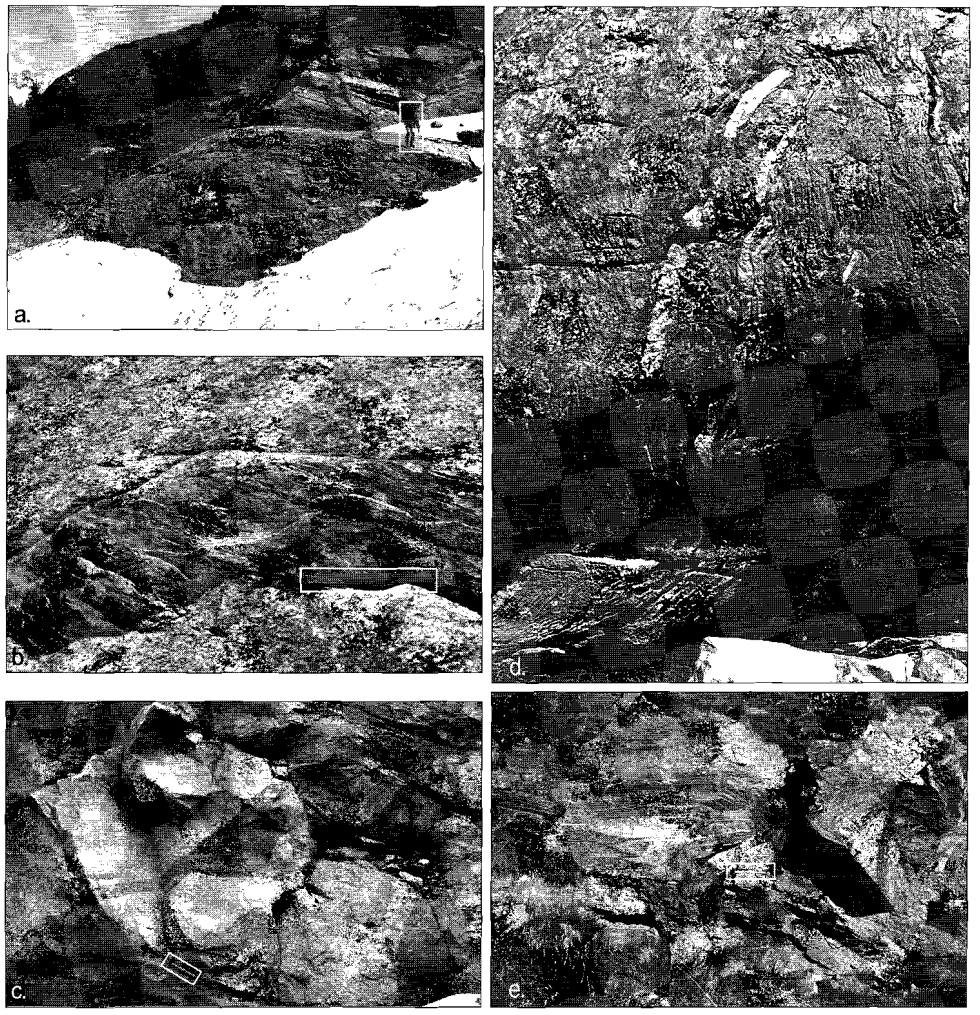

Figure 4.4: Field aspects of relevant outcrops. **a.** Metabasite outcrop along Lago di Telessio; geologist for scale. **b.** Compositional layering in a Gneiss Minuti xenolith in augengneiss, pen for scale. **c.** Different generations of granite; hammer for scale. **d.** Pegmatite in Gneiss Minuti boudinaged during Dm-1; field of view approximately 4 m high. e. Dm or Dm+1 fold in the lake section of fig. 4.6b; field of view about 6 m wide, hammer for scale.

the study area, the main-phase foliation is mostly flat-lying with a roughly EW strike (fig 4.7a), and up to 10 m scale isoclinal folds are locally observed in both the Gneiss Minuti and the augengneisses (fig 4.4e). In most localities, the associated fold axes plunge shallowly eastward (fig 4.7b).

The main-phase structures are overprinted by centimetre to metre scale ductile shear zones with a top-to-the-west sense of shear in all lithologies. These structures are related to a younger phase of deformation (Dm+1) superimposed on the main-phase

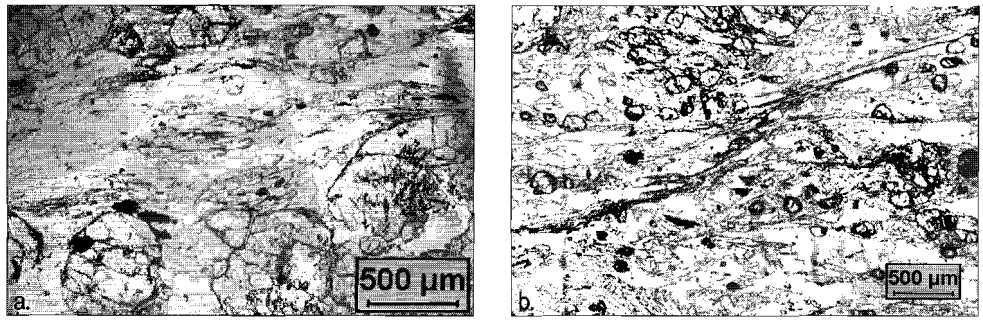

Figure 4.5: Thin sections in plain polarised light. **a.** Dm-1 chloritoid-bearing fabric in augengneiss. **b.** Dm+1 chlorite-bearing shear bands in Gneiss Minuti.

structure. Dm+1 shear bands, developed at both macroscopical and microscopical scales, are usually decorated by elongated chlorite crystals (fig 4.5b). Chlorite stretching lineations on the planes of the shear zones are parallel to stretching lineations observed on foliation planes in both the Gneiss Minuti and the augengneisses (fig 4.7c). It is striking that these stretching lineations are also roughly parallel to the Dm fold axes. This may indicate that the main-phase fold axes passively rotated towards parallelism during Dm+1, or alternatively, that the structures ascribed here to Dm+1 in fact result of progressive main-phase deformation. The common observation that main phase folding intensifies towards Dm+1 (fig 4.6b) shear structures lends support to the latter hypothesis.
The youngest ductile deformational structures identified are centimetre to metre scale shear zones and microscopically observed shear bands formed during Dm+2 top-to-the-east shear. The Dm+2 shear bands are mostly defined by biotite, which often grows around chlorite or white mica. This phase of shearing may be related to the top-to-the-east shear documented in the Entrelor shear zone and as well as along the northern contact of the Gran Paradiso massif with the rocks of the ophiolitic Piemonte zone (Butler and Freeman, 1996).
The youngest Alpine structures are (Dm+3) quartz veins that crosscut all lithologies. These structures clearly indicate a late, essentially post metamorphic phase of brittle deformation.

4.4 Metamorphism of the Gran Paradiso basement

4.4.1 Petrography

Gneiss Minuti (GM)
The earliest mineral assemblage present in the pelitic schists comprises considerable amounts of chloritoid. The other components of the assemblage are garnet, plagioclase, white mica and quartz (assemblage I in fig 4.8a). Sillimanite, mostly replaced by pseudomorphic kyanite, has been reported from outcrops near lake Telessio in the present study area (Callegari et al., 1969), but their finding could not be confirmed in this study.

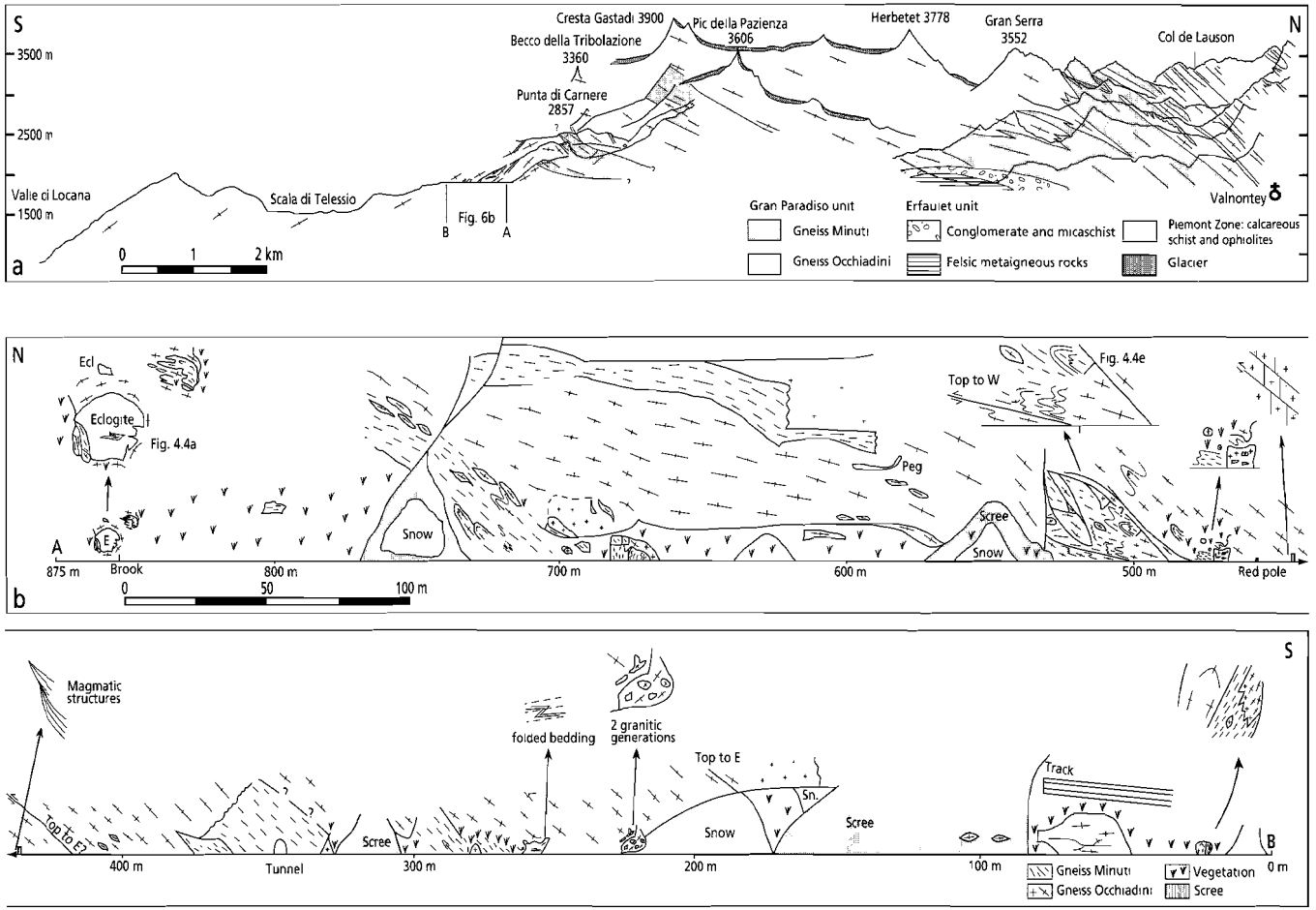

Figure 4.6: NS sections across through the Gran Paradiso nappe. **a.** Composite cross section of the northern half of Gran Paradiso. **b.** Overview of Lake section in the upper Piantonetto valley. Location indicated in fig. 4.6a; note opposite orientation.

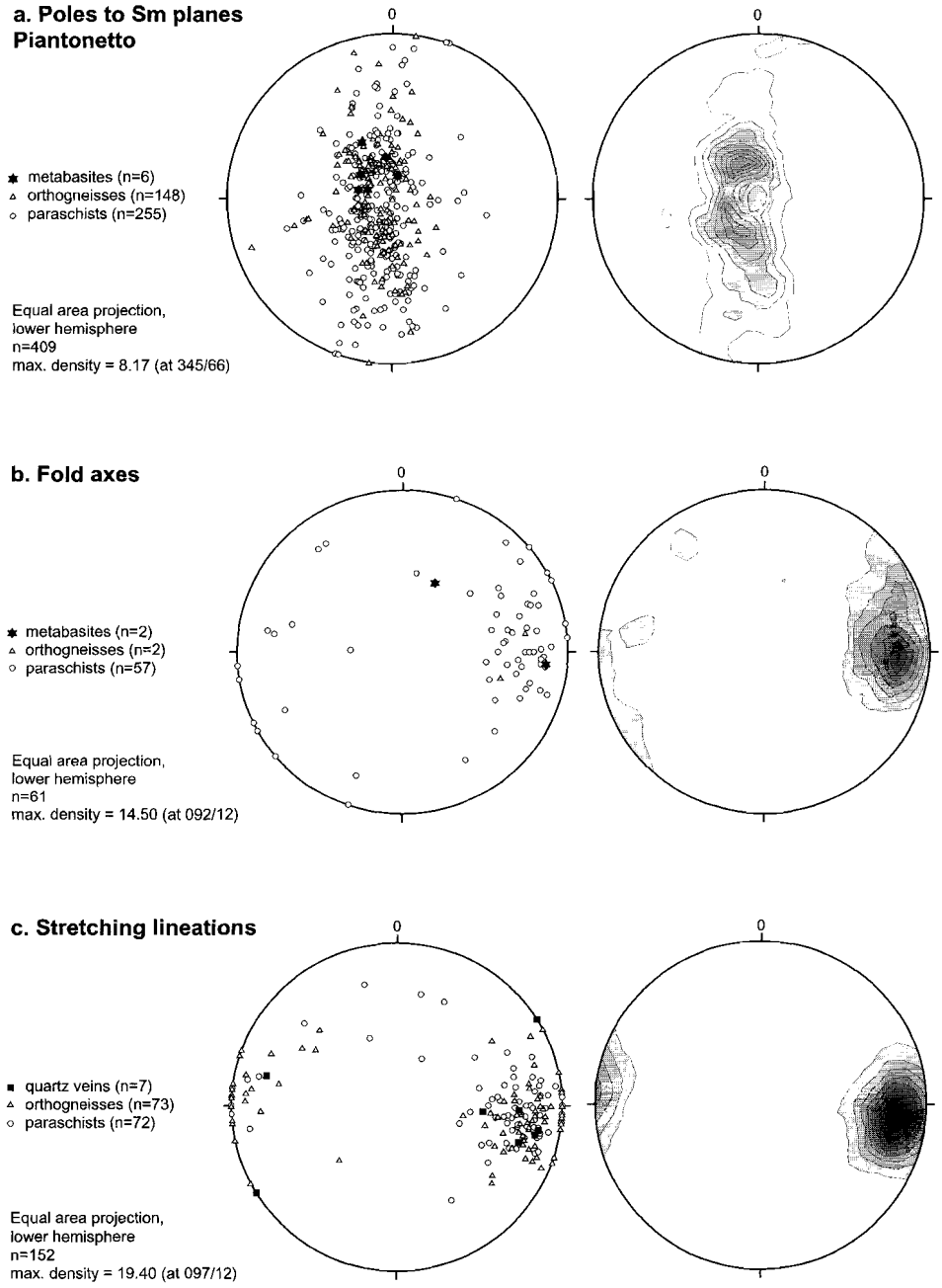

Figure 4.7: Equal area lower hemisphere projections of structural data. **a.** Main-phase foliation, all lithologies. **b.** Dm fold axes, all lithologies. **c.** Dm+1 stretching lineations, all lithologies.

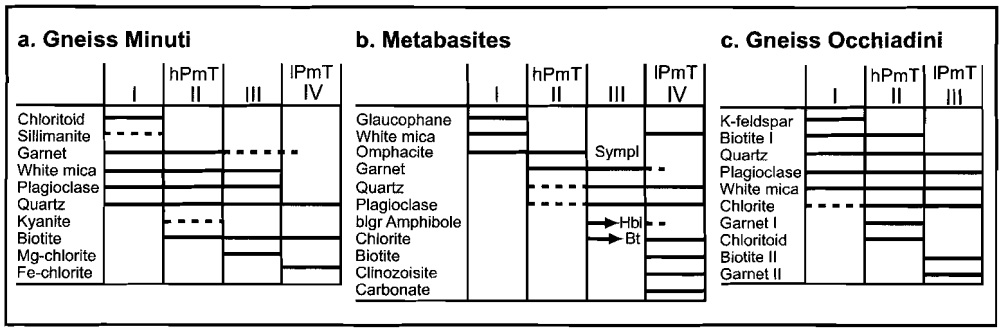

Figure 4.8: Mineral assemblagesin: **a.** Gneiss Minuti (GM). **b.** Metabasites (M). **c.** Gneiss Occhiadini (GO). Mineral assemblages are indicated with roman numerals (I, II, III and IV), hPmT stands for high-pressure, medium-temperature metamorphism, lPmT for low-pressure, medium-temperature metamorphism.

This assemblage predates the main-phase structure, as witnessed for example by micro-folds affecting chloritoid grains and aggregates.

The high-pressure assemblage (II) is made up of garnet aggregates, white mica (partly replacing chloritoid), biotite, plagioclase and quartz (fig 4.8a). Talc coexisting with chloritoid and phengite reported from the "Silvery Micaschists" in the northern part of Gran Paradiso indicates high-pressure metamorphism (i.e. P > 10 kbar, Chopin (1981)). Some kyanite occurs in the Gneiss Minuti (Compagnoni and Prato, 1969), and its rare occurrence has been confirmed in this study. Accessory minerals of the main assemblage are titanite, clinozoisite, carbonates, rutile and tourmaline. Large garnets often have an inclusion-rich core or ring and an inclusion-free rim, indicating that the garnets grew in stages (fig 4.10a). The mineral assemblages of samples used for thermobarometry are listed in table A3.1 of Appendix 3.

Partial replacement of garnet by Mg-chlorite or biotite and opaque minerals reflects retrograde metamorphism (III in figure 4.8). This stage of metamorphism is clearly associated with the development of the main-phase foliation (Sm), as this foliation is principally defined by the chlorite. Quartz, plagioclase and white mica remained stable. Some of the Mg-chlorite shows a rim of biotite. A more iron-rich variety of chlorite developed after these biotite rims. The presence of relics of several subsequent metamorphic assemblages reflects incomplete retrogression.

Metabasites (M)

Like the metapelitic Gneiss Minuti, the enclosed metabasic lenses show a sequence of successive metamorphic mineral assemblages. The earliest of these assemblages, labelled I in figure 4.8b, is represented by inclusions of glaucophane, white mica and omphacite in garnet. This assemblage is overprinted by an assemblage (II) with garnet and omphacite as the dominant minerals, probably associated with plagioclase and quartz, clearly reflecting high-pressure metamorphism.

In many samples, omphacite breaks down to symplectites that mostly consist of plagioclase and blue-green amphibole, whereas garnet remains stable (III in figure 4.8b).

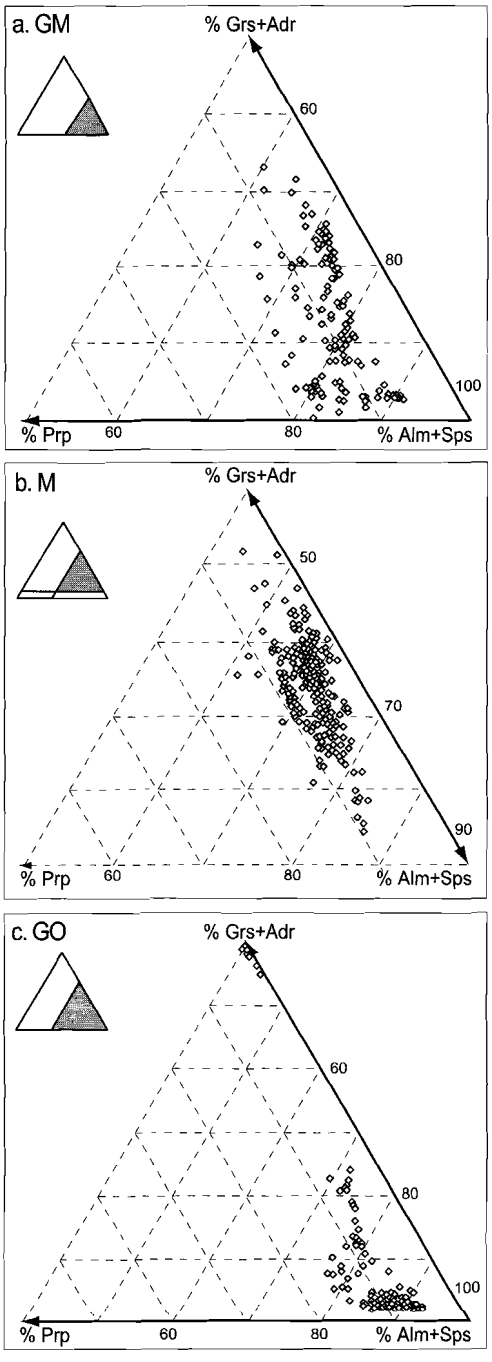

Blue-green amphiboles locally include relics of omphacite and symplectite. The rims of the amphiboles are olive green indicating a higher hornblende component. Plagioclases related to this assemblage are zoned (fig 4.14c) and they sometimes include trails of biotite, chlorite or white mica. Garnet breaks down to green amphibole and later to biotite and locally chlorite. Accessory phases are epidote and white mica.
A final stable assemblage (IV) contains chlorite, biotite, plagioclase, white mica and quartz. Large amounts of carbonate minerals are locally present. Accessory minerals are ilmenite, titanite, epidote and tourmaline.

Augengneisses (Gneiss Occhiadini, GO)
Plagioclase, K-feldspar, sometimes with microcline twinning or a micropertitic texture, quartz, large biotite crystals and white mica are remnants of the initial granitic assemblage (labelled I in figure 4.8c). Accessory minerals are clinozoisite, epidote, zircon and apatite. The presence of garnet, white mica, chlorite and chloritoid as well as rims of secondary biotite around large biotite crystals of igneous origin, indicated as assemble II in figure 4.8c, reflects alpine metamorphism in the augengneisses. During the later stages a second, inclusion free generation of small garnets formed, as well as biotite, white mica and quartz (assemble III). Some of the garnet broke down to chlorite. Accessory clinozoisite and epidote grew at the expense of primary feldspars.

Figure 4.9: Ternary plots of garnet compositions. **a.** Gneiss Minuti (GM). **b.** Metabasites (M). **c.** Gneiss Occhiadini (GO).

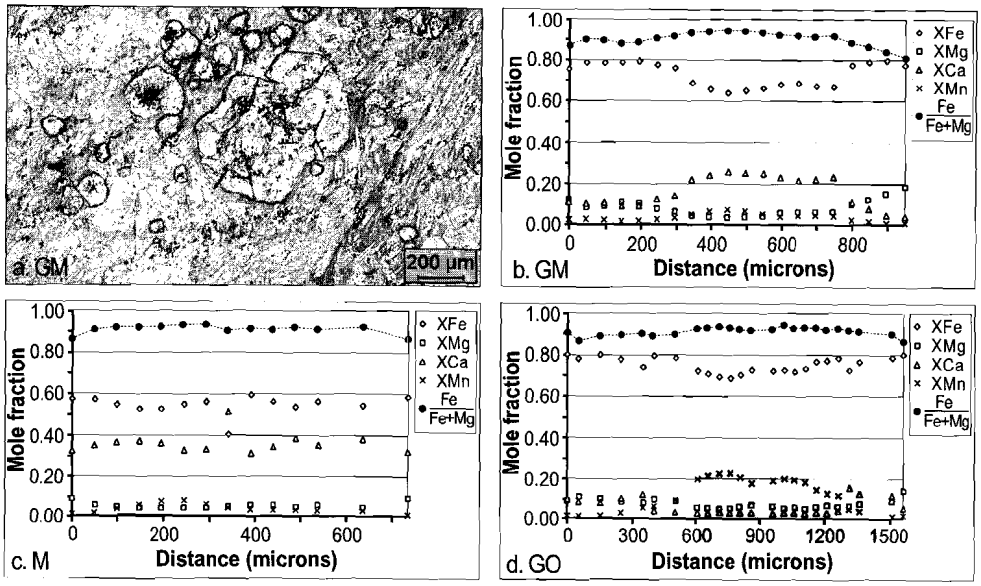

Figure 4.10: Compositional zoning in garnet. **a.** Photomicrograph of zoned garnet from the Gneiss Minuti (GM). **b.** Compositional variation across zoned garnet from the Gneiss Minuti (GM). **c.** Compositional variation across zoned garnet from the metabasites (M). **d.** Compositional variation across zoned garnet from the augengneisses (GO).

4.4.2 Mineral chemistry

Microchemical analyses were carried out using an automated JEOL 8600 microprobe at the EU Geochemical Facility in the University of Bristol, UK. The accelerating voltage during the analyses was 15 kV at a beam current of 15 nA, the spot size was 1-5 microns, with the larger spot size in case of Na bearing phases to minimise alkali volatilisation. Peak counting times ranged between 15 and 20 seconds. The following natural standards were used: albite for Na, olivine for Mg, spinel for Al, diopside for Si, K-feldspar for K, wollastonite for Ca, $SrTiO_3$ for Ti, hematite for Fe, MnO for Mn, Cr_2O_3 for Cr and nickel (metal) for Ni.

The mineral abbreviations used in the following sections are all taken from Kretz (1983). In addition, WhM is used to denote unspecified white mica, and Phen for phengitic white mica, i.e. solid solutions between muscovite, aluminoceladonite and celadonite (Rieder et al., 1999). Representative analyses of Grt, Omp, amphiboles, Pl, Bt, Phen, Chl, Ctd are given in Appendix 3.

Procedures for the estimation of the ferric iron content of analysed minerals were described in section 3.4.2.3. Ferric iron content was estimated using the same methods for garnet, pyroxene, amphibole and biotite. In the case of chloritoid, all trivalent iron is assumed to substitute for Al, so that $Fe^{3+} = 1-(Al^{VI} + Cr + Ti)$ (cf. Deer et al., 1992); all other minerals have been assumed to contain ferrous iron only.

Garnet

Garnet occurs in each of the three main lithologies. In the Gneiss Minuti, the general composition of garnet is $Alm_{60-90}And_{0-5}Grs_{0-30}Prp_{5-20}Sps_{0-20}$ (fig 4.9a), in the metabasites $Alm_{45-74}And_{0-8}Grs_{15-45}Prp_{2-12}Sps_{0-11}$ (fig 4.9b) and in the Gneiss Occhiadini $Alm_{32-84}And_{0-7}Grs_{0-55}Prp_{0-16}Sp_{s0-25}$ (fig 4.9c). Garnets are often strongly zoned. This zoning is likely to be growth zoning because, as deduced below, metamorphic temperatures were not extremely high and cooling took place relatively quickly. Following the calculation of Spear (1993, p. 613), the characteristic diffusion length for Mg in garnet is 4.7 microns per million years at 500 °C, and 0.3 microns at 400 °C. As can been seen in the zoning profiles from Gran Paradiso, the zoning is recorded over much larger distances (figs 4.10 a-d), so it is unlikely that the observed zoning results from diffusion of cations out of or into the garnets during retrograde metamorphism. It is noted however, that due to potential problems of inter-diffusion, calculations of diffusion distances for natural rocks should be viewed with caution.

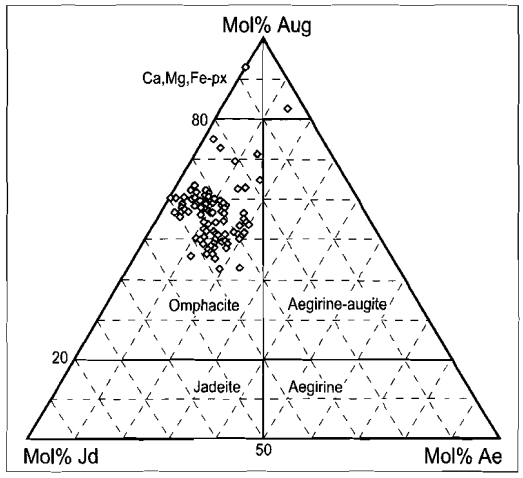

Figure 4.11: Ternary plot of pyroxene compositions (cf. Morimoto et al., 1988).

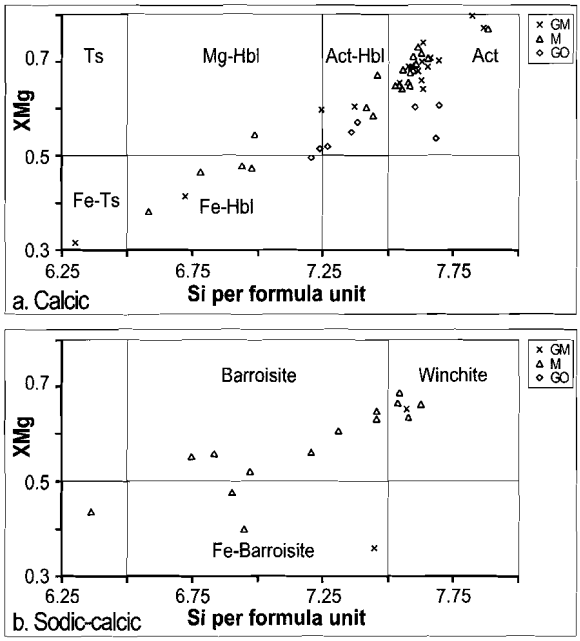

Figure 4.12: Amphibole compositions (cf. Leake, 1978). **a.** Calcic amphiboles. **b.** Sodic-calcic amphiboles.

The relative proportions of iron and magnesium are indicative of ambient temperature during garnet formation (e.g. Råheim and Green, 1974). A decrease of $Fe^{2+}/(Fe^{2+}+Mg)$ indicates an increase in metamorphic temperature (e.g. Spear, 1993, p. 370), such that the observed garnet zoning indicates a temperature increase during garnet growth. The same argument holds for the decrease of the X_{Mn} from core to rim in many garnet crystals.

Omphacite

The compositions of pyroxenes in the metabasic rocks from Gran Paradiso are shown in the ternary diagram of figure 4.11. The nomenclature for sodic-calcic pyroxenes from Morimoto et al. (1988) is followed here. Jadeite contents were calculated as the sodium content minus the amount of acmite (ferric iron). Almost all pyroxene analyses plot well within the omphacite field.

Amphiboles

In figures 4.12a and b, measured amphibole compositions have been plotted in the diagram for calcic and sodic-calcic amphiboles (Leake, 1978). The range of amphibole compositions obtained from microprobe analysis supports the optical observation that amphiboles, particularly in the metabasic samples, show a systematic change in composition towards the rims. It was determined optically that the hornblende component increases from core to rim, indicating increasing metamorphic temperature, and/or decreasing pressure (Ernst, 1979).

Feldspars

Feldspars in the Gneiss Minuti have a general composition of $Ab_{50-100}An_{0-50}Or_{0-23}$, although some pure K-feldspar was analysed as well (fig 4.13a). In the metabasites, compositions are very similar (fig 4.13b), whilst in the augengneisses feldspars form two groups with generalised compositions $Ab_{68-100}An_{0-32}Or_{0-10}$ and $Ab_{2-38}An_{0-5}Or_{62-98}$ (fig 4.13c). Some of these feldspars may still show their original igneous composition. Transects of microprobe analyses across feldspars from the Gneiss Minuti (fig 4.14a) and the metabasites (fig 4.14b) confirm the optical observation that feldspar composi-

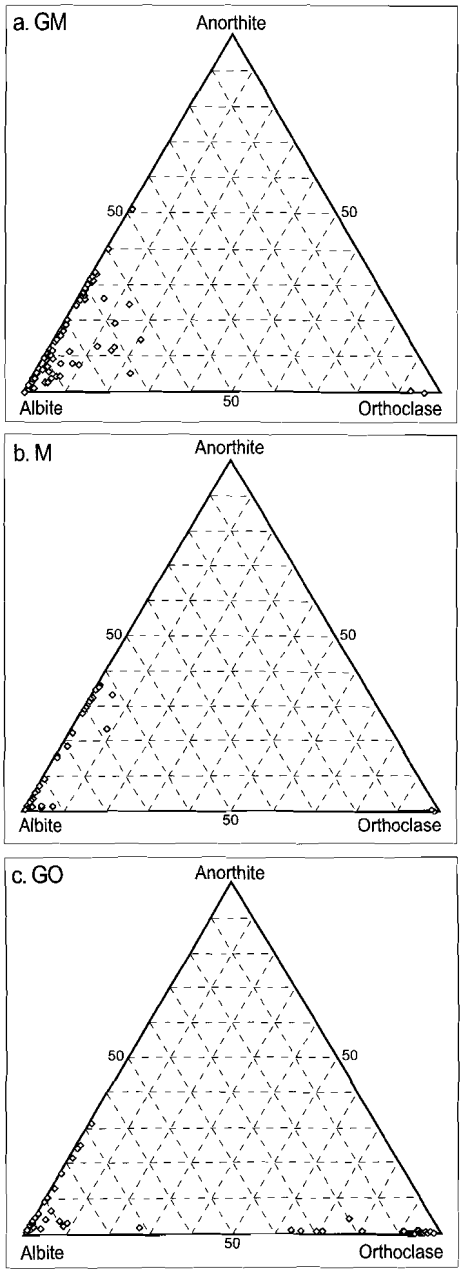

Figure 4.13: Ternary plot of feldspar compositions. **a.** Gneiss Minuti (GM). **b.** Metabasites (M). **c.** Augengneisses (GO).

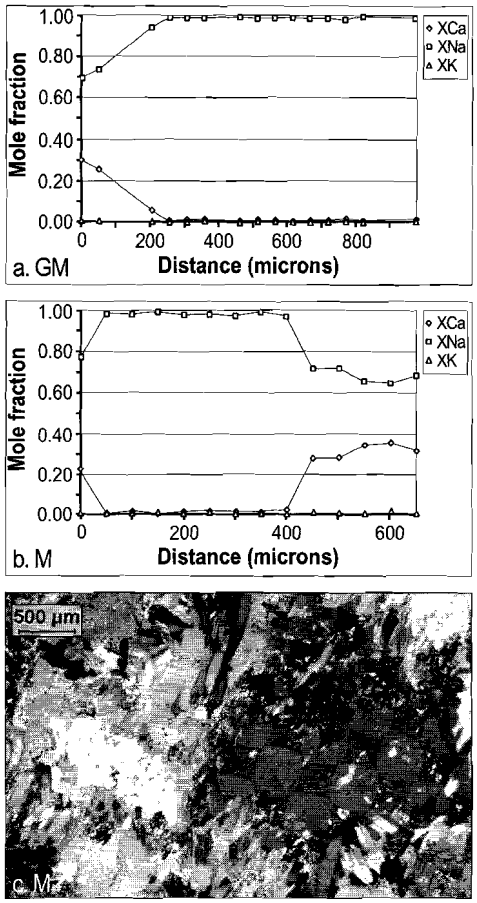

Figure 4.14: Compositional zoning in feldspar. **a.** Compositional variation across zoned feldspar from the Gneiss Minuti (GM). **b.** Compositional variation across zoned feldspar in metabasite (M). **c.** Photomicrograph of zoned feldspar from metabasite (M).

tions change towards the rims of the crystals. The Na (albite) content decreases strongly, while the Ca (anorthite) content increases. Again, the changes observed in feldspar composition reflect an increase of temperature and/or a decrease of pressure during growth of the feldspars in question (Maruyama et al., 1983).

Phengite

White micas occur in two varieties. Most have compositions within the phengite series (Rieder et al., 1999), but some paragonites (containing Na instead of K) occur as well. The compositions of phengites from all three lithologies are plotted in figure 4.15. The micas show a wide variation in number of Si cations per formula unit (p.f.u.), which has been related to the metamorphic pressure during mica growth (e.g. Massonne and Schreyer, 1987). From the study of thin sections it is clear that biotite formation after chlorite in the Gneiss Minuti often took place in the presence of white mica. Strikingly, analyses of white micas from Gneiss Minuti samples show a strongly bimodal distribution with peaks around 3.10 and 3.50 Si p.f.u. respectively (fig 4.16), indicating that the Gneiss Minuti contain two distinctly different white mica populations that must have formed at different pressure conditions. This suggests that the reaction

$$Chl + Ms_1 = Bt + Ms_2 + Qtz + H_2O$$

may be responsible for chlorite breakdown to biotite. In this reaction Ms_2 will have a lower Si p.f.u. (Wang et al., 1986). This argument does not hold for the augengneisses because they are relatively rich in K-feldspar, allowing for biotite growth after Chl + Or.

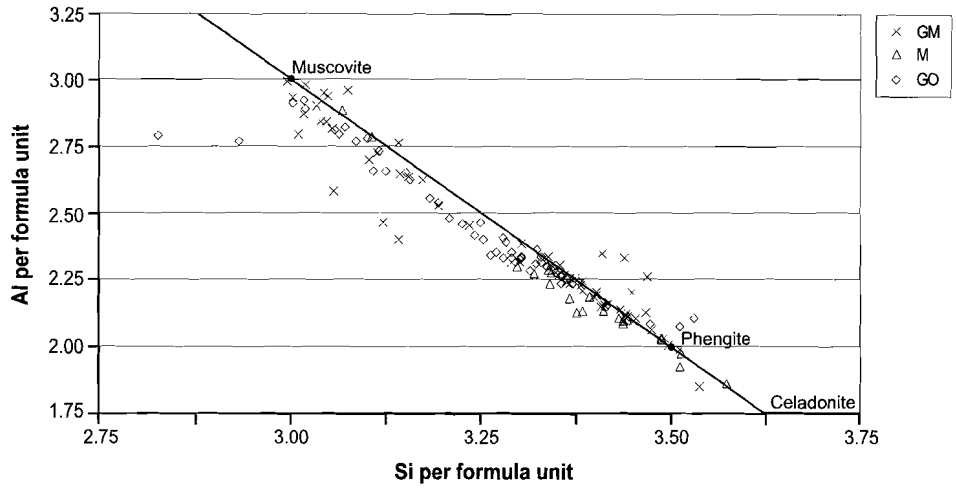

Figure 4.15: Compositional variation of white micas.

4.4.3 Thermobarometry

The rocks from Gran Paradiso contain more than one generation of metamorphic minerals, implying that they preserve at least a partial record of evolving pressure-temperature conditions. In order to apply thermobarometers to assemblages of metamorphic minerals, a given assemblage must have preserved equilibrium mineral compositions during changing pressure-temperature conditions. The preservation of metastable minerals and mineral zonation call for caution when applying thermobarometers to co-existing minerals in order to estimate metamorphic conditions. However, careful examination of textures and microstructures permits selection of mineral pairs most suitable for geothermobarometry, because they are in apparent equilibrium. The exact formulations of thermobarometric calibrations used in this study are described in Appendix 1. The microprobe analyses used for thermobarometry and representative analyses for other minerals are tabulated in Appendix 3.

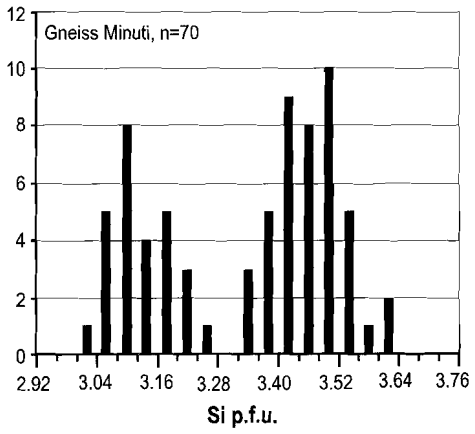

Figure 4.16: Histogram of white mica analyses showing bimodal distribution of Si contents.

Garnet-omphacite pairs

The temperature dependence of iron-magnesium partitioning between garnet and clinopyroxene has long been established (e.g. Råheim and Green, 1974). The early

calibration has been revised several times, and in this study I use two more recent calibrations (Krogh, 1988; Powell, 1985). The distribution coefficient (K_D, for definitions see Appendix 1) has been calculated for pairs of garnet and omphacite. Because the first calibration yields low temperatures for low-Ca garnets, I follow the approach of Carswell et al. (1997) and use Powell's calibration for garnets with $X_{Ca}<0.35$ and Krogh's for all other pairs.
The reaction

$$Ab = Jd + Qtz$$

is pressure dependent with respect to the jadeite content of omphacite (Holland, 1983). This barometer was reformulated by Carswell and Harley (1990) and is applied to several metabasic samples in this study. Because omphacite occurs in equilibrium with quartz, but without plagioclase, the obtained pressures only represent minimum estimates. In table 4.1 results are listed of simultaneous solution of the garnet-clinopyroxene thermometer and the jadeite barometer with the highest PT conditions for core-and-rim pairs of each sample. The results are a mathematical solution of the barometer for the Omp analysis with the highest jadeite content of the sample, and the thermometer for analyses of neighbouring pairs of Grt and Omp that in apparent microstructural equilibrium.

Lith	Sample	Grt	Omp	Omp max Jd	core / rim	X_{Ca}	X_{Jd}	K_D	Po85 / Kr88	T (°C)	P (kbar)
M	A35-2	8.7	8.6	8.5	rim	0.427	0.427	36.976	Po 85	477	11.4
M	GP96-17	1.23	1.20	1.3	core	0.430	0.430	32.176	Kr 88	482	11.5
M	GP96-17	1.28	1.26	1.3	rim	0.430	0.430	21.397	Po 85	515	12.1
M	GP96-28	1.57	1.53	1.59	core	0.397	0.397	34.844	Po 85	485	11.5
M	GP96-28	1.63	1.62	1.59	rim	0.397	0.397	25.916	Po 85	540	12.5
M	GP97-17-1	2.8	2.11	2.34	core	0.390	0.390	38.298	Kr 88	460	11.1
M	GP97-17-1	2.9	2.10	2.34	rim	0.390	0.390	29.827	Kr 88	503	11.8
M	GP97-22A	3.6	3.5	3.5	core	0.390	0.390	44.523	Kr 88	457	11.0
M	GP97-22A	3.17	3.7	3.5	rim	0.390	0.390	52.893	Kr 88	427	10.5
M	GP97-46B1	1.34	1.37	1.65	rim	0.370	0.370	25.449	Po 85	536	12.3
M	GP97-46B1	1.49	1.50	1.65	core	0.370	0.370	41.981	Po 85	464	11.1

Table 4.1: Garnet-omphacite equilibrium pressures and temperatures. Combined solution of Holland (1983) and Powell (1985) or Krogh (1988). Exact formulations are in Appendix 1, complete microprobe analyses are in Appendix 3.

Core pairs equilibrated around 455-485 °C and at least 11.0-11.5 kbar, whereas rim pairs yield 475-540 °C and at least 11.5-12.5 kbar. These results indicate that these minerals grew during prograde metamorphism, because the temperatures yielded by rim pairs are significantly higher than those obtained from pairs of core analyses.

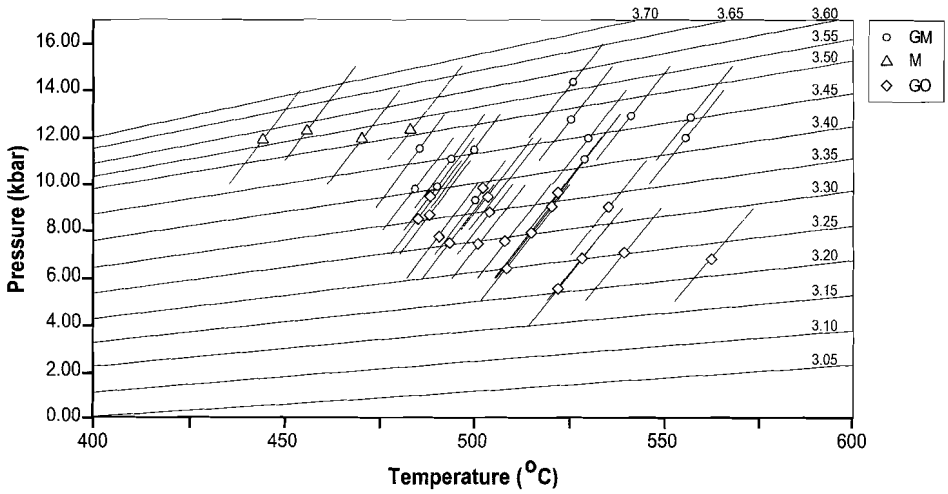

Figure 4.17: Results of garnet-phengite thermobarometry by graphical intersection of the Green and Hellman (1982) and Massonne (1991) formulations.

Garnet-phengite pairs

Iron-magnesium partitioning between garnet and phengitic white mica is another temperature dependent exchange reaction (Green and Hellman, 1982). The celadonite content of phengite can be expressed in terms of its Si content per formula unit and is dependent on pressure (Massonne, 1991; Massonne and Schreyer, 1987). The more recent calibration is an improved version, but has unfortunately not been published. The graphical representation of the 1991 callibration is included in Appendix 1. Pressures obtained with the improved calibration are roughly 0.6 kbar below those obtained with the original calibration (Rötzler et al., 1999). The barometer is based on the reaction

$$\text{Phen} = \text{Kf} + \text{Phl} + \text{Qtz} + \text{H}_2\text{O}$$

and because the studied samples do not contain K-feldspar, the obtained pressures are minimum estimates (Massonne and Schreyer, 1987). The 1987 calibration of the phengite barometer has met some important criticism. The experimental runs on which the calibration was based always contained metastable phases, and the calibration needs to be confirmed with reversed runs without metastable phases as well as by iron bearing experimental runs (Essene, 1989). Despite these fair points of criticism, results of phengite barometry seem to agree well with other thermobarometric results (e.g. Rötzler et al., 1999). For this reason the updated phengite barometer is used here.

In this study, intersections between the improved phengite barometer and K_D lines of the thermometer are graphically combined into a set of PT conditions (fig 4.17) and listed in table 4.2. The metabasite pairs were obtained from phengite inclusions and

their surrounding garnet. Early conditions are thus estimated around 440-485 °C and minimum pressures 12.0-12.5 kbar. Results obtained from garnet-phengite pairs from the Gneiss Minuti coincide with the highest values obtained from Grt-Omp thermobarometry on the metabasites, with calculated peak metamorphic PT conditions of at least 12.0-14.2 kbar and 525-555 °C. Thermobarometric results from Grt-Phen pairs in the augengneisses indicate that equilibration of Fe and Mg in Grt and Phen in these rocks occurred below the peak pressure (fig 4.17 and table 4.2). The results show that after a temperature decrease the rocks were reheated during decompression. The temperature rose to about 525-560 °C, at pressures of at least 7.0-10.0 kbar.

Garnet-biotite pairs

The garnet-biotite Fe^{2+}-Mg exchange thermometer has been calibrated repetitively (e.g. Ferry and Spear, 1978; Hodges and Spear, 1982; Kleemann and Reinhardt, 1994;

									GH82				Massonne (1991)	
Lith	Sample	Grt	Phen	core / rim	Si p.f.u.	K_D	A	B	P1	T (P1)	P2	T (P2)	P (kbar)	T (°C)
M	GP96-28	3.195	3.198	core, incl	3.575	37.889	5170	4.17	10.0	436	14.0	454	12.0	444
M	GP96-28	3.195	3.199	core, incl	3.516	28.838	5170	4.17	10.0	461	14.0	480	11.9	471
M	GP96-28	3.230	3.231	core, incl	3.514	25.781	5170	4.17	11.0	477	15.0	497	12.4	484
M	GP96-28	3.237	3.233	core, incl	3.575	34.023	5170	4.17	11.0	450	15.0	469	12.3	457
GM	GP96-29X	4.73	4.72		3.409	23.566	5560	4.65	8.0	476	12.0	494	9.7	484
GM	GP96-29X	4.78	4.79		3.541	19.261	5560	4.65	12.0	515	16.0	534	14.2	525
GM	GP96-43	4.163	4.162		3.476	17.979	5560	4.65	11.0	517	15.0	536	12.6	524
GM	GP96-43	4.165	4.164		3.421	13.189	5560	4.65	10.0	546	14.0	566	11.8	554
GM	GP96-44-P	4.46	4.49		3.405	22.244	5560	4.65	8.0	481	12.0	500	9.8	490
GM	GP96-44-P	4.54	4.58		3.445	22.671	5560	4.65	9.0	484	13.0	503	10.9	493
GM	GP96-44-P	4.63	4.61		3.445	16.615	5560	4.65	10.0	521	14.0	540	11.9	529
GM	GP96-90L	2.53	2.56	core	3.450	13.535	5560	4.65	11.0	548	15.0	568	12.7	556
GM	GP96-90L	2.60	2.59	core	3.472	25.211	5560	4.65	9.0	474	13.0	492	11.4	484
GM	GP96-90L	2.61	2.62	core	3.456	21.743	5560	4.65	9.0	488	13.0	507	11.4	500
GM	GP96-90L	2.68	2.70	core	3.415	16.120	5560	4.65	9.0	519	13.0	538	11.0	528
GO	GP96-97AP	5.30	5.28	rim	3.367	20.106	5560	4.65	6.0	482	10.0	501	7.9	490
GO	GP96-97A-P	serie6 (Grt)	serie6 (Grt)	core, incl	3.294	16.701	5560	4.65	6.0	501	10.0	520	7.6	508
GO	GP96-97A-P	serie6 (Grt)	serie6 (Grt)	rim	3.389	22.233	5560	4.65	8.0	481	12.0	500	9.5	488
GO	GP96-97A-P	serie7 (Grt)	serie7 (Grt)	rim, incl	3.307	19.239	5560	4.65	6.0	486	10.0	505	7.6	493
GO	GP96-97A-P	4.26	4.25		3.373	19.111	5560	4.65	8.0	496	12.0	515	9.5	503
GO	GP96-97A-P	4.28	4.27		3.358	21.493	5560	4.65	7.0	480	11.0	499	8.7	488
GO	GP96-97A-P	4.30	4.29		3.255	13.405	5560	4.65	5.0	519	9.0	539	6.9	528
GO	GP96-97A-P	4.36	4.35		3.293	17.804	5560	4.65	6.0	494	10.0	513	7.5	501
GO	GP96-97A-P	4.38	4.37		3.365	16.126	5560	4.65	8.0	514	12.0	533	9.6	523
GO	GP96-97A-P	4.40	4.39		3.211	13.365	5560	4.65	4.0	515	8.0	534	5.5	523
GO	GP96-97A-P	4.42	4.41		3.350	18.719	5560	4.65	8.0	499	12.0	518	9.8	502
GM	GP97-5-L	3.181	3.175		3.469	15.599	5560	4.65	11.0	532	15.0	552	12.8	541
GM	GP97-5-L	4.18	4.19		3.369	19.544	5560	4.65	7.0	490	11.0	508	9.3	500
GO	GP97-32-P	3.109	3.110	rim	3.251	12.265	5560	4.65	5.0	529	9.0	549	7.0	540
GO	GP97-32-P	3.151	3.150	core	3.349	18.370	5560	4.65	7.0	496	10.0	510	8.8	504
GO	GP97-32-P	3.152	3.153	rim	3.331	15.995	5560	4.65	6.0	505	10.0	525	7.9	517
GO	GP97-32-P	3.159	3.158	rim	3.227	9.996	5560	4.65	5.0	553	9.0	573	6.8	562
GO	GP97-32-P	3.161	3.160	rim	3.325	15.833	5560	4.65	5.0	501	9.0	521	6.4	508
GO	GP97-32-P	3.168	3.167	rim	3.331	13.861	5560	4.65	7.0	525	11.0	545	9.1	535
GO	GP97-33	2.195	2.192	rim	3.340	15.945	5560	4.65	6.0	506	10.0	525	9.1	521

Table 4.2: Garnet-phengite equilibrium temperatures calculated with Green and Hellman (1982) for given pressures. Combined graphical solution of Green and Hellman (1982) with Massonne (1991). Exact formulations are in Appendix 1, complete microprobe analyses are in Appendix 3.

Lith	Sample	Grt	Bt	X_{Al}	X_{Ti}	FS/HS/KR	K_D	T (°C, 2 kbar)	T (°C, 8 kbar)
GM	GP97-45b	2.18	2.19	0.102	0.051	FS78	0.161	536	558
GM	GP97-45b	2.18	2.19	0.102	0.051	KR94	0.161	485	514
M	GP97-25-2	315	317	0.339	0.013	HS82	*9.675	509	526
M	GP97-25-2	315	317	0.339	0.013	KR94	0.103	471	489
GO	GP96-97A-P	5.12	5.1	0.140	0.028	FS78	0.164	542	564
GO	GP96-97A-P	5.12	5.1	0.140	0.028	KR94	0.164	499	525

*For calculation with Hodges and Spear (1982) K_D is defined differently (see Appendix 1)

Table 4.3: Garnet-biotite equilibrium temperatures calculated with Ferry and Spear (1978) or Hodges and Spear (1982) and with Kleemann and Reinhardt (1994) for comparison. Exact formulations are in Appendix 1, complete microprobe analyses are in Appendix 3.

Kretz, 1990; Perchuk and Lavrent'eva, 1983). In this study I apply the calibration of Ferry and Spear (FS78), which assumes ideal mixing properties of garnet solid solutions. In cases where $X_{Ca}+X_{Mn}$ in garnet is larger than 0.3, FS78 is replaced by Hodges and Spear (HS82) where non-ideality is taken into account. The HS82 themometer was calibrated with a more suitable set of mineral compositions for the Ca and Mn-rich garnet varieties than the FS78 thermometer. Results from these thermometers are compared with those of the Kleemann and Reinhardt (KR94) calibration, which yields lower temperatures for the same mineral pairs than the other calibrations. The results of garnet-biotite thermometry (table 4.3) indicate that in the metabasites garnet and biotite equilibrated around 465 °C (KR94) or 515 °C (HS82) assuming a confining pressure of 4 kbar. For both the Gneiss Minuti and the augengneisses KR94 temperatures are around 495 °C, whereas FS78 yielded 545 °C, which is significantly higher. The difference between the metabasites and the other lithologies may indicate that garnet and biotite in the metabasic rocks were not in equilibrium, because biotite grew at the expense of garnet. On the other hand, garnet and biotite in the metabasites may have equilibrated at lower temperatures.

Amphibole-plagioclase pairs

The exchange of Na and Ca between coexisting amphibole and plagioclase is a temperature-dependent reaction (Holland and Blundy, 1994). Of two calibrated thermometers, one concerns a Si-saturated system, while the other can be applied to assemblages without free quartz. Holland and Blundy emphasise that the reactions must not be combined in order to obtain an estimate of equilibrium pressure, because the pressure residuals were not minimised. They note, however, that the simultaneous use of both thermometers does allow assessment of the validity of the resulting K_D lines.

Judged by the criteria set by

Lith	Sample	Amph	Plag	curve	T_B (°C, 1 kbar)	T_B (°C, 5 kbar)
M	GP96-107c	2.119	2.12	1	456	514
M	GP97-25-2	2.82	2.86	2	469	507
M	GP97-46B1	75	77	3	435	477
M	GP97-46B1	83	82	4	479	504

Table 4.4: Amphibole-plagioclase equilibrium temperatures calculated with Holland and Blundy (1994). Exact formulations are in Appendix 1, complete microprobe analyses are in Appendix 3.

Holland and Blundy (1994), oligoclase rims combined with hornblenditic amphibole rims from three metabasites yield valid results (table 4.4). For an assumed metamorphic pressure of 4 kbar, the temperatures obtained range between 465 and 495 °C. The value of 4 kbar was chosen because it is in line with the Si content of the younger group of phengitic micas related to the late stage of low-pressure, medium-temperature metamorphism, as argued above.

4.4.4 Compilation of the PTt trajectory

The PT path

Figure 4.18 shows a compilation of all thermobarometric results described above. In addition, reactions are included that constrain the evolving PT conditions, on the basis of petrographical observations. The isopleths shown for the Si content of phengite coincide with the distribution of phengite analyses (fig 4.16). As no staurolite occurs in the chloritoid bearing rocks of the Gran Paradiso massif, a maximum metamorphic temperature of 500 °C at 1 kbar and 600 °C at 12 kbar is defined by the chloritoid breakdown reaction to staurolite, garnet and chlorite. A maximum pressure of 15 to 16 kbar is indicated by the breakdown of chlorite, or chlorite + biotite to form chloritoid and talc. The peak metamorphic assemblage of the Silvery Micaschists in the Northern half of Gran Paradiso contains talc, chloritoid and phengite in zones of localised deformation (see paragraph 4.4.1 and Chopin (1981)). This may indicate that peak pressures have been slightly higher, while in other lithologies of the Gneiss Minuti metastable chlorite and biotite were preserved.

Garnet-biotite thermometry yields results that are about 50 °C lower with the KR94 calibration than with FS78 and HS82. Comparison with garnet-phengite thermobarometry results suggests that the KR94 temperatures are too low, whilst results obtained from the Lepontine gneisses near Alpe Arami (Chapter 3) also seem to indicate that the FS78 calibration is more accurate. Amphibole-plagioclase thermometry coincides better with the KR94 results, but may represent a later stage in the history than garnet-biotite equilibrium. Comparison of the results of the two thermometers for metabasite sample GP97-25-2 (tables 4.3 and 4.4) suggests that KR94 is the appropriate calibration, because it yields a lower equilibration temperature than the amphibole-plagioclase thermometer. As shown in figure 4.8, biotite growth in the metabasic rocks post-dates the growth of blue-green amphibole. However, it is not certain that biotite and garnet were in equilibrium in the metabasites, because biotite often seems to have grown at the expense of garnet. My results are thus inconclusive as to which calibration is more appropriate.

Discussion of the thermal history

The retrograde metamorphic evolution of the Gran Paradiso massif, illustrated in figure 4.18, shows cooling by about 35 °C during initial decompression, followed by a conspicuous reheating by about 50 °C at low pressures prior to cooling and decompression related to the final stages of exhumation.

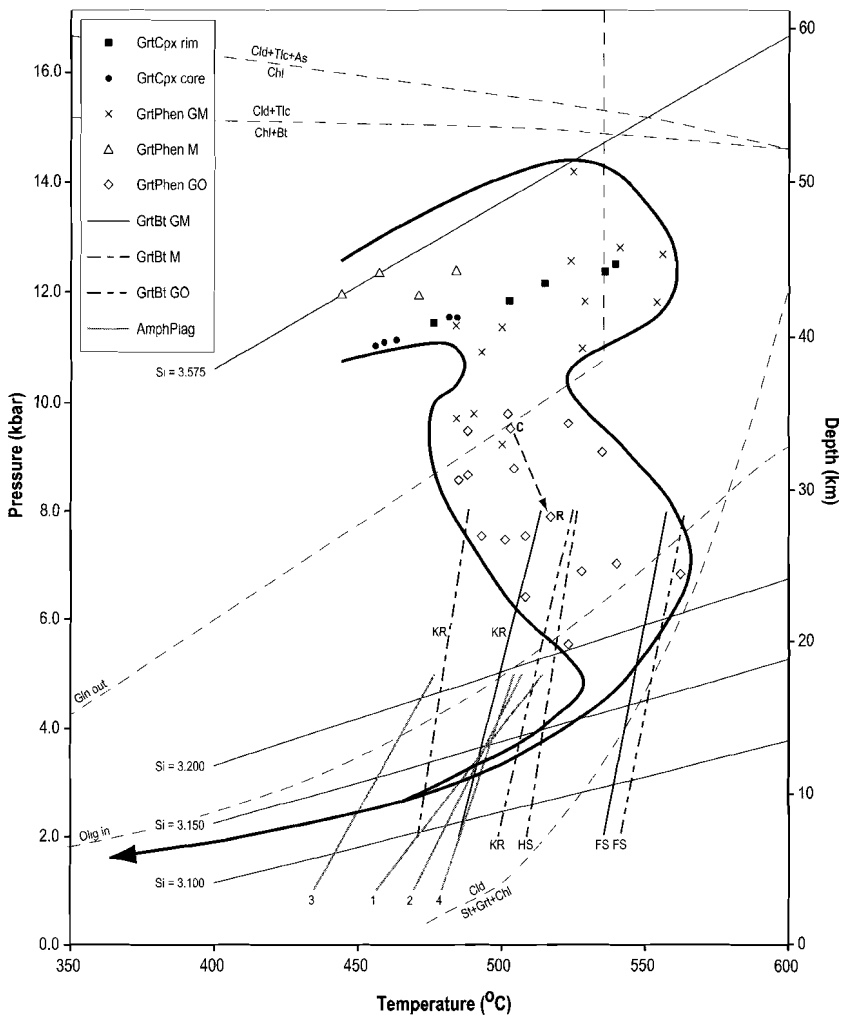

Figure 4.18: Compilation and interpretation of thermobarometric results. Abbreviations: GM = Gneiss Minuti, M = metabasites, GO = augengneisses (Gneiss Occhiadini), C = core, R = rim.
Thermobarometric results were obtained using different calibrations. GrtCpx = garnet-clinopyroxene thermometry (Krogh, 1988; or Powell, 1985) combined with jadeite barometry (Holland, 1983), see table 4.1. GrtPhen = graphical solutions of garnet-phengite thermometry (Green and Hellman, 1982) and phengite barometry (Massonne , 1991), see table 4.2. GrtBt = garnet-biotite thermometry using either the calibration of Kleemann and Reinhardt (KR, 1994) or those of Ferry and Spear (FS, 1978) or Hodges and Spear (HS, 1982), respectively. See also table 4.3. AmphPlag = amphibole-plagioclase thermometry using calibration of Holland and Blundy (1994), see table 4.4.
Isopleths for silica content of phengite, taken from Massonne (1991). They coincide with the groups of phengite analysis shown in figure 4.15. Thin dashed lines are reactions that constrain metamorphic conditions. Gln-out taken from Maresch (1977), Oligoclase-in taken from Maruyama et al. (1983), other reactions taken from the KFMASH petrogenic grid of Spear (1993, p. 375).

Previous petrological studies in the Gran Paradiso massif have argued that peak temperature conditions were reached at low pressures after initial cooling (Borghi et al., 1996; Borghi and Sandrone, 1995). These workers suggested that the Gran Paradiso massif cooled as much as 125 °C during decompression before being re-heated to about 525 °C, implying a late-stage temperature increase of 125 °C. Part of the evidence presented, however, was based on poorly defined reactions (Borghi et al. 1996, reaction 11 of their figure 8) and on combination of minerals from different rock types into one alleged assemblage (Borghi et al. 1996, reaction 5 of figure 8). Consequently, it has been argued that the petrological evolution of the rocks in question could be explained by decompression rather than re-heating (Ballèvre, pers. comm.). However, the principal result reported by Borghi et al., i.e. a late stage of re-heating affecting the Gran Paradiso massif, is supported by the results of this study.

Reheating by about 50 °C at low pressures, before final cooling and decompression, is indicated by the increase of equilibrium temperatures with decreasing pressure shown by garnet-phengite pairs from the augengneisses. Admittedly, both the initial cooling and the late-stage heating are near or within the accepted analytical errors of thermobarometry (± 25-50 °C and ± 0.5-2 kbar, Spear et al. (1989)), but in the present case of garnet-phengite thermometry the inferred temperature changes are at least in part based on core-to-rim variations within one mineral pair such that the errors in the relative temperature changes are much smaller. In relative thermobarometry the errors on ΔT and ΔP are about 5-10 %, which is of course much smaller that a 5-10 % error on the absolute values (Spear, 1989). Furthermore, the late-stage heating inferred here is entirely consistent with petrographical evidence for increasing temperature such as the growth of biotite around chlorite in all lithologies and the change of the amphibole and plagioclase compositions towards the rims. In addition, it is emphasised here that even for the case of the highest temperature estimates at high pressure (600 °C, 13.0 kbar) and the lower temperature estimates at low pressure (500 °C, 6.5 kbar and 450 °C, 3 kbar) the resulting PT path becomes anomalously hot at low pressures. The geodynamic significance of this hot, late stage of the metamorphic history is discussed below.

Relative timing of structures and metamorphism

The Dm-1 chloritoid bearing fabric observed in both the Gneiss Minuti and the in augengneisses is related to the Alpine metamorphic history, because it developed in the augengneisses derived from late-Hercynian granites. Chloritoid is enclosed in garnets that are related to peak metamorphism in the Gneiss Minuti, so it must either predate or be coeval with the high-pressure peak of Alpine metamorphism (fig 4.19).

The age of the main phase chlorite fabric and the Dm+1 top-to-the-west chlorite shear bands with respect to the metamorphic stages is not well constrained. Biotite shear bands indicating a top-to-the-east sense of shear define Dm+2. The biotite often surrounds chlorite and has grown at the expense of the chlorite grains, so biotite must be related to the re-heating stage discussed above. This implies that Dm and Dm+1 affected the rocks between their peak pressure metamorphism and the late-stage heating.

Structures and metamorphism related to radiometric dating

The age of the high-pressure metamorphism in the Gran Paradiso massif has been determined to be 36 Ma by Rb-Sr microsampling of white micas from the Silvery Micaschists (Butler et al., 1997). This result was revised by the same authors to an age of the high-pressure metamorphic stage of 43.0 ± 0.5 Ma using the same method (Meffan-Main et al. in prep; Meffan-Main, pers.comm., 1999). The latter age is thought to be related to metamorphism at minimum pressures of 12-14 kbar and temperatures of 500-550 °C (fig 4.19), whilst the 36.3 ± 0.4 Ma age has been interpreted to reflect closure before or during greenschist facies retrogression.

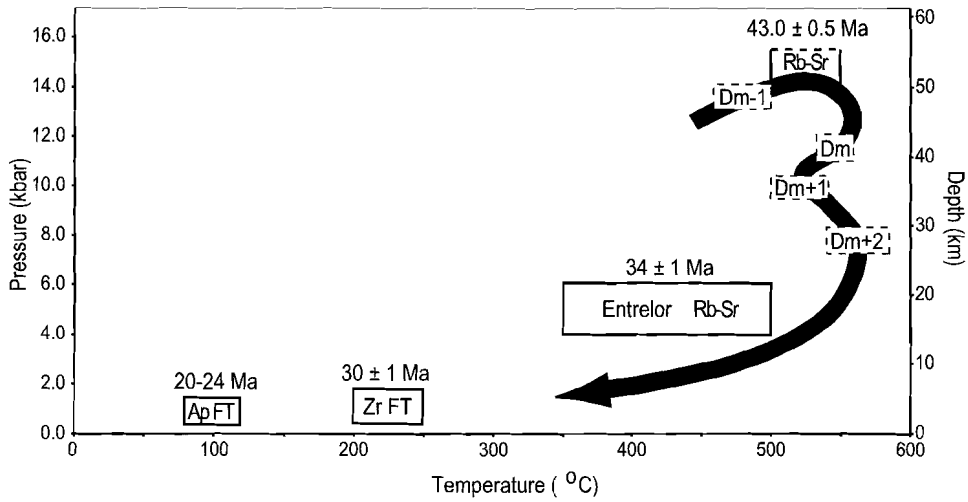

Figure 4.19: Relative and absolute timing of structural and metamorphic events. Rb-Sr high-pressure age from Meffan-Main (pers. comm., 1999), Rb-Sr date on the Entrelor shear zone from Freeman et al. (1997), and fission track ages from Hurford and Hunziker (1989).

The same group of researchers obtained a 34 ± 1 Ma white mica deformation age from the Entrelor shear zone, situated about 1 km above the Gran Paradiso massif in the Piemonte ophiolite zone (Freeman et al., 1997). This age was related to top-to-the-east movement on the shear zone, at 350-500 °C and 4-6 kbar (fig 4.19). The Dm+2 top-to-the-east biotite bearing shear bands in the Gran Paradiso massif are possibly related to this stage of deformation, suggesting that the Entrelor shear zone played a role in the unroofing and exhumation history of the massif. A 38-37 Ma age was also obtained from this shear zone, but this age could not be related to shear zone kinematics. Deformation at the upper margin of the Gran Paradiso massif, again with undetermined kinematics, was dated at 33.2 ± 0.4 Ma.

Zircon fission track cooling ages of Gran Paradiso yield 30 ± 1 Ma for zircons cooling below 225 ± 25 °C while apatite fission track ages are around 20-24 Ma, indicating cooling below 100 ± 20 °C (fig 4.19; both results from Hurford and Hunziker (1989)).

4.5 Geodynamic implications

The exhumation history of the Gran Paradiso massif clearly shows two stages. Stage 1 concerns the initial unroofing of the massif after high-pressure metamorphism (540-550 °C and 12-14 kbar). For average values of crustal densities, the associated peak pressures are equivalent with a depth of 45-50 kilometres. The associated deformation has a dominant top-to-the-west sense of shear reflected by chlorite-decorated shear bands. During stage 1 Gran Paradiso cooled by at least 35 °C. Stage 1 ended before the peak of re-heating at about 550 °C and 6.5 kbar (equivalent to depths of about 25 km). Stage 2 is associated with top-to-the-east movement on biotite bearing shear bands and larger-scale shear zones. This deformation may be related to top-to-the-east normal movement on the Entrelor shear zone. During stage 2 the Gran Paradiso massif underwent low-pressure, medium-temperature metamorphism, followed by cooling and decompression to about 400 °C at 2 kbar (about 6 kilometres depth), and subsequent exhumation to the Earth's surface. The exhumation rate during stage 2 was about 0.6 mm/yr.

Despite a careful search, there is no petrological evidence to show that the Gran Paradiso massif was ever subjected to the ultrahigh-pressure metamorphism ($P < 28$ kbar) documented from the structurally analogous Dora Maira massif. This alleviates the need to invoke an exhumation mechanism for the Gran Paradiso rocks involving buoyant rise of subducted crustal material from mantle depths. A well-established exhumation mechanism for rocks from deep levels in an orogenic wedge in a compressional setting is corner flow in the wedge (Bousquet, 1998; Bousquet et al., 1997; Platt, 1986). Deformation within the wedge is thought to be driven by continuous underplating at the base of the wedge, causing compression and upward flow near an assumed rigid buttress (the overriding plate) and extension in the upper parts of the wedge. It is noted that corner flow cannot be responsible for the initial exhumation of very high-pressure metamorphic rocks such as those from the Dora Maira massif, because the thickness of orogenic wedges is limited to about 60 kilometres (Platt, 1987).

The two stages in the retrograde history of the Gran Paradiso massif may reflect the upward movement of the unit near the overriding plate, followed by extension when the rocks approached the Earth's surface. In this case, the Entrelor shear zone could be one of presumably several large-scale detachments facilitating unroofing of deeper units. Extensional top-to-the-southeast movement on the Gressoney shear zone to the North also supports this scenario (Reddy et al., 1999). If the Gran Paradiso massif was indeed exhumed by corner flow in an orogenic wedge, this means that upward movement in the wedge was rapid. The exhumation rate during stage 1 is about 3.3 mm per year, which is much faster than avarage orogenic erosion rates of 0.5 mm per year (e.g. Hinderer and Kamelger, 1999).

The problem with the proposed scenario, however, is that it does not explain the anomalously hot PT trajectory of the Gran Paradiso rocks. A possible explanation for the inferred late addition of heat to the base of the orogen is slab breakoff (Davies and Von Blanckenburg, 1995; Wortel and Spakman, 1992). Subduction of continental

material increases the tensional stresses within the slab, which eventually ruptures. In case of shallow break-off in particular, the consequent rise of hot asthenospheric material will cause considerable heating at the base of the crust. Thermomechanical numerical simulations of this process suggest, that the temperature at the base of the crust may increase by as much as 400 °C (Van de Zedde and Wortel, 2000), although in case of such large temperature increases melting would be expected to occur.

4.6 Conclusions

Detailed investigation of the structural and metamorphic history of the Gran Paradiso massif has improved constraints on its thermal evolution during exhumation. After high-pressure metamorphism, the rocks of the Gran Paradiso massif cooled during initial decompression, and were then re-heated at shallower depth. The structures observed seem consistent with a two-stage exhumation history by cornerflow in an orogenic wedge, while the observed re-heating is possibly related to the detachment of cold lithospheric mantle underneath the wedge and ascent of hot asthenospheric material toward the base of the crustal wedge.

Chapter 5

Metamorphic history of eclogitic metagabbro blocks from a tectonic mélange in the Voltri Massif, Ligurian Alps, Italy

5.1 Abstract

Iron/titanium-rich metagabbros, derived from the Beigua serpentinite unit, were collected from a tectonic mélange developed along the contact between the Beigua serpentinite unit and the underlying Voltri-Rossiglione calcschist unit of the Voltri Group in the Ligurian Alps, northern Italy. Petrographic study and microchemical analysis have been undertaken to unravel the details of their metamorphic history.
The metagabbros formed during Jurassic oceanisation in the Piemonte-Ligurian realm, and show local evidence of rodingitisation during ocean-floor metamorphism. Together with the country rock serpentinites, they became subject to high-pressure metamorphism during Alpine subduction and eventual collision. The stable high-pressure assemblage consists of garnet, omphacite, glaucophane, rutile and locally white mica. Peak metamorphic conditions, using garnet-omphacite-phengite thermobarometry, were 500 ± 50 °C and 17.5 ± 0.5 kbar, i.e. higher peak pressures than previously estimated for these rocks. The metagabbros studied have cooled continuously during decompression, and no evidence has been found for any heating during exhumation as known from the central and northwestern part of the Penninic Alps. Exhumation initially proceeded along a low-$\Delta T/\Delta P$ trajectory, followed by final exhumation along a higher gradient close to that of a continental geotherm. Lack of geochronological data precludes assessment of the exhumation rates involved. The Voltri massif had arrived at the Earth's surface by 34 millions year ago, because exhumed rocks of the massif are covered by early Oligocene continental scree breccias and conglomerates.
I propose corner flow in the orogenic wedge on top of the subducting Piemonte-Ligurian oceanic lithosphere as a plausible mechanism driving exhumation of the high-pressure rocks of the Voltri Massif.

5.2 Introduction

5.2.1 Geology of the Voltri massif

The Voltri Massif in the Ligurian Alps (fig 5.1) is the largest ophiolite massif in the Alps-Apennine system. The structure of the massif is dominated by sub-horizontal thrust sheets, affected by polyphase deformation and metamorphism (Chiesa et al., 1975; Piccardo et al., 1977). Three main units are commonly distinguished; i.e. from bottom to top: (1) the Voltri-Rossiglione calcschist unit consisting of blueschist to eclogite-

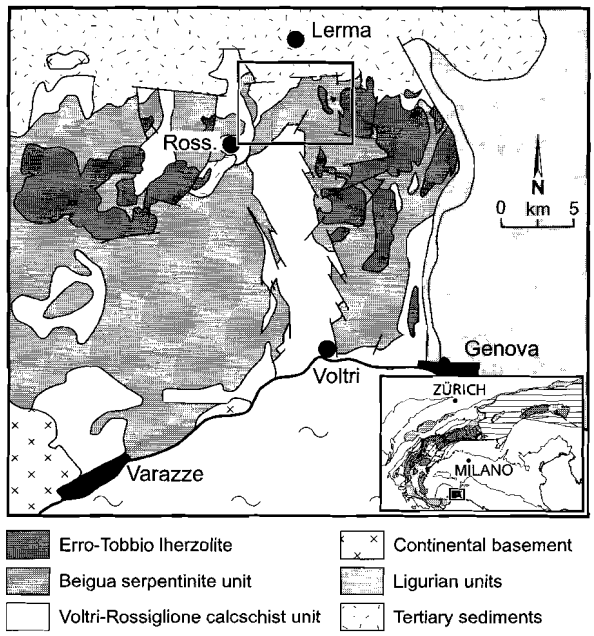

Figure 5.1: Location of the Voltri massif in the Alps, and sketch map of the Voltri massif showing its large-scale structure (area outlined shown in figure 5.2). Abbreviation: Ross.- Rossiglione.

facies calcareous metasediments, metavolcanics, and slices of serpentinite, (2) the Beigua serpentinite unit of heavily serpentinised ultramafics enclosing small amounts of eclogitic metagabbro and locally also metabasalt, and (3) the overlying lherzolite-dominated Erro-Tobbio peridotite. These units, also referred to as the Voltri Group (Chiesa et al., 1975), represent fragments of the subducted lithosphere of the Piemonte-Ligurian ocean, the Alps-Apennine part of the Mesozoic Tethys (Ernst and Piccardo, 1979; Lemoine et al., 1987). This oceanic basin formed during Middle and Late Jurassic extension (Borsi et al., 1996) and became subject to intra-oceanic subduction and subsequent collision after the Early Cretaceous (Hoogerduijn Strating, 1991), leading to imbrication and stacking in the Alpine suture zone and emplacement of oceanic units (ophiolites) onto the European continental crust. On the basis of outcrop- and microscale overprinting relationships, a sequence of deformational structures has been recognised in each thrust unit (Hoogerduijn Strating, 1991), which forms a basis for the relative timing of different metamorphic minerals and mineral assemblages in these units. All thrust units of the Voltri Group show an eclogite, a blueschist-eclogite, and a greenschist-facies stage of deformation.

5.2.2 Tectonic mélange in the northern Voltri massif

The rocks selected for this study are exposed in an area in the northern part of the Voltri massif, SSE of the village of Lerma (figs 5.1, 5.2). Outcrop conditions in the region are generally poor due to dense vegetation, but the bed of the Piota river (fig 5.2) provides excellent exposure in a domain where the contact of the Beigua serpentinite unit and the underlying Voltri-Rossiglione calcschist unit is subhorizontal. In the vicinity of the contact, the structure in the hanging-wall serpentinites is dominated by kink-type crenulations. Towards the base of the serpentinite nappe these crenulations become intense, and veins and patches of talc + chlorite + tremolite + carbonate replace the

original antigorite-dominated assemblage. A layer of intensely foliated serpentine- and actinolite-bearing talc-chlorite-tremolite-carbonate schist, at least several tens of metres thick, marks the thrust itself. This schistose material encloses rounded and lens-shaped (phacoid) blocks, up to 25 metres across (fig 5.3), of eclogitic Fe-Ti and Mg gabbro, commonly with coarse flaser-type microstructures and locally with fine-grained mylonitic fabrics, blocks of greenschist-facies and occasionally eclogitic metabasalt, blocks of massive and foliated serpentinite, and lenses and blocks of calcschist and calcareous marble. The main structural features of this chaotic lithology clearly indicate that it represents a tectonic mélange (Vissers et al., in prep.). The structures and metamorphic mineral assemblages in the wall rock units and those in the mélange indicate that the mélange developed at a relatively late stage of greenschist facies ductile thrusting. The blocks and lenses probably developed during localised deformation in a relatively narrow zone, up to several tens of metres thick, along the thrust through intense stretching of the various lithologies in the foot- and hanging wall. An overall top-to-the-northwest movement sense can be inferred on the basis of shear zone geometries and asymmetric extensional crenulation cleavages in the mélange matrix, in combination with the orientations of stretching fabrics and long axes of elongate lens-shaped blocks (Hoogerduijn Strating, 1991; Vissers et al., in prep.).

The most striking feature of the mélange is the occurrence of rounded blocks of eclogitic metagabbro (fig 5.3, 5.4a), up to some 20 meters in diameter. Where erosion has provided sections across such blocks, they consistently show eclogitic cores, mostly with flaser structures, and dm-scale retrogressed rims (fig 5.4b). The mineral assemblages seen in the cores of the blocks are identical to those in eclogitic metagabbros in the Beigua serpentinite unit (Hoogerduijn Strating, 1991), and allow identification of a stage of high-pressure metamorphism. On the basis of their bulk chemistry the Beigua metagabbros are thought to have originated at a mid-oceanic ridge (Mottana and Bocchio, 1975). They were rodingitised at or near the seafloor (Messiga et al., 1983;

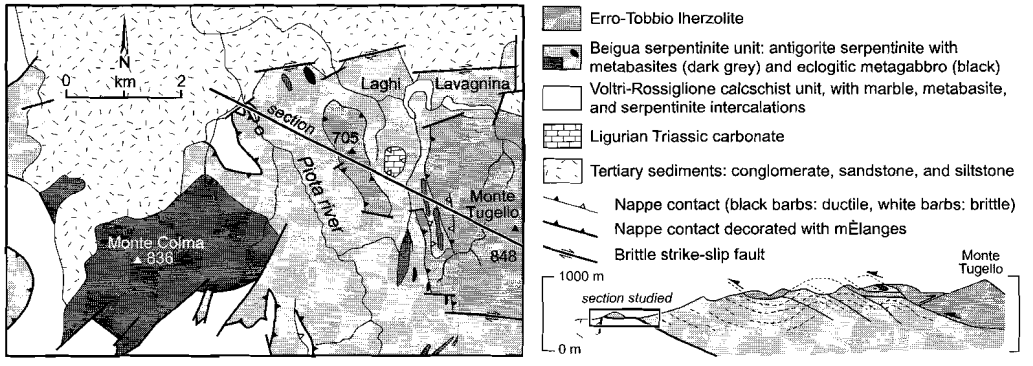

Figure 5.2: Sketch map and cross section of the central northern Voltri massif south of Lerma, showing location of mélange exposures in the Piota riverbed.

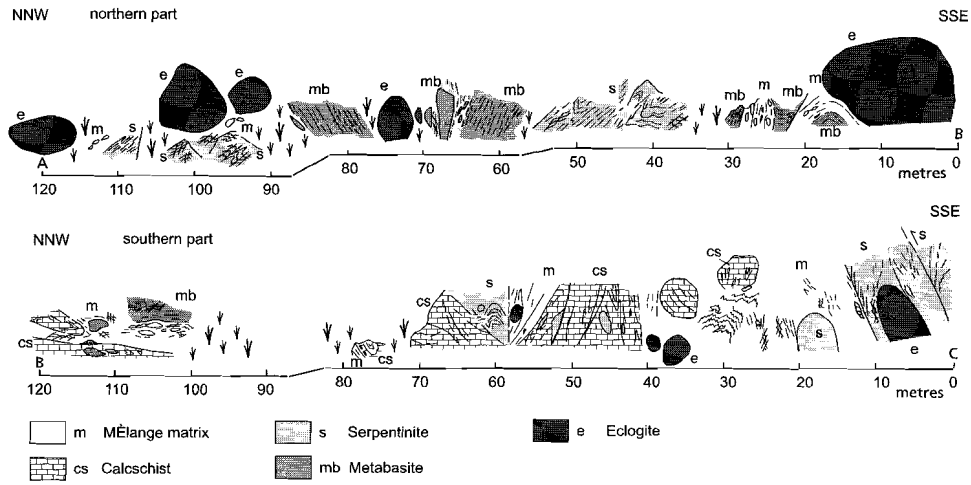

Figure 5.3: Detailed section across part of the mélange exposure in the Piota riverbed.

Morten et al., 1985) before metamorphism at eclogite facies conditions during Alpine convergence. The rims of the blocks are clearly retrogressive and contain actinolite, grown at the expense of blue-green amphibole, in the presence of albite, chlorite, epidote, sphene, magnetite and pyrite, whilst at the contact with the mélange matrix the assemblage may contain Mg-chlorite plus tremolite (Vissers et al., in prep.). Notably, these retrogressive rims are discordant to the flaser structure in the cores of the blocks, so retrogression and mélange formation are younger than the flaser layering. The internal parts of the retrogressive rims may show static assemblages with little evidence of deformation, while in the outer few centimetres the rims often show a distinct foliation passing into the main fabric of the mélange matrix.

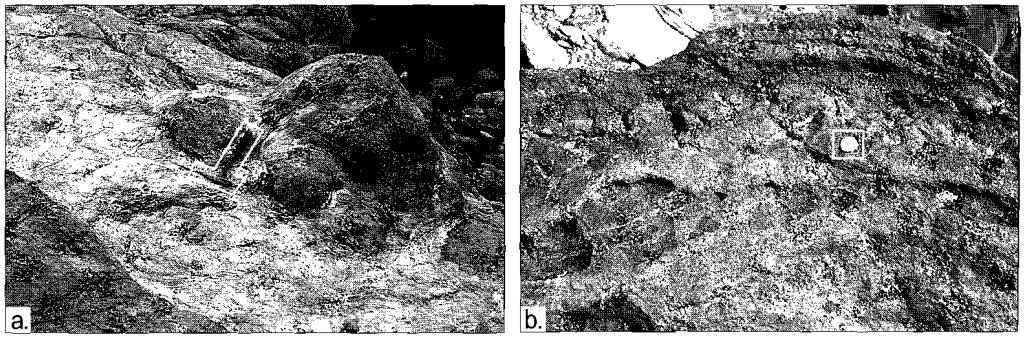

Figure 5.4: Field aspects of the tectonic mélange. **a.** Rounded metagabbro blocks in talc-chlorite-tremolite-carbonate schist; hammer for scale. **b.** Retrogressed rim developed in an eclogitic metagabbro block; coin for scale (diameter 1.5 cm).

I performed a detailed petrographical and microchemical study of 32 samples taken from 9 metagabbro blocks. In order to constrain the retrograde metamorphic history of the rocks, I selected metagabbro samples to optimally cover their variable degree of retrogressive metamorphism.

5.3 Metagabbros of the Voltri mélange

The mineral abbreviations used in the following sections are taken from Kretz (1983). In addition, WhM is used to denote unspecified white mica, while Carb refers to unspecified carbonate minerals, and Op to opaques. The mineral assemblages of the studied samples are listed in table A4.1 of Appendix 4.

5.3.1 Petrography

The cores of the metagabbro blocks from the Voltri mélange often show a high-pressure metamorphic mineral assemblage with garnet, omphacite, and glaucophane crystals and aggregates up to several millimetres across. Towards the rims of the blocks, these high-pressure minerals are gradually replaced by darker amphiboles and plagioclase, such that the retrograde rims show darker colours than the relatively unaltered eclogitic cores (fig 5.4b). The successive mineral assemblages of the metagabbros are listed in figure 5.5. The high-pressure metamorphic mineral assemblage of the metagabbros (fig 5.6a) is dominated by euhedral garnet crystals, large (up to 5 mm in diameter) omphacites, with pressure shadows of smaller omphacite crystals (fig 5.6b), glaucophane and rutile. The cores of these large omphacites locally show exsolution of talc. Because talc only occurs as exsolutions its microstructural relationships with the other minerals of the high-pressure assemblage remains unclear. Minor quantities of white mica, plagioclase and quartz are present in some samples. Glaucophane, rutile, quartz, and white mica constitute the inclusion population within garnet, while lozenge-shaped aggregates of clinozoisite + plagioclase suggest breakdown of precursor lawsonite (fig 5.6c). Small white mica crystals are locally enclosed in omphacite. The presence of substantial amounts of rutile in the matrix as part of the high-pressure mineral assemblage indicates metamorphic pressures of at least 15 kbar (Liou et al., 1998).

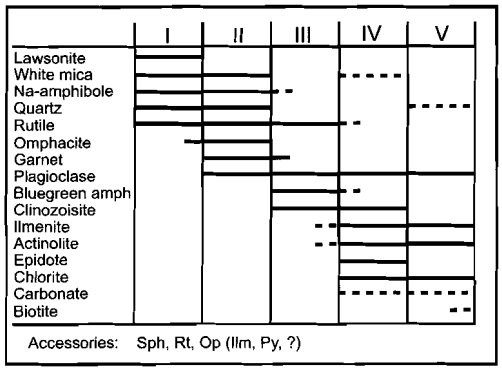

Figure 5.5: Mineral assemblages of the metagabbro blocks. Dashed: present in some, not all samples.

In some samples, omphacite shows thin symplectitic rims developed during retrograde metamorphism. In other samples glaucophane, and later blue-green amphibole and

plagioclase developed at the expense of omphacite. Glaucophane is often rimmed by barroisitic amphiboles and locally have an outer rim of actinolite (fig 5.6d). Rims of clinozoisite, and later epidote and plagioclase often replace garnet. The later stages of retrogression involve the formation of large quantities of chlorite and plagioclase at the expense of garnet. In samples from the retrograde rims of metagabbro blocks, minor quantities of biotite occur at the rims of chlorite crystals. In pelitic systems this can be taken as an indication for increasing temperature, but in the present mafic system biotite growth is inconclusive as to a possible temperature rise. The occurrence of biotite, as well as the presence of some carbonate probably reflects extensive fluid activity and possibly some metasomatism during melange formation and deformation (Vissers et al., in prep.).

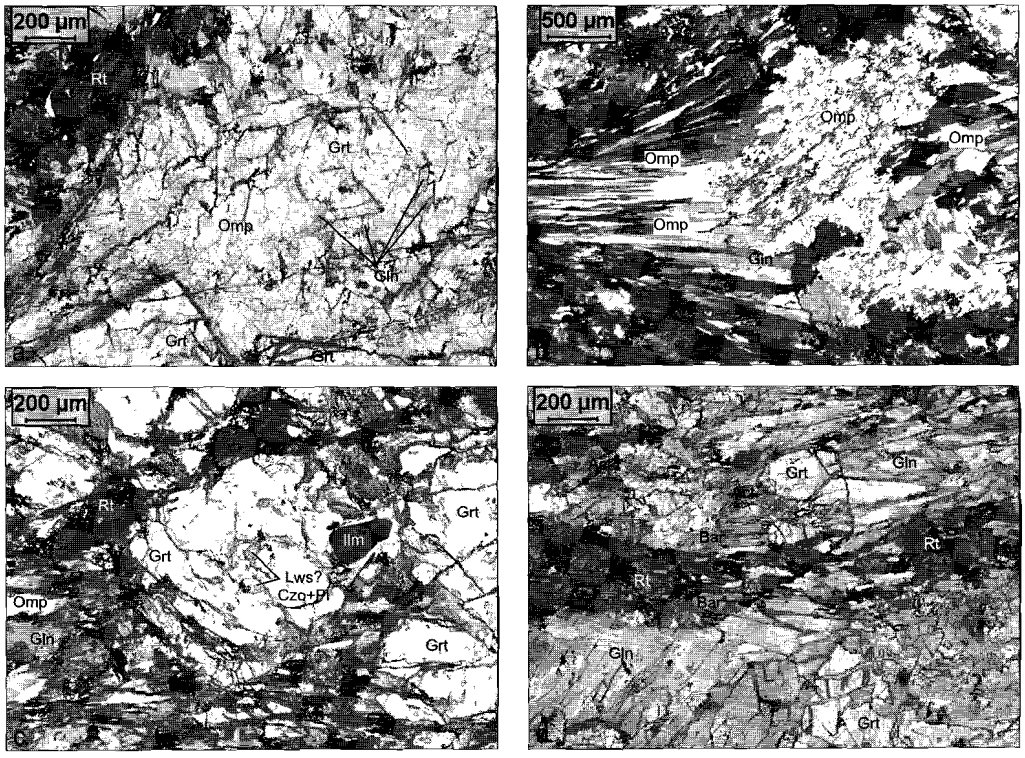

Figure 5.6: Petrography of the metagabbro blocks. **a.** The high-pressure mineral assemblage. **b.** Large omphacites, with smaller omphacites and glaucophane in pressure shadow. Large omphacite contains exsolutions of talc. **c.** Inclusions of clinozoisite and plagioclase, possibly pseudomorphic after lawsonite, within garnet. **d.** Glaucophane breakdown to barroisite and barroisite breakdown to actinolite.

5.3.2 Mineral chemistry

Microchemical analyses were carried out using the automated JEOL 8600 electron microprobe of the EU Geochemical Facility at the University of Bristol, UK. The accelerating voltage during the analyses was 15 kV at a beam current of 15 nA, the spot size was 1-5 microns, with the larger spot size used for Na-bearing phases in order to minimise alkali volatilisation. Peak counting times ranged between 15 and 20 seconds. The following standards were used: albite for Na, olivine for Mg, spinel for Al, diopside for Si, K-feldspar for K, wollastonite for Ca, $SrTiO_3$ for Ti, hematite for Fe, MnO for Mn, Cr_2O_3 for Cr and nickel (metal) for Ni. Procedures for the estimation of the ferric iron content of analysed minerals are as described in section 3.4.2.3. Ferric iron content was estimated for garnet, pyroxene, amphibole and biotite; all other minerals have been assumed to contain ferrous iron only. Representative analyses of Grt, Omp, amphiboles, Ep, Pl, WhM and Chl are listed in Appendix 4.

Garnet

Garnet compositions are fairly similar for all analysed metagabbro samples (fig 5.7a). The garnets analysed have a compositional range of $Alm_{60-75}And_{4-10}Grs_{12-25}Prp_{2-15}Sps_{1-15}$, and they are often strongly zoned (fig 5.8a-d). The molar proportions of iron, magnesium and manganese vary strongly across the crystals. Garnets cores are locally very rich in manganese (Sps_{25-40}) and much poorer in iron (Alm_{35-50}) than

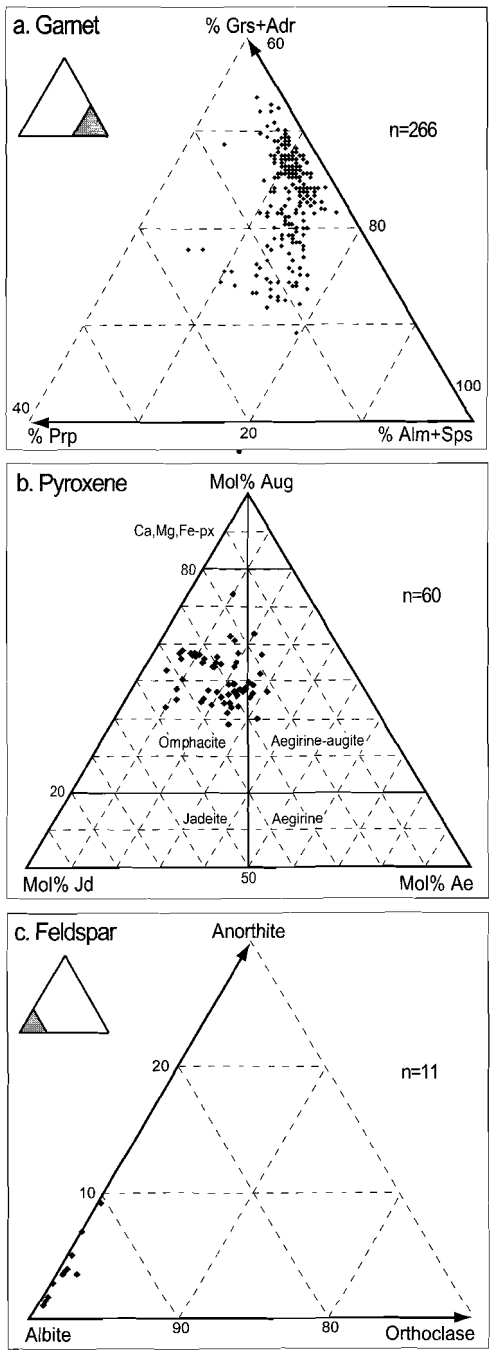

Figure 5.7: Mineral compositions for the metagabbro blocks. **a.** Garnet compositions. **b.** Clinopyroxene compositions [cf. \Morimoto, 1988 #33]. **c.** Plagioclase compositions.

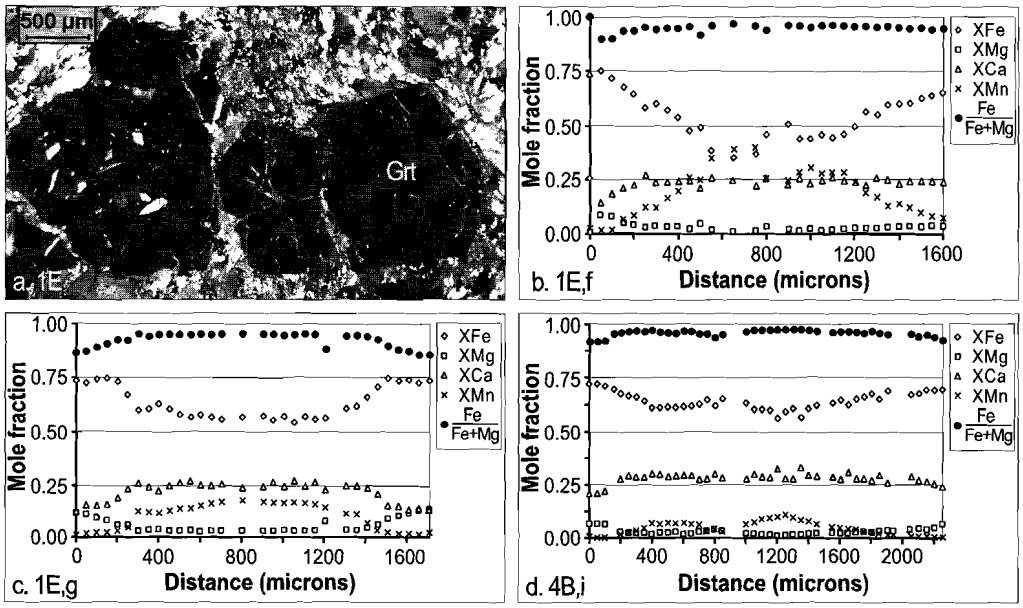

Figure 5.8: Garnet zoning in metagabbro blocks. **a.** Photomicrograph of a zoned metagabbro garnet from sample MEL96-1E. **b.** Compositional variation across a zoned metagabbro garnet. **c.** Id. **d.** Id.

the average garnet. The relative proportions of iron and magnesium are indicative of the temperature during garnet formation (e.g. Råheim and Green, 1974). A decrease of $Fe^{2+}/(Fe^{2+}+Mg)$ indicates an increase in metamorphic temperature (e.g. Spear, 1993, p. 370), such that the garnet zoning shown in fig 5.8 generally indicates a temperature increase during garnet growth. The low-magnesium garnet composition as well as the presence of substantial amounts of rutile as part of the high-pressure mineral assemblage indicates that all of our samples were originally Fe-Ti gabbros, rather than Mg-gabbros.

Clinopyroxene

The composition of pyroxenes analysed in metagabbro samples is shown in the ternary diagram of figure 5.7b. The nomenclature used for sodic-calcic pyroxenes is adapted from Morimoto et al. (1988). Jadeite contents were calculated as the sodium content minus the amount of acmite (ferric iron). Most pyroxene analyses plot within the omphacite field, although some aegirine-augites with compositions close to the omphacite field have been analysed as well.

Amphibole

The optical observation that amphiboles in the metagabbros show a large compositional variation is confirmed by microchemical analyses. Following the nomenclature of Leake (1978), the amphiboles analysed are subdivided in four different groups. The alkali amphiboles are related to high-pressure metamorphism, and they have the composition of glaucophanes or

ferro-glaucophanes, locally ranging to crossite (fig 5.9a). Sodic amphiboles mostly plot in the ferro-winchite field (fig 5.9b). The pargasitic amphiboles are mostly ferro-edenites and locally silicic ferro-edenites (fig 5.9c), tschermakitic amphiboles are mostly actinolite and sometimes ferro-actinolite (fig 5.9d).

Feldspar

The few feldspars analysed cluster closely around the pure albite end-member (fig 5.7c). The maximum analysed anorthite content is almost 10%, whereas a maximum of 3% orthoclase component has been found.

White mica

White micas were only analysed in a few samples (fig 5.10). The white micas generally have a very high Si content, with up to 3.68 Si per formula unit. The high Si content of the white micas indicates that they crystallised at high pressures (e.g. Carswell et al., 1997).

5.4 Metamorphic history

5.4.1 Thermobarometry

The metagabbro samples show evidence for high-pressure metamorphism, followed by several retrograde mineral transformations. This implies that they preserve at least a partial record of evolving pressure-temperature conditions. Deciphering the pressure-temperature record is challenging because of the difficulty in demonstrating that a given assemblages has preserved equilibrium mineral compositions during changing pressure-temperature conditions.

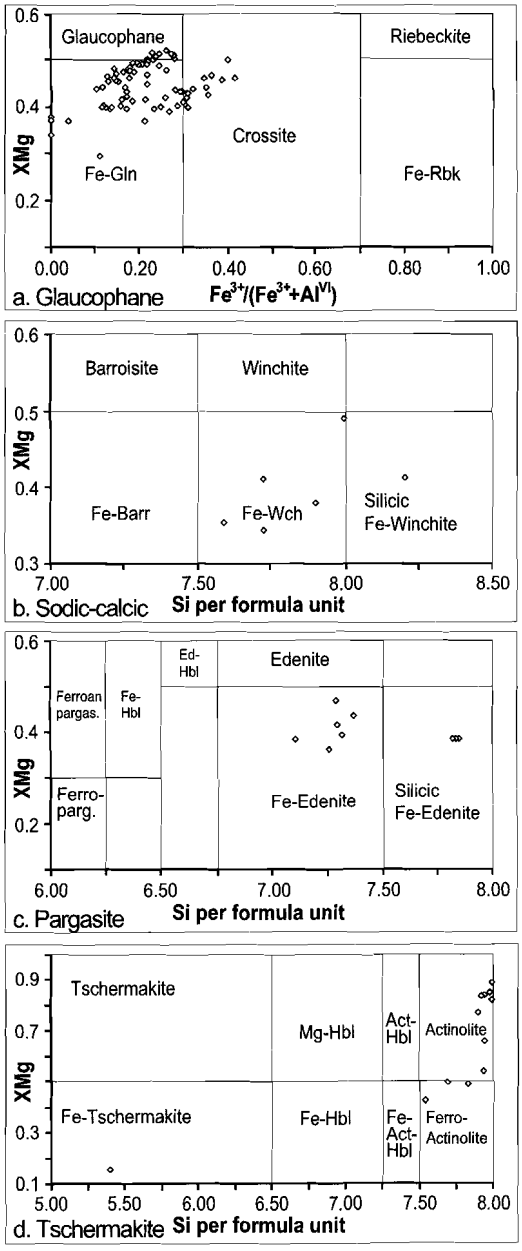

Figure 5.9: Amphibole compositions [cf. \Leake, 1978 #459]. **a.** Alkali amphiboles, glaucophane series. **b.** Sodic-calcic amphiboles. **c.** Calcic amphiboles, pargasite series. **d.** Calcic amphiboles, tschermakite series.

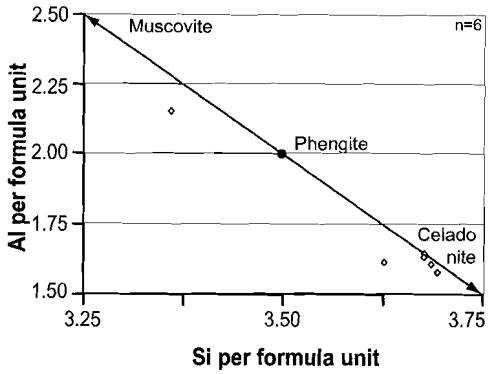

Figure 5.10: White mica compositions of phengite in metagabbro blocks.

The preservation of partial retrogression and mineral zonation demonstrate the need for caution when one attempts to quantify metamorphic temperatures and pressures using the compositions of co-existing minerals. However, careful examination of textures and microstructures permits selection of mineral pairs most suitable for geothermobarometry. The exact formulations of thermobarometric calibrations used in this study are summarised in Appendix 1. Provided that the microprobe analyses are of good quality and that the minerals analysed were in equilibrium, the errors involved in thermobarometric estimates like those applied here are generally of the order of ± 25-50 °C and ± 0.5-2 kbar (Spear, 1989). The microprobe analyses used for thermobarometry and representative analyses for other minerals are tabulated in Appendix 4.

Garnet-omphacite-phengite triplets

The Si content of white mica in phengite bearing mafic eclogites is a measure of the inverse Tschermaks substitution, replacing Al^{T1} (Al^{IV}) with Si. The amount of Si^{T1} increases with pressure (Carswell and Harley, 1990). Waters and Martin (1993) extracted thermochemical data from an internally consistent thermodynamical dataset (Holland and Powell, 1990) for the equilibrium:

$$Mg_3Al_2Si_3O_{12} + 2\ Ca_3Al_2Si_3O_{12} + 3\ K(Al_1Mg_1)^{VI}Si_2^{T2}Si_2^{T1}O_{10}(OH)_2 =$$

$$6\ CaMgSiO_6 + 3\ KAl_2^{VI}Si_2^{T2}Si^{T1}Al^{T1}O_{10}(OH)_2$$

(pyrope + grossular + celadonite = diopside + muscovite). The barometer was then formulated for P as a function of T and a distribution coefficient K_D. The barometer and the recommended activity models were described clearly by Carswell et al. (1997). In this study I have applied an updated version of the barometer, that was published on the internet in 1996 (http://wwwearth.ox.ac.uk/~davewa/research/ecbar.html). The exact formulation used here and documented in Appendix 1 follows Waters and Martin (1996), and is henceforth referred to as WM96.

To obtain an estimate of the PT conditions, the WM96 barometer was combined with the garnet-clinopyroxene thermometer of Powell (1985) and the garnet-phengite thermometer of Green and Hellman (1982). The temperature dependence of iron-magnesium partitioning between garnet and clinopyroxene has long been established (e.g. Råheim and Green, 1974). In this study I follow the approach of Carswell et al. (1997) and use Powell's (1985) calibration, because all analysed garnets from garnet-

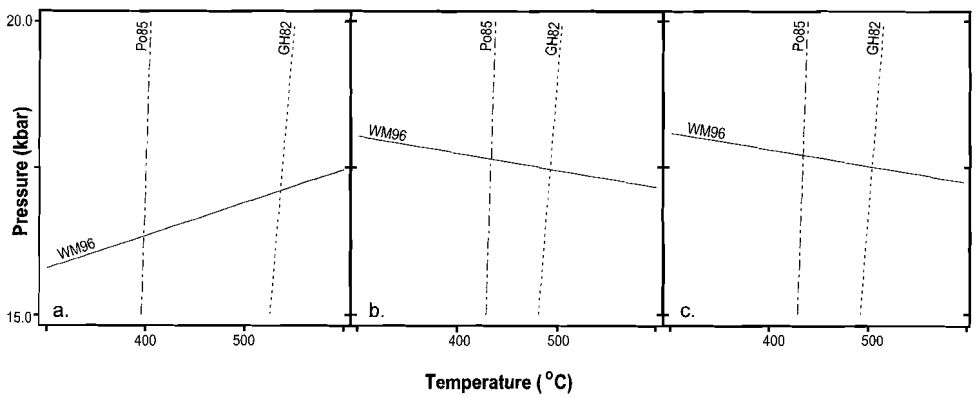

Figure 5.11: Results of garnet-clinopyroxene-phengite thermobarometry. Barometry according to Waters and Martin (1996), combined with the garnet-cpx thermometer of Powell (1985) and the garnet-phengite thermometer of Green and Hellman (1982). A detailed outline of this approach is given by Carswell et al. (997), and outlined in Appendix 1.

omphacite pairs show $X_{Ca} < 0.35$. The distribution coefficient (K_D, for definitions see Appendix 1) has been calculated for pairs of garnet and omphacite. Iron-magnesium partitioning between garnet and phengitic white mica is another temperature dependent exchange reaction (Green and Hellman, 1982, Appendix 1), and was also used as a geothermometer in combination with the WM96 geobarometer.
One of the studied samples (MEL96-4c) contains garnet, clinopyroxene and phengite in apparent mutual equilibrium. Analyses of these minerals in two of such cases yield temperatures of about 475 °C at pressures of 17.5 kbar, whilst in a third case conditions of 460 °C and 17.0 kbar are obtained for the equilibration of garnet, clinopyroxene and phengite (table 5.1, fig. 5.11).

Garnet-omphacite pairs
In phengite-free eclogites WM96 cannot be used to constrain the peak metamorphic pressure. In order to obtain PT data from such phengite-free rocks the garnet-clinopyroxene thermometer has been combined with the jadeite barometer. The reaction

$$Ab = Jd + Qtz$$

							WM96	WM96 + Po85		WM96 + GH82	
Fig 5.11	Sample	Grt	Cpx	Phen p.f.u.	Si p.f.u.	K_D	P (kbar, 500 °C)	P (kbar)	T (°C)	P (kbar)	T (°C)
a	MEL96-4c	3.161	3.159	3.160	3.692	8.693	16.9	16.3	400	17.2	534
b	MEL96-4c	3.161	3.164	3.162	3.676	9.024	17.4	17.4	431	17.6	493
c	MEL96-4c	3.161	3.164	3.163	3.676	8.999	17.5	17.4	430	17.7	508

Table 5.1: Garnet-clinopyroxene-phengite equilibrium pressures calculated with Waters and Martin (1996) for a given temperature of 700 °C. Combined graphical solution of WM96 with Powell (1985) and of WM96 with Green and Hellman (1982). Exact formulations are in Appendix 1, complete microprobe analyses are in Appendix 4.

Sample	Grt	Omp	Omp max Jd	core / rim	X_{Ca}	X_{Jd}	K_D	T (°C)	P (kbar)
MEL96-1B	3.108	3.107	3.105	core	0.181	0.324	28.272	417	10.3
MEL96-1E	3.16	3.17	2.80	rim	0.133	0.310	14.854	485	11.3
MEL96-2B	4.56	4.55	4.64	rim	0.157	0.352	14.265	512	11.9
MEL96-3A	4.75	4.74	4.72	rim	0.180	0.350	17.772	489	11.5
MEL96-4B	3.32	3.33	3.30	rim	0.242	0.327	32.540	436	10.6
MEL96-4c	3.161	3.164	3.159	core	0.192	0.443	27.279	431	10.6
MEL96-4d	2.29	2.28	2.28	core	0.224	0.325	31.966	427	10.4
MEL96-9A	2.100	2.103	2.102	rim	0.207	0.399	31.642	419	10.4

Table 5.2 Garnet-omphacite equilibrium pressures and temperatures. Combined solution of Holland (1983) and Powell (1985). Exact formulations are in Appendix 1, complete microprobe analyses are in Appendix 4.

is pressure dependent with respect to the jadeite content of omphacite (Holland, 1983). This barometer was reformulated by Carswell and Harley (1990) and is applied to several metabasic samples. Because omphacite does not occur in equilibrium with plagioclase, the pressures obtained represent minimum estimates only. Table 5.2 lists the results of simultaneous solution of the garnet-clinopyroxene thermometer and the jadeite barometer with the highest PT conditions for garnet-clinopyroxene pairs of each sample. The results are thus a mathematical solution of the barometer for the Omp analysis with the highest jadeite content of the sample, and the thermometer applied to analyses of neighbouring pairs of Grt and Omp showing apparent (microstructural) equilibrium.

Garnet-omphacite thermobarometry has been performed on several metagabbro samples. The results of garnet-clinopyroxene thermobarometry for these samples are listed in table 5.2. The temperatures obtained range from 412 to 512 °C, at minimum pressures between 10.3 and 11.9 kbar. These pressures are around 5 kbar lower than those obtained using garnet-clinopyroxene-phengite barometry. The actual equilibrium pressures of the garnet-omphacite pairs are likely to be much higher than the minimum estimates obtained here, but because the jadeite barometer yields minimum estimates the obtained results are consistent with those obtained from garnet-clinopyroxene-phengite barometry, as indicated by the arrows in figure 5.12.

Garnet-phengite pairs

The celadonite content of phengite can be expressed in terms of its Si content per formula unit and is dependent on pressure (Massonne, 1991; Massonne and Schreyer, 1987). The more recent calibration is an improved version, but has unfortunately not been published. The graphical representation of the 1991 calibration is included in Appendix 1. Pressures obtained with the improved calibration are roughly 0.6 kbar below those obtained with the 1987 calibration (Rötzler et al., 1999). Because phengite in the metagabbros does not co-exist with K-feldspar, biotite and quartz, Massonne's (1991) barometer should not be applied to these rocks. I have used it here, however, to estimate a suitable pressure range in calculations of garnet-phengite equilibrium temperatures.

The results of garnet-phengite thermometry are listed in table 5.3. The obtained temperatures are 483-542 °C in cases where the Si-content of phengite is high, around 432 °C for intermediate phengite compositions, and around 442 °C for low-Si phengite.

In our reconstruction of the PT trajectory (fig 5.12) these values emerge as steep lines over a pressure range of 5 kbar. Respective triangles on these lines relate to the silica content of the pertinent phengite crystals. These triangles should not be taken to indicate the equilibration pressure of the garnet-phengite pair, because the phengite barometer cannot be applied to the metagabbros studied, as phengite is not in equilibrium with biotite, K-feldspar and quartz. Notably, the obtained pressures are very similar to those obtained using WM96 on garnet-clinopyroxene-phengite triplets, which may indicate that the pressure ranges for which garnet-phengite equilibrium temperatures have been calculated are indeed reasonable.

							GH82				Massonne 1991	
Sample	Grt	Phen	Si p.f.u.	K_D	A	B	P1	T (P1,°C)	P2	T (P2, °C)	P (kbar)	T (°C)
MEL96-4c	3.155	3.156	3.361	33.829	5170	4.17	7.5	434	12.5	458	9.1	442
MEL96-4c	3.161	3.160	3.692	19.687	5170	4.17	15.0	526	20.0	551	18.2	542
MEL96-4c	3.161	3.162	3.676	29.358	5170	4.17	15.0	483	20.0	507	17.3	494
MEL96-4c	3.161	3.163	3.676	26.729	5170	4.17	15.0	493	20.0	517	17.4	504
MEL96-4d	2.6	2.7	3.621	51.469	5170	4.17	12.5	420	17.5	442	15.2	432
MEL96-9A	2.99	2.96	3.684	32.875	5170	4.17	15.0	472	20.0	496	17.3	483

Table 5.3: Garnet-phengite equilibrium temperatures calculated with Green & Hellman (1982) for given pressures. Combined graphical solution of Green and Hellman (1982) with Massonne (1991). Exact formulations are in Appendix 1, complete microprobe analyses are in Appendix 4.

5.4.2 Compilation of the PTt trajectory

The PT path

Figure 5.12 shows a compilation of the thermobarometric results described above. In addition, reaction lines are included that constrain the evolving PT conditions on the basis of petrographical observations. A path is constructed through these results.

The PT trajectory starts at the low-temperature side of the lawsonite breakdown reaction to clinozoisite. Peak metamorphic conditions are constrained by the results of WM96 barometry, combined with the garnet-clinopyroxene (Powell, 1985) and garnet-phengite (Green and Hellman, 1982) thermometers. Peak metamorphic conditions are estimated to be 500 ± 50 °C and 17.5 ± 0.5 kbar. Garnet-phengite pairs that were not in apparent equilibrium with clinopyroxene yielded similar temperature ranges. The stability of glaucophane during prograde metamorphism as well as the initial stages of retrogression indicates that the Gln-out reaction was not or only slightly overstepped at high pressures.

After peak pressure metamorphism the rocks cooled during decompression. The pressures obtained by garnet-clinopyroxene thermobarometry using the jadeite barometer (Holland, 1983) are minimum values only. It should be noted that the true equilibrium pressures most probably coincide with those obtained using the WM96 barometer. Due to the lack of a pressure indicator, the results of garnet-amphibole thermometry do not further constrain the retrograde PT path.

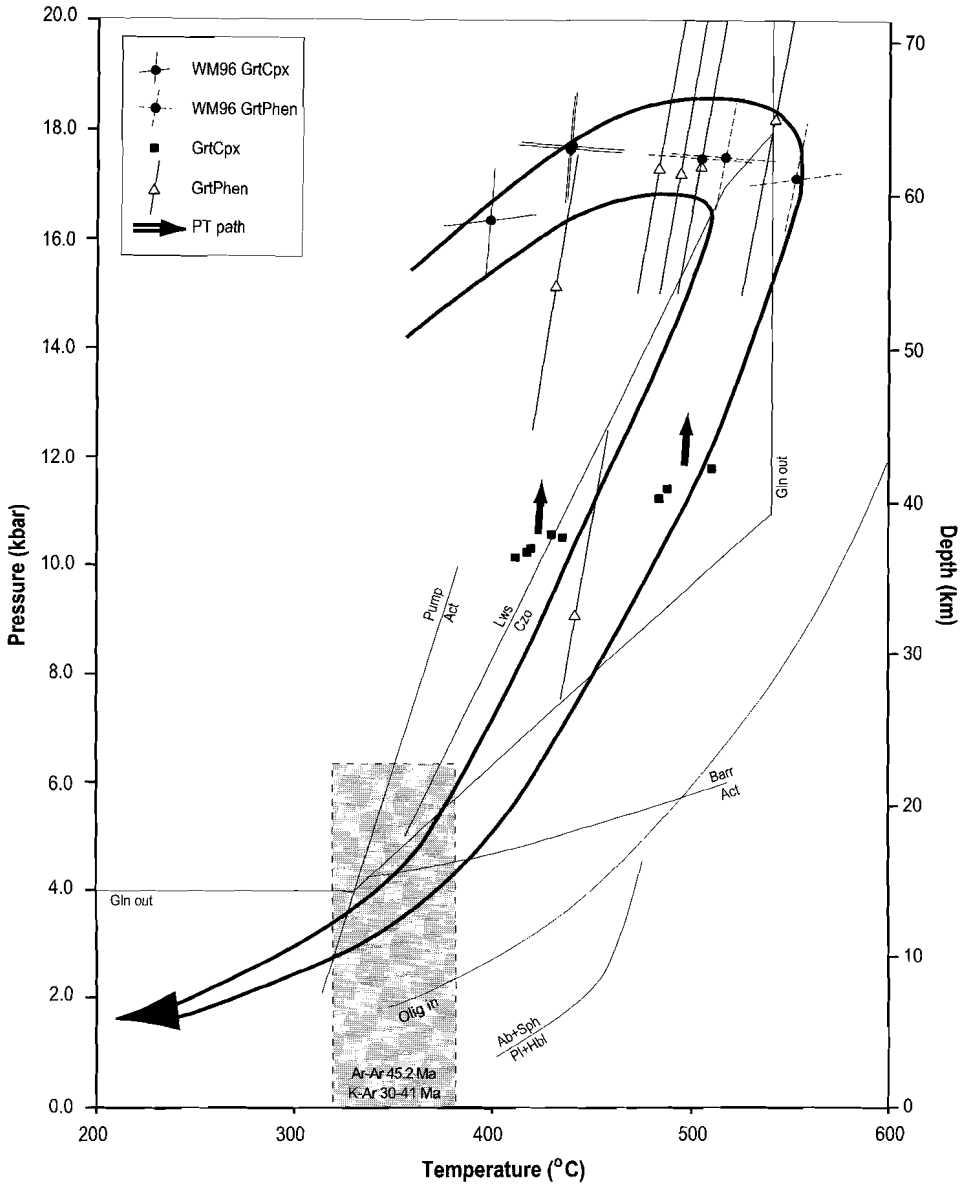

Figure 5.12: Compilation and interpretation of thermobarometric results.
Thermobarometric results obtained using different calibrations. WM96 GrtCpx and WM96 GrtPhen are results of garnet-clinopyroxene-phengite thermobarometry. For details and references see text, figure 5.10, and table 5.3. GrtCpx = garnet-clinopyroxene thermometry (Powell, 1985) combined with jadeite barometry (Holland, 1983), see table 5.1. GrtPhen = graphical solutions of garnet-phengite thermometry (Green, 1982) and phengite barometry (Massonne , 1991), see table 5.2. GrtAmph = garnet-amphibole thermometry using the calibration of Graham and

The retrograde history is further constrained by petrographic observations. Transformations of glaucophane to barroisite and actinolite but no development of hornblende suggest that the rocks had cooled below 470 °C when they reached a low-pressure ($P < 4$ kbar) regime. The presence of clinozoisite and albite and the absence of lawsonite in the matrix indicate that the rocks did not cool below about 350 °C at 5.0 kbar. The stability of the nearly-pure albite end member rather than an intermediate plagioclase lends further support to our inference that the rocks cooled from eclogite-facies peak conditions into the greenschist facies stability field, rather than into the higher-temperature amphibolite facies regime (Spear, 1993). The oligoclase-in reaction for mafic rocks (Maruyama et al., 1983) thus forms an upper temperature limit to the retrograde history of the metagabbros.

Time constraints on metamorphism

Unfortunately, there are very few time constraints available for the Voltri Massif in general and for the mélange rocks addressed in this study in particular. The age of pre-Alpine rifting of the Piemonte-Ligurian oceanic basin was determined to be 150 Ma by U-Pb geochronology on zircon separates from the Beigua serpentinite unit (Borsi et al., 1996) which is in reasonable accordance with stratigraphic data from the Brianconnais sediments suggesting an Oxfordian (ca. 160 Ma) age for breakup in the pertinent segment of the Piemonte Ligurian realm (e.g. Lemoine and Trümpy, 1987). As rifting was followed by oceanic subduction, these ages pose an upper limit to the timing of high-pressure metamorphism. There are no geochronological data from the Voltri massif, however, that further constrain the age of the high-pressure mineral assemblage.

K-Ar ages of white micas from gneisses of the Voltri group have yielded cooling ages of 30-41 Ma (Hunziker et al., 1992; Schamel and Hunziker, 1977). ^{40}Ar-^{39}Ar cooling ages of white mica separates from the Beigua serpentinite unit were determined to be 45.2 ± 1.8 Ma by Dave Rex (Unpublished data, Leeds University, 1989; Hoogerduijn Strating, pers. comm., 2000). Both of these age determinations reflect cooling below 350 ± 30 °C (Lips, 1998; Lips et al., 1998). Additional time constraints are the stratigraphically determined Early Oligocene age of continental scree breccias, conglomerates and local lignites that were deposited on exhumed rocks of the Voltri Group (Capponi et al., 1999; D'Atri et al., 1997), and the observation that high-pressure metamorphic clasts from the Voltri Massif occur in Oligocene sediments (Haccard and Lorenz, 1979). It follows that the rocks of the Voltri Massif were exhumed to superficial levels by about 34 million years ago.

Powell (1984). See also table 5.3. Thin solid lines are reactions that constrain the metamorphic conditions. Gln-out taken from Maresch (1977), the reaction pumpellyite + chlorite = actinolite + epidote after Liou et al. (1983), lawsonite-clinozoisite transition after Barnicoat and Fry (1986), the lower stability limit of baroisite from Ernst (1979), oligoclase-in reaction from Maruyama et al. (1983), and the reaction albite + sphene = plagioclase + hornblende after Moody et al. (1983). Age constraints were taken from the literature, see text for references. By 34 Ma the Voltri massif was exposed at the Earth's surface (D'Atri et al., 1997).

5.5 Discussion

5.5.1 Comparison with previous studies

The metagabbros from the Beigua unit, from which the metagabbro blocks in the tectonic mélange were most probably derived (Vissers et al., in prep.), have extensively been studied. Their bulk chemistry indicates that they were derived from MOR basalts (Mottana and Bocchio, 1975) and that they were rodingitised at or near the seafloor (Messiga et al., 1983; Morten et al., 1985) before being subducted and metamorphosed at eclogite facies conditions. Temperatures during peak pressure metamorphism were previously estimated to be around 400 °C and 13 kbar (Hoogerduijn Strating, 1991; Messiga and Scambelluri, 1991). The widespread occurrence of rutile in the eclogitic mineral paragenesis, however, led Liou et al. (1998) to infer a minimum estimate for the peak pressure of 15 kbar at 475 ± 75 °C. Moreover, the presence of talc in some of their samples suggests a peak metamorphic pressure of about 17 kbar, which is confirmed by the thermobarometric results of the present study (fig 5.12).

The presence of fluid inclusions in omphacite of some deformed eclogitic metagabbros (Vallis and Scambelluri, 1996) suggests that the metagabbros show a variable degree of retrogression due to the presence of fluids, enhancing retrograde mineral transformations. Based on the chemistry of edenite-plagioclase symplectites after omphacite in metagabbros from the Beigua serpentinite unit, an increase of the metamorphic temperature after peak pressure has been inferred (Messiga and Scambelluri, 1991). An amphibolite facies overprint was inferred to have occurred around 550-650 °C and 4 to 8 kbar. Our samples contain similar symplectitic microstructures, but the chemistry of the different components has not been analysed in any detail. However, the PT conditions recorded in samples studied by Messiga et al. (1991) clearly indicate higher peak temperatures than the upper temperature limit inferred above on the basis of the presence of nearly pure albite rather than Ca bearing plagioclase. This illustrates the problems associated with inferring estimated PT- conditions from non-equilibrium microstructural features using thermobarometric methods based on equilibrium thermodynamics. The lack of any evidence for increasing temperatures during decompression such as the growth of intermediate plagioclase or hornblende, leads us to conclude that the inferred PT trajectory (fig 5.12) is appropriate for the samples studied. However, due to the variable degrees of retrogression mentioned above, evidence for an amphibolite facies metamorphic overprint could be lacking due to sluggish kinetics or the local absence of fluids.

5.5.2 Tectonic implications

The thermobarometric results from the eclogitic metagabbros addressed in this study point towards progressive cooling during exhumation. This cooling history is marked by two stages. The early stage of exhumation, from peak pressure metamorphism to greenschist facies conditions, proceeded along an effective thermal gradient of the order of 2.5-4 °C/km. These values are distinctly higher than those of an adiabatic gradient (0.6 °C/km, McKenzie (1984)), which indicates that the studied rocks were effectively

cooled by the surrounding rocks during their early ascent. This was followed by exhumation along a gradient of some 20–25 °C/km, a value close to that of a continental geotherm. There are few time constraints only on this metamorphic history, but it is clear that the rocks of the Voltri Massif were exposed at the Earth's surface by the Early Oligocene (34 Ma, Capponi et al., 1999; D'Atri et al., 1997).

The tectonic setting of the Voltri Massif, located at the junction of the Alps and Apennines orogenic systems, is complicated for several reasons. First, the main tectonic units in the Voltri Massif and in the Ligurian Alps further west have been transported to the WNW (Hoogerduijn Strating, 1991), while the Apennines east of the Voltri massif show NNE directed nappe transport. Tectonic transport in both areas was not coeval, however, and there is evidence that in the western portions of the Apennines westerly directed transport occurred at an early stage, prior to NNE directed movements (Hoogerduijn Strating and Van Wamel, 1989). Secondly, the Ligurian Alps, the ophiolitic Voltri Massif and Sestri-Voltaggio Zone, and the Ligurian Apennines form a relatively narrow mountain range in between the Po Basin to the north and the Mediterranean to the south. The development of these major basins during essentially Oligo-Miocene times further complicates attempts to reconstruct the orogenic geometry of the region during the early Tertiary.

The Voltri Massif and the adjacent Sestri-Voltaggio Zone east of the massif are made up of crustal and mantle fragments derived from the Piemonte Ligurian ocean. During closure of this ocean, its crust and lithosphere were subducted underneath the approaching Adrian continental lithosphere. It is therefore clear, that the metamorphic evolution of the rocks addressed here should fit the orogenic evolution of the pertinent portion of the Alpine subduction system. The motion of Adria is inferred to have changed from northward to NW around 35 Ma (Schmid et al., 1996; Schmid and Kissling, 2000), when the Voltri Massif had already been exhumed and was exposed at the Earth's surface. The metamorphic evolution of the eclogitic metagabbros thus reflects the earlier part of the convergence history, related to northward motion of Adria relative to stable Eurasia. I envisage that exhumation of the high-pressure rocks may be explained by corner flow in the orogenic wedge on top of the subduction zone as suggested by Platt (1986). In this model, exhumation is driven by the continuous underplating of subducted material at the base of the wedge, while coeval extension in the upper portions of the wedge facilitates exhumation. This causes a material flow within the wedge bringing the deep-seated rocks upward. The present peak pressure estimates point to a thickness of the pertinent orogenic wedge of at least 50 kilometres, consistent with the dimensions estimated in Platt's (1986) reconstruction of a Swiss-Italian transect of the Alps.

Detailed structural studies (Hoogerduijn Strating, 1994) have shown that the contact of the ophiolites and calcareous metasediments of the Sestri-Voltaggio Zone overlying the units of the Voltri Massif was reactivated as an extensional detachment during late Paleocene to early Eocene deformation. These extensional structures were overprinted during compression from the Middle Eocene onward. The timing of this change in overall deformation coincides with changes in Africa-Europe convergence rates

(Dercourt et al., 1993; Dewey et al., 1989), which led Hoogerduijn Strating (1991; 1994) to suggest that the decreasing convergence rate during late Paleocene to early Eocene times reduced the basal drag exerted on the accretionary wedge, causing it to become gravitationally unstable. The resulting extensional faults were overprinted by compressional structures when convergence accelerated during the Middle Eocene (Hoogerduijn Strating, 1994). Movements along extensional detachments likely contributed to the exhumation of the eclogite facies rocks of the Voltri Massif, while thrusting and concurrent erosion were possibly responsible for the final stages of exhumation, prior to its erosion (Haccard and Lorenz, 1979), and the deposition of conglomerates and scree breccias on top of it during the Oligocene (Capponi et al., 1999; D'Atri et al., 1997).

5.6 Conclusions

Metagabbro blocks in a tectonic mélange, developed at the overthrust contact of the Beigua unit overlying the Voltri-Rossiglione unit and probably derived from the Beigua serpentinite unit. The metagabbros show metamorphic mineral assemblages and transformations indicating peak metamorphic conditions of 500 ± 50 °C and 17.5 ± 0.5 kbar. After high-pressure metamorphism the rocks cooled during decompression. In contrast with the central and northwestern Penninic Alps, there is no evidence for any heating during exhumation.
Corner flow in the orogenic wedge on top of the subducting Piemonte-Ligurian oceanic lithosphere seems a likely cause for the exhumation of the high-pressure rocks of the Voltri Massif. Extensional faulting in response to decelerating Africa-Europe convergence probably facilitated exhumation. Exhumation was completed by around 34 million years ago, as evidenced by the deposition of Early Oligocene continental scree breccias on the rocks of the present-day Voltri Massif.

The thermal evolution of convergent margins: a numerical modelling study applied to the Alps

6.1 Abstract

During the Alpine orogeny, the Penninic Zone of the Alps was affected by Eoalpine, high-pressure metamorphism. In the central and western Alps, this was followed by Lepontine medium-pressure, high-temperature metamorphism during exhumation, while high-pressure rocks in the Ligurian Alps contain no signs of a thermal overprint. Here, the pressure-temperature-time trajectories we established in these three areas within the Alpine arc, placed in their regional tectonic context, are used as constraints on numerical models regarding the possible causes of Lepontine metamorphism.
Several contending hypotheses exist to explain heating during mountain building. We investigate the thermal implications of the breakoff of a subducting slab as well as those of the presence of a wedge of accreted radiogenic material via 2D numerical models[1]. We find that both mechanisms are capable of producing significant heating during orogeny, but that heating by slab detachment is fast and transient, whereas radiogenic heating requires time spans of the order of tens of millions of years and cessation of the subduction process.
Our results suggest that the metamorphism observed in the central Alps cannot have been caused by radiogenic heating alone, while slab breakoff seems a viable mechanism to account for the documented rise in metamorphic temperatures during exhumation. For the case of the western Alps the possible role of slab detachment is hard to assess due to large-scale block rotations and out-of-section transport in this segment of the Alps, while heating by a wedge of radiogenic material seems unlikely.

6.2 Introduction

The fundamental processes underlying the metamorphic evolution of crustal rocks in orogenic belts have long been subject of study (e.g. Ernst, 1973; Miyashiro, 1961; Miyashiro, 1973; Oxburgh and Turcotte, 1968). Since the advent of plate tectonics high-pressure, low-temperature metamorphism can be understood relatively easily as the result of subduction processes and related crustal thickening. However, Barrovian MP-HT, as well as LP-HT metamorphism are less readily explained in terms of unambiguously identifiable heat sources.

[1] *The research presented in this chapter was carried out in collaboration with D.M.A. van de Zedde and M.J.R. Wortel (Vening Meinesz Research School of Geodynamics, Utrecht University).*

The Alps

The Alps are a relatively narrow, arcuate mountain belt formed in response to subduction of the Piemonte-Ligurian branch of the Neotethys and subsequent collision of Adria, an African promontory, with the Eurasian continent. During this process of subduction and eventual collision, substantial volumes of rock presently exposed in the internal zones of the Alps underwent high-pressure ($P \approx 12$-22 kbar) metamorphism. Peak pressure metamorphism was followed by a stage of high-temperature, medium-pressure metamorphism while the rocks made their way back to the Earth's surface (e.g. Borghi et al., 1996; Meyre et al., 1999, and many others). Magmatism along the Periadriatic lineament occurred in relation to high-temperature metamorphism (e.g. Von Blanckenburg and Davies, 1995). These two stages in Alpine metamorphism, classically referred to as the Eoalpine (HP-LT) metamorphism and the subsequent Lepontine (MP-HT) stage, call for a geodynamic context explaining the increased temperatures during exhumation of the high-pressure rocks.

Study areas in the central, western and Ligurian Alps

Three study areas in the internal Penninic Zone of the Alps (fig. 6.1) were selected for a detailed study of their metamorphic histories. These areas are located in the Lepontine gneisses near Alpe Arami in the central Alps, in the Gran Paradiso basement in the western Alps, and in the Voltri massif in the Ligurian Alps, respectively. They were chosen at spatial intervals of the order of 150 kilometres measured along the Alpine arc, in order to obtain orogen-scale insight into similarities and differences in the metamorphic evolutions of the rocks involved.

The pressure-temperature-time (PTt) trajectories of the three areas studied, documented in detail elsewhere (Chapters 3, 4, 5), show a clear similarity in that the rocks in each of the areas underwent high-pressure metamorphism. They differ, however, in their thermal evolution during decompression. Both the Lepontine gneisses and Gran Paradiso underwent cooling during initial decompression and were then re-heated by 110 and 50 °C, respectively, around 30-35 million years ago. Notably, the amount of re-heating is markedly larger in the Lepontine gneisses than in the Gran Paradiso rocks. There is no evidence for any heating in the rocks of the Voltri massif, which became exposed at the Earth's surface by Oligocene times, coeval with the postcollisional heating in the other two study areas. These differences in the metamorphic histories of the three areas may reflect the different positions of the pertinent rocks in the developing orogen: the central Alps underwent orthogonal collision (e.g Schmid et al., 1996), whereas the western Alps were subject to transpression, oblique convergence, and block rotations (e.g. Schmid and Kissling, 2000; Stampfli and Marchant, 1997), which presumably also affected the Voltri massif.

Geodynamic hypotheses for late orogenic high-temperature metamorphism

Several geodynamic hypotheses have been proposed to explain late-orogenic medium-pressure to low-pressure, high-temperature metamorphism. Here, we explore different tectonic scenarios and inherent potential heat sources that may account for the heat

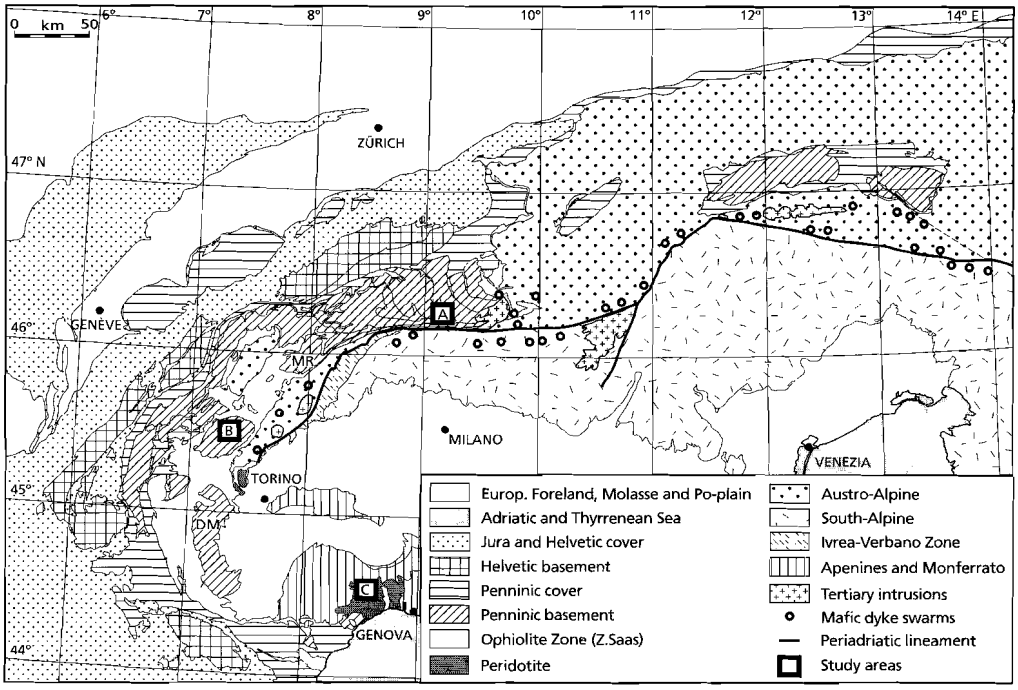

Figure 6.1: Map indicating the three study areas, and main tectonic units and structures in the Alps. A = Lepontine gneisses (Chapter 3), B = Gran Paradiso (Chapter 4), C = Voltri mélange (Chapter 5), DM = Dora Maira, MR = Monte Rosa. Modified after the Structural model of Italy (Bigi et al.,1983), magmatic units after Von Blanckenburg et al. (1998).

budget needed to produce the heating recorded in the PTt histories of our study areas in the central and western Alps. We will focus on two mechanisms that, at first inspection and at least qualitatively, may explain the main features of the PTt evolutions observed in the studied rocks: (a) the detachment or breakoff of the subducting slab and the associated rise of hot asthenosperic material (Davies and Von Blanckenburg, 1995; Wortel and Spakman, 1992), and (b) the heat production by a wedge of tectonically accreted radiogenic material (Jamieson et al., 1998). The mechanisms will be referred to as the two hypotheses, mechanisms, or processes. The two hypotheses seem appropriate to the case of the Alps, as they are both related to the convergence, collision and subduction of continental lithosphere. We use 2D numerical models to investigate the evolution of the temperature field related to these two processes. We present the results of our model studies, to address the principal question whether or not in-situ heating of rocks during their exhumation can be caused by either of the two mechanisms selected, and if so, on what time-scale and under which circumstances we may expect a thermal signal of the kind observed in the metamorphic rocks of the Penninic Alps. We proceed with confrontation of the numerical results with our observations, thus using the

metamorphic datasets to discriminate between the hypotheses. We investigate the relevance of these models for the three study areas, and their significance for the Alps as a whole. Some potential pitfalls regarding modelling studies should be kept in mind when using numerical models to investigate the viability of geodynamic scenarios. The model results strongly depend on the imposed rock properties and boundary conditions. A more general problem is that numerical models are, by definition, underdefined (Oreskes et al., 1994). This means that, although numerical models can falsify scenarios, they cannot be validated in the strict sense. In combination with other tools, numerical modelling is a very powerful tool to narrow down the amount of possible solutions to a problem.

6.3 Possible causes for heating

The occurrence of heating events in orogenic settings has led to several hypotheses, which can be subdivided into two main classes: (1) heating due to processes in the upper mantle, including heating caused by advection of mantle material at or near the base of the crust (e.g. Dewey, 1988; Platt and England, 1994; Wortel and Spakman, 1992) and strain heating within the thickened mantle root (e.g. Kincaid and Silver, 1996), and (2) processes that involve heating within the crust, usually by radiogenic heat production (e.g. Jamieson et al., 1998). Below, we briefly outline and discuss these hypotheses and associated model studies. For the case of the upper mantle we limit our discussion to heat-generating mechanisms genetically related to the orogenic process, and omit other processes such as mantle plume ascent, unrelated to the progressive development of narrow collision belts such as the Alps.

6.3.1 Processes in the upper mantle

Delamination or convective removal of thickened lithosphere

It has been proposed that an anomalously hot upper mantle underneath a developing orogen can be attributed to the convective removal of the thickened mantle root beneath the orogen (e.g. Houseman et al., 1981; Platt and Vissers, 1989). In this hypothesis, continental collision is thought to cause thickening of the entire lithosphere. Because the lithospheric mantle root has a higher density than the surrounding asthenosphere, the root may become gravitationally unstable and detach by delamination (Bird, 1979) or convective removal (Houseman et al., 1981). The lithospheric root is replaced by asthenospheric material, which causes a sudden advection of heat near the base of the remaining lithosphere, made up of thickened crust on top of a presumably thin layer of mechanically strong lithospheric mantle. Convective removal of the thickened lithospheric root has been suggested to explain orogen-scale extensional collapse in the Betic-Alboran orogenic system in the western Mediterranean (Dewey, 1988; Platt and Vissers, 1989) and the associated low-pressure, high-temperature metamorphism in the deeper parts of the remaining lithospheric column (Soto and Platt, 1999; Vissers et al.,

1995). For the case of the Alps this model seems less appropriate, because it is likely that the estimated 500 kilometres of shortening prior to continental collision was accommodated by subduction of oceanic lithosphere and continental fragments (e.g. Schmid et al., 1996; Stampfli and Marchant, 1997), rather than by bulk lithospheric thickening. In addition, the present-day width of the mountain range in the central and western Alps of about 200 kilometres seems difficult to reconcile with widespread extension expected in this scenario.

Slab detachment

An alternative hypothesis regarding heating in an orogenic setting concerns the detachment or breakoff of a subducting slab (Wortel and Spakman, 1992). Shallow detachment and removal of the subducting slab allows an influx of hot asthenospheric material (fig 6.2), and this mechanism has been invoked to explain late orogenic magmatism in the Alps (e.g. Davies and Von Blanckenburg, 1995; Von Blanckenburg and Davies, 1995). Conduction of heat upward through the overriding plate will potentially affect rocks, previously metamorphosed at high-pressures, during their exhumation. In view of the plate-tectonic perspective of this hypothesis, which is in line with current interpretations of the mountain-building process in the Alps, we will address this mechanism in detail below (Section 6.4.1). The thermal response to shallow slab detachment is expected to be essentially identical to that predicted for the case of removal of a lithospheric root (e.g. Dewey, 1988; Platt and Vissers, 1989).

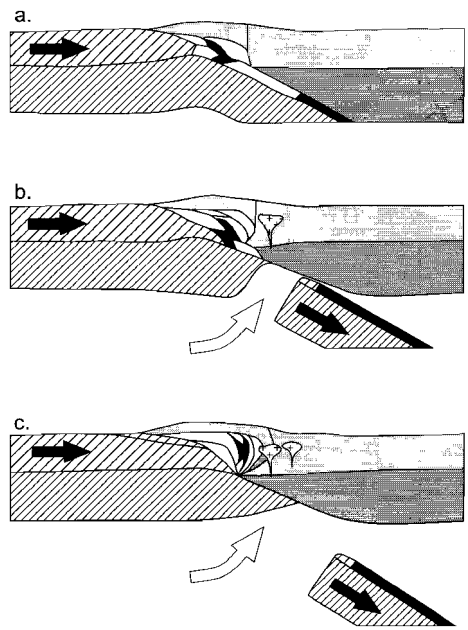

Figure 6.2: Processes associated with slab detachment or breakoff, modified after Davies and Von Blanckenburg (1995). **a.** Oceanic lithosphere subduction is followed by subduction of continental lithosphere. **b.** The subducted lithosphere breaks and sinks into the mantle. The gap fills with asthenospheric material, causing melt generation in the overriding lithosphere. **c.** Rebound due to the increased buoyancy after removal of the slab causes some uplift in the orogen.

Viscous dissipation in the upper mantle

Both convective removal of a thickened lithosphere and detachment of a subducting slab essentially involve a sudden change in the boundary conditions at the base of the orogenic system. Because seismic studies indicate that the mantle root may not be removed in some cases, Kincaid and Silver (1996) investigated an alternative heat-producing mechanism to explain heating within an orogen, which does not require the sudden ascent of asthenospheric mantle in response to removal of part of the lithosphere. Viscous heat dissipation involves

heat produced during viscous flow in the upper mantle, where the amount of heat produced depends on strain rate and on the viscosity of the deforming upper mantle rocks. In this hypothesis the lithosphere must be strong enough to sustain high stresses (220–330 MPa) without localisation of deformation. It is important to note that high convergence rates (4–5 cm/yr), and high lithospheric viscosities are also prerequisites. These aspects render this hypothesis unlikely for the case of the Alps, in particular because there is no evidence for such high convergence rates (e.g. Dewey et al., 1989; Schmid and Kissling, 2000).

6.3.2 Radiogenic heating within the deformed crust

1D models

One-dimensional numerical models of thickened continental crust have been widely used to explain regional metamorphism and the associated pressure-temperature evolution of rocks in orogenic belts. These models essentially describe the thermal evolution of a continental crust instantaneously thickened in the vertical dimension, where the crust may be thickened by doubling, equivalent to lithosphere-scale thrusting, or by homogeneous thickening (England and Thompson, 1984; Peacock, 1989; Thompson and England, 1984). The results of such model studies invariably show that rocks brought to depth during the orogenic process may become metamorphosed due to crustal radiogenic heat production operating at time scales of the order of tens of millions of years. For common parameter values of the thickening factor, radiogenic heat production and erosion rate, such rocks are expected to show clockwise PTt paths. The simple geometries used in these models preclude direct application to the case of orogenic belts such as the Alps, because such models inherently ignore potentially important effects like advective cooling due to subduction, and lateral advective and conductive heat transport related to the specific geometry of subduction and collision zones.

2D models

Advances in computational power as well as in numerical techniques have allowed modelling of more complex and realistic geometries of collision zones. Okaya et al. (1996) developed a 2D forward thermokinematic model to describe the last 35 million years (My) of the evolution of a north-south transect in the central Swiss Alps. The plate geometry was assumed to be static, and virtually identical to the present-day geometry as observed in deep seismic studies. The convergence rate between Europe and Adria was taken to be 5 mm/yr, and the motion of crustal material was confined to a wedge on top of the subducting European plate, with the overriding margin of Adria acting as a backstop. In this model material moves through the crustal wedge and is heated on the way by both heat flow from the mantle and radiogenic heat production within the crust. The convergence rate is varied, in order to fit the cooling rates of tracked material points to the results of radiometric dating studies reflecting cooling after peak temperature metamorphism. Additionally, as only cooling after peak temperature

metamorphism is described, the model of Okaya et al. (1996) does not relate to the part of the metamorphic history preceding the temperature climax.

Bousquet et al. (1997) developed a more sophisticated 2D model involving a similar geometry. In this kinematic model, the orogenic wedge consists of upper crustal material, which is mechanically decoupled from the subducting lower crust and the upper mantle. The maximum thickness of the wedge is about 30 kilometres. The convergence rate in the kinematic part of the model is fixed, and erosion is adjusted to balance the influx of upper crustal material, leading to a steady-state topography. The temperature field obtained is assumed to reach steady-state after about 30 Ma, and is used to determine the distribution of mineral assemblages due to metamorphic reactions. With the transformation from, for instance, a blueschist to an eclogite facies metamorphic mineral assemblage, the density of the volume of rock changes, affecting its predicted seismic signature. As retrograde reactions often proceed very slowly because of the limited availability of fluids it is assumed that, during exhumation, rocks with an eclogitic mineral assemblage at the base of the wedge carry that mineral assemblage, or at least relicts of it, to the Earth's surface. Because in this model material only circulates within the orogenic wedge, the PTt-paths of tracked volumes of rock do not show heating during decompression, nor can inferences be made about rocks that underwent metamorphism at pressures higher than about 12 kbar. However, due to the relatively long residence time of radiogenic upper crustal material in the deeper parts of the wedge, the steady-state temperature field shows a rise of isotherms at the base of the orogenic wedge indicating the presence of a volume of anomalously hot rock near the base of the wedge.

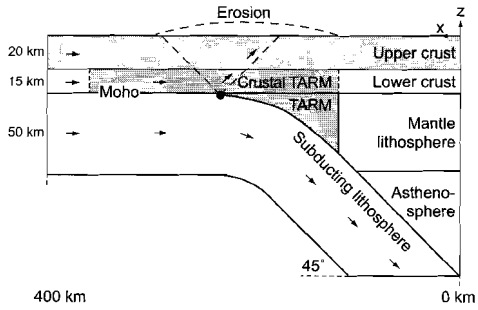

Figure 6.3: Geometry of the TARM model, modified after Jamieson et al. (1998). The model describes a setting of continent-continent collision, where the crust of the downgoing plate is mechanically decoupled from its mantle lithosphere. The crustal material is taken up in the orogen and moves upward along pre-defined zones of weakness. Upward movement of crustal material is counteracted by erosion, to maintain realistic orogenic geometry. The wedges of tectonically accreted radiogenic material (TARM) are shaded in a darker tone than the, also radiogenic, upper crust. Jamieson et al. (1998) tested models with a mantle TARM, a crustal TARM and a combined crustal and mantle TARM.

Accreted radiogenic material in a 2D model

Recently, Jamieson et al. (1998) published results of a model study explicitly aimed at Barrovian metamorphic conditions, i.e. high temperature (500-700 °C) at intermediate pressure (2-10 kbar). In comparison with the previous two models, additional heat is produced due to the accretion of upper crustal radiogenic material in the crustal and/or mantle wedge directly overlying the subducting lithosphere (fig 6.3). This wedge is referred to as Tectonically Accreted Radiogenic Material, or TARM. A crucial result of this model study is that some of the rocks moving through the wedge undergo heating

during the early stages of decompression. As this model seems promising regarding explanation of our field observations, i.e. cooling during initial decompression followed by a stage of re-heating, it will be explored in further detail below (Section 6.4.2).

6.3.3 Selection of possibly viable hypotheses

Two of the possible causes for heating during exhumation from the list above seem at first inspection viable for the case of the Alps on the basis of the geometry and thermal history of the orogen. Below, we investigate the thermal consequences of these two fundamentally different geodynamic scenarios: slab detachment or breakoff (Davies and Von Blanckenburg, 1995; Wortel and Spakman, 1992), and the development of a wedge of tectonically accreted radiogenic material (TARM) at the subduction zone (Jamieson et al., 1998). We select these two scenarios for two reasons. First, among of the hypotheses and models discussed above these two concur optimally with the wealth of geological data indicating that the Alps result from convergence accommodated by progressive subduction and eventual collision. Secondly, these two hypotheses potentially account for a stage of re-heating during exhumation of the kind documented in the metamorphic rocks of our study areas in the central and western Alps.

6.4 Numerical investigations

The PTt trajectories of both the Lepontine gneisses and Gran Paradiso reflect high-pressure metamorphism. Our model studies outlined below describe the thermal evolution of a 2D cross section through a subduction and collision zone. The overriding plate is undeformable, and hence the mechanics of exhumation of deeply subducted material is not incorporated. However, physical and numerical modelling results suggest that the buoyant rise of slivers of subducted material back up the subduction channel is possible (e.g. Chemenda et al., 2000; Chemenda et al., 1996; Van den Beukel, 1990). For this reason we focus attention on the evolution of temperature gradients along the plate contact, assuming, for simplicity, as well as for the lack of viable alternatives, that the pertinent high-pressure rocks move upward along this contact through the evolving temperature field. In this case, a thermal history involving cooling during initial decompression followed by a stage of re-heating at shallower depth prior to final exhumation requires either a transient heat pulse, or an inverted temperature gradient along the plate contact. The latter implies that single isotherms cross the plate contact three times, allowing for cooling, re-heating and final cooling when a slice of rock moves upward along the contact. In order to facilitate immediate comparison of the thermal implications of the two competing hypotheses, we use an identical model setup to describe the slab detachment and TARM hypotheses.

6.4.1 Slab detachment

In this study we use a thermomechanical model of a convergent plate margin (fig 6.4). The basis for this model was laid out by Wong a Ton and Wortel (1997) who investigated

the feasibility of detachment of part of a subducted lithospheric slab. In their model the evolution of the strength of the lithosphere through time is calculated for a combination of a pressure-dependent brittle rheology and a temperature-dependent ductile rheology. Velocities are imposed in this model, however, the model is dynamic in the sense that slab detachment only occurs if and when the forces acting on the slab equals its tensile strength. The authors found that the thermal structure and rheology of the slab control the timing and depth of slab detachment.

On the basis of the Wong a Ton and Wortel (1997) model, a thermomechanical model was developed to investigate the thermal implications of shallow slab detachment (Van de Zedde and Wortel, 2000). The variation of the temperature field with time is calculated by numerically solving the heat transfer equation through finite-difference methods. Heat is generated through friction at the plate contact and by moderate radiogenic heat production in the crust. There is no deformation (i.e. no heat advection) in the overriding plate, so all heat transfer in the overriding plate takes place by conduction. In the pertinent model runs, 50 million years of subduction of oceanic lithosphere is followed by the subduction of continental lithosphere (fig 6.4). After tens of millions of years of oceanic lithosphere subduction steady-state is attained, implying that the temperature and strength distribution in the slab remain constant. At the onset of continental lithosphere subduction, the strength of the slab decreases rapidly due to the introduction of weak crustal material, while the increased buoyancy causes upward directed forces. Breakoff is found to occur within the continental slab, near the transition from oceanic to continental lithosphere, since this is the hottest, hence weakest part of the continental lithospheric slab (Van de Zedde and Wortel, 2000). Once the slab breaks off and sinks into the mantle, hot asthenospheric material replaces the sinking slab.

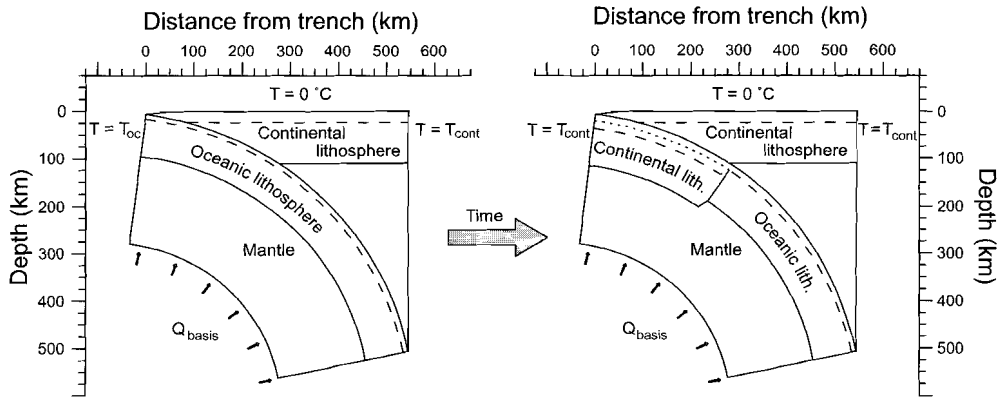

Figure 6.4: Model setup of the slab detachment model indicating the boundary conditions, modified after Van de Zedde and Wortel (2000). The slab can consist of oceanic or continental lithosphere. Boundary conditions are as follows: the temperature is 0 °C at the surface; to the left of the model a stable oceanic (T_{oc}) or continental (T_{cont}) geotherm is assumed; on the right end a continental geotherm is applied; the heat flux (Q_{basis}) at the lower boundary is constant; and heat transfer at the deep end of the slab occurs only conductively parallel to the model boundary.

We focus on the thermal implications of slab detachment on rocks in the overriding plate. The temperature change due to slab detachment (ΔT) mainly depends on the temperature of the overriding plate prior to breakoff, because in the model the temperature of the inflowing asthenospheric mantle is roughly equal to the potential mantle temperature at the base of the lithosphere (1325 °C). The temperature evolution for monitoring points in the overriding plate depends largely on their distance from the plate contact (fig 6.5). Points located at a close distance (5 km) from the plate contact experience a larger and faster temperature increase than points at larger distances. Breakoff in the model is assumed to occur instantaneously along a plane (hence a line in 2D) perpendicular to the plate contact. The dense slab sinks into the mantle, allowing instantaneous introduction of asthenospheric material along the plate contact. More realistic representations of the breakoff process, including stretching or necking of the slab, would imply a slower influx of hot material (see Van de Zedde and Wortel, 2000). The calculated temperature increases shown in figure 6.5 are maximum estimates for localised, instantaneous rupture. Our results indicate, that in case of shallow slab detachment the resulting temperature increase (ΔT) in the overriding lithosphere can be as large as 400 °C in a few million years.

Several parameters affect the thermal evolution of the rocks in the overriding plate (table 6.1) and their effect can be summarised as follows:

- The strength of the subducting slab mainly depends on its rheology and hence, for the ductile part, on temperature. A cold and strong continental lithosphere will yield later and at greater depth, leading to a smaller rise of the temperature in the overriding plate.
- A low convergence rate will cause less advective cooling of the overriding plate. Moreover, breakoff occurs later because the slab moves more slowly, and at a shallower

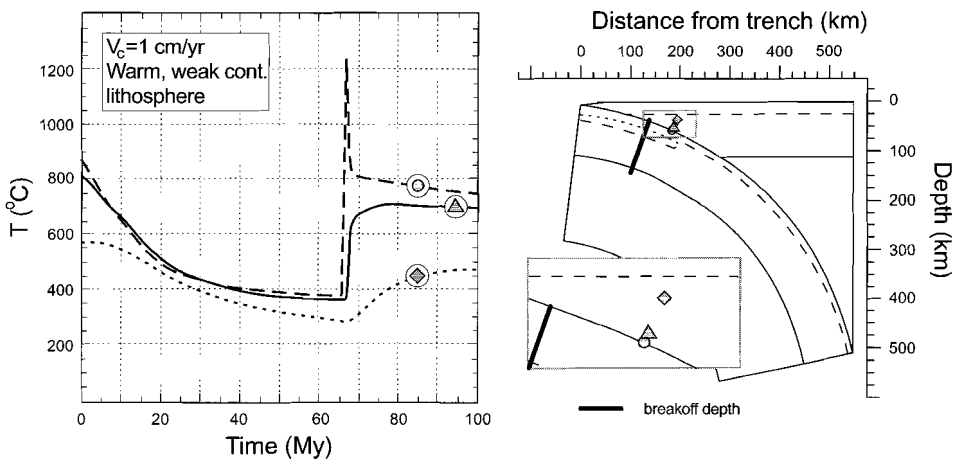

Figure 6.5: Temperature variations as a function of time for markers at different positions in the overriding slab, as a result of slab detachment. The three points are located at 0, 5 and 25 kilometres from the plate contact respectively. The model run starts with 50 million years of oceanic lithosphere subduction, followed by continental lithosphere subduction. Slab breakoff occurs after 16 My of continental subduction, at a depth of about 40 km.

Parameter increased	Breakoff depth	Temperature increase
Slab strength	deeper	smaller
Temperature subducting slab	shallower	larger
Convergence rate	deeper	larger
Age subducting oceanic lithosphere	slightly shallower	larger
Radiogenic heat production overriding plate		smaller
Distance of marker from plate contact		smaller

Table 6.1: The influence of increasing model parameters on the depth of slab detachment, and on the temperature increases after slab detachment. The parameters are listed in order of importance. The distance of marker points from the plate contact is not an input parameter, but does affect the observed temperature increase.

depth than in the case of fast convergence. Due to the higher temperature of the overriding plate before breakoff, ΔT after breakoff is lower.
- The age of the subducting oceanic lithosphere affects its temperature and thereby the strength of the transition from oceanic to continental lithosphere. In the case of young oceanic lithosphere the transition is weak, and breakoff will occur closer to it. This means that if the slab detaches, it detaches at greater depth.
- If the time span of oceanic lithosphere subduction before the onset of continental lithosphere subduction is short, or in case oceanic lithosphere subduction is very slow, a steady-state thermal field may not be achieved. Because of the higher temperatures of the overriding plate before breakoff, ΔT after breakoff will be smaller.

We emphasise that our model is dynamic, to the extent that the depth of breakoff is not an independent and prescribed parameter but is principally controlled by the thermal state, the stress distribution, and the rheology of the continental part of the subducting slab. The depth of breakoff is crucial regarding the thermal evolution of the overriding plate. Summarising our model results, the minimum depth of breakoff is 35 kilometres, and breakoff occurs 2 to 24 million years after the onset of continental lithosphere subduction. Faster convergence, stronger rheology and lower temperatures of the continental part of the slab all shift breakoff to greater depths, in turn reducing its thermal effect on the overriding plate. The thermal effects of breakoff on the overriding plate become negligible if breakoff occurs at a depth deeper than the thickness of the overriding plate (Van de Zedde and Wortel, 2000).

As suggested by Von Blanckenburg and Davies (1995) for the case of the central Alps, it seems possible that slab detachment induces partial melting of rocks in the overriding plate. Our thermomechanical model results also indicate the possibility of local partial melting in the mantle lithosphere, and that asthenospheric melting only occurs in the case of slab breakoff at less than 50 kilometres depth (Van de Zedde and Wortel, 2000). We note, however, that fluids ascending from the subducting oceanic slab may shift the solidus to lower temperatures, and thus enhance partial melting.

6.4.2 Tectonically Accreted Radiogenic Material (TARM)

Jamieson et al. (1998) have applied a coupled thermal-mechanical model of a collisional orogen to investigate the role of radiogenic heating by wedges of tectonically accreted

radiogenic material (TARM) as a cause of Barrovian high-temperature, medium-pressure metamorphism. Crustal and mantle TARM (Jamieson et al., 1998) refer to the depths at which the accreted crustal material resides (fig 6.3).

The model elaborates on mechanical models of collisional orogens, in which the lithospheric mantle subducts while the crust of the downgoing plate is taken up in the orogen and eventually exhumed due to the coupled effects of tectonic transport and erosion (e.g. Beaumont et al., 1994; Willet et al., 1993). The study by Jamieson et al. (1998) involves calculation of the temperature field for each step of progressive deformation in these mechanical models. The incorporation of crustal or mantle TARM in the model causes additional heat production compared to average values expected for a standard distribution of radiogenic material in the crust and upper mantle.

The model results of Jamieson et al. (1998) reveal that there are only two cases in which the presence of a mantle TARM would have a significant effect on the thermal history of rocks that eventually become exhumed: (1) if convergence ceases after about 30 My, such that advective cooling in the subduction zone is effectively stopped, or (2) if erosion rates increase after about 30 My, such that material just above the mantle TARM is exhumed too rapidly to allow conductive cooling during exhumation. The presence of a crustal TARM is more effective in heating material that is eventually exhumed, because when the TARM wedge resides at crustal depths, material from the wedge itself is subject to exhumation. An additional effect is that a crustal TARM is a transient heat source, because it is only active until it is exhumed and eroded (Jamieson et al., 1998). It is important to note that only crustal material can become exhumed in these models. High-pressure metamorphic rocks of mantle origin or derived from crustal material subducted underneath the overriding lithospheric mantle at depths in excess of 50 km will not return to the Earth's surface. Hence, rocks undergoing Barrovian metamorphism in these models have not experienced pressures in excess of 12 kbar during their previous history, nor do they show any cooling during initial decompression followed by a temperature increase.

In order to compare the results of Jamieson et al.'s (1998) TARM model with those of the slab detachment model, we incorporated a wedge of highly radiogenic material in the lithospheric wedge overlying the subducting lithosphere (fig 6.6). The TARM in our model is instantaneously emplaced at the start of the model run, which overestimates the effectiveness of the TARM because accumulation of a TARM wedge in nature would take tens of millions of years. The volume and productivity of the TARM wedge in our model equals that of the combined crustal and mantle TARM of Jamieson et al. (1998). Our model differs from the original TARM model, in that the overriding plate is not deformed, so the material in the crustal TARM wedge is not lost from the system by progressive erosion. This again overestimates the temperature increase due to the presence of a TARM wedge.

The thermal evolution of a volume of rock 5 kilometres above the plate contact shows that temperatures in the overriding plate are higher in the presence of a TARM (fig 6.6). There is, however, no evidence for a fast temperature increase at any monitoring point in the model. In addition, for low convergence rates (1 cm/yr) the advective cooling at the plate contact outweighs the additional heat produced in the TARM wedge. Only in case subduction is assumed to cease, the in situ temperature increase 30

million years after cessation of convergence amounts to about 100 °C. Note that the temperature continues to rise, because, unlike the model of Jamieson et al. (1998), the crustal material in the TARM is not removed by erosion.

6.4.3 Comparison of model results for the two hypotheses

A comparison between the slab detachment and TARM model reveals interesting differences and similarities between the thermal evolutions of the overriding lithosphere (fig 6.7). In both models the isotherms rise during the model run, either due to slab detachment or after the cessation of convergence, so material points within the overriding plate may experience a temperature increase. There are, however, important differences between the models. For slab detachment to occur, a zone of weakness must exist in the subducting lithosphere. The model results from Wong a Ton and Wortel (1997) indicate the transition from oceanic to continental lithosphere as a likely candidate. Breakoff may lead to a temperature increase of up to 400 °C in a few million years. In contrast, any thermal effect of a TARM wedge is entirely independent of the nature and rheology of the downgoing plate. In order for the TARM model to achieve a significant in situ temperature increase convergence must cease. The in situ temperature increase is much slower in the TARM model, i.e. tens of millions of years after subduction ceases, than in the case of slab detachment which leads to an almost instantaneous thermal response (fig 6.7, also compare figs. 6.5 and 6.6).

If we suppose a slice of crustal material moves up along the plate contact, the bulge of

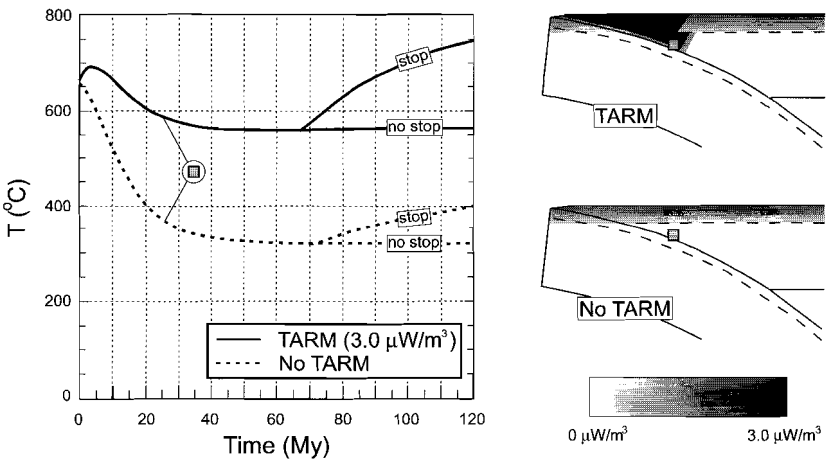

Figure 6.6: TARM incorporated in the overriding plate of the slab detachment model. The left panel shows the temperature increase with and without TARM of a marker located 5 km above the plate contact. The TARM wedge, with an assumed radiogenic heat production of 3 μW/m³, is present at the start of the model run, and subduction continues at a rate of 1 cm/yr. The model run starts with 50 My of oceanic lithosphere subduction, which is followed by continental lithosphere subduction. Subduction either continues, or is stopped after 66 My. If subduction is stopped the temperature in the overriding plate increases considerably. See text for discussion.

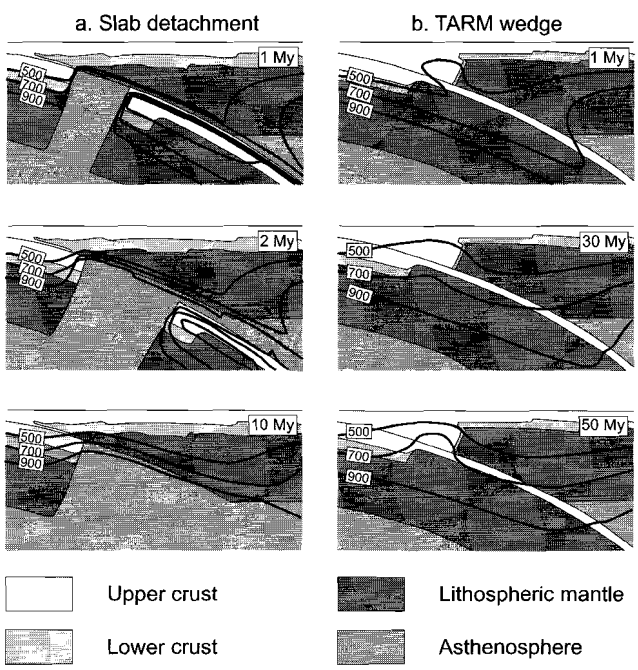

Figure 6.7: Comparison between the evolutions of the thermal field due to slab detachment, with that due to the presence of a TARM wedge. Isotherms at 500, 700, and 900 °C. **a.** Slab detachment occurs after 50 million years of oceanic lithosphere subduction and 16 My of continental lithosphere subduction. Isotherms at 1, 2 and 10 million years after slab detachment. **b.** After 50 million years of oceanic lithosphere subduction and 13 My of continental lithosphere subduction convergence is halted. Isotherms at 1, 30 and 50 million years after the cessation of subduction.

the 500 °C isotherm indicates that initial cooling of the slice could be followed by a stage of re-heating (fig 6.7b, top panel). Note, however, that this bulge only exists because the TARM wedge was present from the start of the model run, and had tens of millions of years to heat up the lower part of the wedge.

The TARM model of Jamieson et al. (1998) is different from ours, in that the rocks constituting a crustal TARM are exhumed in their model. Their preferential exhumation due to weakening induces cooling after peak temperature metamorphism. The temperatures within our TARM model are gross overestimates because the TARM is assumed to exist from the start of oceanic lithosphere subduction onward, which is unlikely to occur in nature. It follows that the temperature increase due to slab detachment is fast but transient, because the additional heat is lost at the Earth's surface by conduction, while the high temperatures due to TARM are persistent in our model because the overriding plate does not deform, precluding removal of the crustal TARM wedge.

The thermal effect of the TARM wedge and that of slab detachment affect similar length scales in the cross section modelled. For cross-sections elsewhere in the orogen, however, their thermal effect may in reality be different. Depending on the geometry of plate convergence, a TARM wedge could extend over long distances along the strike of an orogen, whereas slab breakoff is likely to occur along relatively short sections between major inherited discontinuities such as transform faults (cf. Mason et al., 1998), which limits its thermal effect along the strike of the orogen. However, lateral migration of the detachment process along the orogen may induce an along-strike migration of all breakoff-related effects, including heating, magmatism,

and migration of foreland depocentres (Buiter et al., 1998; Van der Meulen et al., 2000; Wortel and Spakman, 1992).

6.5 Comparison of model results with observations: a test of the hypotheses

Our model results outlined above show that both slab detachment and a TARM wedge may provide enough heat to explain the heating documented in the central Alps as the Lepontine metamorphism. Below, we confront these model results and the inherent controlling parameters with the results of our detailed field-based studies in the central, western and Ligurian Alps, with emphasis on the geodynamic setting of each of the areas and the PTt trajectories inferred for the metamorphic rocks in question. We first summarise the geological data and then proceed to compare the model results with these data.

6.5.1 Geodynamic setting and PTt trajectories of selected areas

Lepontine gneisses surrounding Alpe Arami, central Alps

We have studied the Lepontine gneisses near Alpe Arami in an area situated in the central Alps of southern Switzerland, about ten kilometres north of the main boundary between the European and Adriatic realm, the Insubric Line (A in fig 6.1). The gneisses surrounding the Alpe Arami garnet peridotite body are commonly believed to have been derived from the southern margin of the Eurasian continent (e.g. Pfiffner, 1999; Schmid et al., 1996; Stampfli et al., 1998). Orogenic studies by other workers indicate that subduction of the Piemonte-Ligurian ocean underneath Adria started between 110 and 71 Ma (Froitzheim et al., 1996) and lasted until 65 Ma. The total convergence between Adria and Europe in that time span is estimated at some 300 kilometres (Froitzheim et al., 1996; Schmid et al., 1996). This was followed by subduction of the Briançonnais micro-continent between 65 and 56 Ma and subduction of the Valais oceanic basin between 56 and 50 Ma (Schmid et al., 1996). The European continental margin subducted underneath the northern margin of Adria from about 50 Ma onward, while convergence between Adria and Europe proceeded at an estimated rate of 1.0 to 1.5 cm/yr (Dewey et al., 1989; Schmid et al., 1996; Schmid et al., 1997).

Our study of the Lepontine gneisses near Alpe Arami (Chapter 3) indicates that these rocks underwent high-pressure metamorphism at about 900 °C and 21 kbar (fig 6.8), equivalent to a burial depth of over 70 kilometres. The age of the high-pressure metamorphism has been estimated to be around 40-37 Ma (Becker, 1993; Gebauer, 1996). The rocks cooled to about 630 °C during fast initial exhumation (rates of over 7 mm/yr) and were then re-heated by about 110 °C to peak temperatures up to 740 °C at about 5 kbar, equivalent to some 17 kilometres depth. The age of this re-heating is inferred to be 32.5 Ma (Gebauer, 1996). In summary, the data indicate that continental

collision at or shortly after 50 Ma was followed by a stage of reheating before 32 Ma ago, in which rocks that had undergone high-pressure metamorphism around 40-37 Ma were reheated by about 110 °C at a depth of about 17 kilometres (fig 6.8). After reheating the rocks were exhumed at much more gentle rates of the order of 0.8 mm/yr. Convergence between Adria and Europe continued after continental collision. Lithospheric thickening may have accommodated part of this convergence, but high-pressure metamorphism of continental material indicates that continental lithosphere subduction proceeded to considerable depths. Notably, an episode of magmatism occurred along the Insubric Line in the central and eastern Alps between 42 and 25 million years ago, and some of the magmas have geochemical signatures indicating interaction with mantle-derived melts (Von Blanckenburg et al., 1998).

Gran Paradiso basement, western Alps

Three ten-kilometre scale basement massifs form the core of the Penninic Zone of the western Alps: the Monte Rosa, Gran Paradiso and Dora Maira massifs (fig 6.1). These massifs, also referred to as the Internal Penninic Nappes of the western Alps, are made up of metasediments and orthogneisses that are generally believed to represent basement fragments of the Briançonnais ribbon continent, located paleogeographically in between the Piemonte-Ligurian and Valais oceanic basins (e.g. Schmid and Kissling, 2000; Stampfli, 1993). On the basis of poorly dated sedimentary deposits and selected radiometric age determinations, it has been suggested that the Gran Paradiso massif originates from the north-western margin of Adria (Stampfli et al., 1998). An Adriatic history,

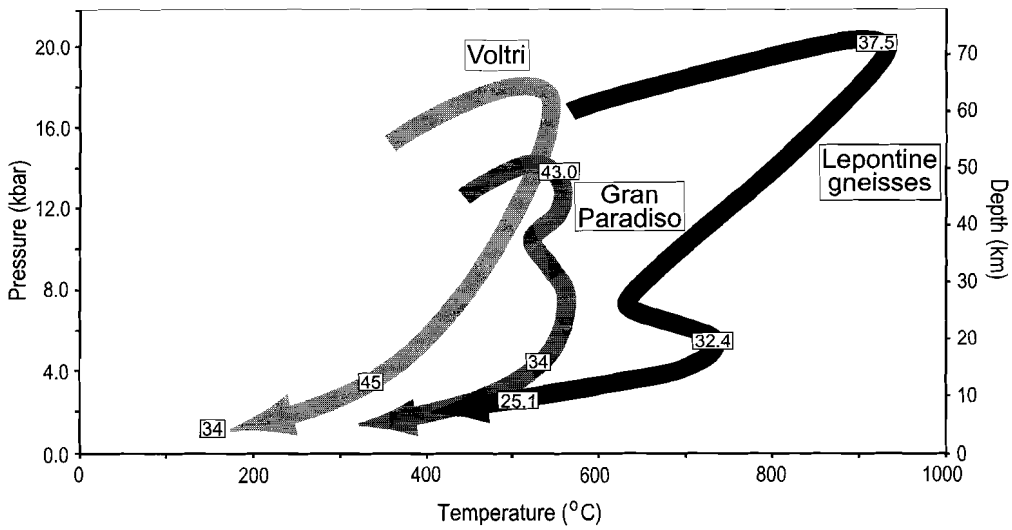

Figure 6.8: PTt paths of the three study areas. Values along paths denote age determinations in Ma, depth assuming lithostatic pressure and a density of $2.8 \cdot 10^3$ kg/m^3. For details see Chapters 3-5.

however, does not fit recent age determinations of high-pressure metamorphism in Gran Paradiso (Meffan-Main, pers. comm.), Dora Maira (Gebauer et al., 1993; Tilton et al., 1989) and Monte Rosa (Rubatto and Gebauer, 1999). We therefore consider a Briançonnais origin of the Internal Penninic Nappes more likely.
The Briançonnais ribbon continent was subducted underneath Adria from about 65 Ma at a rate of about 1 cm/yr (Schmid and Kissling, 2000). Our study in the Gran Paradiso massif (Chapter 4) indicates that these rocks underwent high-pressure metamorphism at about 525 °C and 14 kbar (fig 6.8), equivalent to a depth of about 50 kilometres. The age of this high-pressure metamorphism is inferred to be 43 Ma (Meffan-Main, pers. comm.). The rocks cooled during fast initial exhumation (rates of about 3.3 mm/yr). They were subsequently re-heated by about 50 °C to peak temperatures around 550 °C at a pressure of 6 kbar, equivalent to a depth of some 22 kilometres. This re-heating occurred before 34 Ma (Freeman et al., 1997), but its exact age has not been determined. The Gran Paradiso basement massif was then exhumed at slow rates of around 0.6 mm/yr.

Metagabbros from the Voltri mélange, Ligurian Alps
The Voltri massif is located at the transition from the Ligurian Alps to the Ligurian Apennines (fig 6.1). In this massif we have studied metagabbro blocks, derived from the Beigua serpentinite unit, which occur in a thrust-related tectonic mélange developed at the base of this unit (Chapter 5). The metagabbros of the Beigua unit were formed during rifting of the Piemonte-Ligurian ocean, about 150 million years ago (Borsi et al., 1996). The rocks underwent intra-oceanic subduction (Hoogerduijn Strating, 1991) and high-pressure metamorphism, around 525 °C and 18 kbar (fig 6.8), which is equivalent to a depth of about 65 kilometres. There are as yet no age data from the high-pressure mineral assemblages. White mica cooling ages from the Beigua metagabbros indicate that cooling below about 350 °C occurred by 45 Ma (Hoogerduijn Strating, pers. comm.). The metagabbros studied show no evidence of any heating during exhumation, nor is there any evidence for such heating recorded by other tectonic units in the massif (e.g. Hoogerduijn Strating, 1991). By early Oligocene times (34 Ma) the Voltri massif had returned to the surface, where its erosion products were re-deposited (Haccard and Lorenz, 1979) and where it formed a basement covered by continental scree breccias (Capponi et al., 1999; D'Atri et al., 1997).
As the metagabbros in the Voltri massif show no evidence of heating during exhumation, the geological data available from the Voltri massif are not related to our quantitative analysis of orogenic heat sources.

Effects of the 3D geometry of arc development in the Alps
It is important to note that, while convergence and collision are essentially orthogonal to the strike of the central Alps (e.g Schmid et al., 1996), the western and Ligurian Alps show significant rotation, oblique convergence and out-of section movements (e.g. Schmid and Kissling, 2000; Thomas et al., 1999). During the early stages of collision of Adria with the European plate (50-35 Ma), the NNE-SSW segment of the plate margin served as a zone

of sinistral transpression (e.g. Schmid and Kissling, 2000; Stampfli and Marchant, 1997), to accommodate the northward movement of Adria. From 35 Ma onwards, the movement of Adria with respect to the European plate is inferred to have shifted to a north-westerly direction, leading to another 100 kilometres of shortening along the WNW-ESE oriented ECORS-CROP seismic section running across the Gran Paradiso massif (Schmid and Kissling, 2000). Our 2D models obviously ignore these effects, rendering them appropriate to the geometry of convergence and collision in the central Alps, and less adequate for the case of the Gran Paradiso massif in the western Alps.

6.5.2 Comparison of model results with observations

The results of our numerical models outlined above show that both slab detachment and the development of a TARM wedge can potentially provide the heat required to explain orogenic heating during exhumation, and that the thermal effects of both processes affect similar length scales in 2D. It follows that neither the observed magnitudes of the rise in metamorphic temperature nor the length scale of the medium-pressure, high-temperature metamorphism can as such be used to discriminate between the two processes, although we recall that the temperatures of our TARM model are overestimates. However, the time scales involved, as well as the kinematics of convergence are crucial. Provided that subduction proceeded for a substantial period of time to allow for accretion of a TARM wedge, the TARM model is capable of causing an in situ temperature increase of about 100 °C, 30 My after cessation of subduction (fig 6.7b). In contrast, temperatures in the case of slab detachment increase at geologically high rates (fig 6.7a), which depend on the breakoff mode (i.e. instantaneous rupture of the slab versus localised stretching), with heating being almost instantaneous in the case of rupture. The temperature increase can amount to 400 °C within a few million years. As opposed to the TARM model, convergence may continue, leading to renewed conductive cooling.

TARM in the central and western Alps?

Both the time scale involved in heating and the cessation of convergence, needed in the TARM model to achieve a substantial thermal signal, are in conflict with the geological data from the Penninic zone of the Alps. As outlined above, continental subduction started at or after 50 Ma, while the re-heating culminated at 32.5 Ma in the central Alps. This yields a maximum time span of 17.5 million years between the onset on of continental collision and the observed re-heating, while the 40-37 Ma age of high-pressure metamorphism indicates that subduction of continental lithosphere continued during at least part of this period. On the other hand, all data indicate that there was a considerable period, estimated to have lasted at least 40 but possibly 70 My, of oceanic and continental lithosphere subduction prior to collision. It is therefore quite possible that radiogenic material accumulated in a wedge at the subduction zone trench, although its contribution to heating of material in the wedge can only have been minor because of continuous advective cooling.

Similarly, age and kinematic data for the Gran Paradiso massif point to high-pressure metamorphism at 43 Ma, followed by decompression, cooling and re-heating presumably

before 34 Ma. As cooling and re-heating take place during decompression (fig 6.8) a TARM scenario could be envisaged, in which the Gran Paradiso basement was transported through inverted isotherms (compare fig 6.7b, top panel). However, even if the amount of subducted lithosphere prior to continental collision had allowed for the accretion of a TARM wedge, which for the case of the western Alps is difficult to assess, the time available for cooling followed by re-heating due to the presence of a TARM wedge is insufficient. In addition, the high-pressure metamorphism of continental rocks indicates that a substantial part of convergence after continental collision was taken up by subduction of continental lithosphere, accommodating north-directed convergence, followed from about 35 Ma on by another 100 km of NW-SE directed shortening (Schmid and Kissling, 2000). There is no evidence for the cessation of convergence tens of My before the temperature peak.

In both cases, the time span available for cooling followed by appreciable re-heating clearly precludes a TARM wedge as the principal cause of the Lepontine metamorphism. In addition, continued convergence impedes this mechanism to be effective. This conclusion concurs with the notion that some process in the upper mantle is needed to explain the distinct upper mantle signature documented in the magmatic rocks spatially associated with the Lepontine metamorphism. This upper mantle signature can by no means be accounted for in a TARM scenario.

Slab detachment in the central and western Alps?

In contrast with the TARM model, detachment or breakoff of a subducting slab as proposed previously by Von Blanckenburg and Davies (1995) to explain Tertiary magmatism along the Periadriatic lineament and the mantle signature of some of the pertinent plutons and dike swarms, does seem to be a viable hypothesis to explain the Lepontine metamorphism. For the case of the central Alps, estimated rates and duration of oceanic subduction, accommodating at least 300 km of convergence in a time span of 40-70 My Our model reaches a steady-state temperature and strength distribution in the downgoing slab for these values of the pertinent parameters. More importantly, re-heating is acquired in the model within a few million years, i.e. in a time span smaller than the time available between high-pressure metamorphism and the culmination of re-heating, based on the geochronological data summarised above. The temperature increase recorded by the rocks is substantially less than our maximum model estimates, which could for instance be due to the location of the studied rocks in the wedge at the time of slab detachment, i.e. their distance from the plate contact, but also to a gradual rupture by necking of the slab rather than instantaneous breakoff. For a convergence rate of 1 cm/yr, the model shows slab breakoff 16 My after the onset of continental subduction, at a depth of about 40 kilometres. This value for the timing of shallow slab detachment coincides very nicely with the inferred time span between continental collision (at 50 Ma) and the peak of re-heating (32.5 Ma) in the central Alps.

Like in the central Alps near Alpe Arami, slab detachment seems a viable hypothesis to explain the heating during exhumation documented in the Gran Paradiso massif, as the time scales involved in the PT evolution of these rocks are essentially similar for the two

areas. The rate, duration and direction of subduction in the western Alps are very poorly constrained, however, such that inferences about the occurrence of slab detachment are not trivial. In view of the existing evidence for transpressional deformation (Schmid and Kissling, 2000) and block rotations (e.g. Thomas et al., 1999) in the western Alps it seems likely that, at the time of slab breakoff and re-heating, rocks at present exposed in the western Alps were located much closer to the rocks now found in the central Alps. The rocks of the Gran Paradiso massif may thus have experienced re-heating while residing in a geographical position closer to the rocks of the Lepontine gneiss dome, in response to slab breakoff in that segment of the Alps. The relatively low magnitude of reheating (50 °C) may again reflect position of the pertinent rocks in the system, not only with respect to distance above the plate contact, but also in 3D, i.e. with respect to the precise geographical location of the detaching slab. It follows that re-heating in the rocks of the Gran Paradiso may be due to slab detachment, albeit that the detachment process did not necessarily occur underneath the present-day western Alps.
If slab detachment indeed caused the observed post-collisional heating of the Gran Paradiso rocks, we would expect a similar evolution for the presumably equivalent Monte Rosa unit to the north, and the Dora Maira unit to the south of Gran Paradiso. Additionally, it would be expected that the temperature increase would decrease southwards. Borghi et al. (1996) reported the occurrence of postcollisional re-heating in all three Internal Penninic Nappes: the Monte Rosa massif (to 465 °C), the Gran Paradiso massif (to 494 °C), and the northern part of the Dora Maira massif (to 482 °C). The reported occurrence of staurolite in the Monte Rosa massif (Bocquet et al., 1978; Reinhardt, 1966) suggests that peak temperatures may in fact have been higher than those reported by Borghi et al. (1996). These reports support our inferences of the regional implications of the occurrence of slab detachment. However, it should be noted that the differences between the estimated peak temperatures are very small and the amount of heating for each area poorly constrained, precluding discussion in terms of heating and temperature gradients along the arc of the Alps.

6.6 Exhumation of high-pressure rocks in the Alps

Exhumation rates
Our model study, focussed at the late-stage thermal evolution of collisional orogens, does not specifically address processes involved in the actual exhumation of the pertinent rocks to the Earth's surface. The rocks in our study areas have undergone high-pressure metamorphism at depths of at least 50 to 70 kilometres, and subsequently returned to the surface at geologically high rates (over 7 mm/yr for the Lepontine gneisses near Alpe Arami), while convergence between Africa and Europe continued. On their way up the Lepontine gneisses, as well as the rocks from Gran Paradiso, were re-heated at much shallower depths ranging between 20 and 30 km, after which further exhumation continued at slower rates (up to 0.8 mm/yr). Our model study shows that breakoff of the subducting slab provides a viable explanation for this sudden re-heating. There is no

evidence for such re-heating in the rocks of the Voltri massif, while lack of geochronological data precludes assessment of the exhumation rates of the Voltri rocks.

Exhumation mechanisms

The exhumation of high to very high-pressure rocks carrying evidence for metamorphism at mantle depths remains problematic. It is clear that erosion alone cannot account for the exhumation of rocks from tens of kilometres depth (e.g. Platt, 1993). It has been suggested that buoyancy may drive the exhumation of subducted crustal rocks returning through the subduction channel (e.g. Chemenda et al., 2000; Chemenda et al., 1996; Van den Beukel, 1990). In these models, large slices of coherent crustal material decouple from the mantle lithosphere at great depth, followed by exhumation of the upper part of such slices, driven by the buoyancy of a root of crustal material. The rocks exhumed by this mechanism have not necessarily reached upper mantle depths, and exhumation largely depends on the alleged coherence of the crustal slices involved. Relatively small slices of crustal material would lack such a crustal root protruding into the mantle, and these smaller fragments could only rise to the base of the crust, after which density differences can no longer drive their exhumation. However, it seems unlikely that rocks, subducted to depths of 65 kilometres like the Lepontine gneisses, or to more than 100 kilometres like some of the rocks in the Dora Maira massif (Chopin, 1984) and the Zermatt-Saas unit (Reinecke, 1991) in the western Alps, were pushed back up the subduction zone by the buoyancy of large slices of continental material, because geochronological data indicate that these rocks underwent their high-pressure metamorphism shortly after the onset of continental lithosphere subduction.

While the exhumation of very high-pressure metamorphic rocks from mantle depths remains somewhat enigmatic, several hypotheses exist to explain the exhumation of deeply buried rocks from the base of the deformed crust. All of these hypotheses involve some way of tectonic thinning of the overburden, possibly coupled with erosion. Exhumation from the base of the crust upward has been explained in terms of extensional collapse (Dewey, 1988; Platt and Vissers, 1989). The removal of the thickened lithospheric root, causing advection of hot asthenospheric material at the base of the orogen, causes rebound of the thickened crust, which is no longer in isostatic equilibrium because the dense root has been removed. The thickened crust has an excess potential energy and spreads laterally by extensional faulting, facilitating the exhumation of rocks in the lower crust (Platt and Vissers, 1989). As mentioned before, the large amounts of convergence between Africa and Europe and the lack of widespread evidence for pervasive extension in the Alps are difficult to reconcile with large-scale extensional collapse. In addition, the Tertiary magmatism in the Alps is strongly concentrated along the Periadriatic (Insubric) Lineament (fig 6.1) rather than being distributed over a wider area as expected for the case of extensional collapse.

Exhumation of crustal rocks from the base of the crust to the surface can also be explained in terms of corner flow in the orogenic wedge overlying the subduction

zone (cf. Platt, 1986). In this scenario underplating of material at the base of the wedge drives a material flow within the wedge. The overriding continent acts as a back-stop, causing the flow in the wedge to become upward directed near the contact with the overriding plate. Underplating and upward flow are accommodated by extensional faulting in the upper part of the wedge, such that combined upward flow and extensional faulting facilitate the exhumation of deep-seated rocks. The geometry involved in this scenario is very similar to the geometries of the thermokinematic models of Okaya et al. (1996) and Bousquet et al. (1997) outlined above. These models, however, fail to describe the entire metamorphic history of the studied rocks, as they do not incorporate Eoalpine high-pressure metamorphism, while they require a substantial time of thermally steady-state continental lithosphere subduction in order to explain Lepontine high-temperature, medium-pressure metamorphism. Likewise, the TARM model of Jamieson et al. (1998) strongly resembles the corner flow model of Platt (1986), but in order to achieve sufficient re-heating due to the presence of a TARM wedge, subduction needs to cease, which removes the driving force for corner flow in the orogenic wedge. Underplating at the base of the wedge would come to a halt and exhumation within the wedge would stop.

As matters stand, the PTt trajectories reconstructed for our rocks from the Lepontine gneisses near Alpe Arami and the Gran Paradiso massif, as well as those documented from other locations in the Penninic Zone indicate that at least some of these rocks were metamorphosed at mantle depths. Their exhumation to crustal levels remains problematic, as their ascent along the subduction zone is poorly understood. Once exhumed to crustal levels, the kinematics and dynamics of corner flow in the orogenic wedge may account for further exhumation. Available geochronological data indicate that the thermal signal recorded in our rocks and represented in the central Alps by the Lepontine gneiss dome require a fast and transient heat source, or a high-temperature zone through which the rocks have moved. We have shown that detachment of the subducting slab is a viable hypothesis to account for this heating during exhumation, while the time scales involved preclude radiogenic heat production in the crust as the principal cause of the Lepontine metamorphism. We speculate that the heating involved in the detachment process may have enhanced corner flow and ductile thinning in the wedge, as ductile deformation is thermally activated. In this context it is noted that main phase foliations in the Lepontine area away from the Insubric Line as well as those in the Gran Paradiso are regionally subhorizontal, indicating vertical finite shortening, which contributes to the exhumation of these rocks. We conclude that buoyant rise of subducted crustal material to the base of the crust, followed by further exhumation due to corner flow and concomitant thinning within the orogenic wedge seem at present the most appropriate scenario to explain the exhumation of the high-pressure metamorphic rocks. Our modelling study outlined above indicates that detachment or breakoff of the subducting slab during continental collision is a viable hypothesis to explain the Lepontine re-heating during exhumation.

6.7 Conclusions

Pressure-temperature-time trajectories of metamorphic rocks in three study areas located in the central, western and Ligurian Alps, all show an early stage of high-pressure metamorphism. Fast initial decompression and concomitant cooling was followed, in the central and western Alps, by a stage of re-heating at shallow depths, itself followed by further exhumation at moderate rates.

Several causes have been proposed for late-stage heating in an orogenic setting. Among the different contending hypotheses, those of a wedge of tectonically accreted radiogenic material (TARM) and detachment or breakoff of the subducting slab concur optimally with the overwhelming amount of data indicating that the Alps were formed by progressive subduction and eventual collision during convergence of the Adriatic promontory and the Eurasian plate. 2D numerical models of the two hypotheses show that both mechanisms can potentially provide enough heat to cause considerable heating in the developing orogen. We find, however, that heating due to a TARM wedge requires tens of millions of years, while removal of the slab by detachment or breakoff causes an instantaneous, but transient rise of the temperature in the overriding lithosphere. In view of the time constraints following from geochronological as well as kinematic data we reject the presence of a TARM wedge as the principal cause for the Lepontine late-stage heating. Slab detachment on the other hand seems a viable hypothesis to account for the thermal evolution of the metamorphic rocks of the Penninic Zone in the central Alps, where the 2D models most readily apply because convergence and collision were essentially orthogonal to the strike of the belt in this segment of the Alps.

In the western Alps, the geodynamics are complicated due to block rotations and oblique motions. However, like in the central Alps, it is unlikely that a TARM wedge caused the temperature increase observed, because of the short time span available for cooling and subsequent heating, as well as continuing oblique subduction when the rocks were re-heated. It is not possible to determine whether the observed re-heating in the western Alps occurred in response to slab detachment in that segment of the belt. We propose that the metamorphic rocks studied in the Gran Paradiso massif may have experienced re-heating due to a slab breakoff event in the central Alps, followed by transport away from that domain due to out-of-section movements and block rotations related to large scale transpression. Our metamorphic studies on the rocks from the Voltri massif show that these rocks did not experience heating during exhumation.

The PTt trajectory reconstructed for the Lepontine gneisses near Alpe Arami is most easily explained by the buoyant rise of high-pressure metamorphic rocks to the base of the crust, where they were incorporated into the orogenic wedge. While corner flow in the orogenic wedge facilitated their exhumation, detachment of the subducting slab caused a fast and transient heat pulse leading to re-heating of the rocks during exhumation. Final exhumation is likely to have occurred in response to a combination of upward flow in the wedge and extensional faulting and erosion at the top of the orogenic wedge.

Chapter 7

Conclusions and future research

The conclusions of the study presented in this thesis are:

1. The Lepontine gneisses surrounding the Alpe Arami garnet peridotite body in the central Alps underwent high-pressure metamorphism at peak pressures of about 21 kbar, equivalent to a depth of about 70 kilometres, at temperatures of up to 900 °C. This was followed by cooling below approximately 650 °C during fast initial decompression (exhumation rates in excess of 7 mm/yr). The rocks were subsequently re-heated by 110 °C, at around 20 kilometres depth, before their final exhumation occurring at low rates of around 0.8 mm/yr. Geochronological studies by other workers suggest an age of peak pressure metamorphism around 40-37 Ma, while the high-temperature overprint is inferred to have occurred around 32.5 Ma. The structural and metamorphic history of the Lepontine gneisses leaves three possible scenarios for the juxtaposition of the Alpe Arami garnet peridotite body with its present-day country rocks: (1) the Alpe Arami peridotite body may owe its ultra- high-pressure microstructures and assemblages to a previous orogenic cycle, and have become subducted during the Alpine orogeny together with the Lepontine country rocks; (2) the peridotite may have been enclosed in the Lepontine country rocks at great depth, or (3) the peridotite and eclogites may have become juxtaposed with the country rock gneisses at intermediate depths.

2. The basement rocks of the Gran Paradiso massif in the western Alps were metamorphosed at high pressures. Peak conditions were 525 °C and 12-14 kbar, equivalent to a depth of about 50 kilometres. The age of this stage of Alpine metamorphism is estimated by other workers at 43 Ma. The rocks cooled by about 35 °C during initial exhumation, and were then re-heated to about 550 °C at a depth of around 18 kilo- metres, before 34 Ma. Again, fast initial exhumation (3.3 mm/yr) is followed by a stage of exhumation at a much slower rate (0.6 mm/yr). Admittedly, the amounts of cooling and re-heating are near or within the accepted analytical errors of thermo-barometry (± 25-50 °C and ± 0.5-2 kbar; Spear et al. (1989)), but there are strong indications that my results reflect true cooling and re-heating during exhumation.

3. Metagabbro blocks from a tectonic mélange in the ophiolitic Voltri Massif in theLigurian Alps reflect high-pressure metamorphism at 525 °C and 18 kbar, equivalent to about 55 kilometres depth. The rocks cooled continuously during decompression to temperatures below 350 °C around 45 Ma. There is no evidence whatsoever for alate re-heating stage in the metagabbros studied, nor is any evidence for such re-heating documented by other workers. The basement of the Voltri massif was exposed atthe Earth's surface by 34 Ma.

4. The present study indicates that significant heating took place during exhumation of the high-pressure metamorphic rocks that are currently exposed in the central and western Alps. The rocks from the Ligurian Alps show no evidence for heating during their exhumation. A numerical model study indicates that the re-heating documented in the central and western Alps cannot have been caused by radiogenic heating alone, even in case radiogenic material was accumulated in an accretionary wedge at the subduction zone. On the other hand, the model results indicate that the hypothesis of slab detachment or breakoff as a cause for re-heating in the central Alps is viable. The interpretation of my results is less straightforward for the case of the western Alps where the geometry of collision is complicated in 3D, such that the model results are not decisive as to whether slab breakoff was responsible for the late-stage heating observed. As a possible explanation I propose that the Gran Paradiso massif was heated by the same cause as the Lepontine gneisses, and that the massif moved away from a position close to the Lepontine domain by subsequent out-of-section deformation and concomitant rigid-body rotations during Tertiary transpression. As the rocks from the Voltri massif were exposed at the Earth's surface by the time the rocks from the other two areas became re-heated, and there is no evidence for such re-heating in the Voltri rocks.

5. The present study does not constrain the physical mechanisms involved in the exhumation of the high-pressure rocks in the central and western Alps. Inasmuch as these rocks reached sub-crustal depths, a tentative scenario involves buoyancy-driven exhumation to the base of the crust, followed by exhumation via corner flow in the orogenic wedge driven by continuous underplating at the base of the wedge (Platt, 1986). The changes in exhumation rates inferred in both the Lepontine gneisses and the Gran Paradiso basement rocks point to a combination of exhumation mechanisms, although the depth at which this change in exhumation rate occurred is not well constrained. I infer that slab detachment may have occurred in the central Alps, with implications for the PTt trajectory of the rocks presently exposed in the western Alps, as it can explain the re-heating documented in these areas. The role of this process in the exhumation of the studied high-pressure rocks, however, is unclear.

6. The study of retrograde mineral assemblages and reactions, rather than assessment of peak metamorphic conditions alone, can yield important additional information on the history of the pertinent rocks. The additional information in the PTt trajectory may provide additional constraints geodynamic scenarios.

7. This study shows the merits of combining conventional field based techniques with numerical modelling. Model results may falsify hypotheses that could not be discarded on observational grounds alone, while model-based hypotheses can be tested against field observations. The interdisciplinary approach involved may allow a better understanding of orogeny, not only in the Alps but equally in other mountain ranges.

Some recommendations for future research following from this study are:

1. More quantitative data on the absolute timing of structural and metamorphic events are needed in order to further and better constrain the mechanism(s) responsible for the exhumation and metamorphism of high-pressure metamorphic rocks in the Alps. Structural control on radiometric age data, as well as dating of minerals that are part of a metamorphic mineral assemblage for which the PT conditions are constrained, would strongly increase the return on investment in geochronological studies.

2. Constraints on the evolution of metamorphic conditions can be improved by careful analysis of retrograde mineral reactions, analysis of mineral zoning and metastable mineral relics. The use of internally consistent thermodynamic datasets like TWEEQU (Berman, 1990) and Thermocalc (Holland and Powell, 1990; Powell and Holland, 1988) may improve quantitative estimates of metamorphic conditions compared to those assessed via application of individual thermometers and barometers alone.

References

Amato, J.M., Johnson, C.M., Baumgartner, L.P., and Beard, B.L., 1999, Rapid exhumation of the Zermatt- Saas ophiolite deduced from high-precision Sm-Nd and Rb-Sr geochronology. Earth Planet. Sci. Lett., v. 171, p. 425-438.

Argand, E., 1916, Sur l'arc des Alpes Occidentales. Eclog. geol. Helv., v. 14, p. 145-191.

Avigad, D., 1996, Pre-collisional ductile extension in the internal western Alps (Sesia zone, Italy). Earth Planet. Sci. Lett., v. 137, p. 175-188.

Barnicoat, A.C., and Fry, N., 1986, High-pressure metamorphism of the Zermatt-Saas ophiolite zone, Switzerland. J. Geol. Soc. London, v. 143, p. 607-618.

Beaumont, C., Fullsack, P., and Hamilton, J., 1994, Styles of crustal deformation in compressional orogens caused by subduction of the underlying lithosphere. Tectonoph., v. 232, p. 119-132.

Becker, H., 1993, Garnet peridotite and eclogite Sm-Nd mineral ages from the Lepontine dome (Swiss Alps): New evidence for Eocene high-pressure metamorphism in the central Alps. Geology, v. 21, p. 599-602.

Berman, R.G., 1990, Mixing properties of Ca-Mg-Fe-Mn garnets. Am. Mineral., v. 75, p. 328-344.

Berman, R.G., 1991, Thermobarometry using multi-equilibrium calculations: A new technique, with petrological applications. Can. Mineral., v. 29, p. 833-855.

Berman, R.G., and Aranovich, L.Y., 1996, Optimized standard state and solution properties of minerals. I. Model calibration for olivine, orthopyroxene, cordierite, garnet, and ilmenite in the system FeO-MgO-CaO-Al_2O_3-TiO_2-SiO_2. Contrib. Mineral. Petrol., v. 126, p. 1-24.

Bigi, G., Cosentino, D., Parotto, M., Sartori, R., and Scandone, P., 1983, Structural model of Italy., C.N.R.

Biino, G., and Pognante, U., 1989, Paleozoic continental-type gabbros in the Gran Paradiso nappe (Western Alps, Italy): Early-Alpine eclogitization and geochemistry. Lithos, v. 24, p. 3-19.

Bird, P., 1979, Continental delamination and the Colorado Plateau. J. Geoph. Res., v. 84, p. 7561-7571.

Bocchio, R., 1975, Le eclogiti retrometamorfiche di Gorduno (Canton Ticino, Svizzera). Period. Mineral., v. 44, p. 245-256.

Bocchio, R., 1977, Ferropargasite alluminifera in un'eclogite di Gorduno (Svizzera). Rend. Soc. It. Geol. Min. Petrol., v. 33, p. 519-529.

Bocchio, R., Liborio, G., and Mottana, A., 1985, Petrology of the amphibolitized eclogites of Gorduno, Lepontine Alps, Switzerland. Chem. Geol., v. 50, p. 65-86.

Bocchio, R., Ungaretti, L., and Rossi, G., 1978, Crystal chemical study of eclogitic amphiboles from Alpe Arami, Lepontine Alps, Southern Switzerland. Rend. Soc. It. Geol. Min. Petrol., v. 34, p. 453-470.

Bocquet, J., Dal Piaz, G.V., Hunziker, J.C., Martinotti, G., and Pêcher, A., 1978, Paleogeographical and structural outline of the western Alps., in Zwart, H.J., Sobolev, V.S., and Nigli, E., eds., Metamorphic map of Europe, 1:2.500.000. Explanatory text. Leiden, Unesco, Paris, p. 185-208.

Bocquet, J., Delanoye, M., Hunziker, J.C., and Krummenacher, D., 1974, K-Ar and Rb-Sr dating of blue amphiboles, micas, and associated minerals from the Western Alps. Contrib. Mineral. Petrol., v. 47, p. 7-26.

Borghi, A., Compagnoni, R., and Sandrone, R., 1996, Composite P-T paths in the Internal Penninic Massifs of the western Alps: Petrological constraints to their thermomechanical evolution. Eclog. geol. Helv., v. 89, p. 345-367.

Borghi, A., and Sandrone, R., 1995, Petrological constraints on the Alpine P-T history of the Internal Pennine Nappes of the Western Alps. Supp. Boll. Mus. Reg. Sci. Nat., v. 13, p. 241-272.

Borsi, L., Schärer, U., Gaggero, L., and Crispini, L., 1996, Age, origin and geodynamic significance of plagiogranites in lherzolites and gabbros of the Piemont-Ligurian ocean basin. Earth Planet. Sci. Lett., v. 140, p. 227-241.

Bousquet, R., 1998, L'exhumation des roches métamorphiques de haute pression - basse température: de l'étude de terrain à la modelisation numérique. [Unpublished PhD-thesis]. Paris, Université de Paris XI - Orsay.

Bousquet, R., Goffé, B., Henry, P., Le Pichon, X., and Chopin, C., 1997, Kinematic, thermal and petrological model of the Central Alps: Lepontine metamorphism in the upper crust and eclogitisation in the lower crust. Tectonoph., v. 273, p. 105-127.

Bozhilov, K.N., Green, H.W.II, and Dobrzhinetskaya, L., 1999, Clinoenstatite in Alpe Arami peridotite: Additional evidence of very high pressure. Science, v. 284, p. 128-132.

Brenker, F.E., and Brey, G.P., 1997, Reconstruction of the exhumation path of the Alpe Arami garnet-peridotite body from depths exceeding 160 km. J. Metam. Geol., v. 15, p. 581-592.

Buchs, A., Chessex, R., Krummenacher, D., and Vuagnat, M., 1962, Ages "plomb total" déterminés par fluorescence X sur les zircons de quelques roches des Alpes. Schweiz. Mineral. Petrogr. Mitt., v. 42, p. 295-305.

Buiskool Toxopeus, J.M.A., 1976, Petrofabrics, microstructures and dislocation substructures of olivine in a peridotite mylonite (Alpe Arami, Switzerland). Leidse Geol. Meded., v. 51, p. 1-36.

Buiter, S.J.H., Wortel, M.J.R., and Govers, R., 1998, The role of subduction in the evolution of the Apennines foreland basin. Tectonoph., v. 296, p. 249-268.

Butler, R., Freeman, S., Cliff, B., Meffan-Main, S., Barnicoat, A., Wheeler, J., Reddy, S., and Pickles, C., 1997, Integrated structural, chemical and geochronological analysis to obtain deformation ages: implications for tectonic evolution in the western Alps. Abstr. 3rd Alpine Workshop, Biella 1997, p. 23-24.

Butler, R.W.H., and Freeman, S., 1996, Can crustal extension be distinguished from thrusting in the internal parts of mountain belts? A case history of the Entrelor shear zone, Western Alps. J. Struct. Geol., v. 18, p. 909-923.

Callegari, E., Compagnoni, R., and Dal Piaz, G.V., 1969, Relitti di strutture intrusive erciniche e scisti a sillimanite nel Massiccio del Gran Paradiso. Boll. Soc. Geol. It., v. 88, p. 59-69.

Capponi, G., Crispini, L., Cancino, E., and Cavanna, F., 1999, The Gargassino Valley Thrust: evidence of Oligocene-Early Miocene thrust tectonics in the Voltri Group (Ligurian Alps). Boll. Soc. Geol. It., v. 118, p. 479-484.

Carswell, D.A., and Harley, S.L., 1990, Mineral barometry and thermometry., in Carswell, D.A., ed., Eclogite facies rocks. Glasgow, London, Blackie & Son Ltd., p. 83-110.

Carswell, D.A., O'Brien, P.J., Wilson, R.N., and Zhai, M., 1997, Thermobarometry of phengite-bearing eclogites in the Dabie Mountains of central China. J. Metam. Geol., v. 15, p. 239-252.

Cawthorn, R.G., and Collerson, K.D., 1974, The recalculation of pyroxene end-member parameters and the estimation of ferrous and ferric iron content from electron microprobe analysis. Am. Mineral., v. 59, p. 1203-1208.

Channell, J.E.T., and Kozur, H.W., 1997, How many oceans? Meliata, Vardar, and Pindos oceans in Mesozoic Alpine paleogeography. Geology, v. 25, p. 183-186.

Chemenda, A.I., Burg, J.P., and Mattauer, M., 2000, Evolutionary model of the Himalaya-Tibet system: geopoem based on new modelling, geological and geophysical data. Earth Planet. Sci. Lett., v. 174, p. 397-409.

Chemenda, A.I., Mattauer, M., and Bokun, A.N., 1996, Continental subduction and a mechanism for exhumation of high-pressure rocks: new modeling and field data from Oman. Earth Planet. Sci. Lett., v. 143, p. 173-182.

Chessex, R., Delanoye, M., Krummenacher, D., and Vuagnat, M., 1964, Nouvelles déterminations d'âges "plomb total" sur des zircons alpins. Schweiz. Mineral. Petrogr. Mitt., v. 44, p. 43-60.

Chiesa, S., Cortesogno, L., Forcella, F., Galli, M., Messiga, B., Pasquare, G., Pedemonte, G.M., Piccardo, G., and Rossi, P.M., 1975, Assetto strutturale ed interpretazione geodinamica del Gruppo di Voltri. Boll. Soc. Geol. It., v. 94, p. 555-581.

Chopin, C., 1981, Talc-phengite: a widespread assemblage in high-grade pelitic blueschists of the Western Alps. J. Petrol., v. 22, p. 628-650.

Chopin, C., 1984, Coesite and pure pyrope in high-grade blueschists of the Western Alps: a first record and some consequences. Contrib. Mineral. Petrol., v. 86, p. 107-118.

Chopin, C., and Maluski, H., 1980, ^{40}Ar-^{39}Ar dating of high pressure metamorphic micas from the Gran Paradiso area (Western Alps): evidence against the blocking temperature concept. Contrib. Mineral. Petrol., v. 74, p. 109-122.

Compagnoni, R., Elter, G., and Lombardo, B., 1974, Eterogeneita stratigrafica del complesso degli "Gneiss Minuti" nel massiccio cristallino de Gran Paradiso. Mem. Soc. Geol. It. Suppl., v. 13, p. 227-239.

Compagnoni, R., and Lombardo, B., 1974, The Alpine age of the Gran Paradiso eclogites. Rend. Soc. It. Min. Petr., v. 30, p. 223-237.

Compagnoni, R., and Prato, R., 1969, Paramorfosi di cianite su sillimanite in scisti pregranitici de massiccio del Gran Paradiso. Boll. Soc. Geol. It., v. 88, p. 537-549.

Dal Piaz, G.V., and Lombardo, B., 1986, Early Alpine eclogite metamorphism in the Penninic Monte Rosa Gran Paradiso basement nappes of the northwestern Alps., in Evans, B.W., and

Brown, E.H., eds., Blueschists and Eclogites, Geol. Soc. Am. Mem., v. 164, p. 249-265.

Dal Vesco, E., 1953, Genesi e metamorfosi delle rocce basiche e ultrabasiche nell'ambiente mesozonale del l'orogene pennidico. Schweiz. Mineral. Petr. Mitt., v. 33, p. 173-480.

D'Atri, A., Piana, F., Tallone, S., Bodrato, G., and Roz Gastaldi, M., 1997, Tettonica Oligo-Miocena nell'Alto Monferrato (Bacino Terziario Piemontese) e nel settore nord-occidentale del Gruppo di Voltri (Asqui Terme - Cassinelle, AL). Atti Tic. Sc. Terra Serie spec., v. 5, p. 85-100.

Davies, J.H., and Von Blanckenburg, F., 1995, Slab breakoff: A model of lithosphere detachment and its test in the magmatism and deformation of collisional orogens. Earth Planet. Sci. Lett., v. 129, p. 85-102.

Deer, W.A., Howie, R.A., and Zussman, J., 1992, An introduction to rock-forming minerals. Harlow, UK, Longman Group, 696 p.

Den Tex, E., 1971, Age, origin and emplacement of some Alpidic peridotites in the light of recent petrofabric researches. Fortschr. Miner., v. 48, p. 69-74.

Dercourt, J., Ricou, L.E., and Vrielynck, B., 1993, Atlas Tethys Palaeoenvironmental maps. Paris, Gauthier-Villars, p. 307, 14 maps, 1 pl.

Desmons, J., Compagnoni, R., and Cortesogno, L., 1999, Alpine metamorphism of the Western Alps: II. High-P/T and related pre-greenschist metamorphism. Schweiz. Mineral. Petrogr. Mitt., v. 79, p. 111-134.

Dewey, J.F., 1988, Extensional collapse of orogens. Tectonics, v. 7, p. 1123-1139.

Dewey, J.F., Helman, M.L., Turco, E., Hutton, D.H.W., and Knott, S.D., 1989, Kinematics of the western Mediterranean., in Coward, M.P., Dietrich, D., and Park, R.G., eds., Alpine Tectonics, Geol. Soc. Spec. Publ., v. 45, p. 265-283.

Dobrzhinetskaya, L., Bozhilov, K.N., and Green, H.W.II, 1999, The solubility of TiO_2 in olivine: implications for the mantle wedge environment. Chem. Geol., v. 160, p. 357-370.

Dobrzhinetskaya, L., Green, H.W.II, and Wang, S., 1996, Alpe Arami: A peridotite massif from depths of more than 300 kilometers. Science, v. 271, p. 1841-1845.

Droop, G.T.R., 1987, A general equation for estimating Fe^{3+} concentrations in ferromagnesian silicates and oxides from microprobe analysis, using stoichiometric criteria. Mineral. Mag., v. 51, p. 431-435.

Droop, G.T.R., Lombardo, B., and Pognante, U., 1990, Formation and distribution of eclogite facies rocks in the Alps., in Carswell, D.A., ed., Eclogite facies rocks. Glasgow, London, Blackie & Son Ltd., p. 225-259.

Duchêne, S., Blichert-Toft, J., Luais, B., Télouk, P., Lardeaux, J.M., and Albarède, F., 1997, The Lu-Hf dating of garnets and the ages of the Alpine high-pressure metamorphism. Nature, v. 387, p. 586-589.

Engi, M., Todd, C.S., and Schmatz, D.R., 1995, Tertiary metamorphic conditions in the eastern Lepontine Alps. Schweiz. Mineral. Petrogr. Mitt., v. 75, p. 347-369.

England, P.C., and Thompson, A.B., 1984, Pressure-temperature-time paths of regional metamorphism 1. Heat transfer during evolutionof regions of thickened continental crust. J. Petrol., v. 25, p. 894-928.

Ernst, W.G., 1973, Blueschist metamorphism and P-T regimes in active subduction zones. Tectonoph., v. 17, p. 255-272.

Ernst, W.G., 1977, Mineralogic study of eclogitic rocks from Alpe Arami, Lepontine Alps, southern Switzerland. J. Petrol., v. 18, p. 371-398.

Ernst, W.G., 1979, Coexisting sodic and calcic amphiboles from high-pressure metamorphic belts and the stability of barroisitic amphibole. Mineral. Mag., v. 43, p. 269-278.

Ernst, W.G., 1981, Petrogenesis of eclogites and peridotites from the Western and Ligurian Alps. Am. Mineral., v. 66, p. 443-472.

Ernst, W.G., and Piccardo, G.B., 1979, Petrogenesis of some Ligurian peridotites - I. Mineral and bulk-rock chemistry. Geoch. Cosmoch. Acta, v. 43, p. 219-237.

Escher von der Linth, A., 1841, Geologische Karte des Cantons Glarus und seiner Umgebungen. Verh. Schw. Naturf. Ges., v. 26, p. 54-62.

Essene, E.J., 1989, The current status of thermobarometry in metamorphic rocks., in Daly, J.S., Cliff, R.A., and Yardley, B.W.D., eds., Evolution of metamorphic belts, Geol. Soc. Spec. Publ., v. 43, p. 1-44.

Ferry, J.M., and Spear, F.S., 1978, Experimental calibration of the partitioning of Fe and Mg between biotite and garnet. Contrib. Mineral. Petrol., v. 66, p. 113-117.

Fischer, H., 1974, Geologischer Atlas der Schweiz, sheet 1313, Bellinzona. Bern, Schweizerischen Geologischen Kommission.

Florineth, D., and Froitzheim, N., 1994, Transition

from continental to oceanic basement in the Tasna nappe (Engadine window, Graubünden, Switzerland): evidence for Early Cretaceous opening of the Valais ocean. Schweiz. Mineral. Petrogr. Mitt., v. 74, p. 437-448.

Freeman, S.R., Inger, S., Butler, R.W.H., and Cliff, R.A., 1997, Dating deformation using Rb-Sr in white mica: Greenschist facies deformation ages from the Entrelor shear zone, Italian Alps. Tectonics, v. 16, p. 57-76.

Frey, M., Bucher, K., Frank, E., and Mullis, J., 1980, Alpine metamorphism along the Geotraverse Basel- Chiasso - a review. Eclog. geol. Helv., v. 73, p. 527546.

Frey, M., and Ferreiro Mählmann, R., 1999, Alpine metamorphism in the Central Alps. Schweiz. Mineral. Petrogr. Mitt., v. 79, p. 135-154.

Frisch, W., 1981, Plate motions in the Alpine region and their correlation to the opening of the Atlantic ocean. Geol. Rundsch., v. 70, p. 402-411.

Froitzheim, N., Schmid, S.M., and Frey, M., 1996, Mesozoic paleogeography and the timing of eclogite- facies metamorphism in the Alps: A working hypothesis. Eclog. geol. Helv., v. 89, p. 81-110.

Gebauer, D., 1996, A P-T-t path for an (Ultra?-) High-Pressure ultramafic/mafic rock-association and its felsic country-rocks based on SHRIMP-dating of magmatic and metamorphic zircon domains. Example: Alpe Arami (Central Swiss Alps)., in Basu, A., and Hart, S., eds., Earth processes: Reading the isotopic code, Geophysical Monograph, v. 95. Washington, American Geophysical Union, p. 307-330.

Gebauer, D., 1999, Alpine geochronology of the Central and Western Alps: new constraints for a complex geodynamic. Schweiz. Mineral. Petrogr. Mitt., v. 79, p. 191-208.

Gebauer, D., Schertl, H.-P., Brix, M., and Schreyer, W., 1997, 35 Ma old ultrahigh-pressure metamorphism and evidence for very rapid exhumation in the Dora Maira massif, Western Alps. Lithos, v. 41, p. 5-24.

Gebauer, D., Tilton, G.R., Schertl, H.-P., and Schreyer, W., 1993, Eocene/Oligocene ultrahigh-pressure (UHP)-metamorphism in the Dora Maira massif (Western Alps) and its geodynamic implications. Terra Nova Abstr. Suppl., v. 4, p. 10-11.

Godard, G., and Mabit, J.L., 1998, Peraluminous sapphirine formed during retrograssion of a kyanite- bearing eclogite from Pays de Léon, Armorican Massif, France. Lithos, v. 43, p. 15-29.

Graham, C.M., and Powell, R., 1984, A garnet-hornblende geothermometer: calibration, testing, and application to the Pelona Schist, Southern California. J. Metam. geol., v. 2, p. 13-31.

Green, H.W.II, Dobrzhinetskaya, L., and Bozhilov, K., 2000, Mineralogical and experimental evidence for very deep exhumation from subduction zones. J. Geodyn., v. 30, p. 61-76.

Green, H.W.II, Dobrzhinetskaya, L., Riggs, E.M., and Jin, Z.M., 1997, Alpe Arami: a peridotite massif from the mantle transition zone? Tectonoph., v. 279, p. 1-21.

Green, T.H., and Hellman, P.L., 1982, Fe-Mg partitioning between coexisting garnet and phengite at high pressure, and comments on a garnet-phengite geothermometer. Lithos, v. 15, p. 253-266.

Grond, R., Wahl, F., and Pfiffner, M., 1995, Mehrphasige alpine Deformation und Metamorphose in der nördlichen Cima-Lunga-Einheit, Zentralalpen (Schweiz). Schweiz. Mineral. Petrogr. Mitt., v. 75, p. 371-386.

Grubenmann, U., 1908, Granatolivinfels des Gordunotales und seine Begeleitgesteine. Viertelj. Naturf. Ges. Zürich, v. 53, p. 129-156.

Grujic, D., and Mancktelow, N.S., 1996, Structure of the northern Maggia and Lebendun Nappes, Central Alps, Switzerland. Eclog. geol. Helv., v. 89, p. 461-504.

Haccard, D., and Lorenz, C., 1979, Les déformations de l'Éocène supérieur au Stampien de la terminaison septentrionale de la zone de Sestri-Voltaggio. Bull. Soc. géol. France, v. 21, p. 401-413.

Hacker, B., Zhang, R.-Y., Liou, J., and Hervig, R., 1997, TiO_2 contents of Sulu and Alpe Arami olivines. Terra Nova Abstr. Suppl., v. 9, p. 13-14.

Heinrich, C.A., 1986, Eclogite facies regional metamorphism of hydrous mafic rocks in the Central Alpine Adula nappe. J. Petrol., v. 27, p. 123-154.

Hinderer, M., and Kamelger, A., 1999, Uplift versus erosion: a comparison of modern process rates for some major drainage basins of the Alps. Tübinger Geow. Arb. Ser. A, v. 52, p. 158-159.

Hirajima, T., and Compagnoni, R., 1995, Petrology of a jadeite-quartz/coesite-almandine-phengite fels with retrograde ferro-nyboite from the Dora-Maira Massif, Western Alps. Eur. J.

Mineral., v. 5, p. 943-955.

Hodges, K.V., and Royden, L., 1984, Geologic thermobarometry of retrograde metamorphic rocks: An indication of the uplift trajectory of a protion of the northern Scandinavian Caledonides. J. Geoph. Res., v. 89, p. 7077-7090.

Hodges, K.V., and Spear, F.S., 1982, Geothermometry, geobarometry and the Al_2SiO_5 triple point at Mt. Moosilauke, New Hampshire. Am. Mineral., v. 67, p. 1118-1134.

Holland, T., and Blundy, J., 1994, Non-ideal interactions in calcic amphiboles and their bearing on amphibole-plagioclase thermometry. Contrib. Mineral. Petrol., v. 116, p. 433-447.

Holland, T.J.B., 1980, The reaction albite=jadeite+quartz determined experimentally in the range 600-1200°C Am. Mineral., v. 65, p. 129-134.

Holland, T.J.B., 1983, The experimental determination of activities in disordered and short-range ordered jadeitic pyroxenes. Contrib. Mineral. Petrol., v. 82, p. 214-220.

Holland, T.J.B., 1990, Activities of components in omphacitic solid solutions. An application of Landau theory to mixtures. Contrib. Mineral. Petrol., v. 105, p. 446-453.

Holland, T.J.B., and Powell, R., 1990, An enlarged and updated internally consistent thermodynamic dataset with uncertainties and correlations: the system K_2O-Na_2O-CaO-MgO-MnO-FeO-Fe_2O_3-Al_2O_3-TiO_2-SiO_2-C-H_2-O_2. J. Metam. Geol., v. 8, p. 89-124.

Hoogerduijn Strating, E.H., 1991, The evolution of the Piemonte-Ligurian ocean. A structural study of ophiolite complexes in Liguria (NW Italy). Geol. Ultraiect., v. 74, 144 p.

Hoogerduijn Strating, E.H., 1994, Extensional faulting in an intraoceanic subduction complex - working hypothesis for the Paleogene of the Alps-Apennine system. Tectonoph., v. 238, p. 255-273.

Hoogerduijn Strating, E.H., and Van Wamel, W.A., 1989, The structure of the Bracco ophiolite complex (Ligurian Appenines, Italy) - a change from Alpine to Apennine polarity. J. Geol. Soc. London, v. 146, p. 933-944.

Houseman, G.A., McKenzie, D.P., and Molnar, P., 1981, Convective instability of a thickened boundary layer and its relevance for the thermal evolution of continental convergent belts. J. Geoph. Res., v. 86, p. 6115-6132.

Hsü, K.J., 1989, Time and place in Alpine orogenesis - the Fermor Lecture., in Coward, M.P., Dietrich, D., and Park, R.G., eds., Alpine tectonics, Geol. Soc. Spec. Publ., v. 45, p. 421-443.

Hunziker, J.C., Desmons, J., and Hurford, A.J., 1992, Thirty-two years of geochronological work in the Central and Western Alps: a review on seven maps. Mémoires de Géologie (Lausanne), 13. Lausanne, 59 p.

Hunziker, J.C., Desmons, J., and Martinotti, G., 1989, Alpine thermal evolution in the central and western Alps., in Coward, M.P., Dietrich, D., and Park, R.G., eds., Alpine tectonics, Geol. Soc. Spec. Publ., v. 45, p. 353-367.

Hunziker, J.C., Hurford, A.J., and Calmbach, L., 1997, Alpine cooling and uplift., in Pfiffner, O.A., Lehner, P., Heitzmann, P., Mueller, S., and Steck, A., eds., Deep structures of the Swiss Alps - Results of NRP 20. Basel, Switzerland, Birkhäuser Verlag, p. 260-264.

Hurford, A.J., 1986, Cooling and uplift patterns in the Lepontine Alps, South Central Switzerland and an age of vertical movement on the Insubric fault line. Contrib. Mineral. Petrol., v. 92, p. 413-427.

Hurford, A.J., Flisch, M., and Jager, E., 1989, Unraveling the thermo-tectonic evolution of the Alps: a contribution from fission track analysis and mica dating., in Coward, M.P., Dietrich, D., and Park, R.G., eds., Alpine Tectonics, Geol. Soc. Spec. Publ., v. 45, p. 369-398.

Hurford, A.J., and Hunziker, J.C., 1989, A revised thermal history for the Gran Paradiso massif. Schweiz. Mineral. Petr. Mitt., v. 69, p. 319-329.

Jamieson, R.A., Beaumont, C., Fullsack, P., and Lee, B., 1998, Barrovian metamorphism: where's the heat?, in Treloar, P.J., and O'Brien, P.J., eds., What drives metamorphism and metamorphic reactions?, Geol. Soc. Spec. Publ., v. 138, p. 23-51.

Johannes, W., and Holtz, F., 1990, Formation and composition of H2O-undersaturated granitic melts., in Ashworth, J.R., and Brown, M., eds., High-temperature metamorphism and crustal anatexis. London, Unwin Hyman, p. 87-104.

Johansson, L., and Möller, C., 1986, Formation of sapphirine during retrogression of a basic high-pressure granulite, Western Gneiss Region, Norway. Contrib. Mineral. Petrol., v. 94, p. 29-41.

Kincaid, C., and Silver, P., 1996, The role of viscous

dissipation in the orogenic process. Earth Planet. Sci. Lett., v. 142, p. 271-288.

Kleemann, U., and Reinhardt, J., 1994, Garnet-biotite thermometry revisited: The effect of Al^{VI} and Ti in biotite. Eur. J. Mineral., v. 6, p. 925-941.

Kohn, M.J., and Spear, F.S., 1989, Empirical calibration of geobarometers for the assemblage garnet + hornblende + plagioclase + quartz. Am. Mineral., v. 74, p. 77-84.

Kohn, M.J., and Spear, F.S., 1990, Two new geobarometers for garnet amphibolites, with applications to southeastern Vermont. Am. Mineral., v. 75, p. 89-96.

Koziol, A.M., and Newton, R.C., 1988, Redetermination of the anorthite breakdown reaction and improvement of the plagioclase-garnet-Al_2SiO_5-quartz geobarometer. Am. Mineral., v. 73, p. 216-223.

Kretz, R., 1983, Symbols for rock-forming minerals. Am. Mineral., v. 68, p. 277-279.

Kretz, R., 1990, Biotite and garnet compositional variation and mineral equiilibria in Grenville gneisses of the Otter Lake area, Quebec. J. Metam. Geol., v. 8, p. 493-506.

Krogh, E.J., 1988, The garnet-clinopyroxene Fe-Mg geothermometer - a reinterpretation of existing experimental data. Contrib. Mineral. Petrol., v. 99, p. 44-48.

Leake, B.E., 1978, Nomenclature of amphiboles. Mineral. Mag., v. 42, p. 533-563.

Lemoine, M., Tricart, P., and Boillot, G., 1987, Ultramafic and gabbroic ocean floor of the Ligurian Tethys (Alps, Corsica, Apennines): In search of a genetic model. Geology, v. 15, p. 622-625.

Lemoine, M., and Trümpy, R., 1987, Pre-oceanic rifting in the Alps. Tectonoph., v. 133, p. 305-320.

Liati, A., and Seidel, E., 1994, Sapphirine and högbomite in overprinted kyanite-eclogites of central, N. Greece: first evidence of granulite-facies metamorphism. Eur. J. Mineral., v. 6, p. 733-738.

Liati, A., and Seidel, E., 1996, Metamorphic evolution and geochemistry of kyanite eclogites in central Rhodope, northern Greece. Contrib. Mineral. Petrol., v. 123, p. 293-307.

Liou, J.G., Kim, H.S., and Maruyama, S., 1983, Prehnite-epidote equilibria and their petrologic applications. J. Petrol., v. 24, p. 321-342.

Liou, J.G., Zhang, R., Ernst, W.G., Liu, J., and McLimans, R., 1998, Mineral parageneses in the Piampaludo eclogitic body, Gruppo di Voltri, Western Ligurian Alps. Schweiz. Mineral. Petrogr. Mitt., v. 78, p. 317-335.

Lips, A.L.W., 1998, Temporal constraints on the kinematics of the destabilization of an orogen; syn- to post-orogenic extensional collapse of the Northern Aegean region., Geol. Ultraiect., v. 166, 224 p.

Lips, A.L.W., White, S.H., and Wijbrans, J.R., 1998, $^{40}Ar/^{39}Ar$ laserprobe direct dating discrete deformational events: a continuous record of early Alpine tectonics in the Pelagonian Zone, NW Aegean area, Greece. Tectonoph., v. 298, p. 133-153.

Maresch, W.V., 1977, Experimental studies on glaucophane: an analysis of present knowledge. Tectonoph., v. 43, p. 109-125.

Martignole, J., and Sisi, J.C., 1981, Cordierite-Garnet-H_2O equilibrium: A geological thermometer, barometer and water fugacity indicator. Contrib. Mineral. Petrol., v. 77, p. 38-46.

Maruyama, S., Suzuki, K., and Liou, J.G., 1983, Greenschist-amphibolite transition equilibria at low pressures. J. Petrol., v. 24, p. 583-604.

Mason, P.R.D., Sghedi, I., Szákacs, A., and Downs, H., 1998, Magmatic constraints on geodynamic models of subduction in the East Carpathians, Romania. Tectonoph., v. 297, p. 157-176.

Massonne, H.J., 1991, High-pressure, low-temperature metamorphism of pelitic and other protoliths based on experiments in the system K2O-MgO-Al2O3-SiO2-H2O. [Unpublished Post-Doc thesis]. Bochum, University of Bochum.

Massonne, H.J., and Schreyer, W., 1987, Phengite geobarometry based on the limiting assemblage with K-feldspar, phlogopite, and quartz. Contrib. Mineral. Petrol., v. 96, p. 212-224.

Mattauer, M., Malavieille, J., and Monié, P., 1987, Une coupe lithospérique des Alpes Occidentales dans l'hypothèse où Sezia n'est pas d'origine Sud-Alpine. C. R. Acad. Sci. Paris, v. 304 Série II, p. 43-48.

McKenzie, D., 1984, The generation and compaction of partially molten rock. J. Petrol., v. 25, p. 713-765.

Merle, O., 1994, Syn-convergence exhumation of the Central Alps. Geodin. Acta (Paris), v. 7, p. 129-138.

Merle, O., Cobbold, P.R., and Schmid, S., 1989, Tertiary kinematics in the Lepontine dome., in Coward, M.P., Dietrich, D., and Park, R.G.,

eds., Alpine tectonics, Geol. Soc. Spec. Publ., v. 45, p. 113-134.

Messiga, B., Piccardo, G.B., and Ernst, W.G., 1983, High-pressure eo-Alpine parageneses developed in magnesian metagabbros, Gruppo di Voltri, Western Liguria, Italy. Contrib. Mineral. Petrol., v. 83, p. 1-15.

Messiga, B., and Scambelluri, M., 1991, Retrograde P-T-t path for the Voltri Massif eclogites (Ligurian Alps, Italy): some tectonic implications. J. Metam. Geol., v. 9, p. 93-109.

Meyre, C., De Capitani, C., Zack, T., and Frey, M., 1999, Petrology of high-pressure metapelites from the Adula nappe (Central Alps, Switzerland). J. Petrol., v. 40, p. 199-213.

Michard, A., Chopin, C., and Henry, C., 1993, Compression versus extension in the exhumation of the Dora Maira coesite-bearing unit, Western Alps, Italy. Tectonoph., v. 221, p. 173-193.

Miyashiro, A., 1961, Evolution of metamorphic belts. J. Petrol., v. 2, p. 277-311.

Miyashiro, A., 1973, Metamorphism and metamorphic belts. London, George Allen & Unwin, 492 p.Möckel, J.R., 1969, Structural petrology of the garnet-peridotite of Alpe Arami (Ticino, Switzerland). Leidse Geol. Meded., v. 42, p. 61-130.

Moody, J.B., Meyer, D., and Jenkins, J.E., 1983, Experimental characterization of the greenschist/amphibolite boundary in mafic systems. Am. J. Sci., v. 283, p. 48-92.

Morimoto, N., Ferguson, A.K., Ginzburg, I.V., Ross, M., Seifert, F.A., Zussman, J., Aoki, K., and Gottardi, G., 1988, Nomenclature of pyroxenes. Mineral. Mag., v. 52, p. 535-550.

Morten, L., Bocchio, R., and Mottana, A., 1985, Transformation of a superferroan eclogite within serpentinite: a case study from the Voltri Group, Italy. Chem. Geol., v. 50, p. 111-127.

Mottana, A., and Bocchio, R., 1975, Superferric eclogites of the Voltri Group (Pennidic Belt, Apennines). Contrib. Mineral. Petrol., v. 49, p. 201-210.

Nagel, T., and Frey, M., 1999, The exhumation of the Lepontine Alps: Indications for an Oligocene metamorphic core complex from the lower Valle Mesolcina. J. Conf. Abstr., v. 4, p. 32.

Neumann, E.R., 1976, Two refinements for the calculation of structural formulae for pyroxenes and amphiboles. Nor. Geol. Tidsskr., v. 56, p. 1-6.

Newton, R.C., and Haselton, H.T., 1981, Thermodynamics of the garnet-plagioclase-Al_2SiO_5-quartz geobarometer., in Newton, R.C., Navrotski, A., and Wood, B.J., eds., Thermodynamics of minerals and melts. Advances in physical geochemistry, v. 1. New York, Springer Verlag, p. 131-147.

Niggli, E., and Niggli, C.R., 1965, Karten der Verbreitung einiger Mineralien der alpidischen Metamorphose in den Schweizer Alpen (Stilpnomelan, Alkali-Amphibol, Chloritoid, Staurolith, Disthen, Sillimanit). Eclog. geol. Helv., v. 58, p. 335-368.

Nimis, P., Trommsdorff, V., and Russo, U., 1999, Revised thermobarometry of grt-peridotite from Cima Lunga-Adula nappe complex, Central Alps. Ofioliti, v. 24, p. 143-144.

O'Hara, M.J., and Mercy, E.L.P., 1966, Garnet-peridotite and eclogite from Bellinzona, Switzerland. Earth Planet. Sci. Lett., v. 1, p. 295-300.

Okaya, N., Freeman, R., Kissling, E., and Mueller, S., 1996, A lithospheric cross-section through the Swiss Alps - I. Thermokinematic modeling of the Neoalpine orogeny. Geophys. J. Int., v. 125, p. 504-518.

Oreskes, N., Shrader-Frechette, K., and Belitz, K., 1994, Verification, validation and confirmation of numerical models in the earth sciences. Science, v. 263, p. 641-646.

Oxburgh, E.R., and Turcotte, D.L., 1968, Problems of high heat flow and volcanism associated with zones of descending mantle convective flow. Nature, v. 218, p. 1041-1043.

Pangaud, G., Lameyre, J., and Michel, R., 1957, Age absolu des migmatites du massif du Grand Paradis (Alpes franco-italiennes). C. R. Acad. Sci. Paris Sér. D, v. 245, p. 331-333.

Peacock, S.M., 1989, Thermal modeling of metamorphic pressure-temperature-time paths: a forward approach., in Spear, F.S., and Peacock, S.M., eds., AGU short course in geology. Metamorphic pressure-temperature-time paths., p. 57-79.

Perchuk, L.L., and Lavrent'eva, I.V., 1983, Experimental investigation of exchange equilibria in the system cordierite-garnet-biotite., in Saxena, S.K., ed., Kinetics and equilibrium in mineral reactions. Advances in physical chemistry, v. 3. New York, Springer Verlag, p. 199-239.

Pfiffner, M., and Trommsdorff, V., 1998, The high-pressure ultramafic-mafic-carbonate suite of

Cima Lunga-Adula, Central Alps: Excursions to Cima di Gagnone and Alpe Arami. Schweiz. Mineral. Petrogr. Mitt., v. 78, p. 337-354.

Pfiffner, M.A., 1999, Genese der hochdruckmetamorphen ozeanischen Abfolge der Cima Lunga-Einheit (Zentralalpen). [PhD thesis No. 13011]. Zürich, ETH, 297 p.

Pfiffner, O.A., Lehner, P., Heitzmann, P., Mueller, S., and Steck, A., 1997, Deep structure of the Swiss Alps: results of NRP 20. Basel, Birkhäuser Verlag, 380 p.

Piccardo, G.B., Cortesogno, L., Messiga, B., Galli, M., and Pedemonte, G.M., 1977, Excursion to the metamorphic ophiolites of the Gruppo di Voltri - guide book. Rend. Soc. It. Geol. Min. Petrol., v. 33, p. 295-314.

Platt, J.P., 1986, Dynamics of orogenic wedges and the uplift of high-pressure metamorphic rocks. Geol. Soc. Am. Bull., v. 97, p. 1037-1053.

Platt, J.P., 1987, The uplift of high-pressure-low-temperature metamorphic rocks. Phil. Trans. R. Soc. London, v. A 321, p. 87-103.

Platt, J.P., 1993, Exhumation of high-pressure rocks: a review of concepts and processes. Terra Nova, v. 5, p. 119-133.

Platt, J.P., and England, P.C., 1994, Convective removal of lithosphere beneath mountain belts: Thermal and mechanical consequences. Am. J. Sci., v. 294, p. 307-336.

Platt, J.P., and Vissers, R.L.M., 1989, Extensional collapse of thickened continental lithosphere: A working hypothesis for the Alboran Sea and Gibraltar arc. Geology, v. 17, p. 540-543.

Powell, R., 1985, Regression diagnostics and robust regression in geothermometer/geobarometer calibration: the garnet-clinopyroxene geothermometer revisited. J. Metam. Geol., v. 3, p. 231-243.

Powell, R., and Holland, T.J.B., 1988, An internally consistent dataset with uncertainties and correlations: 3. Applications to geobarometry, worked examples and a computer program. J. Metam. Geol., v. 6, p. 173-204.

Radelli, L., and Desmons, J., 1987, Pennique, Téthys et orogenèse crétacé moyen dans les Alpes. C. R. Acad. Sci. Paris, v. 305, Série II, p. 1375-1378.

Råheim, A., and Green, D.H., 1974, Experimental determination of the temperature and pressure dependence of the Fe-Mg partition coefficient for coexisting garnet and clinopyroxene. Contrib. Mineral. Petrol., v. 48, p. 179-203.

Rampone, E., Reusser, E., Piccardo, G.B., and Trommsdorff, V., 1999, Trace element chemistry of high pressure minerals in prograde garnet lherzolites of the Central Alps. Ofioliti, v. 24, p. 157.

Reddy, S.M., Wheeler, J., and Cliff, R.A., 1999, The geometry and timing of orogenic extension: an example from the Western Italian Alps. J. Metam. Geol., v. 17, p. 573-589.

Reinecke, T., 1991, Very-high-pressure metamorphism and uplift of coesite-bearing metasediments from the Zermatt-Saas zone, Western Alps. Eur. J. Mineral., v. 3, p. 7-17.

Reinhardt, B., 1966, Geologie und Petrographie der Monte Rosa-Zone, der Sesia-Zone und des Canavese im Gebiet zwischen Valle d'Ossola und Valle Loana (Prov. di Novara, Italien). Schweiz. Mineral. Petrogr. Mitt., v. 46, p. 553-678.

Ricou, L.E., 1994, Tethys reconstructed: plates, continental fragments and their boundaries since 260 Ma from Central America to Southeastern Asia. Geodyn. Acta, v. 7, p. 169-218.

Rieder, M., Cavazzini, G., D'yakonov, Y.S., Frank-Kamenetskii, V.A., Gottardi, G., Guggenheim, S., Koval, P.V., Müller, G., Neiva, A.M.R., Radoslovich, E.W., Robert, J.L., Sassi, F.P., Takeda, H., Weiss, Z., and Wones, D.R., 1999, Nomenclature of the micas. Mineral. Mag., v. 63, p. 267-279.

Ring, U., 1992, The kinematic history of the Pennine nappes east of the Lepontine dome: Implications for the tectonic evolution of the Central Alps. Tectonics, v. 11, p. 1139-1158.

Risold, A.-C., Trommsdorff, V., Reusser, E., and Ulmer, P., 1997, Genesis of $FeTiO_3$ inclusion in garnet peridotites from the Central Alps. Terra Nova Abstr. Suppl., v. 9, p. 28-29.

Rolland, Y., Lardeaux, J.M., Guillot, S., and Nicollet, C., 2000, Extension syn-convergence, poinçonnement vertical et unités métamorphiques contrastées en bordure ouest du Grand Paradis (Alpes Franco-Italiennes). Geodyn. Acta, v. 13, p. 133-148.

Rötzler, J., Carswell, D.A., Gerstenberger, H., and Haase, G., 1999, Transitional blueschist-epidote amphibolite facies metamorphism in the Frankenberg massif, Germany, and geotectonic implications. J. Metam. Geol., v. 17, p. 109-125.

Roure, F., Bergerat, F., Damotte, B., Mugnier, J.L., and Polino, R., 1996, The ECORS-CROP Alpine seismic traverse., Mem. Soc. géol. France, v. 170. Paris, p. 113.

Roure, F., Heitzmann, P., and Polino, R., 1990, Deep structure of the Alps., Mem. Soc. géol. France, v. 156. Paris, p. 367.

Rubatto, D., 1998, Dating of pre-Alpine magmatism, Jurassic ophiolites and Alpine subductions in the Western Alps. [PhD thesis No. 12620]. Zürich, ETH, 185 p.

Rubatto, D., and Gebauer, D., 1999, Eo/Oligocene high-pressure metamorphism in the Gornergrat Zone (Monte Rosa, Western Alps): implications for paleogeography. Schweiz. Mineral. Petrogr. Mitt., v. 79, p. 353-362.

Schamel, S., and Hunziker, J., 1977, Eocene-Oligocene blueschist facies metamorphism in Liguria, Italy, and Alpine Corsica. GSA Abstr. Progr., v. 9, p. 1158-1159.

Schlunegger, F., and Willet, S., 1999, Spatial and temporal variations in exhumation of the central Swiss Alps and implications for exhumation mechanisms., in Ring, U., Brandon, M.T., Lister, G.S., and Willet, S.D., eds., Exhumation processes: Normal faulting, ductile flow and erosion, Geol. Soc. Spec. Publ., v. 154, p. 157-179.

Schmid, S.M., and Kissling, E., 2000, The arc of the western Alps in the light of geophysical data on deep structure. Tectonics, v. 19, p. 62-85.

Schmid, S.M., Pfiffner, O.A., Froitzheim, N., Schönborn, G., and Kissling, E., 1996, Geophysical-geological transect and tectonic evolution of the Swiss-Italian Alps. Tectonics, v. 15, p. 1036-1064.

Schmid, S.M., Pfiffner, O.A., and Schreurs, G., 1997, Rifting and collision in the Penninic zone of eastern Switzerland., in Pfiffner, O.A., Lehner, P., Heitzmann, P., Mueller, S., and Steck, A., eds., Deep structures of the Swiss Alps - Results of NRP 20. Basel, Switzerland, Birkhäuser Verlag, p. 160-185.

Schönborn, G., 1992, Alpine tectonics and kinematic models of the central Southern Alps. Mem. Inst. Geol. Mineral. Padova, v. 44, p. 229-393.

Schumacher, J.C., 1991, Empirical ferric iron corrections: necessity, assumptions, and effects on selected geothermobarometers. Mineral. Mag., v. 55, p. 3-18.

Soto, J.I., and Platt, J.P., 1999, Petrological and structural evolution of high-grade metamorphic rocks from the floor of the Alboran Sea Basin, Western Mediterranean. J. Petrol., v. 40, p. 21-60.

Spear, F.S., 1989, Relative thermobarometry and metamorphic P-T paths., in Daly, J.S., Cliff, R.A., and Yardley, B.W.D., eds., Evolution of metamorphic belts, Geol. Soc. Spec. Publ., v. 43, p. 63-81.

Spear, F.S., 1993, Metamorphic phase equilibria and pressure-temperature-time paths. Washington D.C., Mineralogical Society of America, 799 p.

Spear, F.S., and Cheney, J.T., 1989, A petrogenitic grid for pelitic schists in the system SiO_2-Al_2O_3-FeO-MgO-K_2O-H_2O. Contrib. Mineral. Petrol., v. 101, p. 149-164.

Spicher, A., 1980, Tektonische Karte der Schweiz. Bern, Schweizerischen Geologischen Kommission.

Stampfli, G.M., 1993, Le Briançonnais, terrain exotique dans les Alpes? Eclog. geol. Helv., v. 86, p. 1-45.

Stampfli, G.M., and Marchant, R.H., 1997, Geodynamic evolution of the Tethyan margins of the Western Alps., in Pfiffner, O.A., Lehner, P., Heitzmann, P., Mueller, S., and Steck, A., eds., Deep structures of the Swiss Alps - Results of NRP 20. Basel, Switzerland, Birkhäuser Verlag, p. 223-239.

Stampfli, G.M., Mosar, J., Marquer, D., Marchant, R., Baudin, T., and Borel, G., 1998, Subduction and obduction processes in the Swiss Alps. Tectonoph., v. 296, p. 159-204.

Steck, A., and Hunziker, J., 1994, The Tertiary structural and thermal evolution of the Central Alps - compressional and extensional structures in an orogenic belt. Tectonoph., v. 238, p. 229-254.

Thomas, J.C., Claudel, M.E., Collombet, M., Tricart, P., Chauvin, A., and Dumont, T., 1999, First paleomagnetic data from the sedimentary cover of the French Penninic Alps: evidence for tertiary couterclockwise rotations in the Western Alps. Earth Planet. Sci. Lett., v. 171, p. 561-674.

Thompson, A.B., and England, P.C., 1984, Pressure-temperature-time paths of regional metamorphism 2. Their inference and interpretation using mineral assemblages in metamorphic rocks. J. Petrol., v. 25, p. 929-955.

Tilton, G.R., Schreyer, W., and Schertl, H.-P., 1989, Pb-Sr-Nd isotopic behavior of deeply subducted crustal rocks from the Dora Maira Massif, Western Alps, Italy. Geoch. Cosmoch. Acta, v. 53, p. 1391-1400.

Tilton, G.R., Schreyer, W., and Schertl, H.-P., 1991, Pb-Sr-Nd isotopic behaviour of deeply subducted crustal rocks from the Dora Maira massif, Western Alps, Italy-II: what is the age of

the ultrahigh- pressure metamorphism? Contrib. Mineral. Petrol., v. 108, p. 22-33.

Todd, C.S., 1998, Limits on the precision of geobarometry at low grossular and anorthite content. Am. Mineral., v. 83, p. 1161-1167.

Todd, C.S., and Engi, M., 1997, Metamorphic field gradients in the Central Alps. J. Metam. Geol., v. 15, p. 513-530.

Trommsdorff, V., 1990, Metamorphism and tectonics in the central Alps: the Alpine lithospheric mélange of Cima Lunga and Adula. Mem. Soc. Geol. It., v. 45, p. 39-49.

Trommsdorff, V., Hermann, J., Müntener, O., Pfiffner, M., and Risold, A.C., 2000, Geodynamic cycles of subcontinental lithosphere in the Central Alps and the Arami enigma. J. Geodyn., v. 30, p. 77-92.

Ulmer, P., and Trommsdorff, V., 1997, Titanium content of mantle olivine: An experimental study to 10 GPa. Terra Nova Abstr. Suppl., v. 9, p. 39.Vallis, F., and Scambelluri, M., 1996, Redistribution of high-pressure fluids during retrograde metamorphism of eclogite-facies rocks (Voltri Massif, Italian Western Alps). Lithos, v. 39, p. 81-92.

Van de Zedde, D.M.A., and Wortel, M.J.R., 2000, Shallow slab detachment as a transient source of heat at mid-lithospheric dephts. Tectonics, Submitted July 2000.

Van den Beukel, J., 1990, Breakup of young oceanic lithosphere in the upper part of a subduction zone: implications for the emplacement of ophiolites. Tectonics, v. 9, p. 825-844.

Van der Meulen, M.J., Buiter, S.J.H., Meulenkamp, J.E., and Wortel, M.J.R., 2000, An early Pliocene uplift of the central Apenninic foredeep and its geodynamic significance. Tectonics, v. 19, p. 300-313.

Vance, D., and O'Nions, R.K., 1992, Prograde and retrograde thermal histories from the central Swiss Alps. Earth Planet. Sci. Lett., v. 114, p. 113-129.

Vearncombe, J.R., 1985, The structure of the Gran Paradiso basement massif and its envelope, Western Alps. Eclog. geol. Helv., v. 78, p. 49-72.

Vialon, P., Rochette, P., and Ménard, G., 1989, Indentation and rotation in the western Alpine arc., in Coward, M.P., Dietrich, D., and Park, R.G., eds., Alpine Tectonics, Geol. Soc. Spec. Publ., v. 45, p. 329-338.

Vissers, R.L.M., Hoogerduijn Strating, E.H., Heijmans, M., and Krabbendam, M., in prep., Transformation-enhanced ductility and the development of a greenschist-facies tectonic mélange.

Vissers, R.L.M., Platt, J.P., and Van der Wal, D., 1995, Late orogenic extension of the Betic Cordillera and the Alboran Domain: A lithospheric view. Tectonics, v. 14, p. 786-803.

Von Blanckenburg, F., and Davies, J.H., 1995, Slab breakoff: A model for syncollisional magmatism and tectonics in the Alps. Tectonics, v. 14, p. 120-131.

Von Blanckenburg, F., Kagami, H., Deutsch, A., Oberli, F., Meier, M., Wiedenbeck, M., Barth, S., and Fischer, H., 1998, The origin of Alpine plutons along the Periadriatic lineament. Schweiz. Mineral. Petrogr. Mitt., v. 78, p. 55-66.

Wagner, G.A., Reimer, G.M., and Jäger, E., 1977, Cooling ages derived by apatite fission-track, mica Rb-Sr and K-Ar dating: the uplift and cooling history of the Central Alps. Mem. Inst. Geol. Mineral. Padova, v. 30, p. 28.

Wang, G.F., Banno, S., and Takeuchi, K., 1986, Reactions to define the biotite isograd in the Ryoke metamorphic belt, Kii Peninsula, Japan. Contrib. Mineral. Petrol., v. 93, p. 9-17.

Waters, D.J., and Martin, H.N., 1993, Geobarometry in phengite-bearing eclogites. Terra Nova Abstr. Suppl., v. 5, p. 410-411.

Wenk, E., 1956, Die lepontinische Gneissregion und die jungen Granite der Valle della Mera. Eclog. geol. Helv., v. 49, p. 251-265.

Westphal, M., Bazhenov, M.L., Lauer, J.P., Pechersky, D.M., and Sibuet, J.C., 1986, Paleomagnetic implications on the evolution of the Tethys belt from the Atlantic ocean to the Pamirs since the Triassic. Tectonoph., v. 123, p. 37-82.

Willet, S., Beaumont, C., and Fullsack, P., 1993, Mechanical model for the tectonics of doubly vergent compressional orogens. Geology, v. 21, p. 371-374.

Williams, M.L., and Grambling, J.A., 1990, Manganese, ferric iron, and the equilibrium between garnet and biotite. Am. Mineral., v. 75, p. 886-908.

Wong A Ton, S.Y.M., and Wortel, M.J.R., 1997, Slab detachment in continental collision zones: An analysis of controlling parameters. Geoph. Res. Lett., v. 24, p. 2095-2098.

Wortel, M.J.R., and Spakman, W., 1992, Structure and dynamics of subducted lithosphere in the Mediterranean region. Proc. Kon. Ned. Akad. v. Wetensch., v. 95, p. 325-347.

Appendix 1

Thermobarometry

A1.1 Introduction

Dozens of thermobarometers are available, for many different mineral assemblages (e.g. Spear, 1993, chapter 15). Unfortunately, thermometers and barometers are often not very clearly described in the original publications, making it difficult to check results obtained using them. To ensure reproducibility of the thermobarometric results of the present study all formulations that were used are explicitly given in this appendix in the form in which they were used. Definition: X_B^A = mole fraction of component B in mineral A

A1.2 Garnet-omphacite thermobarometry

A1.2.1 Krogh (1988)
Garnet-omphacite Fe-Mg exchange thermometer, as calibrated by Krogh (1988)

$$T(°C) = \frac{(-6173 \cdot (X_{Ca}^{Grt})^2 + 6731 \cdot X_{Ca}^{Grt} + 1879 + 10 \cdot P(kbar))}{(\ln K_D + 1.393)} - 273 \qquad (A1.1)$$

Where:

$$X_{Ca}^{Grt} = \frac{Ca}{Ca + Mg + Fe^{2+} + Mn} \qquad (A1.2)$$

And:

$$K_D = \frac{(Fe^{2+}/Mg)^{Grt}}{(Fe^{2+}/Mg)^{Cpx}} \qquad (A1.3)$$

A1.2.2 Holland (1983)
The jadeite barometer was first calibrated by Holland (1980; 1983) and rewritten by Carswell and Harley (1990). I used the latter calibration:

$$P - P_0(kbar) = -\frac{RT(K)}{1000 \cdot \Delta V_0} \cdot \ln\left(\frac{a_{Jd}^{Cpx} \cdot a_{SiO_2}^{Qtz}}{a_{Ab}^{Pl}}\right) \qquad (A1.4)$$

Where:

$$P_0(\text{kbar}) = 0.35 + 0.0265 \cdot T(°C) \pm 0.50 \tag{A1.5}$$

The volume change of the reaction for high albite is

ΔV_o = -1.734 kJ/kbar = -1.734 J/bar

And (cpx mixing model):

$$a_{Jd}^{Cpx} = (X_{Jd}^{Cpx})^2 \cdot \gamma_{Jd}^{Cpx} \tag{A1.6}$$

The activity coefficient of jadeite in clinopyroxene is

$$\gamma_{Jd}^{Cpx} = \exp\left(\frac{W}{RT(K)} \cdot (1 - X_{Jd}^{Cpx})^2\right) \tag{A1.7}$$

W = 24000 J/mol , R = 8.3144 J/mol·K,

And:

$$a_{SiO_2}^{Qtz} = 1$$

$$a_{Ab}^{Pl} = 1$$

Because plagioclase is often not present, obtained pressures for coexisting clinopyroxene and quartz are minimum estimates.

For simultaneous solution of the garnet-omphacite thermometer and the jadeite barometer equations A1.1 and A1.5 were combined. Define A, B and C as follows:

$$A = \frac{-R \cdot \ln((X_{Jd}^{Cpx})^2)}{1000 \cdot \Delta V_0} + 0.0265 \tag{A1.8}$$

$$B = \frac{-R \cdot 273 \cdot \ln((X_{Jd}^{Cpx})^2) + W \cdot (1 - X_{Jd}^{Cpx})^2}{1000 \cdot \Delta V_0} - 0.35 \tag{A1.9}$$

$$C = \frac{-6173 \cdot (X_{Ca}^{Grt})^2 + 6731 \cdot X_{Ca}^{Grt} + 1879}{\ln K_D + 1.393} \tag{A1.10}$$

Then

$$T(°C) = \frac{\frac{C + 10 \cdot B}{\ln K_D + 1.393}}{1 - \frac{10 \cdot A}{\ln K_D + 1.393}} - 273 \qquad \text{(A1.11)}$$

$$P(kbar) = \frac{-R \cdot (T(°C) + 273)}{1000 \cdot \Delta V_0} \cdot \ln((X_{Jd}^{Cpx})^2) \cdot \exp\left(\frac{W}{R \cdot (T(°C) + 273) \cdot (1 - X_{Jd}^{Cpx})^2}\right) + 0.35 + 0.0265 \cdot T(°C) \qquad \text{(A1.12)}$$

again with

$R = 8.3144$ J/mol·K
$\Delta V_o = -1.734$ kJ/kbar
$W = 24000$ J/mol

A1.2.3 Powell (1985)
In cases where X_{Ca}^{Grt} is smaller than 0.35 the thermometer calibration of Krogh (1988) is replaced by that of Powell (1985).

$$T(K) = \frac{2790 + 10 \cdot P(kbar) + 3140 \cdot X_{Ca}^{Grt}}{1.735 + \ln K_D} \qquad \text{(A1.13)}$$

Where:

$$K_D = \frac{(Fe^{2+}/Mg)^{Grt}}{(Fe^{2+}/Mg)^{Cpx}} \qquad \text{(A1.14)}$$

The formulae for simultaneous solution then become:

$$A' = \frac{-R \cdot \ln((X_{Jd}^{Cpx})^2)}{1000 \cdot \Delta V_0} + 0.0265 \qquad \text{(A1.15)}$$

$$B' = \frac{-R \cdot 273 \cdot \ln((X_{Jd}^{Cpx})^2) + W \cdot (1 - X_{Jd}^{Cpx})^2}{1000 \cdot \Delta V_0} - 0.35 \qquad \text{(A1.16)}$$

$$C' = \frac{3140 \cdot X_{Ca}^{Grt} + 2790}{1.735 + \ln K_D} \qquad \text{(A1.17)}$$

$$T(°C) = \frac{\frac{C'+10 \cdot B'}{1.735 + \ln K_D}}{1 - \frac{10 \cdot A'}{1.735 + \ln K_D}} - 273 \qquad \text{(A1.18)}$$

$$P(kbar) = \frac{-R \cdot (T(°C) + 273)}{1000 \cdot \Delta V_0} \cdot \ln((X_{Jd}^{Cpx})^2) \cdot \exp\left(\frac{W}{R \cdot (T(°C) + 273) \cdot (1 - X_{Jd}^{Cpx})^2}\right) + 0.35 + 0.0265 \cdot T(°C) \qquad \text{(A1.19)}$$

A1.3 Garnet-phengite thermometry

The garnet-phengite Fe-Mg exchange thermometer of Green and Hellman (1982) is defined as follows:

$$T(°C) = \frac{A + 36.0 \cdot P(kbar)}{\ln K_D + B} - 273 \qquad \text{(A1.20)}$$

Where:

$$K_D = \frac{(Fe^{2+}/Mg)^{Grt}}{(Fe^{2+}/Mg)^{Phen}} \qquad \text{(A1.21)}$$

A and B depend on the bulk composition of the rock as follows. Define

$$mg = \frac{100 \cdot MgO_{bulk}}{MgO_{bulk} + FeO_{bulk}} \text{ of the bulk rock composition.}$$

Then for pelitic (low Ca ≤ 2%) rocks with mg ≈ 67
A = 5560 and B = 4.65
For pelitic (low Ca ≤ 2%) rocks with mg = 20-30
A = 5680 and B = 4.38
For basaltic (Ca rich) rocks with mg ≈ 67
A = 5170 and B = 4.17

A1.4 Phengite barometry

The latest calibration of the phengite barometer (fig A1.1) was taken from Massonne (1991). This calibration is unfortunately unpublished. Resulting pressures are about 0.6 kbar lower than with the original calibration (Massonne and Schreyer, 1987; Rötzler et al., 1999).

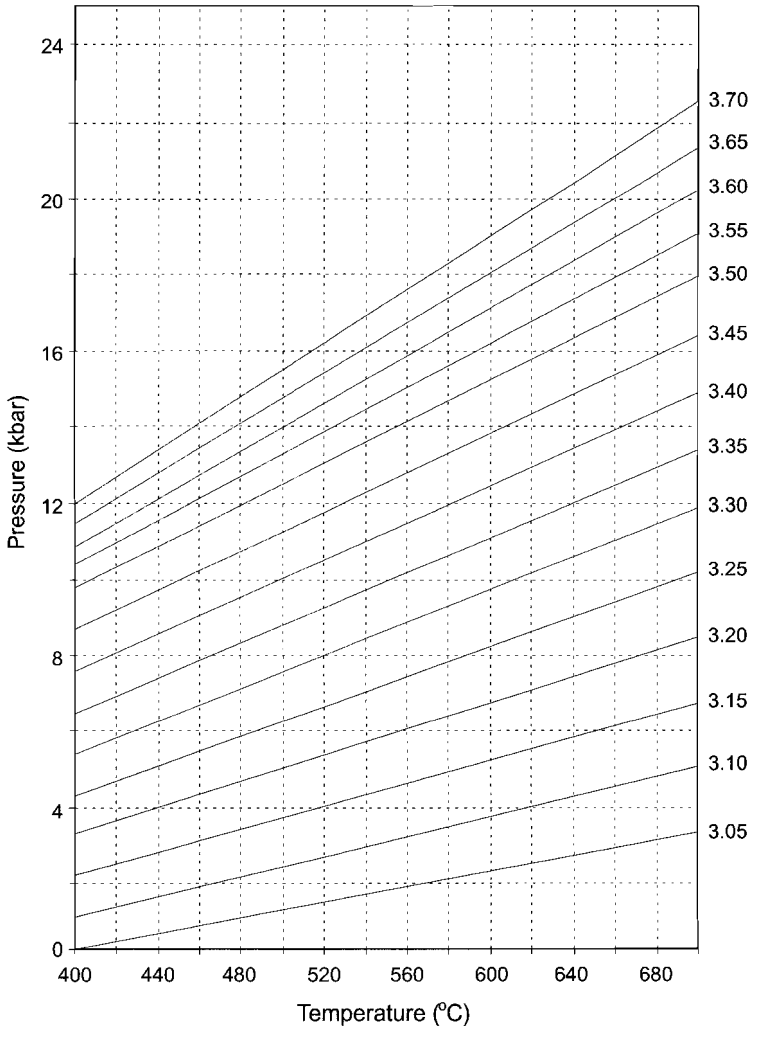

Figure A1.1: Si-isopleths for phengite in association with K-feldspar, phlogopite and quartz (redrawn and interpolated after Massonne (1991)). Minimum pressures are obtained if phengite does not coexist with K-feldspar, phlogopite and quartz. The isopleths are of Si per formula unit, on the basis of 11 oxygens.

A1.5 Garnet-clinopyroxene-phengite barometry

Because of lack of an accurate barometer for mafic eclogites Waters and Martin (1993) extracted a new barometer from the internally consistent thermodynamic database of Holland and Powell (1990) (Carswell et al., 1997). The barometer is based on the inverse tschermak's substitution in phengite for triplets of garnet, omphacite and phengite in apparent equilibrium. The reaction in question is:

$$Mg_3Al_2Si_3O_{12} + 2\,Ca_3Al_2Si_3O_{12} + 3\,K(Al_1Mg_1)^{VI}Si_2^{T2}Si_2^{T1}O_{10}(OH)_2 = 6\,CaMgSi_2O_6 + 3\,KAl_2^{VI}Si_2^{T2}Si_1^{T1}Al^{T1}O_{10}(OH)_2 \quad \text{(A1.22)}$$

(or pyrope + 2 grossular + 3 celadonite = 6 diopside + 3 muscovite, otherwise written as pyrope + 2 grossular = 6 diopside + 3 $Al_2Mg_{-2}Si_{-1}$). A revised and improved version of this barometer was published on the internet (Waters and Martin, 1996; http://www.earth.ox.ac.uk/~davewa/research/ecbarcal.html), which is the formulation that was used in the present study:

$$P(kbar) = 28.05 + 0.02044 \cdot T(K) - 0.003539 \cdot T(K) \cdot \ln K_D \quad \text{(A1.23)}$$

The term $\ln K_D$ is a distribution coefficient, which is calculated as follows:

$$\ln K_D = 6 \cdot \ln a_{Di}^{Cpx} - \ln a_{Prp}^{Grt} - 2 \cdot \ln a_{Grs}^{Grt} + 3 \cdot \ln a_{Al_2Mg_{-2}Si_{-1}}^{Phen} \quad \text{(A1.24)}$$

Calculation of garnet activities:
Normalise the garnet analysis to 12 oxygens and 8 cations and use simple Mg-Ca mixing. Then:

$$X_{Mg}^{Grt} = \frac{Mg}{3}$$

$$X_{Ca}^{Grt} = \frac{Ca}{3}$$

$$X_{Al}^{Grt} = \frac{Al}{2}$$

where Mg, etc represent the number of Mg cations per formula unit. Then (from Newton and Haselton, 1981, with units converted to J/mol):

$$\ln(\gamma_{Mg}^{Grt}) = \frac{(13807 - 6.276 \cdot T(K)) \cdot X_{Ca}^{Grt} \cdot (1 - X_{Mg}^{Grt})}{R \cdot T(K)} \quad \text{and}$$

$$\ln(\gamma_{Ca}^{Grt}) = \frac{(13807 - 6.276 \cdot T(K)) \cdot X_{Mg}^{Grt} \cdot (1 - X_{Ca}^{Grt})}{R \cdot T(K)} \quad \text{after which}$$

$$\ln a^{Grt}_{Prp} = 3 \cdot \ln(X^{Grt}_{Mg}) + 3 \cdot \ln(\gamma^{Grt}_{Mg}) + 2 \cdot \ln(X^{Grt}_{Al})$$
$$\ln a^{Grt}_{Grs} = 3 \cdot \ln(X^{Grt}_{Ca}) + 3 \cdot \ln(\gamma^{Grt}_{Ca}) + 2 \cdot \ln(X^{Grt}_{Al})$$

with R = 8.314 J/mol·K

Calculation of clinopyroxene activities:
Normalise the pyroxene analysis to 6 oxygens and 4 cations and use the reciprocal salt-solution model of Holland (1990).

$$X^{Cpx}_{Mg,M1} = Mg - cations$$
$$X^{Cpx}_{Ca,M2} = Ca - cations \quad \text{per 6 oxygens.}$$

For long-range-disordered or Fe^{3+}-bearing pyroxenes use:

$$\ln(\gamma^{Cpx}_{Ca,Mg}) = \frac{X^{Cpx}_{Na,M2} \cdot [W_A \cdot (X^{Cpx}_{Al,M1} + X^{Cpx}_{Fe^{3+},M1}) + (W_A - W_B) \cdot X^{Cpx}_{Fe^{2+},M1}]}{R \cdot T(K)}$$

where W_A = 26000 J, and W_B = 25000 J. And then:

$$\ln a_{di} = \ln(X_{Ca,M2} \cdot X_{Mg,M1}) + \ln(\gamma_{Ca\,Mg})$$

Calculation of phengite tschermak's exchange activity:
The activity expression were taken from Holland and Powell (1990).

$$a^{Phen}_{Al_2Mg_{-1}Si_{-1}} = \frac{X^{Phen}_{Al,M2} \cdot X^{Phen}_{Al,T2}}{X^{Phen}_{Mg,M2} \cdot X^{Phen}_{Si,T2}}$$

For a microprobe analysis normalised to 11 oxygens, i.e. without taking H_2O into account, this can be expressed in terms of cations as:

$$a^{Phen}_{Al_2Mg_{-1}Si_{-1}} = \frac{(Al + Si - 4) \cdot (4 - Si)}{Mg \cdot (Si - 2)}$$

A1.6 Garnet-amphibole thermometry

The exchange of Fe^{2+} and Mg between garnet and amphibole is another temperature dependent equilibrium (Graham and Powell, 1984):

$$3\,NaCa_2Fe_4Al_3Si_6O_{22}(OH) + 4\,Mg_3Al_2Si_3O_{12} = 3\,NaCa_2Mg_4Al_3Si_6O_{22}(OH) + 4\,Fe_3Al_2Si_3O_{12} \quad \text{(A1.25)}$$

or 3 ferro-pargasite + 3 pyrope = 4 pargasite + almandine. The thermometer was calibrated for temperatures below 850 °C, for garnets with $X_{Mn} \leq 0.1$ and for common hornblendes of a fairly wide range of compositions ($0.09 \leq X_{Na,M4} \leq 0.52$).
Amphibole site occupations are calculated using the scheme of Holland and Blundy (1994), which is described in section A1.8. All iron must be assumed ferrous in accordance with the calibration dataset.
The thermometer is:

$$T(K) = \frac{2880 + 3280 \cdot X_{Ca}^{Grt}}{\ln K_D + 2.426} \quad \text{(A1.26)}$$

Where:

$$K_D = \frac{(Fe^{2+}/Mg)^{Grt}}{(Fe^{2+}/Mg)^{Amph}}$$

and X_{Ca}^{Grt} as in section A1.5

A1.7 Garnet-amphibole barometry

Two reactions in the mineral assemblage garnet-amphibole-quartz-plagioclase (from here on called garnet-amphibole barometer) can be used as barometers (Kohn and Spear, 1990). One of the reactions involves the Fe-endmembers (1) of garnet and amhibole, whereas the other concerns the Mg-endmembers (2).

(1)
$$6\,CaAl_2Si_2O_8 + 3\,Ca_2Mg_5Si_8O_{22}(OH)_2 = 2\,Ca_3Al_2Si_3O_{12} + Mg_3Al_2Si_3O_{12} + 3\,Ca_3Mg_4Al_2Si_7O_{22}(OH)_2 + 6\,SiO_2 \quad \text{(A1.27)}$$

(6 anorthite + 3 tremolite = 2 grossular + pyrope + 3 tschermakite + 6 quartz) and

(2)
$$6\,CaAl_2Si_2O_8 + 3\,Ca_2Fe_5Si_8O_{22}(OH)_2 = 2\,Ca_3Al_2Si_3O_{12} + Fe_3Al_2Si_3O_{12} + 3\,Ca_3Fe_4Al_2Si_7O_{22}(OH)_2 + 6\,SiO_2 \quad \text{(A1.28)}$$

(6 anorthite + 3 Fe-actinolite = 2 grossular + almandine + 3 Fe-tschermakite + 6 quartz). Where:

$$K_D(1) = \frac{(a_{Grs}^{Grt})^2 \cdot a_{Prp}^{Grt} \cdot (a_{Tsch}^{Amph})^3 \cdot (a_{SiO_2}^{Qtz})^6}{(a_{An}^{Pl})^6 \cdot (a_{Trem}^{Amph})^3} \quad \text{(A1.29)}$$

$$K_D(2) = \frac{(a_{Grs}^{Grt})^2 \cdot a_{Alm}^{Grt} \cdot (a_{Fe-Tsch}^{Amph})^3 \cdot (a_{SiO_2}^{Qtz})^6}{(a_{An}^{Pl})^6 \cdot (a_{Fe-Trem}^{Amph})^3} \quad \text{(A1.30)}$$

The barometers are:

$$P_{Mg}(kbar) = \frac{79507 + T(K) \cdot (29.14 + (8.3100 \cdot \ln K_D(1)))}{1000 \cdot 10.988} \quad \text{and} \quad \text{(A1.31)}$$

$$P_{Fe}(kbar) = \frac{35327 + T(K) \cdot (56.09 + (8.3100 \cdot \ln K_D(2)))}{1000 \cdot 11.906} \quad \text{(A1.32)}$$

The compositional criteria to be met are:

Garnet: Mn: less than 0.45 cations per 12 oxygens (i.e. <15 % Sps)

Plagioclase: Ca: less than 0.15 and preferably less than 0.7 cations per 8 oxygens (i.e. $0.15 < X_{An} < 0.7$)

Amphibole: Al: between 1.9 and 3.75 cations per 23 oxygens
Ti: less than 0.275 cations
Ca: greater than 1.5 cations
Na: between 0.3 and 0.6 cations
K: less than 0.4 cations
Fe/(Fe+Mg): preferably between 0.4 and 0.6 cations

These calculations are carried out for total Fe; the ferric iron content is not estimated, because the calibration was made on total Fe analyses. The mole fractions are calculated as follows (Kohn and Spear, 1989):

Garnet:

$$X_{Prp}^{Grt} = \frac{Mg}{Mg + Fe + Mn + Ca}$$

$$X_{Alm}^{Grt} = \frac{Fe}{Mg + Fe + Mn + Ca}$$

$$X_{Sps}^{Grt} = \frac{Mn}{Mg + Fe + Mn + Ca}$$

$$X_{Grs}^{Grt} = \frac{Ca}{Mg + Fe + Mn + Ca}$$

Plagioclase:

$$X_{An}^{Pl} = \frac{Ca}{Ca + Na + K}$$

$$X_{Ab}^{Pl} = \frac{Na}{Ca + Na + K}$$

$Si^{T1} = Si - 4.0$ $\quad Al^{T1} = 8.0 - Si$

$Al^{M2} = Al + Si - 8.0$ $\quad Ti^{M2} = Ti$

$Fe^{3+,M2} = Fe^{3+}$ (if any)

Amphibole: $Fe^{M2} = (2-(Al^{M2}+Ti^{M2}+Fe^{3+,M2})) \cdot (Fe/(Fe+Mg))$

$Mg^{M2} = (2-(Al^{M2}+Ti^{M2}+Fe^{3+,M2})) \cdot (Mg/(Fe+Mg))$

$Na^{A} = Si + Al + Ti + Fe^{3+} + Mg + Fe + Mn + Ca + Na - 15$

$\square^{A} = 1 - Na^{A} - K = 16 - Si + Al + Ti + Fe^{3+} + Mg + Fe + Mn + Ca + Na + K$

And then:

$$X_{Si,T1}^{Amph} = \frac{Si^{T1}}{4.0}$$

$$X_{Al,M2}^{Amph} = \frac{Al^{M2}}{2.0}$$

$$X_{Fe,M2}^{Amph} = \frac{Fe^{M2}}{2.0}$$

$$X_{\square^A}^{Amph} = \square^{A}$$

The following activity models should be used:
For garnet (Hodges and Spear, 1982):

$$a_{Prp}^{Grt} = \left(X_{Prp}^{Grt} \cdot \exp\left(\frac{(13800 - 6.28 \cdot T(K)) \cdot ((X_{Grs}^{Grt})^2 + X_{Alm}^{Grt} \cdot X_{Grs}^{Grt} + X_{Grs}^{Grt} \cdot X_{Sps}^{Grt})}{R \cdot T(K)} \right) \right)^3$$

$$a_{Grs}^{Grt} = \left(X_{Grs}^{Grt} \cdot \exp\left(\frac{(13800 - 6.28 \cdot T(K)) \cdot ((X_{Prp}^{Grt})^2 + X_{Alm}^{Grt} \cdot X_{Prp}^{Grt} + X_{Prp}^{Grt} \cdot X_{Sps}^{Grt})}{R \cdot T(K)} \right) \right)^3$$

$$a_{Alm}^{Grt} = \left(X_{Alm}^{Grt} \cdot \exp\left(\frac{(13800 - 6.28 \cdot T(K)) \cdot (-X_{Prp}^{Grt} \cdot X_{Grs}^{Grt})}{R \cdot T(K)} \right) \right)^3$$

where R = 8.314 J/mol·K.
For plagioclase (Hodges and Royden, 1984):

$$a_{An}^{Pl} = X_{An}^{Pl} \cdot \exp\left(\left(\frac{610.34}{T(K)} \right) - 0.3837 \right)$$

$$a_{Ab}^{Pl} = X_{Ab}^{Pl}$$

For amphibole (Kohn and Spear, 1990):

$$a_{tsch}^{Amph} = \frac{256}{27} \cdot X_{Al,T1}^{Amph} \cdot (X_{Si,T1}^{Amph})^3 \cdot \frac{Mg}{Fe+Mg}$$

$$a_{trem}^{Amph} = (X_{Si,T1}^{Amph})^4 \cdot \left(\frac{Mg}{Fe+Mg}\right)^2$$

$$a_{Fe-tsch}^{Amph} = \frac{256}{27} \cdot X_{Al,T1}^{Amph} \cdot (X_{Si,T1}^{Amph})^3 \cdot \frac{Fe}{Fe+Mg}$$

$$a_{Fe-trem}^{Amph} = (X_{Si,T1}^{Amph})^4 \cdot \left(\frac{Fe}{Fe+Mg}\right)^2$$

For quartz (Kohn and Spear, 1990):

$$a_{SiO_2}^{Qtz} = 1.0$$

A1.8 Amphibole-plagioclase thermometry

Holland and Blundy (1994) formulated two thermometers for coexisting amphibole and plagioclase.

A) edenite + 4 quartz = tremolite + albite (for assemblages with quartz)

For this reaction:

$$T_A(K) = \frac{-76.95 + 0.79 \cdot P(kbar) + Y_{Ab} + 39.4 \cdot X_{Na}^{A} + 22.4 \cdot X_{K}^{A} + (41.5 - 2.89 \cdot P(kbar)) \cdot X_{Al}^{M2}}{-0.0650 - R \cdot \ln\left(\frac{27 \cdot X_{sq}^{A} \cdot X_{Si}^{T1} \cdot X_{Ab}^{Plag}}{256 \cdot X_{Na}^{A} \cdot X_{Al}^{T1}}\right)} \qquad (A1.33)$$

Where: $Y_{Ab} = 0$ for $X_{Ab} > 0.5$

and $Y_{Ab} = 12.0 \cdot (1-X_{Ab})^2 - 3.0$ kJ for $X_{Ab} \leq 0.5$

R=0.0083144 kJ/mol·K

Other definitions are:

$$cm = Si + Al + Ti + Fe^{3+} + Fe^{2+} + Mg + Mn - 13.0$$

$$X_{Si}^{T1} = \frac{Si - 4}{4}$$

$$X_{Al}^{T1} = \frac{8 - Si}{4}$$

$$X_{Al}^{M2} = \frac{Al + Si - 8}{4}$$

$$X_{K}^{A} = K$$

$$X_{sq}^{A} = 3 - Ca - Na - K - cm$$

$$X_{Na}^{A} = Ca + Na + cm - 2$$

$$X_{Na}^{M4} = \frac{2 - Ca - cm}{2}$$

$$X_{Ca}^{M4} = \frac{Ca}{2}$$

Ferric iron is as explained in Appendix B of Holland and Blundy (1994).

B) edenite + albite = richterite + anorthite (for assemblages with or without quartz)

In this case:

$$T_B(K) = \frac{78.44 + Y_{Ab-An} - 33.6 \cdot X_{Na}^{M4} - (66.8 - 2.92 \cdot P(kbar)) \cdot X_{Al}^{M2} + 78.5 \cdot X_{Al}^{T1} + 9.4 \cdot X_{Na}^{A}}{0.0721 - R \cdot \ln\left(\frac{27 \cdot X_{Na}^{M4} \cdot X_{Si}^{T1} \cdot X_{An}^{plag}}{64 \cdot X_{Ca}^{M4} \cdot X_{Al}^{T1} \cdot X_{Ab}^{Plag}}\right)} \qquad (A1.34)$$

Where: $Y_{Ab\text{-}An} = 3.0$ kJ for $X_{Ab} > 0.5$

and $Y_{Ab} = 12.0 \cdot (2X_{Ab}-1)+3.0$ kJ for $X_{Ab} \leq 0.5$

Thermometer A is valid in the range 400-900 °C, for amphiboles which have $Na^{A} > 0.02$ p.f.u., $Al^{VI} < 1.8$ p.f.u. and Si between 6.0 and 7.7 p.f.u, and for plagioclases with $X_{An} < 0.90$. Thermometer B is valid in the range 500-900 °C, for feldspars with X_{An} between 0.1 and 0.9, and for amphiboles with $X_{Na,M4} > 0.03$, $Al^{VI} < 1.8$ p.f.u. and Si between 6.0 and 7.7 p.f.u.
When both thermometers are applied to a silica saturated rock, they should both yield the same temperature for a given pressure. When the rocks are undersaturated with respect to silica, T_A should be consistently higher than T_B. In this case T_B represents the equilibrium temperature. If $T_A < T_B$ plagioclase and amphibole may not have been in equilibrium or ferric iron has been wrongly estimated and the results should be ignored. The intersection of the two thermometers should not be used to obtain an estimate of pressure, because the coefficients were not optimised on the basis of minimising pressure residuals (Holland and Blundy, 1994).

A1.9 GASP barometry

The maximum pressure stability of anorthite is delimited by the reaction:

$$3\ CaAl_2Si_2O_8 = Ca_3Al_2Si_3O_{12} + 2\ Al_2SiO_5 + SiO_2 \qquad (A1.35)$$

or: anorthite = grossular + kyanite (or sillimanite) + quartz. For mineral assemblages with coexisting garnet, plagioclase, quartz and aluminosillicate the GASP geobarometer has been derived. An early callibration by Newton and Haselton (1981) was improved with new experimental data by Koziol and Newton (1988). Spear (1993, p. 525) has reformulated this calibration to the following barometer:

$$P(bar) = \frac{-48357 + 150.66 \cdot T(K) + 6.608 + R \cdot T(K) \cdot \ln K_{eq}}{6.608} \qquad (A1.36)$$

Where R = 8.3141 J/mol·K and

$$K_{eq} = \left(\frac{\alpha_{grs}^{Grt}}{\alpha_{an}^{Pl}} \right)^3 \qquad (A1.37)$$

The activity models used by Newton and Haselton (1981) when they calibrated this barometer should be used in this updated calibration. The activities of the grossular and anorthite endmembers are calculated as follows:

$$\alpha_{grs}^{Grt} = X_{grs}^{Grt} \cdot \exp\left(\frac{W_{Ca-Mg} \cdot \left(\left(X_{py}^{Grt}\right)^2 + X_{py}^{Grt} \cdot X_{alm}^{Grt} \right)}{R \cdot T(K)} \right) \qquad (A1.38)$$

Where $W_{Ca-Mg} = 3 \cdot 4.184 \cdot (3300 - 1.5 \cdot T(K))$ J/mol.

$$\alpha_{an}^{Pl} = \frac{X_{an}^{Pl} \cdot \left(1 + X_{an}^{Pl}\right)^2}{4} \cdot \exp\left(\frac{\left(1 - X_{an}^{Pl}\right)^2}{R \cdot T(K)} \cdot 4.184 \cdot \left(2050 + 9392 \cdot X_{an}^{Pl}\right) \right) \qquad (A1.39)$$

Great care should be taken when applying the GASP barometer to rocks with calcium-poor garnet and plagioclase. For garnets with $X_{grs} < 0.10$, plagioclases with $X_{an} < 0.30$ and $X_{grs} \cdot X_{an} < 0.05$ the GASP barometer should only be used with great caution (Todd, 1998).

A1.10 Garnet-biotite thermometry

A1.10.1 Ferry and Spear (1978)

The garnet-biotite Fe-Mg exchange thermometer of Ferry and Spear (1978) was recalculated to more convenient units (e.g. joule instead of calorie) by Spear (1993, his eqn. 15-44). Both garnet and biotite are assumed to have ideal mixing properties.

$$52112 - 19.51 \cdot T(K) + 0.238 \cdot P(bar) + 3 \cdot R \cdot T(K) \cdot \ln K_D = 0 \qquad \text{(A1.40)}$$

This can be rewritten to:

$$T(°C) = \frac{52112 + 0.238 \cdot P(bar)}{19.51 - 3 \cdot R \cdot \ln K_D} - 273 \qquad \text{(A1.41)}$$

Where R = 8.3144 J/mol·K

$$K_D = \frac{\left(Mg/Fe^{2+}\right)^{Grt}}{\left(Mg/Fe^{2+}\right)^{Bt}} \qquad \text{(A1.42)}$$

A1.10.2 Hodges and Spear (1982)

The Ferry and Spear (1978) thermometer was reformulated by Hodges and Spear (1982). Non-ideal mixing of garnet was incorporated into the calibration and this calibration seems to work better than FS78 in cases where $X_{Ca}+X_{Mn}$ in garnet is larger than 0.3. The thermometer was rewritten by Dave Waters (Oxford University), who published the equations on the internet (http://www.earth.ox.ac.uk/~davewa/pt/tools/grt-bt.xls).

$$T(°C) = \frac{\dfrac{12454}{3 \cdot \left(\dfrac{1.987}{8.3144}\right) \cdot R} + \dfrac{0.057}{3 \cdot \left(\dfrac{1.987}{8.3144}\right) \cdot R} \cdot 1000 \cdot P(kbar) + 1661 \cdot A}{\ln K_D + \dfrac{4.662}{3 \cdot \left(\dfrac{1.987}{8.3144}\right) \cdot R} + 0.755 \cdot A} - 273 \qquad \text{(A1.43)}$$

Where R = 8.3144 J/mol·K, and A is the HS82 compensation term:

$$A = (X_{Grs}^{Grt})^2 + (X_{Alm}^{Grt} \cdot X_{Grs}^{Grt}) + (X_{Sps}^{Grt} \cdot X_{Grs}^{Grt}) + (X_{Prp}^{Grt} \cdot X_{Grs}^{Grt}) \quad \text{and} \qquad \text{(A1.44)}$$

$$X_{Grs}^{Grt} = \frac{Ca}{Ca + Fe^{2+} + Mn + Mg} \qquad \text{(A1.45)}$$

etc.

$$K_D = \frac{1-\left(\frac{Mg}{Mg+Fe^{2+}}\right)^{Grt}}{\left(\frac{Mg}{Mg+Fe^{2+}}\right)^{Grt}} \cdot \frac{\left(\frac{Mg}{Mg+Fe^{2+}}\right)^{Bt}}{1-\left(\frac{Mg}{Mg+Fe^{2+}}\right)^{Bt}} = \left(\frac{Fe^{2+}}{Mg}\right)^{Grt} \cdot \left(\frac{Fe^{2+}}{Mg}\right)^{Bt} = \frac{(Fe^{2+}/Mg)^{Grt}}{(Fe^{2+}/Mg)^{Bt}} \qquad (A1.46)$$

A1.10.3 Kleemann and Reinhardt (1994)

A recent calibration of the garnet-biotite thermometer was published by Kleemann and Reinhardt (1994). It was derived from the datasets of two earlier calibrations (Ferry and Spear, 1978; Perchuk and Lavrent'eva, 1983). The new formulations takes non-ideal mixing of both garnet and biotite into account.

$$T(°C) = \frac{20253 + \Delta W_H^{Grt} + 77785 \cdot X_{Al}^{Bt} - 18138 \cdot X_{Ti}^{Bt} + (\Delta V_0 + \Delta W_V^{Grt}) \cdot P(bar)}{10.66 - R \cdot \ln K_D + \Delta W_S^{Grt} + 94.1 \cdot X_{Al}^{Bt} - 11.7 \cdot X_{Ti}^{Bt}} - 273 \qquad (A1.47)$$

Where:

$$X_{Al}^{Bt} = \frac{Al^{VI}}{Al^{VI} + Ti + Fe^{2+} + Mg + Mn} \qquad (A1.48)$$

$$X_{Ti}^{Bt} = \frac{Ti}{Al^{VI} + Ti + Fe^{2+} + Mg + Mn} \qquad (A1.49)$$

$$K_D = \frac{(Mg/Fe^{2+})^{Grt}}{(Mg/Fe^{2+})^{Bt}} \qquad (A1.50)$$

And R=8.3144 J/mol·K, ΔV_0 = 0.100 J/mol·K.
Garnet mixing properties were taken from Berman (1990):

$$\Delta W_H^{Grt} = 2620\,J/mol$$
$$\Delta W_V^{Grt} = 0.09\,J/bar$$
$$\Delta W_S^{Grt} = 5.08\,J/mol \cdot K$$

A1.11 Simultaneous solution of GASP and garnet-biotite

In chapter 3 I applied simultaneous solution of the GASP barometer (as described in Section A1.9) with two different calibrations of the garnet-biotite Fe-Mg exchange thermometer (FS78 and KR94, as described in Section A1.10). To this end the equations to be solved for P (A1.36) and T (A1.40 for FS78 and A1.47 for KR94, respectively) were rewritten. In order to apply this method the mineral assemblage containing garnet, plagioclase, aluminosillicate, biotite and quartz must be in apparent equilibrium. The exact formulations are printed below (Sections A1.11.1 and A1.11.2).

A1.11.1 GASP and Ferry and Spear (1978)

$$A = \frac{-48357 + 124265 \cdot \left(\left(X_{py}^{Grt}\right)^2 + X_{py}^{Grt} \cdot X_{alm}^{Grt}\right) - 12.55 \cdot \left(1 - X_{an}^{Pl}\right)^2 \cdot \left(2050 + 9392 \cdot X_{an}^{Pl}\right) + 6.608}{6608} \quad \text{(A1.51)}$$

$$B = \frac{3 \cdot R \cdot \ln K_{eq}^{GASP} - 56.48 \cdot \left(\left(X_{py}^{Grt}\right)^2 + X_{py}^{Grt} \cdot X_{alm}^{Grt}\right) + 150.66}{6608} \quad \text{(A1.52)}$$

$$C = \frac{52112}{19.51 - 3 \cdot R \cdot \ln K_D^{GrtBt}} \quad \text{(A1.53)}$$

$$D = \frac{238}{19.51 - 3 \cdot R \cdot \ln K_D^{GrtBt}} \quad \text{(A1.54)}$$

$$P(\text{kbar}) = \frac{A + B \cdot C}{1 - B \cdot D} \quad \text{(A1.55)}$$

$$T(^\circ\text{C}) = \frac{52112 + 238 \cdot P(\text{kbar})}{19.51 - 3 \cdot R \cdot \ln K_D^{GrtBt}} - 273 \quad \text{(A1.56)}$$

A1.11.2 GASP and Kleemann and Reinhardt (1994)

$$A = \frac{-48357 + 124265 \cdot \left(\left(X_{py}^{Grt}\right)^2 + X_{py}^{Grt} \cdot X_{alm}^{Grt}\right) - 12.55 \cdot \left(1 - X_{an}^{Pl}\right)^2 \cdot \left(2050 + 9392 \cdot X_{an}^{Pl}\right) + 6.608}{6608} \quad \text{(A1.57)}$$

$$B = \frac{3 \cdot R \cdot \ln K_{eq}^{GASP} - 56.48 \cdot \left(\left(X_{py}^{Grt}\right)^2 + X_{py}^{Grt} \cdot X_{alm}^{Grt}\right) + 150.66}{6608} \quad \text{(A1.58)}$$

$$C = \frac{20253 + 2620 + 77785 \cdot X_{Al}^{Bt} - 18138 \cdot X_{Ti}^{Bt}}{10.66 - R \cdot \ln K_D^{GrtBt} + 5.08 + 94.1 \cdot X_{Al}^{Bt} - 11.7 \cdot X_{Ti}^{Bt}} \quad \text{(A1.59)}$$

$$D = \frac{190}{10.66 - R \cdot \ln K_D^{GrtBt} + 5.08 + 94.1 \cdot X_{Al}^{Bt} - 11.7 \cdot X_{Ti}^{Bt}} \quad \text{(A1.60)}$$

$$P(\text{kbar}) = \frac{A + B \cdot C}{1 - B \cdot D} \quad \text{(A1.61)}$$

$$T(^\circ\text{C}) = \frac{20253 + 2620 + 77785 \cdot X_{Al}^{Bt} - 18138 \cdot X_{Ti}^{Bt} + 190 \cdot P(\text{kbar})}{10.66 - R \cdot \ln K_D^{GrtBt} + 5.08 + 94.1 \cdot X_{Al}^{Bt} - 11.7 \cdot X_{Ti}^{Bt}} - 273 \quad \text{(A1.62)}$$

Appendix 2

Representative electron microprobe analyses from the Lepontine gneisses

SAMPLE	UNIT	LITHOLOGY	MAIN	INCL / EARLY	RIMS / LATE	ACCESSORIES
AA97-4	CLE	EA	Grt, Omp, Ky, Amph, Rt		Amph, sympl, Plag	Qtz, Ttn, Plag
AA97-5	CLE	EA	Grt, Omp, Ky, Amph, Rt		Amph, sympl, Plag	Qtz, Plag, Ilm
AA97-6	CLE	EA	Grt, Omp, Ky, Amph, Rt		Amph, sympl	Qtz, Plag
AA97-7	CLE	EA	Grt, sympl (Omp, Ky), Amph, Rt, Czo	Omp, Ky	Amph, Plag, Ep	Qtz, Plag, WhM
AA97-8	CLL	MP	Ky, Bt, St, Grt, Qtz, Plag, Ilm	Grt	Sill, Kf, Bt	Rt, Ap, Zrn
AA97-10A,B	Arb	EA	Grt, sympl (Omp), Qtz, Plag	Omp	Ep Amph	Rt, Ttn
AA97-11	Arb	EA	Amph, Plag, Qtz	Ky, Czo		
AA97-15	Arb	EA	Grt, Amph, Plag, Qtz		Amph, Qtz, Chl	Ilm
AA97-16(1,2)	Arb	EA	Grt, Amph, Ky, Bt, Plag, Qtz, St		Sill, Bt, Qtz	Ilm
AA97-18	Arb	CAL	Bt, Amph, Qtz, Kf		Chl	Carb, Ttn
AA97-20	Arb	OR	Bt, Kf, Plag, Qtz, Ep			Zrn
AA97-22	CLL	AM	Grt, Amph, Plag, Qtz			Op
AA97-24	CLL	MP	Grt, Bt, St, Qtz, Plag, Kf, WhM		Chl	Carb, Ilm
AA97-25	CLL	MP	Grt, St, Plag, Kf, Qtz		Chl	Ilm
AA97-26P	CLL	MP	Grt, Ky, St, Bt, Plag, Kf, Qtz	Ctd	Sill, Chl (later)	Op
AA97-28	CLL	OR	Grt, Plag, Qtz, Bt		Bt, Chl (later)	Op
AA97-31A	CLL	AM	Grt, Amph, Bt, Qtz, Plag		Chl, Qtz	Ilm, Py
AA97-32//	CLL	MP	Grt, Ky, St, Plag, Qtz		Sill, Chl (later)	Rt, Op
AA97-33	CLE	EA	Grt, Omp, Amph		sympl (Omp)	Rt
AA98-3P	CLL	AM	Grt, Amph, Plag, Qtz, Di	Bt, Amph, Plag, Ep	Amph, Chl	Ilm, Ttn
AA98-6L	CLL	OR	Plag, Qtz, Bt, Amph, Zo	Grt	Bt	Op
AA98-8A	CLL	MP	Grt, Ky, Bt, St, Qtz, Plag	Ctd, St, Chl, WhM	Crd, Sill, Bt, Kf, Chl (later)	Rt, Apt, Zrn, Op
AA98-9	CLL	AM / OR	Grt, Amph, Qtz, Plag		Bt, Chl (later)	Op, Zo
AA98-11	CLL	AM / OR	Grt, Amph, Plag, Qtz, Di, Scp	Grt	Bt, Chl (later)	Op, Carb
AA98-12	CLL	AM / OR	Grt, Ky, Bt, St, Plag, Qtz	Grt	Bt, Sill, Chl (later)	Op
AA98-13B	CLL	AM / OR	Ky, Plag, Bt, Qtz	Grt, Ep, WhM	Chl	Op
AA98-21BL	Arb	AM	Ep, Czo, Amph, Carb, Plag, Qtz			Ttn
AA98-23	Arb	Aplite	Amph, Plag, Qtz, Bt		Chl	
AA98-26L	Arb	OR	Plag, Qtz, Bt	WhM, Grt	Chl, Czo	
AA98-32	Arb	EA	Amph, Plag, Qtz	Grt	sympl (Amph), Bt	Ilm, Ttn
AA98-33A,B	Arb	EA	Grt, Amph, Plag, sympl (Omp), Di		Amph, Bt, Chl (later)	Qtz, Rt, Hem
AA98-35	Arb	CAL	Amph, Carb, Scp, Di, Plag, Qtz		Bt	Op
AA98-36	Arb	CAL	Amph, Carb, Scp, Di, Plag, Qtz	Ep	Bt	Op
AA98-37	Arb	CAL	Grt, Amph, Carb, Plag, Qtz	Ep	Bt	WhM, Ttn
AA98-51	Arb	EA	Grt, Ky, WhM, Plag, Qtz		Amph, Plag, Bt (later)	Op
AA98-54P	Arb	CAL	Grt, Amph, Carb, Plag, Kf	Ep, Qtz	Amph, Bt (later)	Ttn
AA98-59Y	CLL	MP	Grt, Bt, Plag, St, Qtz		Bt, Chl (later)	Op
AA98-65	Arb	EA	Grt, Amph, Czo, Di, Plag			Hem, Qtz
AA98-66B	Arb	EA	Grt, Amph, Plag, Qtz	Omp, Ep	Bt, Chl (later)	Rt, Op

Table A2.1: Mineral assemblages of studied samples. In this and the following tables: EA = eclogite-amphibolite, MP = metapelite, OR = orthogneiss, AM = amphibolite, CAL = calc-silicate.

Unit	CLE	CLE	CLE	CLE	CLE	CLE	CLE	CLE	CLL	CLL	Arb	Arb	Arb	Arb	Arb	Arb	Arb
Lithology	EA	EA	EA	EA	EA	EA	EA	EA	MP	MP	EA	EA	EA	EA	EA	EA	EA
Mineral	Grt	Grt	Grt	Grt	Grt	Grt	Grt	Grt	Grt	Grt	Grt	Grt	Grt	Grt	Grt	Grt	Grt
Point	4.1	4.2	3.50	1.9	1.15	4.26	4.34	4.49	2.14	2.18	1.171	2.146	2.165	3.2	1.109	1.137	1.91
Core or rim	core	rim	core	rim	core	rim	core										
Thin section	AA97-4	AA97-4	AA97-5	AA97-6	AA97-6	AA97-7	AA97-7	AA97-7	AA97-8	AA97-8	AA97-10A	AA97-10B	AA97-10B	AA97-10B	AA97-15	AA97-1	AA97-16-(1)
Na_2O	0.03	0.00	0.03	0.02	0.03	0.06	0.00	0.03	0.00	0.04	0.02	0.02	0.05	0.00	0.02	0.00	0.00
MgO	8.27	8.24	9.07	9.79	9.65	8.33	8.61	8.62	4.52	4.76	6.64	6.79	6.82	6.73	3.74	5.14	6.31
SiO_2	39.12	39.14	39.56	39.71	39.06	39.00	38.96	39.26	37.68	37.56	38.31	38.93	39.29	38.87	37.72	37.24	38.13
Al_2O_3	22.06	22.28	21.63	22.28	21.72	22.21	22.07	21.98	20.69	20.73	21.60	21.65	21.84	21.44	21.08	21.63	21.36
K_2O	0.01	0.02	0.00	0.01	0.01	0.00	0.00	0.00	0.01	0.00	0.00	0.00	0.02	0.01	0.00	0.00	0.00
CaO	10.64	10.23	9.99	8.06	9.30	9.64	9.68	9.76	2.66	2.63	11.48	10.81	9.11	10.82	8.65	8.59	5.42
TiO_2	0.00	0.01	0.00	0.00	0.01	0.01	0.02	0.01	0.00	0.01	0.11	0.09	0.05	0.11	0.00	0.03	0.04
FeO	19.65	19.89	19.19	19.90	18.61	19.92	19.80	19.94	33.44	34.04	21.32	21.87	23.46	21.69	27.45	26.06	27.47
MnO	0.41	0.45	0.48	0.52	0.36	0.59	0.44	0.44	1.43	1.13	0.72	0.73	0.92	0.62	0.94	0.58	1.49
Cr_2O_3	0.00	0.00	0.06	0.03	0.12	0.09	0.06	0.09	0.00	0.01	0.03	0.04	0.07	0.01	0.00	0.05	0.00
NiO			0.01		0.00				0.02	0.00							0.03
Total	100.14	100.22	99.92	100.26	98.82	99.78	99.57	100.01	100.42	100.85	100.17	100.86	101.51	100.28	99.56	99.25	100.18
Si	2.96	2.96	2.99	2.99	2.98	2.97	2.96	2.97	2.99	2.97	2.93	2.96	2.98	2.98	2.98	2.92	2.97
Al	1.97	1.99	1.93	1.98	1.95	1.99	1.98	1.96	1.93	1.93	1.95	1.94	1.95	1.93	1.96	2.00	1.96
Ti	0.00	0.00	0.00	0.00	0.00	0.00	0.00	0.00	0.00	0.00	0.01	0.01	0.00	0.01	0.00	0.00	0.00
Fe^{tot}	1.24	1.26	1.21	1.25	1.19	1.27	1.26	1.26	2.22	2.25	1.37	1.39	1.49	1.39	1.82	1.71	1.79
Mn	0.03	0.03	0.03	0.03	0.02	0.04	0.03	0.03	0.10	0.08	0.05	0.05	0.06	0.04	0.06	0.04	0.10
Mg	0.93	0.93	1.02	1.10	1.10	0.94	0.98	0.97	0.53	0.56	0.76	0.77	0.77	0.77	0.44	0.60	0.73
Ca	0.86	0.83	0.81	0.65	0.76	0.79	0.79	0.79	0.23	0.22	0.94	0.88	0.74	0.89	0.73	0.72	0.45
Ni			0.00		0.00				0.00	0.00		0.00	0.00	0.00			0.00
Cr	0.00	0.00	0.00	0.00	0.01	0.01	0.00	0.01	0.00	0.00	0.00				0.00	0.00	0.00
Cations	8.00	8.00	8.00	8.00	8.00	8.00	8.00	8.00	8.00	8.00	8.00	8.00	8.00	8.00	8.00	8.00	8.00
Fe^{3+} (Droop)	0.10	0.08	0.09	0.05	0.09	0.07	0.09	0.09	0.09	0.14	0.17	0.12	0.07	0.10	0.07	0.15	0.10
Fe^{2+}	1.14	1.18	1.13	1.21	1.10	1.20	1.17	1.24	2.13	2.11	1.19	1.27	1.41	1.29	1.75	1.56	1.69
XPyrope	31.49	31.36	34.18	36.75	36.81	31.81	32.92	30.07	17.88	18.88	25.76	25.93	25.83	25.76	14.76	20.55	24.66
XAndradite	5.00	4.04	4.23	2.25	4.28	3.30	4.32	4.21	4.34	6.74	8.34	6.14	3.83	5.29	3.37	6.95	5.07
XAlmandine	38.49	39.67	37.72	40.39	36.91	40.44	39.52	41.68	71.28	71.08	40.64	42.79	47.37	43.16	58.57	53.43	56.76
XUvarovite	0.01	0.00	0.17	0.10	0.36	0.26	0.16	0.34	0.00	0.03	0.10	0.13	0.20	0.04	0.00	0.15	0.00
XSpessartine	0.88	0.97	1.03	1.11	0.77	1.29	0.95	1.43	3.22	2.54	1.58	1.59	1.98	1.34	2.10	1.33	3.31
XGrossular	24.12	23.95	22.64	19.42	20.86	22.90	22.13	22.27	3.23	0.74	23.59	23.41	20.80	24.41	21.20	17.60	10.15

Table A2.2: Representative analyses of garnet. Analyses in wt%, recalculated to 12 oxygens and 8 cations.

Unit	Arb	Arb	CLL	CLL	CLL	CLL	CLL	CLL	CLL	CLL	CLL	CLL	CLL	CLE	CLE	CLL
Lithology	EA	OR	AM	MP	MP	MP	OR	OR	AM	AM	AM	MP	MP	EA	EA	OR
Mineral	Grt	Grt	Grt	Grt	Grt	Grt	Grt	Grt	Grt	Grt	Grt	Grt	Grt	Grt	Grt	Grt
Point	2.19	3.62	4.84	2.242	1.123	2.96	2.257	2.272	3.40	3.44	3.50	1.85	1.87	1.18	1.31	3.29
Core or rim																
Thin section	AA97-16(2)	AA97-18	AA97-22	AA97-24	AA97-25	AA97-26P	AA97-28	AA97-28	AA97-31A	AA97-31A	AA97-31A	AA97-32//	AA97-32//	AA97-33	AA97-33	AA98-6L
Na_2O	0.00	0.04	0.03	0.00	0.00	0.03	0.04	0.14	0.00	0.00	0.00	0.00	0.00	0.00	0.06	0.00
MgO	7.25	1.55	4.19	4.61	4.69	6.20	5.50	4.90	4.01	4.00	3.79	4.32	3.61	9.79	10.62	4.02
SiO_2	38.46	37.65	37.73	37.71	37.21	38.00	38.11	37.64	37.60	37.95	37.41	37.13	36.65	39.33	39.73	37.36
Al_2O_3	21.51	20.16	20.18	21.03	20.65	21.15	21.38	21.28	20.83	20.96	20.55	20.87	20.63	22.20	22.48	20.55
K_2O	0.00	0.00	0.01	0.02	0.00	0.00	0.00	0.01	0.01	0.01	0.01	0.01	0.01	0.00	0.00	0.00
CaO	6.27	11.07	4.55	2.89	3.01	1.85	4.78	5.17	4.54	5.79	5.57	1.56	1.82	8.35	8.67	3.79
TiO_2	0.00	0.04	0.00	0.00	0.00	0.00	0.00	0.00	0.03	0.01	0.06	0.00	0.04	0.03	0.03	0.01
FeO	24.98	22.43	32.58	34.47	34.00	29.65	27.91	27.60	30.96	29.61	30.49	33.49	33.63	19.57	18.13	30.35
MnO	0.69	8.10	1.56	0.46	0.53	2.79	2.69	2.84	2.06	1.64	1.79	2.70	3.03	0.75	0.64	3.36
Cr_2O_3	0.00	0.00	0.00	0.01	0.03	0.06	0.00	0.00	0.04	0.00	0.00	0.00	0.00	0.13	0.06	0.04
NiO		0.05	0.00									0.04	0.00			0.05
Total	99.16	100.97	100.78	101.18	100.08	99.63	100.37	99.56	99.99	99.96	99.65	100.07	99.38	100.12	100.27	99.43
Si	2.99	2.97	2.98	2.97	2.96	3.00	2.98	2.98	2.99	3.01	2.98	2.97	2.96	2.96	2.97	2.99
Al	1.97	1.88	1.88	1.95	1.93	1.97	1.97	1.99	1.95	1.96	1.93	1.96	1.96	1.97	1.98	1.94
Ti	0.00	0.00	0.00	0.00	0.00	0.00	0.00	0.00	0.00	0.00	0.00	0.00	0.00	0.00	0.00	0.00
Fe^{tot}	1.63	1.48	2.15	2.27	2.26	1.96	1.83	1.83	2.06	1.96	2.03	2.24	2.27	1.23	1.13	2.03
Mn	0.05	0.54	0.10	0.03	0.04	0.19	0.18	0.19	0.14	0.11	0.12	0.18	0.21	0.05	0.04	0.23
Mg	0.84	0.18	0.49	0.54	0.56	0.73	0.64	0.58	0.47	0.47	0.45	0.51	0.44	1.10	1.18	0.48
Ca	0.52	0.94	0.39	0.24	0.26	0.16	0.40	0.44	0.39	0.49	0.48	0.13	0.16	0.67	0.69	0.33
Ni	0.00	0.00	0.00	0.00	0.00			0.00	0.00	0.00	0.00	0.00	0.00	0.01	0.00	0.00
Cr		0.00	0.00	0.00		0.00	0.00					0.00	0.00			0.00
Cations	8.00	8.00	8.00	8.00	8.00	8.00	8.00	8.00	8.00	8.00	8.00	8.00	8.00	8.00	8.00	8.00
Fe^{3+} (Droop)	0.04	0.17	0.15	0.12	0.15	0.03	0.06	0.05	0.07	0.03	0.09	0.10	0.11	0.09	0.08	0.08
Fe^{2+}	1.58	1.31	2.00	2.15	2.11	1.93	1.76	1.77	1.99	1.93	1.94	2.13	2.16	1.14	1.05	1.96
XPyrope	28.10	6.13	16.53	18.22	18.78	24.31	21.52	19.38	15.88	15.71	15.07	17.32	14.68	37.08	39.80	16.03
XAndradite	2.07	8.39	7.54	5.59	7.14	1.50	3.19	2.65	3.45	1.49	4.75	4.51	5.35	4.42	3.92	3.79
XAlmandine	52.93	44.08	67.05	72.54	71.36	64.26	59.07	59.51	66.54	64.27	64.97	71.91	73.01	38.56	35.47	65.38
XUvarovite	0.00	0.00	0.00	0.03	0.08	0.20	0.00	0.00	0.12	0.00	0.00	0.00	0.00	0.38	0.18	0.11
XSpessartine	1.51	18.21	3.51	1.04	1.20	6.22	5.97	6.39	4.64	3.67	4.05	6.16	6.96	1.62	1.36	7.61
XGrossular	15.39	23.08	5.37	2.59	1.44	3.51	10.25	12.06	9.38	14.86	11.17	0.00	0.00	17.95	19.27	6.96

Table A2.2: Continued.

Unit	CLL	CLL	CLL	CLL	CLL	CLL	CLL	CLL	Arb	Arb	Arb	Arb	Arb	Arb	CLL	Arb
Lithology	MP	MP	MP	AM / OR	AM / OR	AM / OR	MP	MP	EA	EA	EA	EA	EA	CAL	MP	EA
Mineral	Grt	Grt	Grt	Grt	Grt	Grt	Grt	Grt	Grt	Grt	Grt	Grt	Grt	Grt	Grt	Grt
Point	2.216	2.221	2.222	3.130	2.63	2.67	2.106	1.106	1.58	1.66	1.67	3.9	2.150	3.132	3.86	1.434
Core or rim																
Thin section	AA98-8A	AA98-8A	AA98-8A	AA98-9	AA98-11	AA98-11	AA98-12	AA98-13B	AA98-32	AA98-32	AA98-32	AA98-33A	AA98-33B	AA98-54P	AA98-59Y	AA98-66B
Na_2O	0.03	0.00	0.03	0.00	0.01	0.03	0.00	0.00	0.05	0.03	0.00	0.00	0.01	0.05	0.00	0.06
MgO	5.91	7.92	5.58	4.91	4.22	4.68	3.93	4.33	7.46	7.36	7.72	8.41	7.35	2.17	4.52	5.85
SiO_2	37.54	38.18	37.40	37.75	37.32	36.50	36.37	37.00	38.85	38.87	38.84	38.74	37.84	37.47	36.83	38.28
Al_2O_3	21.55	21.63	21.36	20.19	20.65	20.87	20.93	20.82	21.90	22.11	21.91	21.52	22.12	21.35	21.02	21.84
K_2O	0.00	0.00	0.01	0.00	0.00	0.01	0.00	0.00	0.00	0.00	0.00	0.00	0.00	0.01	0.00	0.02
CaO	2.17	2.70	2.31	4.79	4.68	4.57	2.29	2.15	7.89	7.80	9.26	8.28	9.50	13.44	1.89	9.41
TiO_2	0.00	0.00	0.00	0.00	0.01	0.00	0.00	0.00	0.00	0.05	0.09	0.03	0.05	0.09	0.00	0.15
FeO	31.11	28.02	31.30	30.21	31.04	31.41	34.60	34.10	23.74	23.12	21.32	21.68	22.75	22.46	34.92	24.04
MnO	2.67	1.08	2.45	2.41	2.33	2.14	1.69	2.31	0.65	0.92	0.63	0.63	0.60	2.79	1.07	0.74
Cr_2O_3	0.00	0.05	0.00	0.00	0.06	0.00	0.01	0.00	0.02	0.08	0.02	0.02	0.04	0.11	0.08	0.03
NiO				0.01				0.00								
Total	100.94	99.53	100.40	100.26	100.24	100.17	99.83	100.71	100.49	100.24	99.78	99.27	100.21	99.90	100.32	100.31
Si	2.93	2.97	2.94	2.98	2.96	2.89	2.92	2.94	2.97	2.98	2.97	2.97	2.89	2.95	2.93	2.95
Al	1.99	1.98	1.98	1.88	1.93	1.95	1.98	1.95	1.97	1.99	1.98	1.95	1.99	1.98	1.97	1.99
Ti	0.00	0.00	0.00	0.00	0.00	0.00	0.00	0.00	0.00	0.00	0.01	0.00	0.00	0.01	0.00	0.01
Fe^{tot}	2.03	1.82	2.06	2.00	2.06	2.08	2.32	2.26	1.52	1.48	1.36	1.39	1.45	1.48	2.32	1.55
Mn	0.18	0.07	0.16	0.16	0.16	0.14	0.12	0.16	0.04	0.06	0.04	0.04	0.04	0.19	0.07	0.05
Mg	0.69	0.92	0.65	0.58	0.50	0.55	0.47	0.51	0.85	0.84	0.88	0.96	0.84	0.26	0.54	0.67
Ca	0.18	0.22	0.19	0.41	0.40	0.39	0.20	0.18	0.65	0.64	0.76	0.68	0.78	1.13	0.16	0.78
Ni					0.00	0.00	0.00	0.00	0.00	0.01	0.00	0.00	0.00	0.00	0.01	0.00
Cr	0.00	0.00	0.00	0.00				0.00						0.01		
Cations	8.00	8.00	8.00	8.00	8.00	8.00	8.00	8.00	8.00	8.00	8.00	8.00	8.00	8.00	8.00	8.00
Fe^{3+} (droop)	0.15	0.07	0.13	0.16	0.15	0.27	0.19	0.18	0.09	0.04	0.07	0.10	0.21	0.10	0.16	0.09
Fe^{2+}	1.89	1.76	1.93	1.84	1.91	1.81	2.14	2.09	1.43	1.44	1.30	1.29	1.24	1.38	2.16	1.46
XPyrope	23.44	30.92	22.23	19.37	16.85	19.10	16.12	17.43	28.63	28.18	29.57	32.33	28.92	8.63	18.27	22.70
XAndradite	6.81	3.24	6.09	7.75	7.24	12.20	6.80	6.21	4.21	2.17	3.57	5.00	9.72	4.97	5.25	4.64
XAlmandine	64.34	59.12	65.61	61.62	64.44	62.54	73.18	71.06	48.19	48.32	43.54	43.39	42.88	46.71	73.78	49.41
XUvarovite	0.00	0.15	0.00	0.00	0.17	0.00	0.04	0.00	0.05	0.25	0.07	0.05	0.12	0.33	0.24	0.09
XSpessartine	5.41	2.40	5.54	5.41	5.29	4.96	3.94	5.29	1.42	2.01	1.37	1.39	1.34	6.30	2.45	1.64
XGrossular	0.00	4.18	0.53	5.85	6.00	1.20	0.00	0.00	17.51	19.08	21.87	17.84	17.01	33.06	0.00	21.52

Table A2.2: Continued.

Unit	CLE	CLE	CLE	CLE	CLE	CLE	CLE	CLE	CLE	CLE	CLE	CLE	CLE	CLE	CLE
Litholgy	EA	EA	EA	EA	EA	EA	EA	EA	EA	EA	EA	EA	EA	EA	EA
Mineral	Omp	Omp	Omp	Omp	Omp	Omp	Omp	Omp	Omp	Omp	Omp	Omp	Omp	Omp	Omp
Point	4.4	4.7	4.12	4.16	3.43	3.49	3.51	3.53	1.8	1.18	1.36	1.61	4.27	4.29	4.47
Thin section	AA97-4	AA97-4	AA97-4	AA97-4	AA97-5	AA97-5	AA97-5	AA97-5	AA97-6	AA97-6	AA97-6	AA97-6	AA97-7	AA97-7	AA97-7
Na_2O	5.67	6.69	5.40	5.25	6.88	6.48	6.68	6.14	5.16	5.98	6.98	6.99	3.53	5.59	5.66
MgO	8.80	8.46	9.12	9.60	8.62	8.58	8.01	8.89	9.70	9.15	8.09	8.39	11.85	9.03	9.07
SiO_2	53.72	55.73	53.60	53.93	56.44	56.19	55.97	55.27	52.91	54.07	54.85	55.29	50.98	53.14	53.26
Al_2O_3	11.89	12.37	11.19	10.74	11.99	11.98	13.00	11.67	11.02	11.83	12.65	12.49	10.07	11.74	11.38
K_2O	0.00	0.00	0.01	0.00	0.00	0.01	0.00	0.00	0.01	0.02	0.00	0.01	0.00	0.00	0.00
CaO	15.02	13.57	15.74	15.79	13.84	13.81	13.42	14.65	15.69	15.01	12.97	13.13	17.07	15.55	15.52
TiO_2	0.24	0.09	0.25	0.16	0.08	0.07	0.15	0.15	0.13	0.23	0.10	0.05	0.12	0.22	0.25
FeO	3.99	2.97	4.09	4.40	2.69	2.78	2.97	3.36	5.16	3.44	3.02	2.49	6.01	4.01	3.89
MnO	0.05	0.02	0.07	0.04	0.00	0.05	0.03	0.00	0.01	0.11	0.00	0.02	0.12	0.04	0.01
NiO	0.00	0.06	0.06	0.00	0.09	0.07	0.00	0.00	0.04	0.02	0.02	0.00	0.05	0.08	0.12
Cr_2O_3					0.00	0.04	0.02	0.00			0.09				
Total	99.34	99.88	99.40	99.87	100.55	99.90	100.20	100.13	99.77	99.83	98.66	98.83	99.75	99.29	99.15
Si	1.93	1.97	1.92	1.93	1.98	1.99	1.98	1.96	1.90	1.92	1.96	1.97	1.84	1.91	1.91
Al^{IV}	0.07	0.03	0.08	0.07	0.02	0.01	0.02	0.04	0.10	0.08	0.04	0.03	0.16	0.09	0.09
Al^{VI}	0.43	0.49	0.40	0.38	0.48	0.49	0.52	0.45	0.36	0.42	0.49	0.49	0.27	0.40	0.40
Ti	0.01	0.00	0.01	0.00	0.00	0.00	0.00	0.00	0.00	0.01	0.00	0.00	0.00	0.01	0.01
Cr	0.00	0.00	0.00	0.00	0.00	0.00	0.00	0.00	0.00	0.00	0.00	0.00	0.00	0.00	0.00
Fe^{tot}	0.12	0.09	0.12	0.13	0.08	0.08	0.09	0.10	0.15	0.10	0.09	0.07	0.18	0.12	0.12
Mg	0.47	0.45	0.49	0.51	0.45	0.45	0.42	0.47	0.52	0.49	0.43	0.45	0.64	0.48	0.49
Mn	0.00	0.00	0.00	0.00	0.00	0.00	0.00	0.00	0.00	0.00	0.00	0.00	0.00	0.00	0.00
Ca	0.58	0.51	0.61	0.61	0.52	0.52	0.51	0.56	0.60	0.57	0.50	0.50	0.66	0.60	0.60
Na	0.39	0.46	0.38	0.36	0.47	0.44	0.46	0.42	0.36	0.41	0.48	0.48	0.25	0.39	0.39
Ni					0.00	0.00	0.00	0.00	0.00	0.00	0.00	0.00			
Cations	4.00	4.00	4.00	4.00	4.00	4.00	4.00	4.00	4.00	4.00	4.00	4.00	4.00	4.00	4.00
Fe^{3+} (C&C 1974)	0.00	0.00	0.00	0.00	0.00	0.00	0.00	0.00	0.00	0.00	0.00	0.00	0.00	0.00	0.00
Fe^{2+}	0.12	0.09	0.12	0.13	0.08	0.08	0.09	0.10	0.15	0.10	0.09	0.07	0.18	0.12	0.12
XJd (=XNa-XAcm (Fe^{3+}))															
XJd	0.39	0.46	0.38	0.36	0.47	0.44	0.46	0.42	0.36	0.41	0.48	0.48	0.25	0.39	0.39

Table A2.3: Representative analyses of pyroxenes. Analyses in wt%, normalised to 6 oxygens and 4 cations.

Unit	CLE	Arb	Arb	CLE	CLE	CLE	CLE	Arb	Arb	Arb	Arb	Arb	Arb	Arb
Lithology	EA	EA	EA	EA	EA	EA	EA	CAL	CAL	CAL	EA	EA	EA	EA
Mineral	Omp	Di	Di	Omp	Omp	Omp	Omp	Di	Di	Di	Di	Di	Di	Di
Point	4.52	1.53	1.56	1.13	1.19	1.28	1.51	3.135	3.140	3.151	2.47	2.52	2.58	2.68
Thin section	AA97-7	AA97-10A	AA97-10A	AA97-33	AA97-33	AA97-33	AA97-33	AA98-36	AA98-36	AA98-36	AA98-65	AA98-65	AA98-65	AA98-65
Na_2O	5.06	1.00	1.91	5.92	3.85	5.86	6.77	0.14	0.21	0.36	0.43	0.45	1.65	0.74
MgO	9.44	14.24	13.24	9.52	11.96	9.64	9.14	14.13	12.93	12.77	13.37	12.44	13.93	13.86
SiO_2	53.68	53.26	53.26	55.00	53.21	55.17	55.59	53.65	52.91	53.07	53.04	52.28	53.83	53.17
Al_2O_3	10.53	1.84	1.75	11.14	8.23	11.05	12.04	0.49	0.81	1.36	0.94	1.16	3.02	1.72
K_2O	0.00	0.00	0.00	0.00	0.00	0.00	0.00	0.01	0.00	0.00	0.00	0.00	0.00	0.00
CaO	16.14	22.43	20.61	14.57	17.68	14.85	13.99	25.16	24.60	24.34	23.90	24.14	21.67	22.68
TiO_2	0.29	0.09	0.09	0.10	0.14	0.07	0.09	0.00	0.04	0.03	0.07	0.05	0.13	0.05
FeO	4.49	6.58	8.14	3.00	4.26	3.19	2.87	6.66	8.53	8.52	8.00	9.14	6.02	7.71
MnO	0.06	0.06	0.13	0.04	0.16	0.02	0.00	0.21	0.33	0.27	0.73	0.70	0.11	0.17
NiO	0.08	0.02	0.03	0.09	0.08	0.04	0.00	0.11	0.14	0.12	0.00	0.06	0.06	0.01
Cr_2O_3								0.03	0.06	0.01				
Total	99.64	99.44	99.13	99.32	99.49	99.83	100.48	100.56	100.45	100.81	100.47	100.36	100.36	100.09
Si	1.93	1.97	1.98	1.96	1.92	1.96	1.95	1.98	1.97	1.97	1.97	1.95	1.96	1.97
Al^{IV}	0.07	0.03	0.02	0.04	0.08	0.04	0.05	0.02	0.03	0.03	0.03	0.05	0.04	0.03
Al^{VI}	0.37	0.05	0.05	0.43	0.27	0.42	0.45	0.00	0.00	0.03	0.01	0.00	0.09	0.04
Ti	0.01	0.00	0.00	0.00	0.00	0.00	0.00	0.00	0.00	0.00	0.00	0.00	0.00	0.00
Cr	0.00	0.00	0.00	0.00	0.00	0.00	0.00	0.00	0.00	0.00	0.00	0.00	0.00	0.00
Fe^{tot}	0.13	0.20	0.25	0.09	0.13	0.09	0.08	0.21	0.27	0.26	0.25	0.29	0.18	0.24
Mg	0.51	0.78	0.73	0.51	0.64	0.51	0.48	0.78	0.72	0.71	0.74	0.69	0.76	0.76
Mn	0.00	0.00	0.00	0.00	0.00	0.00	0.00	0.01	0.01	0.01	0.02	0.02	0.00	0.01
Ca	0.62	0.89	0.82	0.56	0.68	0.57	0.53	0.99	0.98	0.97	0.95	0.96	0.85	0.90
Na	0.35	0.07	0.14	0.41	0.27	0.40	0.46	0.01	0.01	0.03	0.03	0.03	0.12	0.05
Ni								0.00	0.00	0.00				
Cations	4.00	4.00	4.00	4.00	4.00	4.00	4.00	4.00	4.00	4.00	4.00	4.00	4.00	4.00
Fe^{3+} (C&C 1974)	0.00	0.00	0.06	0.00	0.00	0.00	0.00	0.00	0.00	0.00	0.00	0.00	0.00	0.00
Fe^{2+}	0.13	0.20	0.20	0.09	0.13	0.09	0.08	0.21	0.27	0.26	0.25	0.29	0.18	0.24
XJd (=XNa-XAcm (Fe^{3+}))														
XJd	0.35	0.07	0.08	0.41	0.27	0.40	0.46	0.01	0.01	0.03	0.03	0.03	0.12	0.05

Table A2.3: Continued.

Unit	CLE	CLE	Arb	Arb	Arb	Arb	Arb	Arb	Arb	Arb	CLL	CLL	CLL	CLL	CLL
Lithology	EA	EA	EA	EA	EA	EA	EA	EA	EA	EA	AM	AM	AM	AM	AM
Mineral	Amph	Amph	Amph	Amph	Amph	Amph	Amph	Amph	Amph	Amph	Amph	Amph	Amph	Amph	Amph
Point	4.40	4.50	3.5	3.7	3.14	3.24	1.111	1.99	2.24	2.25	4.89	3.43	3.45	3.51	3.54
Thin section	AA97-7	AA97-7	AA97-10B	AA97-10B	AA97-10B	AA97-11	AA97-15	AA97-16(1)	AA97-16(2)	AA97-16(2)	AA97-22	AA97-31A	AA97-31A	AA97-31A	AA97-31A
Na_2O	3.88	3.64	3.73	3.24	2.49	1.55	1.28	1.94	1.72	1.69	1.34	1.33	1.49	1.40	1.38
MgO	14.13	11.63	10.82	11.85	13.62	12.20	12.49	11.56	12.46	12.05	8.38	8.03	8.20	7.95	8.08
SiO_2	42.49	38.93	38.88	40.27	43.05	43.46	45.81	41.21	44.23	44.13	40.98	40.51	39.92	40.01	40.49
Al_2O_3	15.88	18.42	18.93	16.79	14.20	12.00	8.35	13.77	11.50	11.08	14.67	15.04	15.74	15.50	15.60
K_2O	0.27	0.12	0.06	0.30	0.52	0.87	0.08	0.68	0.24	0.26	0.41	0.54	0.68	0.69	0.45
CaO	9.91	11.19	11.52	12.08	11.51	12.42	10.63	10.51	10.50	10.28	10.50	10.63	10.84	10.83	10.40
TiO_2	0.54	0.05	2.14	1.68	1.55	0.79	0.01	1.01	0.62	0.91	0.61	0.62	0.64	0.73	0.67
FeO	9.36	12.40	11.44	11.19	10.22	13.26	16.53	15.02	15.80	15.21	19.62	18.77	18.80	18.91	18.55
MnO	0.07	0.16	0.06	0.01	0.01	0.21	0.09	0.19	0.13	0.26	0.18	0.19	0.21	0.19	0.18
Cr_2O_3	0.03	0.04	0.00	0.05	0.12	0.00	0.00	0.07	0.01	0.02	0.02	0.00	0.00	0.00	0.00
NiO						0.00		0.12			0.00				
Total	96.46	96.53	97.53	97.40	97.28	96.75	95.26	96.00	97.20	95.88	96.70	95.65	96.53	96.21	95.79
Si	6.21	5.73	5.72	5.93	6.28	6.43	6.82	6.11	6.44	6.53	6.13	6.13	5.99	6.03	6.10
Al^{IV}	1.73	2.27	2.04	1.88	1.55	1.48	1.18	1.77	1.49	1.37	1.80	1.80	1.94	1.88	1.82
Al^{VI}	1.00	0.93	1.25	1.03	0.89	0.61	0.28	0.63	0.48	0.56	0.78	0.88	0.85	0.87	0.95
Ti	0.06	0.01	0.24	0.19	0.17	0.09	0.00	0.11	0.07	0.10	0.07	0.07	0.07	0.08	0.08
Fe^{tot}	1.14	1.53	1.41	1.38	1.25	1.64	2.06	1.86	1.92	1.88	2.45	2.37	2.36	2.38	2.34
Mn	0.01	0.02	0.01	0.00	0.00	0.03	0.01	0.02	0.02	0.03	0.02	0.02	0.03	0.02	0.02
Mg	3.08	2.55	2.38	2.60	2.96	2.69	2.77	2.56	2.70	2.66	1.87	1.81	1.83	1.79	1.81
Ca	1.55	1.76	1.82	1.91	1.80	1.97	1.69	1.67	1.64	1.63	1.68	1.72	1.74	1.75	1.68
Ni						0.00		0.01			0.00				
Na	1.10	1.04	1.06	0.93	0.71	0.44	0.37	0.56	0.48	0.49	0.39	0.39	0.43	0.41	0.40
K	0.05	0.02	0.01	0.06	0.10	0.16	0.02	0.13	0.05	0.05	0.08	0.10	0.13	0.13	0.09
Cr	0.00	0.00	0.00	0.01	0.01	0.00	0.00	0.01	0.00	0.00	0.00	0.00	0.00	0.00	0.00
Cations	15.94	15.85	15.93	15.91	15.72	15.54	15.20	15.46	15.29	15.30	15.27	15.30	15.38	15.36	15.29
Fe^{3+}	0.00	0.70	0.00	0.00	0.00	0.41	0.88	0.90	0.96	0.75	0.94	0.82	0.90	0.85	0.78
Fe^{2+}	1.14	0.82	1.41	1.38	1.25	1.23	1.18	0.96	0.96	1.13	1.52	1.56	1.46	1.54	1.56

Table A2.4: Representative analyses of amphibole. Analyses in wt%, recalculated to 23 oxygens, following the method of Holland and Blundy (1994).

Unit	CLE	CLL	CLL	CLL	Arb	Arb	Arb	Arb	Arb	Arb	Arb	Arb	Arb	Arb	Arb
Lithology	EA	AM	AM / OR	AM / OR	AM	aplite	EA	EA	EA	EA	CAL	CAL	CAL	EA	EA
Mineral	Amph	Amph	Amph	Amph	Amph	Amph	Amph	Amph	Amph	Amph	Amph	Amph	Amph	Amph	Amph
Point	1.32	2.48	3.113	2.68	3.58	1.181	1.63	1.64	2.189	2.190	2.50	3.127	3.139	2.44	2.48
Thin section	AA97-33	AA98-3P	AA98-9	AA98-11	AA98-21BL	AA98-23	AA98-32	AA98-32	AA98-33B	AA98-33B	AA98-35	AA98-37	AA98-54P	AA98-65	AA98-65
Na_2O	4.00	1.31	1.44	1.22	1.28	1.08	2.94	2.65	2.17	2.43	1.17	1.21	1.37	1.36	1.40
MgO	13.33	8.10	14.99	8.93	9.74	7.27	10.81	11.86	13.19	11.05	9.03	9.16	8.28	12.84	11.08
SiO_2	40.57	39.78	41.46	40.10	42.20	40.30	38.46	40.90	42.41	38.76	41.60	41.21	41.13	45.65	42.96
Al_2O_3	18.42	15.55	9.68	16.07	11.79	13.66	18.17	14.61	13.73	18.17	11.34	12.94	12.33	9.23	10.57
K_2O	0.06	0.76	0.40	0.53	0.76	1.85	0.87	0.59	0.77	0.75	1.73	1.81	1.76	0.33	1.30
CaO	10.67	10.88	10.79	10.57	11.86	11.34	10.99	11.17	11.66	11.35	11.91	11.58	11.62	12.28	11.97
TiO_2	0.35	0.80	0.72	0.78	0.76	0.95	1.17	0.57	1.48	1.56	1.07	1.24	1.14	0.64	1.29
FeO	8.68	18.19	16.48	17.72	17.34	20.08	12.97	12.75	10.75	12.30	18.44	17.22	18.66	13.74	16.18
MnO	0.09	0.19	0.34	0.21	0.35	0.37	0.13	0.14	0.08	0.02	0.26	0.29	0.39	0.44	0.52
Cr_2O_3	0.03	0.11	0.15	0.04	0.04	0.07	0.12	0.00	0.13	0.10	0.13	0.00	0.02	0.04	0.00
NiO			0.05								0.00				
Total	96.07	95.67	96.45	96.13	96.08	96.90	96.61	95.25	96.28	96.47	96.68	96.69	96.68	96.50	97.27
Si	5.95	6.02	6.20	5.99	6.37	6.16	5.77	6.19	6.28	5.73	6.35	6.25	6.30	6.73	6.42
Al^{IV}	2.01	1.89	1.71	1.93	1.54	1.73	2.09	1.74	1.55	2.10	1.53	1.61	1.57	1.20	1.43
Al^{VI}	1.17	0.89	0.00	0.90	0.55	0.73	1.12	0.87	0.84	1.07	0.51	0.71	0.66	0.40	0.43
Ti	0.04	0.09	0.08	0.09	0.09	0.11	0.13	0.07	0.17	0.17	0.12	0.14	0.13	0.07	0.14
Fe^{tot}	1.07	2.30	2.06	2.21	2.19	2.57	1.63	1.62	1.33	1.52	2.35	2.18	2.39	1.69	2.02
Mn	0.01	0.02	0.04	0.03	0.04	0.05	0.02	0.02	0.01	0.00	0.03	0.04	0.05	0.05	0.07
Mg	2.91	1.83	3.34	1.99	2.19	1.66	2.42	2.68	2.91	2.43	2.05	2.07	1.89	2.82	2.47
Ca	1.68	1.77	1.73	1.69	1.92	1.86	1.77	1.81	1.85	1.80	1.95	1.88	1.91	1.94	1.92
Ni			0.01								0.00				
Na	1.14	0.38	0.42	0.35	0.38	0.32	0.85	0.78	0.62	0.70	0.35	0.36	0.41	0.39	0.41
K	0.01	0.15	0.08	0.10	0.15	0.36	0.17	0.11	0.15	0.14	0.34	0.35	0.34	0.06	0.25
Cr	0.00	0.01	0.02	0.01	0.00	0.01	0.01	0.00	0.02	0.01	0.02	0.00	0.00	0.00	0.00
Cations	15.99	15.35	15.68	15.28	15.43	15.55	15.99	15.88	15.73	15.68	15.60	15.59	15.65	15.37	15.56
Fe^{3+}	0.00	0.81	0.85	0.91	0.66	0.56	0.00	0.00	0.00	0.50	0.48	0.42	0.37	0.51	0.55
Fe^{2+}	1.07	1.49	1.21	1.30	1.53	2.00	1.63	1.62	1.33	1.03	1.88	1.76	2.02	1.18	1.47

Table A2.4: Continued.

Unit	CLE	CLL	Arb	Arb	Arb	Arb	Arb	Arb	CLL	CLL	CLL	CLL	CLL	CLL	CLL
Lithology	EA	MP	EA	EA	EA	EA	EA	OR	AM	MP	MP	MP	AM	AM	AM
Mineral	Fsp	Fsp	Fsp	Fsp	Fsp	Fsp	Fsp	Fsp	Fsp	Fsp	Fsp	Fsp	Fsp	Fsp	Fsp
Point	4.39	2.21	3.1	3.12	3.21	1.100	2.23	3.67	4.94	1.47	1.117	2.93	3.41	3.48	3.52
Thin section	AA97-7	AA97-8	AA97-10B	AA97-10B	AA97-11	AA97-16(1)	AA97-16(2)	AA97-18	AA97-22	AA97-24	AA97-25	AA97-26P	AA97-31A	AA97-31A	AA97-31A
Na_2O	9.93	7.34	8.36	9.11	4.16	8.65	8.08	0.73	7.18	6.98	7.30	7.22	6.55	7.63	7.83
MgO	0.00	0.00	0.00	0.01	0.00	0.00	0.00	0.00	0.00	0.00	0.00	0.00	0.00	0.00	0.00
SiO_2	63.71	58.55	61.14	62.35	52.25	62.10	59.94	64.77	58.81	57.94	58.38	59.00	57.12	59.43	59.64
Al_2O_3	22.21	24.60	24.14	23.12	29.58	22.89	25.01	17.95	25.56	25.47	25.58	25.55	27.14	25.43	24.80
K_2O	0.03	0.07	0.05	0.23	0.09	0.09	0.11	15.96	0.05	0.09	0.10	0.07	0.04	0.06	0.07
CaO	3.37	7.52	5.73	4.68	13.30	4.91	6.90	0.00	7.95	7.89	7.82	7.48	9.55	7.13	7.09
TiO_2	0.00	0.04	0.00	0.13	0.00	0.00	0.00	0.00	0.00	0.00	0.00	0.00	0.00	0.00	0.00
FeO	0.07	0.04	0.28	0.20	0.09	0.12	0.17	0.02	0.19	0.15	0.08	0.10	0.06	0.21	0.08
MnO	0.00	0.00	0.00	0.00	0.03	0.03	0.02	0.01	0.00	0.00	0.00	0.00	0.02	0.00	0.00
Cr_2O_3	0.04	0.00	0.00	0.04	0.02	0.00	0.03	0.04	0.00	0.00	0.02	0.02	0.00	0.01	0.00
NiO		0.03			0.00	0.00		0.00	0.00	0.00					
Total	99.25	98.08	99.70	99.80	99.38	98.77	100.21	99.41	99.73	98.51	99.18	99.42	100.39	99.90	99.51
Si	2.82	2.66	2.73	2.77	2.38	2.79	2.66	3.01	2.64	2.63	2.63	2.65	2.55	2.66	2.67
Al	1.16	1.32	1.27	1.21	1.59	1.21	1.31	0.98	1.35	1.36	1.36	1.35	1.43	1.34	1.31
Ca	0.16	0.37	0.27	0.22	0.65	0.24	0.33	0.00	0.38	0.38	0.38	0.36	0.46	0.34	0.34
Na	0.85	0.65	0.72	0.78	0.37	0.75	0.70	0.07	0.62	0.61	0.64	0.63	0.57	0.66	0.68
K	0.00	0.00	0.00	0.01	0.01	0.01	0.01	0.94	0.00	0.00	0.01	0.00	0.00	0.00	0.00
Cations	5.00	5.00	5.00	5.00	5.00	5.00	5.00	5.00	5.00	5.00	5.00	5.00	5.00	5.00	5.00
XAb	0.84	0.64	0.72	0.77	0.36	0.76	0.68	0.07	0.62	0.61	0.62	0.63	0.55	0.66	0.66
XAn	0.16	0.36	0.27	0.22	0.64	0.24	0.32	0.00	0.38	0.38	0.37	0.36	0.45	0.34	0.33
XOr	0.00	0.00	0.00	0.01	0.01	0.01	0.01	0.93	0.00	0.00	0.01	0.00	0.00	0.00	0.00

Table A2.5: Representative analyses of feldspars. Analyses in wt%, normalized to 5 cations.

Unit	CLL	CLL	CLL	CLL	CLL	CLL	CLL	CLL	Arb	Arb	Arb	Arb	Arb	Arb	Arb
Lithology	MP	MP	AM	OR	MP	AM / OR	AM / OR	AM / OR	AM	aplite	EA	EA	EA	CAL	CAL
Mineral	Fsp	Fsp	Fsp	Fsp	Fsp	Fsp	Fsp	Fsp	Fsp	Fsp	Fsp	Fsp	Fsp	Fsp	Fsp
Point	1.83	1.86	2.49	3.32	2.225	2.61	2.64	2.65	3.57	1.182	1.62	1.65	2.188	2.52	3.124
Thin section	AA97-32//	AA97-32//	AA98-3P	AA98-6L	AA98-8A	AA98-11	AA98-11	AA98-11	AA98-21BL	AA98-23	AA98-32	AA98-32	AA98-33B	AA98-35	AA98-37
Na_2O	8.52	8.07	3.15	7.50	7.30	2.59	5.62	5.92	6.52	8.66	7.30	7.53	7.87	7.42	4.92
MgO	0.00	0.00	0.01	0.01	0.00	0.00	0.01	0.02	0.00	0.00	0.00	0.00	0.00	0.00	0.00
SiO_2	61.54	60.61	49.02	59.43	58.27	47.76	54.63	55.17	56.75	60.81	57.95	58.40	57.75	59.16	58.39
Al_2O_3	23.09	23.91	32.02	24.57	26.15	32.27	28.32	28.10	26.78	24.21	26.26	25.94	25.33	24.29	24.60
K_2O	0.17	0.09	0.04	0.08	0.03	0.00	0.01	0.04	0.15	0.26	0.05	0.05	0.04	0.36	4.12
CaO	5.07	5.98	14.95	7.41	8.02	15.42	10.28	10.42	8.74	5.72	8.12	7.69	7.32	7.23	6.98
TiO_2	0.00	0.00	0.00	0.00	0.00	0.00	0.00	0.00	0.00	0.00	0.00	0.00	0.00	0.00	0.16
FeO	0.00	0.05	0.12	0.08	0.04	0.11	0.03	0.07	0.21	0.05	0.13	0.31	0.18	0.08	0.08
MnO	0.00	0.00	0.00	0.00	0.01	0.00	0.00	0.00	0.00	0.00	0.00	0.03	0.00	0.06	0.00
Cr_2O_3	0.00	0.00	0.00	0.00	0.00	0.04	0.02	0.00	0.00	0.00	0.01	0.03	0.00	0.00	0.07
NiO	0.02	0.02		0.09										0.00	
Total	98.40	98.66	99.31	98.99	99.77	98.14	98.85	99.65	99.14	99.65	99.81	99.92	98.50	98.46	99.26
Si	2.77	2.73	2.25	2.68	2.60	2.22	2.48	2.49	2.57	2.70	2.59	2.61	2.61	2.68	2.66
Al	1.23	1.27	1.73	1.30	1.38	1.77	1.52	1.49	1.43	1.27	1.38	1.37	1.35	1.30	1.32
Ca	0.24	0.29	0.74	0.36	0.38	0.77	0.50	0.50	0.42	0.27	0.39	0.37	0.35	0.35	0.34
Na	0.74	0.70	0.28	0.65	0.63	0.23	0.50	0.52	0.57	0.75	0.63	0.65	0.69	0.65	0.43
K	0.01	0.01	0.00	0.00	0.00	0.00	0.00	0.00	0.01	0.01	0.00	0.00	0.00	0.02	0.24
Cations	5.00	5.00	5.00	5.00	5.00	5.00	5.00	5.00	5.00	5.00	5.00	5.00	5.00	5.00	5.00
XAb	0.75	0.71	0.28	0.64	0.62	0.23	0.50	0.51	0.57	0.72	0.62	0.64	0.66	0.64	0.43
XAn	0.24	0.29	0.00	0.35	0.38	0.00	0.50	0.49	0.42	0.26	0.38	0.36	0.34	0.34	0.34
XOr	0.01	0.01	0.72	0.00	0.00	0.77	0.00	0.00	0.01	0.01	0.00	0.00	0.00	0.02	0.24

Table A2.5: Continued.

Unit	CLE	Arb	Arb	CLL	Arb	Arb	Arb	Arb	Arb	Arb	Arb	Arb	Arb	Arb	Arb	Arb
Lithology	EA	EA	EA	MP	AM	AM	AM	EA	EA	EA	EA	EA	EA	EA	EA	EA
Mineral	(C)Zo	Ep	Ep	(C)Zo	Ep	Ep	Ep	Ep	Ep	Ep	(C)Zo	(C)Zo	Ep	Ep	Ep	Ep
Point	4.24	3.3	3.16	3.49	3.60	2.27	2.34	2.244	2.245	2.182	2.43	2.45	2.66	2.67	1.390	1.436
Thin section	AA97-4	AA97-10B	AA97-10B	AA98-13B	AA98-21BL	AA98-21BL	AA98-21BL	AA98-33A	AA98-33A	AA98-33B	AA98-65	AA98-65	AA98-65	AA98-65	AA98-66B	AA98-66B
Na_2O	0.00	0.01	0.00	0.00	0.01	0.00	0.01	0.00	0.00	0.02	3.65	1.44	0.00	0.01	0.07	0.03
MgO	0.07	0.22	0.21	0.36	0.09	0.02	0.04	0.11	0.06	0.58	0.03	0.00	0.14	0.16	0.20	0.16
SiO_2	38.72	38.46	38.48	41.67	37.42	38.15	37.85	37.84	37.63	35.82	46.14	45.79	37.69	37.99	37.78	38.14
Al_2O_3	31.88	28.97	28.85	22.83	25.73	24.83	24.22	28.11	27.75	26.99	26.72	34.06	24.80	25.64	28.13	27.29
K_2O	0.00	0.00	0.01	0.06	0.00	0.00	0.00	0.02	0.02	0.02	0.04	0.00	0.00	0.00	0.02	0.02
CaO	24.27	23.75	23.82	25.60	23.11	23.57	23.72	23.29	23.23	21.55	17.96	18.29	23.58	23.51	23.55	23.28
TiO_2	0.00	0.19	0.19	0.01	0.17	0.11	0.11	0.15	0.08	0.10	0.00	0.00	0.09	0.08	0.46	0.17
FeO	1.74	4.99	5.48	2.90	9.18	9.89	10.59	6.63	6.77	5.86	0.08	0.13	10.41	9.63	6.36	7.94
MnO	0.00	0.06	0.05	0.00	0.16	0.11	0.16	0.21	0.11	0.02	0.02	0.00	0.14	0.10	0.11	0.11
Cr_2O_3	0.01	0.05	0.00	0.00	0.06	0.00	0.00	0.08	0.00	0.19	0.00	0.00	0.10	0.02	0.00	0.09
NiO						0.05	0.02									
Total	96.68	96.58	97.03	93.43	95.87	96.67	96.68	96.35	95.67	91.08	94.58	99.71	96.95	97.11	96.66	97.21
Si	2.98	2.99	2.99	3.37	2.97	3.02	3.00	2.97	2.98	2.96	3.55	3.38	2.97	2.98	2.95	2.98
Al^{IV}	0.02	0.01	0.01	0.00	0.03	0.00	0.00	0.03	0.02	0.04	0.00	0.00	0.03	0.02	0.05	0.02
Al^{VI}	2.88	2.65	2.62	2.18	2.38	2.31	2.26	2.57	2.56	2.59	2.42	2.96	2.28	2.36	2.54	2.49
Ti	0.00	0.01	0.01	0.00	0.01	0.01	0.01	0.01	0.00	0.01	0.00	0.00	0.01	0.00	0.03	0.01
Fe^{tot}	0.11	0.32	0.36	0.20	0.60	0.65	0.70	0.42	0.43	0.40	0.00	0.01	0.69	0.63	0.42	0.50
Mn	0.00	0.00	0.00	0.00	0.01	0.01	0.01	0.01	0.01	0.00	0.00	0.00	0.01	0.01	0.01	0.01
Mg	0.01	0.03	0.02	0.04	0.01	0.00	0.00	0.01	0.01	0.07	0.00	0.00	0.02	0.02	0.02	0.02
Ca	2.00	1.98	1.98	2.22	1.97	2.00	2.01	1.96	1.97	1.91	1.48	1.45	1.99	1.98	1.97	1.95
Na	0.00	0.00	0.00	0.00	0.00	0.00	0.00	0.00	0.00	0.00	0.54	0.21	0.00	0.00	0.01	0.01
Cr	0.00	0.00	0.00	0.00	0.00	0.00	0.00	0.01	0.00	0.01	0.00	0.00	0.01	0.00	0.00	0.01
Cations	8.00	8.00	8.00	8.00	7.99	8.00	8.00	7.99	7.98	8.00	8.00	8.00	8.00	8.00	8.00	7.98
Fe^{3+}	0.11	0.32	0.36	0.20	0.60	0.65	0.70	0.42	0.43	0.40	0.00	0.01	0.69	0.63	0.42	0.50
Fe^{2+}	0.00	0.00	0.00	0.00	0.00	0.00	0.00	0.00	0.00	0.00	0.00	0.00	0.00	0.00	0.00	0.00
$Si+Al^{IV}$	3.00	3.00	3.00	3.37	3.00	3.02	3.00	3.00	3.00	3.00	3.55	3.38	3.00	3.00	3.00	3.00
$Al^{VI}+Ti+Fe^{3+}+Cr$	2.99	2.99	2.99	2.37	3.00	2.98	2.97	3.01	3.00	3.01	2.43	2.97	2.98	2.99	2.99	3.01
Rest	2.01	2.01	2.01	2.26	1.99	2.01	2.03	1.98	1.98	1.98	2.03	1.65	2.02	2.01	2.01	1.98

Table A2.6: Representative analyses of epidote group minerals. Analyses in wt%, recalculated to 12.5 oxygens and 8 cations.

Unit	CLL	Arb	Arb	Arb	CLL	CLL	CLL	CLL	CLL	CLL	CLL	CLL	CLL	CLL	CLL
Lithology	MP	EA	CAL	OR	AM	MP	MP	MP	MP	OR	AM	MP	MP	MP	AM
Mineral	Bt	Bt	Bt	Bt	Bt	Bt	Bt	Bt	Bt	Bt	Bt	Bt	Bt	Bt	Bt
Point	2.22	2.37	3.60	3.69	4.97	1.59	1.115	2.94	2.95	2.273	3.47	1.81	1.82	1.88	2.53
Thin section	AA97-8	AA97-16(2)	AA97-18	AA97-20	AA97-22	AA97-24	AA97-25	AA97-26P	AA97-26P	AA97-28	AA97-31A	AA97-32//	AA97-32//	AA97-32//	AA98-3P
Na_2O	0.16	0.48	0.06	0.03	0.61	0.18	0.36	0.46	0.59	0.08	0.18	0.47	0.46	0.24	0.23
MgO	10.57	15.48	8.73	8.49	12.74	10.33	10.13	12.71	13.23	12.35	13.66	9.61	9.80	9.39	12.85
SiO_2	34.79	37.48	35.24	35.70	36.38	34.46	34.34	36.02	36.94	33.63	36.42	34.54	35.42	34.63	34.59
Al_2O_3	17.49	16.57	15.01	15.31	16.49	18.02	18.41	18.11	18.50	17.04	16.78	18.21	18.19	18.26	15.94
K_2O	9.07	7.93	9.52	9.70	8.06	8.46	9.38	7.43	8.30	7.44	8.47	8.40	8.65	9.36	8.46
CaO	0.01	0.06	0.01	0.03	0.02	0.02	0.04	0.02	0.00	0.02	0.03	0.07	0.00	0.00	0.11
TiO_2	1.88	1.61	3.44	2.89	1.65	1.47	1.93	2.13	1.67	0.90	1.98	2.26	2.55	2.21	2.03
FeO	19.33	13.91	22.09	22.62	17.59	19.71	18.34	15.84	15.62	20.48	15.54	18.86	18.64	19.64	18.61
MnO	0.08	0.13	0.56	0.45	0.09	0.01	0.04	0.11	0.10	0.29	0.03	0.00	0.08	0.07	0.09
Cr_2O_3	0.03	0.02	0.00	0.00	0.00	0.00	0.13	0.10	0.02	0.06	0.00	0.07	0.08	0.05	0.02
NiO	0.15		0.05	0.00	0.05	0.02						0.05	0.00	0.03	
Total	93.44	93.65	94.66	95.19	93.61	92.62	93.06	92.91	94.95	92.21	93.03	92.43	93.71	93.74	92.90
Si	2.71	2.80	2.76	2.78	2.78	2.70	2.68	2.74	2.75	2.65	2.77	2.70	2.72	2.69	2.70
Al^{IV}	1.29	1.20	1.24	1.22	1.22	1.30	1.32	1.26	1.25	1.35	1.23	1.30	1.28	1.31	1.30
Al^{VI}	0.31	0.26	0.15	0.19	0.26	0.36	0.37	0.36	0.37	0.24	0.28	0.38	0.37	0.36	0.17
Ti	0.11	0.09	0.20	0.17	0.10	0.09	0.11	0.12	0.09	0.05	0.11	0.13	0.15	0.13	0.12
Fe^{tot}	1.26	0.87	1.45	1.48	1.12	1.29	1.20	1.01	0.97	1.35	0.99	1.23	1.20	1.28	1.21
Mn	0.01	0.01	0.04	0.03	0.01	0.00	0.00	0.01	0.01	0.02	0.00	0.00	0.01	0.00	0.01
Mg	1.23	1.73	1.02	0.99	1.45	1.21	1.18	1.44	1.47	1.45	1.55	1.12	1.12	1.09	1.50
Ca	0.00	0.00	0.00	0.00	0.00	0.00	0.00	0.00	0.00	0.00	0.00	0.01	0.00	0.00	0.01
Ni	0.01		0.00	0.00	0.00	0.00						0.00	0.00	0.00	
Na	0.02	0.07	0.01	0.00	0.09	0.03	0.05	0.07	0.09	0.01	0.03	0.07	0.07	0.04	0.04
K	0.90	0.76	0.95	0.96	0.79	0.85	0.93	0.72	0.79	0.75	0.82	0.84	0.85	0.93	0.84
Cr	0.00	0.00	0.00	0.00	0.00	0.00	0.01	0.01	0.00	0.00	0.00	0.00	0.00	0.00	0.00
Cations	7.84	7.79	7.82	7.83	7.82	7.82	7.85	7.72	7.78	7.88	7.79	7.78	7.76	7.83	7.89
Fe^{3+}	0.19	0.13	0.22	0.22	0.17	0.19	0.18	0.15	0.15	0.20	0.15	0.18	0.18	0.19	0.18
Fe^{2+}	1.07	0.74	1.23	1.25	0.96	1.10	1.02	0.85	0.83	1.15	0.84	1.05	1.02	1.08	1.03
XAl	0.11	0.09	0.06	0.07	0.10	0.13	0.14	0.13	0.13	0.08	0.10	0.14	0.14	0.14	0.06
XTi	0.04	0.03	0.08	0.06	0.03	0.03	0.04	0.04	0.03	0.02	0.04	0.05	0.06	0.05	0.04

Table A2.7: Representative analyses of micas. Analyses in wt%, recalculated to 11 oxygens. Fe^{3+} estimated following Williams and Grambling (1990).

Unit	CLL	CLL	CLL	CLL	CLL	CLL	CLL	CLL	Arb	Arb	Arb	Arb	Arb	Arb	CLL
Lithology	OR	MP	MP	MP	AM / OR	MP	MP	MP	OR	OR	EA	CAL	CAL	CAL	MP
Mineral	Bt	Bt	Bt	Bt	Bt	Bt	WhM	Bt	WhM	Bt	Bt	Bt	Bt	Bt	Bt
Point	3.27	2.217	2.223	2.228	2.88	2.90	3.43	1.107	3.107	3.115	1.291	2.46	3.148	3.126	3.87
Thin section	AA98-6L	AA98-8A	AA98-8A	AA98-8A	AA98-11	AA98-12	AA98-13B	AA98-13B	AA98-26L	AA98-26L	AA98-32	AA98-35	AA98-36	AA98-37	AA98-59Y
Na_2O	0.39	0.69	0.64	0.61	0.18	0.25	0.03	0.00	0.26	0.10	0.26	0.22	0.09	0.06	0.54
MgO	12.43	15.42	15.67	15.51	11.08	9.06	2.93	10.41	2.37	11.22	15.24	12.13	13.98	10.72	10.17
SiO_2	36.58	36.72	37.97	37.08	34.78	34.27	47.26	30.55	44.90	35.82	35.47	36.31	37.61	34.74	34.34
Al_2O_3	15.87	17.17	17.40	17.07	16.93	18.74	28.03	18.70	31.18	18.15	18.06	14.06	15.22	14.86	17.76
K_2O	8.53	7.76	7.97	7.60	8.84	9.17	10.27	5.52	10.59	9.68	9.56	9.17	9.77	8.23	8.26
CaO	0.01	0.09	0.02	0.03	0.05	0.00	0.04	0.07	0.03	0.07	0.05	0.18	0.03	0.31	0.04
TiO_2	2.11	1.45	0.94	1.41	1.58	2.14	0.76	1.56	0.45	2.28	4.59	3.24	2.05	2.09	1.80
FeO	18.29	14.58	13.97	13.87	19.74	20.65	5.16	24.13	4.49	16.40	12.30	18.71	15.94	22.27	20.70
MnO	0.15	0.09	0.00	0.05	0.06	0.12	0.00	0.02	0.00	0.46	0.03	0.29	0.21	0.24	0.03
Cr_2O_3	0.00	0.11	0.00	0.06	0.06	0.10	0.04	0.07	0.00	0.05	0.17	0.16	0.13	0.05	0.01
NiO	0.02							0.11				0.02	0.11		
Total	94.37	94.09	94.55	93.17	93.19	94.49	94.44	90.93	94.25	94.17	95.69	94.47	95.04	93.45	93.61
Si	2.79	2.75	2.81	2.78	2.72	2.66	3.24	2.47	3.09	2.73	2.61	2.80	2.83	2.74	2.68
Al^{IV}	1.21	1.25	1.19	1.22	1.28	1.34	0.76	1.53	0.91	1.27	1.39	1.20	1.17	1.26	1.32
Al^{VI}	0.22	0.26	0.32	0.29	0.27	0.37	1.50	0.25	1.62	0.36	0.18	0.07	0.18	0.12	0.31
Ti	0.12	0.08	0.05	0.08	0.09	0.12	0.04	0.10	0.02	0.13	0.25	0.19	0.12	0.12	0.11
Fe^{tot}	1.17	0.91	0.86	0.87	1.29	1.34	0.30	1.63	0.26	1.04	0.76	1.21	1.00	1.47	1.35
Mn	0.01	0.01	0.00	0.00	0.00	0.01	0.00	0.00	0.00	0.03	0.00	0.02	0.01	0.02	0.00
Mg	1.41	1.72	1.73	1.73	1.29	1.05	0.30	1.26	0.24	1.27	1.67	1.39	1.57	1.26	1.18
Ca	0.00	0.01	0.00	0.00	0.00	0.00	0.00	0.01	0.00	0.01	0.00	0.02	0.00	0.03	0.00
Ni	0.00							0.01				0.00	0.01		
Na	0.06	0.10	0.09	0.09	0.03	0.04	0.00	0.00	0.04	0.01	0.04	0.03	0.01	0.01	0.08
K	0.83	0.74	0.75	0.73	0.88	0.91	0.90	0.57	0.93	0.94	0.90	0.90	0.94	0.83	0.82
Cr	0.00	0.01	0.00	0.00	0.00	0.01	0.00	0.00	0.00	0.00	0.01	0.01	0.01	0.00	0.00
Cations	7.82	7.83	7.81	7.79	7.87	7.83	7.04	7.83	7.11	7.80	7.81	7.84	7.85	7.86	7.85
Fe^{3+}	0.18	0.14	0.13	0.13	0.19	0.20		0.24		0.16	0.11	0.18	0.15	0.22	0.20
Fe^{2+}	0.99	0.78	0.73	0.74	1.10	1.14		1.39		0.89	0.64	1.02	0.85	1.25	1.15
XAl	0.08	0.09	0.11	0.10	0.10	0.14	0.72	0.08	0.77	0.13	0.07	0.03	0.07	0.04	0.11
XTi	0.04	0.03	0.02	0.03	0.03	0.05	0.02	0.03	0.01	0.05	0.09	0.07	0.04	0.04	0.04

Unit	CLE	CLE	CLL	CLL	Arb	Arb	CLL	CLL	CLL	CLL	CLL	CLL	CLL	CLL	Arb
Lithology	EA	EA	MP	MP	EA	EA	MP	MP	MP	MP	MP	MP	MP	MP	EA
Mineral	Ky	Ky	Ky	Ky	Ky	Ky	Ky	Ky	Sill	Ky	Ky	Ky	Sill	Sill	Ky
Point	4.14	1.20	2.7	2.23	1.90	2.1	2.92	2.111	2.193	1.84	2.220	2.226	2.94	3.50	3.55
Thinsection	AA97-4	AA97-6	AA97-8	AA97-8	AA97-16(1)	AA97-16(2)	AA97-26P	AA97-26P	AA97-32//	AA97-32//	AA98-8A	AA98-8A	AA98-12	AA98-13B	AA98-51
Na_2O	0.00	0.02	0.01	0.00	0.00	0.00	0.03	0.00	0.03	0.00	0.00	0.00	0.03	0.00	0.00
MgO	0.00	0.00	0.00	0.00	0.00	0.00	0.00	0.02	0.01	0.00	0.00	0.00	0.02	0.00	0.01
SiO_2	36.28	36.43	36.85	36.58	36.43	36.70	36.85	36.83	35.78	36.65	36.35	36.37	36.00	36.11	36.38
Al_2O_3	62.06	61.95	60.92	60.80	62.24	62.75	62.95	62.47	62.14	62.02	62.83	62.55	62.32	61.92	62.17
K_2O	0.01	0.00	0.02	0.00	0.00	0.02	0.00	0.00	0.01	0.00	0.02	0.00	0.07	0.01	0.00
CaO	0.00	0.04	0.01	0.00	0.00	0.04	0.02	0.01	0.00	0.00	0.01	0.01	0.01	0.00	0.01
TiO_2	0.02	0.01	0.18	0.00	0.01	0.00	0.00	0.00	0.01	0.00	0.00	0.00	0.00	0.00	0.00
FeO	0.28	0.34	0.67	0.81	0.49	0.43	0.63	0.76	0.67	0.48	0.70	0.51	0.85	0.94	0.47
MnO	0.00	0.00	0.00	0.00	0.00	0.02	0.00	0.00	0.06	0.00	0.01	0.00	0.00	0.04	0.00
Cr_2O_3	0.28	0.09	0.15	0.05	0.01	0.00	0.00	0.06	0.00	0.00	0.04	0.06	0.04	0.06	0.01
NiO		0.00	0.01	0.04	0.07					0.05					
Total	98.90	98.76	98.78	98.19	99.17	99.91	100.42	100.07	98.59	99.15	99.88	99.43	99.23	98.97	99.02
Si	3.97	3.98	4.04	4.03	3.97	3.97	3.97	3.98	3.93	4.00	3.94	3.96	3.93	3.96	3.97
Al	8.00	7.99	7.87	7.90	8.00	8.01	8.00	7.97	8.04	7.97	8.03	8.02	8.03	7.99	8.00
Ti	0.00	0.00	0.01	0.00	0.00	0.00	0.00	0.00	0.00	0.00	0.00	0.00	0.00	0.00	0.00
Fe	0.03	0.03	0.06	0.07	0.05	0.04	0.06	0.07	0.06	0.04	0.06	0.05	0.08	0.09	0.04
Mn	0.00	0.00	0.00	0.00	0.00	0.00	0.00	0.00	0.01	0.00	0.00	0.00	0.00	0.00	0.00
Mg	0.00	0.00	0.00	0.00	0.00	0.00	0.00	0.00	0.00	0.00	0.00	0.00	0.00	0.00	0.00
Ca	0.00	0.00	0.00	0.00	0.00	0.00	0.00	0.00	0.00	0.00	0.00	0.00	0.00	0.00	0.00
Ni		0.00	0.00	0.00	0.01					0.00					
Na	0.00	0.01	0.00	0.00	0.00	0.00	0.01	0.00	0.01	0.00	0.00	0.00	0.01	0.00	0.00
K	0.00	0.00	0.00	0.00	0.00	0.00	0.00	0.00	0.00	0.00	0.00	0.00	0.01	0.00	0.00
Cr	0.02	0.01	0.01	0.00	0.00	0.00	0.00	0.00	0.00	0.00	0.00	0.00	0.00	0.01	0.00
Cations	12.02	12.02	12.01	12.02	12.03	12.03	12.03	12.03	12.05	12.02	12.04	12.03	12.06	12.05	12.02

Table A2.8: Representative analyses of kyanite. Analyses in wt%, recalculated to 20 oxygens.

Unit	CLL	CLL	CLL	CLL	Arb	Arb	Arb	Arb
Lithology	MP	MP	MP	MP	EA	EA	EA	EA
Mineral	St	St	St	St	St	St	St	St
Point	2.117	2.8	2.11	2.19	1.95	1.98	1.103	2.3
Thin section	AA97-8	AA97-8	AA97-8	AA97-8	AA97-16(1)	AA97-16(1)	AA97-16(1)	AA97-16(2)
Na_2O	0.00	0.00	0.00	0.02	0.02	0.05	0.03	0.06
MgO	2.06	1.95	1.98	1.87	3.39	3.35	2.91	3.11
SiO_2	26.57	27.09	27.14	27.21	25.48	25.97	25.79	26.13
Al_2O_3	53.44	52.01	52.22	51.21	53.20	52.41	53.17	53.32
K_2O	0.01	0.00	0.00	0.00	0.00	0.01	0.00	0.01
CaO	0.00	0.01	0.01	0.00	0.03	0.03	0.02	0.01
TiO_2	0.29	0.62	0.52	0.80	0.20	0.61	0.53	0.36
FeO	14.94	14.33	14.55	13.56	13.69	13.89	12.80	12.39
MnO	0.06	0.15	0.25	0.19	0.15	0.15	0.19	0.25
Cr_2O_3	0.09	0.11	0.08	0.00	0.06	0.00	0.07	0.05
NiO		0.00	0.03	0.00	0.00	0.06	0.05	
Total	97.38	96.26	96.67	94.84	96.14	96.46	95.39	95.56
Si	7.79	8.01	8.00	8.14	7.55	7.68	7.65	7.72
Al	18.46	18.14	18.14	18.06	18.57	18.26	18.60	18.57
Ti	0.06	0.14	0.12	0.18	0.04	0.14	0.12	0.08
Fe	3.66	3.55	3.59	3.39	3.39	3.43	3.18	3.06
Mn	0.02	0.04	0.06	0.05	0.04	0.04	0.05	0.06
Mg	0.90	0.86	0.87	0.83	1.50	1.48	1.29	1.37
Ca	0.00	0.00	0.00	0.00	0.01	0.01	0.01	0.00
Ni		0.00	0.01	0.00	0.00	0.01	0.01	
Na	0.00	0.00	0.00	0.01	0.01	0.03	0.02	0.03
Cr	0.02	0.03	0.02	0.00	0.01	0.00	0.02	0.01
Cations	30.91	30.76	30.80	30.66	31.12	31.07	30.93	30.92

Table A2.9: Representative analyses of staurolite. Analyses in wt%, recalculated to 28 oxygens.

Unit	CLL	CLL
Lithology	MP	MP
Mineral	Crd	Crd
Point	2.219	2.224
Thin section	AA98-8A	AA98-8A
Na_2O	0.19	0.28
MgO	10.36	10.09
SiO_2	48.48	48.14
Al_2O_3	32.94	32.93
K_2O	0.01	0.01
CaO	0.00	0.00
TiO_2	0.03	0.00
FeO	5.21	5.52
MnO	0.15	0.21
Cr_2O_3	0.00	0.01
NiO		
Total	97.34	97.17
Si	4.98	4.96
Al	3.98	4.00
Ti	0.00	0.00
Fe	0.45	0.48
Mn	0.01	0.02
Mg	1.59	1.55
Ca	0.00	0.00
Na	0.04	0.06
K	0.00	0.00
Cr	0.00	0.00
Cations	11.05	11.07

Table A2.10: Representative analyses of cordierite. Analyses in wt%, recalculated to 18 oxygens.

Unit	Arb	Arb	Arb	Arb	Arb	Arb	Arb
Lithology	CAL	CAL	CAL	CAL	CAL	CAL	CAL
Mineral	Scp	Scp	Scp	Scp	Scp	Scp	Scp
Point	2.36	2.40	3.149	3.136	3.139	3.146	3.153
Thin section	AA98-35	AA98-35	AA98-36	AA98-36	AA98-36	AA98-36	AA98-36
Na_2O	3.35	3.47	2.98	3.06	2.92	3.22	3.06
MgO	0.02	0.00	0.04	0.00	0.00	0.00	0.00
SiO_2	46.55	46.28	45.09	45.69	45.33	45.68	45.54
Al_2O_3	26.38	25.92	27.18	26.90	27.10	26.84	26.84
K_2O	0.14	0.11	0.12	0.14	0.13	0.15	0.14
CaO	18.17	17.86	18.81	18.87	19.02	18.57	18.73
TiO_2	0.00	0.00	0.00	0.00	0.00	0.00	0.00
FeO	0.09	0.09	0.11	0.07	0.03	0.06	0.00
MnO	0.03	0.00	0.03	0.00	0.04	0.00	0.03
Cr_2O_3	0.00	0.00	0.02	0.05	0.01	0.00	0.00
NiO	0.00	0.00	0.00	0.00	0.12	0.05	0.01
Total	94.68	93.72	94.34	94.67	94.62	94.45	94.31
Si	7.19	7.23	7.02	7.08	7.04	7.09	7.08
Al	4.81	4.77	4.98	4.92	4.96	4.91	4.92
Ti	0.00	0.00	0.00	0.00	0.00	0.00	0.00
Fe	0.01	0.01	0.01	0.01	0.00	0.01	0.00
Mn	0.00	0.00	0.00	0.00	0.01	0.00	0.00
Mg	0.00	0.00	0.01	0.00	0.00	0.00	0.00
Ca	3.01	2.99	3.14	3.14	3.16	3.09	3.12
Ni	0.00	0.00	0.00	0.00	0.02	0.01	0.00
Na	1.00	1.05	0.90	0.92	0.88	0.97	0.92
K	0.03	0.02	0.02	0.03	0.03	0.03	0.03
Cr	0.00	0.00	0.00	0.01	0.00	0.00	0.00
Cations	16.06	16.07	16.09	16.10	16.10	16.10	16.08
Rest	4.06	4.07	4.09	4.10	4.10	4.10	4.08
X Meionite	0.75	0.74	0.77	0.77	0.78	0.76	0.77

Table A2.11: Representative analyses of scapolite. Analyses in wt%,recalculated to 24 oxygens and 12 Si + Al).

Appendix 3

Representative electron microprobe analyses from Gran Paradiso

SAMPLE	LITHOLOGY	MAIN	INCL / EARLY	RIMS / LATE	ACCESSORIES
A35-2	M	Grt, Omp	Gln	Amph, Ep, Bt	Qtz, Czo, WhM
GP96-17	M	Grt, Omp		Amph, WhM	Qtz, Czo
GP96-22	GO	Amph, Ab, Czo		Bt, Chl	Qtz, Ttn, WhM
GP96-26L	M	Kf, Plag, Qtz, Bt, Grt, WhM	Chl		Zo, Czo
GP96-28	M	Grt, Omp		Amph, WhM	Qtz
GP96-29X	GM	Grt, Qtz, WhM, Bt, Plag, Kf?			Op
GP96-35c	GM	Plag, Bt, Qtz, Hbl, Grt, Kf		WhM, Chl	Op
GP96-37A	GM	Grt, WhM, Qtz, Plag	Ctd	Chl, WhM	
GP96-43	GM	Grt, Bt, WhM, Chl, Qtz	Grt, Ctd		
GP96-44P	GM	Grt, Qtz, Bt, WhM (Pg)	Grt, Ctd	WhM	Ttn
GP96-82	M	Grt, Amph, Plag, Qtz		Chl, Qtz	Op
GP96-89*	GM	Amph, Qtz, Carb, Chl, Grt, Kf, Plag			Ilm, Pt, Rt
GP96-90L	GM	Grt, Bt, Qtz, WhM	Grt, Ctd	Bt	
GP96-94-P	GO	Qtz, Bt, WhM, Plag, Kf, Grt			
GP96-97AP	GO	Grt, WhM, Qtz, Plag		Bt, Chl	
GP96-107c	M	Amph, Qtz, Czo	Grt, sympl (Omp)	Bt, Ep	
GP96-126//	GM	Grt, Qtz, WhM, Bt, Plag		Bt, Chl	Op, Ttn, Tml
GP97-2L	GM	Grt, WhM, Qtz, Plag		Bt, Chl	Zrn
GP97-5L	GM	Grt, WhM, Qtz, Plag		Bt, Chl,	Ap
GP97-10	M	Amph, Ep, Czo, Plag, Qtz			Op, Ttn, Carb
GP97-16A	M	Carb, Ep, Amph, Czo	Grt	Bt	
GP97-17-1	M	Grt, Omp, Plag		Amph, Czo, Bt	Qtz
GP97-22A	M	Grt, Omp (sympl)		Amph, Ep, Czo	Carb, Ep, Op, Qtz
GP97-25-2	M	Grt, sympl (Omp), Amph, Qtz, Plag, Czo		Bt, WhM	Op
GP97-32P	GO	Plag, Qtz, WhM, Grt	Grt	Chl	
GP97-33	GO	Grt, Plag, Qtz, WhM, Bt	Ctd	Chl	Ilm, Rt
GP97-39B	M	Amph, Plag, Grt	Chl, WhM	Bt, Chl	Op
GP97-44-1	GO	Kf, Plag, Qtz, Bt, WhM		Bt	
GP97-45A,b	GM	Grt, Plag, Qtz, WhM, Bt	WhM	Bt	Carb
GP97-46B1	M	Grt, Omp		Amph, sympl (Omp)	Ttn, Op, Czo, Rt, WhM, Qtz

Table A3.1: Mineral assemblages of studied samples.

Lithology	M	M	M	M	M	M	M	M	GM	GM	GM	GM	GM	GM	GM	GM
Mineral	Grt	Grt	Grt	Grt	Grt	Grt	Grt	Grt	Grt	Grt	Grt	Grt	Grt	Grt	Grt	Grt
Point	8.7	1.23	1.28	1.57	1.63	3.195	3.230	3.237	4.73	4.78	6.13	series 2	4.163	4.165	4.46	4.54
Core or rim	rim	core	rim	core	rim	core, incl	core, incl	core, incl								
Thin section	A35-2	GP96-17	GP96-17	GP96-28	GP96-28	GP96-28	GP96-28	GP96-28	GP96-29X	GP96-29X	GP96-37A	GP96-37A	GP96-43	GP96-43	GP96-44P	GP96-44P
Na_2O	0.06	0.03	0.07	0.00	0.00	0.04	0.03	0.10	0.02	0.05	0.07	0.02	0.01	0.02	0.05	0.05
MgO	1.48	1.40	1.81	2.29	2.14	2.12	2.27	2.09	1.31	1.82	2.51	3.30	4.02	3.85	4.02	3.71
SiO_2	37.74	37.38	37.12	37.61	37.53	37.16	37.36	36.97	35.75	36.26	37.57	37.16	36.73	36.74	36.83	36.79
Al_2O_3	21.25	21.32	21.05	21.04	21.01	21.20	21.19	21.02	20.17	20.62	21.34	21.02	21.15	21.16	21.17	21.39
K_2O	0.01	0.00	0.01	0.00	0.01	0.02	0.01	0.03	0.00	0.00	0.01	0.01	0.02	0.02	0.01	0.01
CaO	11.80	12.68	9.07	11.80	12.24	10.52	9.80	12.36	6.60	3.78	3.59	0.85	1.27	1.20	1.06	1.58
TiO_2	0.00	0.18	0.12	0.17	0.22	0.06	0.08	0.34	1.60	0.17	0.07	0.00	0.04	0.03	0.03	0.00
FeO	27.75	26.24	29.75	25.67	25.46	27.94	28.28	25.49	31.50	35.51	34.12	36.44	35.31	35.04	36.36	36.20
MnO	0.22	0.60	0.67	0.45	0.48	0.32	0.42	0.42	1.27	1.11	1.42	0.84	0.19	0.32	0.33	0.47
Cr_2O_3	0.00	0.00	0.05	0.07	0.08	0.01	0.01	0.06	0.04	0.09	0.07	0.00	0.00	0.00	0.09	0.01
NiO																
Total	100.24	99.79	99.60	99.03	99.07	99.32	99.40	98.83	98.20	99.28	100.62	99.61	98.69	98.31	99.85	100.14
Si	2.99	2.97	2.98	3.00	2.99	2.97	2.98	2.96	2.94	2.97	3.00	3.00	2.98	2.99	2.97	2.96
Al	1.99	2.00	1.99	1.98	1.97	2.00	2.00	1.99	1.95	1.99	2.01	2.00	2.02	2.03	2.01	2.03
Ti	0.00	0.01	0.01	0.01	0.01	0.00	0.00	0.02	0.10	0.01	0.00	0.00	0.00	0.00	0.00	0.00
Fe^{tot}	1.84	1.75	2.00	1.71	1.70	1.87	1.89	1.71	2.16	2.43	2.28	2.46	2.40	2.38	2.45	2.43
Mn	0.02	0.04	0.05	0.03	0.03	0.02	0.03	0.03	0.09	0.08	0.10	0.06	0.01	0.02	0.02	0.03
Mg	0.17	0.17	0.22	0.27	0.25	0.25	0.27	0.25	0.16	0.22	0.30	0.40	0.49	0.47	0.48	0.44
Ca	1.00	1.08	0.78	1.01	1.04	0.90	0.84	1.06	0.58	0.33	0.31	0.07	0.11	0.10	0.09	0.14
Ni																
Cr	0.00	0.00	0.00	0.00	0.00	0.00	0.00	0.00	0.00	0.01	0.00	0.00	0.00	0.00	0.01	0.00
Cations	8.01	8.02	8.02	8.00	8.01	8.02	8.01	8.02	7.99	8.03	7.99	8.00	8.01	8.00	8.03	8.03
Fe^{3+} (Droop)	0.04	0.05	0.05	0.01	0.02	0.07	0.04	0.06	0.00	0.08	0.00	0.00	0.02	0.00	0.08	0.09
Fe^{2+}	1.80	1.69	1.94	1.70	1.67	1.80	1.85	1.64	2.17	2.34	2.28	2.46	2.37	2.38	2.36	2.34
XPyrope	0.06	0.06	0.07	0.09	0.08	0.09	0.09	0.08	0.05	0.07	0.10	0.13	0.16	0.16	0.16	0.15
XAndradite	0.02	0.03	0.03	0.01	0.02	0.04	0.02	0.04	0.05	0.05	0.00	0.00	0.01	0.00	0.04	0.04
XAlmandine	0.60	0.57	0.65	0.56	0.56	0.60	0.62	0.55	0.72	0.79	0.76	0.82	0.80	0.80	0.80	0.79
XUvarovite	0.00	0.00	0.00	0.00	0.00	0.00	0.00	0.00	0.00	0.00	0.00	0.00	0.00	0.00	0.00	0.00
XSpessartine	0.01	0.01	0.02	0.01	0.01	0.01	0.01	0.01	0.03	0.03	0.03	0.02	0.00	0.01	0.01	0.01
XGrossular	0.32	0.33	0.23	0.32	0.33	0.27	0.26	0.31	0.14	0.06	0.10	0.02	0.02	0.03	0.00	0.00

Table A3.2: Representative analyses of garnet. Analyses in wt%, cations recalculated for 12 oxygens.

Lithology	GM	GM	GM	GM	GM	GM	GO	GO	GO	GO	GO	GO	GO	GO
Mineral	Grt	Grt	Grt	Grt	Grt	Grt	Grt	Grt	Grt	Grt	Grt	Grt	Grt	Grt
Point	4.63	4.123	2.53	2.60	2.61	2.68	series1	4.186	5.12	5.30	series 6	series 6	series 7	4.26
Core or rim			core	core	core	core			core	rim	core, incl	rim	rim, incl	
Thin section	GP96-44-P	GP96-89*	GP96-90L	GP96-90L	GP96-90L	GP96-90L	GP96-94//	GP96-94//	GP96-97AP	GP96-97AP	GP96-97AP	GP96-97AP	GP96-97AP	GP96-97AP
Na_2O	0.09	0.03	0.00	0.04	0.05	0.11	0.02	0.03	0.00	0.01	0.11	0.09	0.01	0.05
MgO	3.81	1.74	3.76	1.77	3.17	3.62	0.16	0.18	2.20	1.65	2.72	2.07	1.79	2.20
SiO_2	37.04	37.68	37.89	36.96	37.58	37.98	38.22	37.68	37.09	37.72	37.00	37.25	37.07	37.02
Al_2O_3	21.40	20.40	20.55	20.25	20.62	20.89	21.48	21.24	21.23	21.42	21.35	21.29	21.12	21.41
K_2O	0.00	0.01	0.00	0.00	0.00	0.00	0.00	0.00	0.00	0.03	0.02	0.01	0.00	0.01
CaO	1.33	11.51	5.67	5.10	8.02	6.65	20.94	20.48	3.76	6.68	1.07	3.41	1.55	4.74
TiO_2	0.00	0.12	0.14	0.00	0.18	0.09	0.02	0.02	0.03	0.06	0.00	0.18	0.00	0.03
FeO	36.74	27.84	31.12	32.84	29.13	30.64	16.28	16.62	35.30	33.30	36.78	35.82	34.98	34.06
MnO	0.31	0.36	1.05	3.03	0.63	0.70	3.63	3.10	0.33	0.20	1.90	0.63	3.86	0.54
Cr_2O_3	0.01	0.02	0.13	0.00	0.04	0.05	0.08	0.03	0.00	0.00	0.02	0.03	0.15	0.00
NiO		0.01	0.06	0.00	0.00	0.03								
Total	100.73	99.66	100.31	99.95	99.32	100.67	100.72	99.29	99.91	101.07	100.95	100.75	100.53	99.99
Si	2.96	3.01	3.01	3.00	3.00	3.00	2.98	2.98	2.99	3.00	2.97	2.99	2.99	2.98
Al	2.02	1.92	1.92	1.94	1.94	1.95	1.97	1.98	2.02	2.01	2.02	2.01	2.01	2.03
Ti	0.00	0.01	0.01	0.00	0.01	0.01	0.00	0.00	0.00	0.00	0.00	0.01	0.00	0.00
Fe^{tot}	2.46	1.86	2.07	2.23	1.95	2.02	1.06	1.10	2.38	2.21	2.47	2.40	2.36	2.29
Mn	0.02	0.02	0.07	0.21	0.04	0.05	0.24	0.21	0.02	0.01	0.13	0.04	0.26	0.04
Mg	0.45	0.21	0.45	0.21	0.38	0.43	0.02	0.02	0.26	0.20	0.33	0.25	0.22	0.26
Ca	0.11	0.99	0.48	0.44	0.69	0.56	1.75	1.74	0.32	0.57	0.09	0.29	0.13	0.41
Ni		0.00	0.00	0.00	0.00	0.00								
Cr	0.00	0.00	0.01	0.00	0.00	0.00	0.00	0.00	0.00	0.00	0.00	0.00	0.01	0.00
Cations	8.03	8.02	8.02	8.03	8.01	8.02	8.03	8.03	8.00	8.00	8.02	8.00	7.99	8.01
Fe^{3+} (Droop)	0.08	0.06	0.06	0.10	0.04	0.06	0.09	0.08	0.00	0.00	0.05	0.00	0.00	0.02
Fe^{2+}	2.37	1.80	2.00	2.12	1.90	1.96	0.97	1.01	2.38	2.21	2.42	2.40	2.37	2.27
XPyrope	0.15	0.07	0.15	0.07	0.13	0.14	0.01	0.01	0.09	0.07	0.11	0.08	0.07	0.09
XAndradite	0.04	0.03	0.03	0.05	0.03	0.03	0.04	0.04	0.00	0.00	0.02	0.01	0.00	0.01
XAlmandine	0.80	0.60	0.67	0.71	0.63	0.65	0.33	0.34	0.80	0.74	0.82	0.80	0.79	0.76
XUvarovite	0.00	0.00	0.00	0.00	0.00	0.00	0.00	0.00	0.00	0.00	0.00	0.00	0.00	0.00
XSpessartine	0.01	0.01	0.02	0.07	0.01	0.02	0.08	0.07	0.01	0.00	0.04	0.01	0.09	0.01
XGrossular	0.00	0.29	0.12	0.10	0.20	0.15	0.54	0.54	0.11	0.19	0.01	0.09	0.04	0.13

Table A3.2: Continued.

Lithology	GO	GO	GO	GO	GO	GO	M	GM	GM	GM	M	M	M	M
Mineral	Grt	Grt	Grt	Grt	Grt	Grt	Grt	Grt	Grt	Grt	Grt	Grt	Grt kern	Grt rand
Point	4.28	4.30	4.36	4.38	4.40	4.42	2.118	2.129	3.181	4.18	3.74	3.86	2.8	2.9
Core or rim													core	rim
Thin section	GP96-97AP	GP96-97AP	GP96-97AP	GP96-97AP	GP96-97AP	GP96-97AP	GP96-107c	GP97-2L	GP97-5-L	GP97-5L	GP97-16A	GP97-16A	GP97-17-1	GP97-17-1
Na_2O	0.00	0.05	0.07	0.03	0.00	0.02	0.00	0.02	0.04	0.06	0.00	0.04	0.12	0.05
MgO	1.90	2.25	2.14	2.74	2.22	2.65	2.90	1.11	4.30	4.05	1.35	0.61	1.56	2.01
SiO_2	37.00	37.09	36.91	36.91	36.75	36.81	37.98	37.19	37.43	37.21	37.67	37.27	37.66	37.81
Al_2O_3	20.91	21.09	21.28	20.85	21.17	20.95	20.88	21.18	21.32	21.11	21.19	21.15	20.99	21.30
K_2O	0.02	0.01	0.00	0.02	0.03	0.01	0.01	0.00	0.01	0.00	0.01	0.00	0.06	0.01
CaO	7.87	4.31	4.45	1.53	4.32	1.36	10.30	9.68	2.51	3.89	15.68	14.33	13.14	13.44
TiO_2	0.13	0.00	0.00	0.02	0.00	0.10	0.06	0.04	0.00	0.01	0.13	0.04	0.12	0.00
FeO	31.21	35.00	35.34	36.73	35.09	36.51	26.97	29.32	33.07	31.52	23.26	24.57	27.04	25.79
MnO	0.46	0.33	0.24	0.47	0.28	0.68	0.61	0.97	0.76	0.52	0.37	1.54	0.39	0.49
Cr_2O_3	0.07	0.04	0.03	0.00	0.02	0.00	0.02	0.00	0.00	0.05	0.03	0.05	0.01	0.00
NiO							0.05							
Total	99.51	100.07	100.35	99.24	99.86	99.07	99.71	99.44	99.40	98.30	99.65	99.47	101.08	100.84
Si	2.98	2.99	2.97	3.00	2.97	3.00	3.01	2.99	3.00	3.00	2.98	2.98	2.97	2.97
Al	1.99	2.00	2.02	2.00	2.02	2.01	1.95	2.01	2.01	2.01	1.98	1.99	1.95	1.97
Ti	0.01	0.00	0.00	0.00	0.00	0.01	0.00	0.00	0.00	0.00	0.01	0.00	0.01	0.00
Fe^{tot}	2.10	2.36	2.38	2.50	2.37	2.49	1.79	1.97	2.21	2.13	1.54	1.64	1.79	1.70
Mn	0.03	0.02	0.02	0.03	0.02	0.05	0.04	0.07	0.05	0.04	0.03	0.10	0.03	0.03
Mg	0.23	0.27	0.26	0.33	0.27	0.32	0.34	0.13	0.51	0.49	0.16	0.07	0.18	0.24
Ca	0.68	0.37	0.38	0.13	0.37	0.12	0.87	0.83	0.22	0.34	1.33	1.23	1.11	1.13
Ni							0.00							
Cr	0.00	0.00	0.00	0.00	0.00	0.00	0.00	0.00	0.00	0.00	0.00	0.00	0.00	0.00
Cations	8.02	8.01	8.02	8.00	8.02	7.99	8.01	8.00	8.00	7.99	8.02	8.02	8.04	8.04
Fe^{3+} (Droop)	0.05	0.03	0.06	0.00	0.06	0.00	0.04	0.01	0.00	0.00	0.06	0.07	0.13	0.12
Fe^{2+}	2.05	2.32	2.31	2.50	2.30	2.49	1.75	1.96	2.21	2.13	1.47	1.57	1.65	1.56
XPyrope	0.08	0.09	0.09	0.11	0.09	0.11	0.11	0.04	0.17	0.16	0.05	0.02	0.06	0.08
XAndradite	0.03	0.02	0.03	0.00	0.03	0.00	0.02	0.01	0.00	0.00	0.04	0.03	0.06	0.06
XAlmandine	0.69	0.78	0.78	0.83	0.78	0.84	0.58	0.66	0.74	0.71	0.49	0.53	0.56	0.53
XUvarovite	0.00	0.00	0.00	0.00	0.00	0.00	0.00	0.00	0.00	0.00	0.00	0.00	0.00	0.00
XSpessartine	0.01	0.01	0.01	0.01	0.01	0.02	0.01	0.02	0.02	0.01	0.01	0.04	0.01	0.01
XGrossular	0.20	0.11	0.10	0.04	0.10	0.04	0.27	0.27	0.07	0.11	0.41	0.38	0.31	0.32

Table A3.2: Continued.

Lithology	M	GO	GO	GO	GO	GO	GO	GO	M	GM	GM	GM	GM	M	M
Mineral	Grt	Grt	Grt	Grt	Grt	Grt	Grt	Grt	Grt	Grt	Grt	Grt	Grt	Grt	Grt
Point	3.6	3.109	3.151	3.152	3.159	3.161	3.168	2.195	315	4.170	4.171	4.181	2.18	1.34	1.49
Core or rim	core	rim	core	rim	rim	rim	rim	rim	serie11			rim		rim	core
Thin section	GP97-22A	GP97-32P	GP97-32P	GP97-32P	GP97-32P	GP97-32P	GP97-32P	GP97-33	GP97-25-2	GP97-45A	GP97-45A	GP97-45A	GP97-45b	GP97-46B1	GP97-46B1
Na_2O	0.04	0.01	0.06	0.00	0.00	0.01	0.08	0.05	0.09	0.15	0.03	0.06	0.03	2.50	0.02
MgO	0.54	3.18	3.87	3.23	3.27	2.59	3.50	3.22	1.25	2.12	2.19	2.87	1.76	2.29	1.40
SiO_2	37.67	37.36	37.13	37.08	37.13	36.88	36.88	36.76	37.20	36.88	37.22	36.95	36.87	35.85	37.68
Al_2O_3	21.02	21.04	21.19	21.12	21.27	20.93	21.18	20.96	21.15	21.05	21.26	20.23	21.13	20.28	21.28
K_2O	0.00	0.02	0.00	0.02	0.02	0.02	0.00	0.01	0.01	0.00	0.02	0.00	0.04	0.32	0.00
CaO	15.01	3.23	1.89	2.79	3.59	4.11	1.98	0.79	9.22	7.03	7.22	5.56	5.10	11.34	12.14
TiO_2	0.09	0.03	0.03	0.04	0.00	0.01	0.01	0.05	0.13	0.06	0.06	2.19	0.11	0.10	0.07
FeO	25.92	34.49	34.77	33.98	33.06	33.16	34.30	37.35	28.65	28.93	29.37	31.47	33.92	24.82	27.76
MnO	0.24	1.02	0.61	0.50	0.65	0.74	0.78	0.40	2.90	2.32	2.05	0.65	0.41	0.30	0.65
Cr_2O_3	0.04	0.10	0.00	0.01	0.06	0.02	0.02	0.03	0.00	0.06	0.03	0.05	0.05	0.01	0.00
NiO												0.00			
Total	100.49	100.44	99.46	98.73	98.97	98.40	98.69	99.53	100.59	98.54	99.38	99.98	99.33	97.81	100.97
Si	2.98	2.99	2.99	3.00	2.99	3.00	2.99	2.98	2.97	2.99	2.99	2.95	2.99	2.98	2.98
Al	1.96	1.98	2.01	2.02	2.02	2.01	2.03	2.00	1.99	2.01	2.01	1.91	2.02	1.99	1.98
Ti	0.01	0.00	0.00	0.00	0.00	0.00	0.00	0.00	0.01	0.00	0.00	0.13	0.01	0.01	0.00
Fe^{tot}	1.72	2.31	2.34	2.30	2.23	2.26	2.33	2.53	1.91	1.96	1.97	2.10	2.30	1.73	1.83
Mn	0.02	0.07	0.04	0.03	0.04	0.05	0.05	0.03	0.20	0.16	0.14	0.04	0.03	0.02	0.04
Mg	0.06	0.38	0.46	0.39	0.39	0.31	0.42	0.39	0.15	0.26	0.26	0.34	0.21	0.28	0.16
Ca	1.27	0.28	0.16	0.24	0.31	0.36	0.17	0.07	0.79	0.61	0.62	0.48	0.44	1.01	1.03
Ni												0.00			
Cr	0.00	0.01	0.00	0.00	0.00	0.00	0.00	0.00	0.00	0.00	0.00	0.00	0.00	0.00	0.00
Cations	8.03	8.01	8.01	7.99	7.99	7.99	7.99	8.01	8.02	8.00	8.00	7.96	8.00	8.02	8.03
Fe^{3+} (Droop)	0.08	0.04	0.02	0.00	0.00	0.00	0.00	0.04	0.07	0.00	0.00	0.00	0.00	0.05	0.09
Fe^{2+}	1.63	2.26	2.32	2.30	2.23	2.26	2.33	2.50	1.84	1.96	1.97	2.11	2.30	1.67	1.74
XPyrope	0.02	0.13	0.16	0.13	0.13	0.11	0.14	0.13	0.05	0.09	0.09	0.11	0.07	0.10	0.06
XAndradite	0.04	0.02	0.01	0.00	0.00	0.00	0.00	0.02	0.04	0.00	0.00	0.07	0.00	0.03	0.04
XAlmandine	0.55	0.76	0.78	0.78	0.75	0.76	0.78	0.84	0.62	0.66	0.66	0.71	0.77	0.56	0.58
XUvarovite	0.00	0.00	0.00	0.00	0.00	0.00	0.00	0.00	0.00	0.00	0.00	0.00	0.00	0.00	0.00
XSpessartine	0.01	0.02	0.01	0.01	0.01	0.02	0.02	0.01	0.07	0.05	0.05	0.01	0.01	0.01	0.01
XGrossular	0.38	0.07	0.04	0.08	0.10	0.12	0.06	0.00	0.23	0.20	0.20	0.09	0.14	0.31	0.30

Table A3.2: Continued.

Litholgy	M	M	M	M	M	M	M	M	M	M	M	M	M	M	M
Mineral	Omp	Omp	Omp	Omp	Omp	Omp	Omp	Omp	Omp	Omp	Omp	Omp	Omp	Omp	Omp
Point	8.5	8.6	1.3	1.20	1.26	1.53	1.59	1.62	2.10	2.11	2.34	3.5	1.37	1.50	1.65
Core or rim									rim	core	rim	core			rim
Thin section	A35-2	A35-2	GP96-17	GP96-17	GP96-17	GP96-28	GP96-28	GP96-28	GP97-17-1	GP97-17-1	GP97-17-1	GP97-22A	GP97-46B1	GP97-46B1	GP97-46B1
Na_2O	8.42	7.81	6.27	5.19	5.62	3.92	5.75	5.78	7.07	7.33	7.18	7.31	6.62	6.29	6.34
MgO	6.76	6.99	9.02	8.89	8.61	11.71	9.73	9.28	8.06	7.72	7.88	6.00	8.41	8.75	8.85
SiO_2	56.23	56.02	55.95	55.03	54.22	55.40	56.11	55.97	55.52	55.46	55.92	55.35	55.39	55.82	55.58
Al_2O_3	10.31	9.88	10.21	7.66	8.77	5.70	9.43	8.88	8.63	8.59	9.23	9.09	8.75	8.59	8.71
K_2O	0.00	0.01	0.00	0.00	0.01	0.00	0.00	0.01	0.02	0.01	0.00	0.00	0.02	0.00	0.02
CaO	12.12	12.55	14.47	15.95	14.24	18.73	15.38	15.40	13.12	12.89	12.77	12.15	14.39	14.87	14.67
TiO_2	0.00	0.00	0.05	0.00	0.07	0.00	0.00	0.04	0.01	0.08	0.02	0.02	0.02	0.04	0.01
FeO	7.16	7.66	4.18	6.27	6.97	4.74	3.32	5.02	7.40	8.03	6.65	10.18	6.36	6.37	5.40
MnO	0.05	0.00	0.00	0.06	0.06	0.05	0.00	0.00	0.03	0.02	0.01	0.02	0.05	0.00	0.01
Cr_2O_3	0.00	0.00	0.03	0.00	0.05	0.07	0.05	0.02	0.01	0.00	0.00	0.06	0.09	0.00	0.07
Total	100.99	100.91	100.15	98.99	98.50	100.20	99.72	100.34	99.82	100.12	99.61	100.08	99.90	100.74	99.58
Si	1.98	1.98	1.99	2.01	1.98	1.99	2.00	1.99	1.99	1.98	2.00	2.00	1.98	1.99	1.99
Al^{IV}	0.02	0.02	0.01	0.00	0.02	0.01	0.00	0.01	0.01	0.02	0.00	0.00	0.02	0.01	0.01
Al^{VI}	0.40	0.39	0.41	0.33	0.36	0.23	0.40	0.37	0.35	0.34	0.39	0.39	0.35	0.34	0.36
Ti	0.00	0.00	0.00	0.00	0.00	0.00	0.00	0.00	0.00	0.00	0.00	0.00	0.00	0.00	0.00
Cr	0.00	0.00	0.00	0.00	0.00	0.00	0.00	0.00	0.00	0.00	0.00	0.00	0.00	0.00	0.00
Fe^{tot}	0.21	0.23	0.12	0.19	0.21	0.14	0.10	0.15	0.22	0.24	0.20	0.31	0.19	0.19	0.16
Mg	0.35	0.37	0.48	0.48	0.47	0.63	0.52	0.49	0.43	0.41	0.42	0.32	0.45	0.46	0.47
Mn	0.00	0.00	0.00	0.00	0.00	0.00	0.00	0.00	0.00	0.00	0.00	0.00	0.00	0.00	0.00
Ca	0.46	0.48	0.55	0.62	0.56	0.72	0.59	0.59	0.50	0.49	0.49	0.47	0.55	0.57	0.56
Na	0.57	0.54	0.43	0.37	0.40	0.27	0.40	0.40	0.49	0.51	0.50	0.51	0.46	0.43	0.44
K	0.00	0.00	0.00	0.00	0.00	0.00	0.00	0.00	0.00	0.00	0.00	0.00	0.00	0.00	0.00
Cations	4.00	4.00	4.00	4.00	4.00	4.00	4.00	4.00	4.00	4.00	4.00	4.00	4.00	4.00	4.00
Fe^{3+} (C&C 1974)	0.15	0.12	0.00	0.04	0.02	0.03	0.00	0.02	0.13	0.14	0.11	0.12	0.09	0.07	0.07
Fe^{2+}	0.06	0.10	0.12	0.15	0.20	0.11	0.10	0.12	0.10	0.10	0.09	0.19	0.10	0.12	0.09
XJd (=XNa-XAcm (Fe^{3+}))															
XJd	0.43	0.41	0.43	0.33	0.38	0.24	0.40	0.37	0.36	0.36	0.39	0.39	0.37	0.36	0.37

Table A3.3: Representative analyses of omphacite. Analyses in wt%, normalised to 6 oxygens and 4 cations.

Lithology	M	M	M	M	M	GM	GM	GM	GM	GM	GM	GM	GM	GM	GM
Mineral	Wh mica	Wh mica	Wh mica	Wh mica	Wh mica	Wh mica	Wh mica	wh mica	Wh mica	Wh mica	Wh mica	Wh mica	Wh mica	Wh mica	Wh mica
Point	4.22	3.198	3.199	3.231	3.233	4.72	4.79	6.20	4.162	4.164	4.49	4.58	4.61	2.56	2.59
Thin section	GP96-26L	GP96-28	GP96-28	GP96-28	GP96-28	GP96-29X	GP96-29X	GP96-37A	GP96-43	GP96-43	GP96-44P	GP96-44P	GP96-44P	GP96-90L	GP96-90L
Na_2O	0.15	0.08	0.12	0.50	0.41	0.15	0.12	1.03	0.35	0.48	0.25	0.12	0.37	0.63	0.93
MgO	2.40	5.44	4.71	4.70	5.15	3.13	4.55	1.49	4.33	3.66	3.87	4.19	4.22	2.50	1.59
SiO_2	50.72	54.36	52.80	51.52	53.22	50.59	52.82	48.33	52.70	51.97	51.82	52.38	52.38	52.16	52.62
Al_2O_3	27.71	24.01	25.12	23.99	23.54	27.07	23.42	34.22	26.56	27.93	28.49	27.46	27.26	28.28	29.10
K_2O	9.19	9.63	9.43	9.21	9.05	9.17	8.70	9.21	8.72	8.62	9.25	9.09	8.54	9.39	8.57
CaO	0.04	0.01	0.01	0.30	0.08	0.00	0.00	0.00	0.00	0.00	0.02	0.01	0.01	0.01	0.00
TiO_2	0.28	0.17	0.14	0.19	0.20	0.53	0.59	0.25	0.15	0.16	0.13	0.13	0.14	0.27	0.23
FeO	4.59	1.82	2.07	2.23	1.77	3.19	4.43	2.07	2.09	2.53	1.52	1.73	2.36	1.48	1.11
MnO	0.03	0.00	0.01	0.00	0.00	0.03	0.00	0.00	0.02	0.01	0.01	0.00	0.00	0.01	0.00
Cr_2O_3	0.01	0.00	0.06	0.00	0.00	0.03	0.02	0.00	0.06	0.02	0.01	0.10	0.03	0.00	0.01
NiO														0.01	0.01
Total	95.08	95.51	94.39	92.63	93.41	93.83	94.63	96.62	94.90	95.34	95.33	95.20	95.26	94.70	94.16
Si	3.39	3.57	3.52	3.51	3.57	3.41	3.54	3.16	3.48	3.42	3.40	3.45	3.44	3.45	3.47
Al^{IV}	0.61	0.43	0.48	0.49	0.43	0.59	0.46	0.84	0.52	0.58	0.60	0.55	0.56	0.55	0.53
Al^{VI}	1.58	1.44	1.49	1.44	1.44	1.56	1.39	1.79	1.54	1.59	1.61	1.57	1.56	1.65	1.73
Ti	0.01	0.01	0.01	0.01	0.01	0.03	0.03	0.01	0.01	0.01	0.01	0.01	0.01	0.01	0.01
Fe^{tot}	0.26	0.10	0.12	0.13	0.10	0.18	0.25	0.11	0.12	0.14	0.08	0.10	0.13	0.08	0.06
Mn	0.00	0.00	0.00	0.00	0.00	0.00	0.00	0.00	0.00	0.00	0.00	0.00	0.00	0.00	0.00
Mg	0.24	0.53	0.47	0.48	0.52	0.31	0.45	0.15	0.43	0.36	0.38	0.41	0.41	0.25	0.16
Ca	0.00	0.00	0.00	0.02	0.01	0.00	0.00	0.00	0.00	0.00	0.00	0.00	0.00	0.00	0.00
Ni														0.00	0.00
Na	0.02	0.01	0.02	0.07	0.05	0.02	0.02	0.13	0.04	0.06	0.03	0.01	0.05	0.08	0.12
K	0.78	0.81	0.80	0.80	0.78	0.79	0.74	0.77	0.73	0.72	0.78	0.76	0.72	0.79	0.72
Cr	0.00	0.00	0.00	0.00	0.00	0.00	0.00	0.00	0.00	0.00	0.00	0.00	0.00	0.00	0.00
Cations	6.90	6.90	6.90	6.95	6.90	6.89	6.88	6.96	6.87	6.88	6.89	6.87	6.87	6.87	6.81
Mg-number	48.29	84.21	80.23	78.99	83.85	63.64	64.66	56.16	78.69	72.05	81.94	81.17	76.14	75.06	71.78
Si (p.f.u).	3.395	3.575	3.516	3.514	3.575	3.409	3.541	3.157	3.476	3.421	3.405	3.445	3.445	3.450	3.472
Oct (p.f.u.)	2.093	2.077	2.081	2.057	2.063	2.084	2.125	2.063	2.093	2.095	2.081	2.092	2.109	1.997	1.964

Table A3.4: Representative analyses of white mica. Analyses in wt%, recalculated to 11 oxygens.

Lithology	GM	GM	GO	GO	GO	GO	GO	GO	GO	GO	GO	GO	GO	GO
Mineral	Wh mica	Wh mica	Wh mica	Wh mica	Wh mica	Wh mica	Wh mica	Wh mica	Wh mica	Wh mica	Wh mica	Wh mica	Wh mica	Wh mica
Point	2.62	2.70	4.182	5.13	5.28	serie6 (Grt)	serie6 (Grt)	serie7 (Grt)	4.25	4.27	4.29	4.35	4.37	4.39
Thin section	GP96-90L	GP96-90L	GP96-94P	GP96-97AP	GP96-97AP	GP96-97AP	GP96-97AP	GP96-97AP	GP96-97AP	GP96-97AP	GP96-97AP	GP96-97AP	GP96-97AP	GP96-97AP
Na_2O	0.39	0.41	0.19	0.34	0.51	0.64	0.52	0.69	0.37	0.36	0.58	0.40	0.40	0.56
MgO	3.89	3.69	1.34	3.30	2.80	2.84	3.39	2.77	3.31	3.41	2.70	2.93	3.33	2.50
SiO_2	52.11	50.85	46.49	51.25	50.57	48.32	52.18	47.90	51.24	50.49	49.52	49.91	51.04	48.30
Al_2O_3	26.96	27.22	32.81	29.36	30.43	27.46	29.10	28.56	28.85	28.51	31.00	30.29	28.97	31.67
K_2O	9.74	9.72	9.66	9.11	4.21	9.02	8.65	8.46	8.85	9.44	8.91	9.27	8.75	8.94
CaO	0.00	0.04	0.02	0.00	0.02	0.00	0.01	0.06	0.02	0.03	0.01	0.00	0.01	0.05
TiO_2	0.12	0.16	0.24	0.25	0.37	2.36	0.14	0.17	0.22	0.25	0.42	0.30	0.18	0.30
FeO	1.61	1.88	2.63	2.41	2.80	2.25	2.64	2.82	2.65	2.53	3.09	2.64	2.78	2.87
MnO	0.00	0.00	0.00	0.02	0.01	0.00	0.04	0.04	0.02	0.00	0.00	0.00	0.00	0.01
Cr_2O_3	0.03	0.02	0.00	0.01	0.00	0.11	0.00	0.09	0.06	0.04	0.00	0.02	0.04	0.01
NiO	0.00	0.00												
Total	94.82	93.97	93.37	96.03	91.69	92.87	96.62	91.44	95.49	95.01	96.21	95.74	95.44	95.17
Si	3.46	3.42	3.16	3.36	3.37	3.29	3.39	3.31	3.37	3.36	3.26	3.29	3.36	3.21
Al^{IV}	0.54	0.58	0.84	0.64	0.63	0.71	0.61	0.69	0.63	0.64	0.74	0.71	0.64	0.79
Al^{VI}	1.56	1.57	1.79	1.62	1.75	1.50	1.62	1.63	1.61	1.59	1.66	1.65	1.61	1.69
Ti	0.01	0.01	0.01	0.01	0.02	0.12	0.01	0.01	0.01	0.01	0.02	0.01	0.01	0.01
Fe^{tot}	0.09	0.11	0.15	0.13	0.16	0.13	0.14	0.16	0.15	0.14	0.17	0.15	0.15	0.16
Mn	0.00	0.00	0.00	0.00	0.00	0.00	0.00	0.00	0.00	0.00	0.00	0.00	0.00	0.00
Mg	0.38	0.37	0.14	0.32	0.28	0.29	0.33	0.29	0.33	0.34	0.26	0.29	0.33	0.25
Ca	0.00	0.00	0.00	0.00	0.00	0.00	0.00	0.00	0.00	0.00	0.00	0.00	0.00	0.00
Ni	0.00	0.00												
Na	0.05	0.05	0.02	0.04	0.07	0.08	0.07	0.09	0.05	0.05	0.07	0.05	0.05	0.07
K	0.82	0.83	0.84	0.76	0.36	0.78	0.72	0.75	0.74	0.80	0.75	0.78	0.74	0.76
Cr	0.00	0.00	0.00	0.00	0.00	0.01	0.00	0.01	0.00	0.00	0.00	0.00	0.00	0.00
Cations	6.92	6.94	6.95	6.90	6.63	6.91	6.88	6.94	6.89	6.94	6.93	6.93	6.89	6.95
Mg-number	81.18	77.80	47.61	70.89	64.02	69.24	69.60	63.67	69.02	70.59	60.91	66.42	68.15	60.79
Si (p.f.u).	3.456	3.415	3.158	3.358	3.367	3.294	3.389	3.307	3.373	3.358	3.255	3.293	3.365	3.211
Oct (p.f.u.)	2.046	2.053	2.083	2.093	2.208	2.044	2.098	2.096	2.098	2.086	2.112	2.098	2.106	2.115

Table A3.4: Continued.

Lithology	GO	GM	GM	GM	GM	GO	GO	GO	GO	GO	GO	GO	GO	GM
Mineral	Wh mica	Wh mica	Wh mica	Wh mica	Wh mica	Wh mica	Wh mica	Wh mica	Wh mica	Wh mica	Wh mica	Wh mica	Wh mica	Wh mica
Point	4.41	2.123	2.125	3.175	4.19	3.110	3.150	3.153	3.158	3.160	3.167	2.192	3.7	4.167
Thin section	GP96-97AP	GP97-2L	GP97-2L	GP97-5L	GP97-5L	GP97-32P	GP97-32P	GP97-32P	GP97-32P	GP97-32P	GP97-32P	GP97-33	GP97-44-1	GP97-45A
Na_2O	0.45	0.22	0.29	0.17	0.32	0.56	0.38	0.47	0.55	0.46	0.47	0.35	0.64	0.21
MgO	3.28	3.52	3.16	3.85	3.78	2.46	3.50	3.16	2.53	3.12	2.88	3.14	0.44	3.16
SiO_2	50.75	50.60	49.06	52.44	50.50	49.30	50.95	50.58	48.41	49.95	50.77	50.27	46.02	49.62
Al_2O_3	29.32	28.46	28.68	27.32	28.45	31.68	29.54	29.86	31.34	29.46	30.21	29.38	35.85	29.54
K_2O	8.99	9.30	9.58	8.31	9.63	9.00	9.19	9.06	9.06	9.00	9.19	9.24	10.66	9.72
CaO	0.00	0.02	0.04	0.02	0.00	0.01	0.00	0.00	0.01	0.03	0.01	0.01	0.00	0.03
TiO_2	0.16	0.15	0.21	0.15	0.14	0.28	0.15	0.21	0.31	0.14	0.20	0.18	0.22	0.57
FeO	2.42	1.73	2.74	1.90	1.51	2.13	1.70	2.08	2.56	2.53	2.04	2.25	1.05	2.02
MnO	0.00	0.00	0.04	0.07	0.05	0.01	0.03	0.02	0.02	0.03	0.01	0.00	0.00	0.03
Cr_2O_3	0.00	0.02	0.05	0.00	0.00	0.02	0.08	0.04	0.06	0.03	0.06	0.00	0.01	0.03
NiO													0.02	
Total	95.37	93.98	93.77	94.15	94.33	95.41	95.41	95.43	94.78	94.68	95.76	94.81	94.89	94.86
Si	3.35	3.38	3.32	3.47	3.37	3.25	3.35	3.33	3.23	3.33	3.33	3.34	3.07	3.30
Al^{IV}	0.65	0.62	0.68	0.53	0.63	0.75	0.65	0.67	0.77	0.67	0.67	0.66	0.93	0.70
Al^{VI}	1.63	1.62	1.60	1.60	1.61	1.71	1.64	1.65	1.69	1.64	1.67	1.64	1.89	1.62
Ti	0.01	0.01	0.01	0.01	0.01	0.01	0.01	0.01	0.02	0.01	0.01	0.01	0.01	0.03
Fe^{tot}	0.13	0.10	0.16	0.11	0.08	0.12	0.09	0.11	0.14	0.14	0.11	0.12	0.06	0.11
Mn	0.00	0.00	0.00	0.00	0.00	0.00	0.00	0.00	0.00	0.00	0.00	0.00	0.00	0.00
Mg	0.32	0.35	0.32	0.38	0.38	0.24	0.34	0.31	0.25	0.31	0.28	0.31	0.04	0.31
Ca	0.00	0.00	0.00	0.00	0.00	0.00	0.00	0.00	0.00	0.00	0.00	0.00	0.00	0.00
Ni													0.00	
Na	0.06	0.03	0.04	0.02	0.04	0.07	0.05	0.06	0.07	0.06	0.06	0.04	0.08	0.03
K	0.76	0.79	0.83	0.70	0.82	0.76	0.77	0.76	0.77	0.76	0.77	0.78	0.91	0.83
Cr	0.00	0.00	0.00	0.00	0.00	0.00	0.00	0.00	0.00	0.00	0.00	0.00	0.00	0.00
Cations	6.91	6.90	6.96	6.82	6.94	6.92	6.91	6.91	6.95	6.92	6.90	6.91	7.00	6.93
Mg-number	70.74	78.37	67.26	78.33	81.72	67.29	78.64	73.04	63.77	68.77	71.57	71.33	43.00	73.59
Si (p.f.u).	3.350	3.381	3.318	3.469	3.369	3.251	3.349	3.331	3.227	3.325	3.331	3.340	3.073	3.304
Oct (p.f.u.)	2.095	2.078	2.093	2.095	2.075	2.088	2.088	2.088	2.103	2.097	2.074	2.086	2.008	2.080

Table A3.4: Continued.

Lithology	M	GM	GM	GM	GO	GO	GO	GM	GM	M	M	GM	GM	GM	GM
Mineral	Bt	Bt	Bt	Bt	Bt	Bt	Bt	Bt	Bt	Bt	Bt	Bt	Bt	Bt	Bt
Point	3.249	4.158	4.56	3.89	4.183	5.1	5.26	2.128	2.144	3.73	317	4.168	4.174	7.22	2.19
Thin section	GP96-28	GP96-43	GP96-44P	GP96-44P	GP96-94-P	GP96-97AP	GP96-97AP	GP97-2-L	GP97-2-L	GP97-16A	GP97-25-2	GP97-45A	GP97-45A	GP97-45b	GP97-45b
Na_2O	0.05	0.15	0.23	0.10	0.14	0.16	0.31	0.08	0.08	0.49	2.77	0.04	0.09	0.29	0.14
MgO	10.28	11.15	11.33	11.95	5.29	7.84	8.27	9.08	9.27	15.24	5.56	9.13	8.36	6.45	6.60
SiO_2	35.05	35.36	35.90	34.54	32.35	33.22	35.86	35.48	35.54	38.07	43.49	35.30	35.53	34.52	34.94
Al_2O_3	17.93	19.99	18.65	18.65	17.92	18.77	19.41	17.15	17.89	16.37	18.63	18.45	17.07	17.96	16.29
K_2O	10.22	9.23	9.48	7.88	7.69	7.84	8.76	9.88	9.65	8.59	6.61	9.83	9.21	9.34	9.53
CaO	0.37	0.00	0.01	0.00	0.08	0.03	0.02	0.03	0.05	0.04	1.41	0.01	0.02	0.03	0.05
TiO_2	0.95	0.37	1.39	1.07	1.25	1.29	1.16	1.63	1.63	1.12	0.57	1.79	2.23	2.12	2.43
FeO	20.15	17.19	17.52	19.24	28.18	24.33	22.15	19.43	18.97	13.43	14.86	19.83	21.70	24.04	24.16
MnO	0.10	0.02	0.03	0.02	0.19	0.03	0.00	0.21	0.16	0.07	0.10	0.10	0.17	0.10	0.21
Cr_2O_3	0.00	0.07	0.03	0.00	0.05	0.00	0.06	0.08	0.09	0.05	0.06	0.04	0.03	0.00	0.03
NiO				0.04									0.01		
Total	95.06	93.44	94.50	93.43	93.07	93.52	95.92	93.06	93.33	93.35	94.00	94.41	94.37	94.75	94.35
Si	2.71	2.71	2.73	2.66	2.63	2.63	2.73	2.78	2.77	2.85	3.19	2.72	2.76	2.71	2.77
Al^{IV}	1.29	1.29	1.27	1.34	1.37	1.37	1.27	1.22	1.23	1.15	0.81	1.28	1.24	1.29	1.23
Al^{VI}	0.34	0.51	0.40	0.36	0.36	0.39	0.47	0.37	0.41	0.30	0.80	0.40	0.33	0.37	0.29
Ti	0.06	0.02	0.08	0.06	0.08	0.08	0.07	0.10	0.10	0.06	0.03	0.10	0.13	0.13	0.15
Fe^{tot}	1.30	1.10	1.11	1.24	1.92	1.61	1.41	1.27	1.23	0.84	0.91	1.28	1.41	1.58	1.60
Mn	0.01	0.00	0.00	0.00	0.01	0.00	0.00	0.01	0.01	0.00	0.01	0.01	0.01	0.01	0.01
Mg	1.18	1.27	1.28	1.37	0.64	0.93	0.94	1.06	1.08	1.70	0.61	1.05	0.97	0.76	0.78
Ca	0.03	0.00	0.00	0.00	0.01	0.00	0.00	0.00	0.00	0.00	0.11	0.00	0.00	0.00	0.00
Ni				0.00									0.00		
Na	0.01	0.02	0.03	0.01	0.02	0.02	0.05	0.01	0.01	0.07	0.39	0.01	0.01	0.04	0.02
K	1.01	0.90	0.92	0.77	0.80	0.79	0.85	0.99	0.96	0.82	0.62	0.97	0.91	0.94	0.96
Cr	0.00	0.00	0.00	0.00	0.00	0.00	0.00	0.01	0.01	0.00	0.00	0.00	0.00	0.00	0.00
Cations	7.93	7.83	7.83	7.82	7.84	7.82	7.78	7.83	7.80	7.81	7.48	7.82	7.79	7.82	7.82
Fe^{3+}	0.20	0.17	0.17	0.19	0.29	0.24	0.21	0.19	0.19	0.13	0.14	0.19	0.21	0.24	0.24
Fe^{2+}	1.11	0.94	0.95	1.05	1.63	1.37	1.20	1.08	1.05	0.72	0.77	1.09	1.20	1.34	1.36
XAl	0.117	0.175	0.139	0.117	0.118	0.140	0.162	0.131	0.144	0.102	0.339	0.141	0.116	0.132	0.102
XTi	0.019	0.007	0.028	0.020	0.025	0.028	0.023	0.034	0.034	0.022	0.013	0.036	0.046	0.044	0.051

Table A3.5: Representative analyses of biotite. Analyses in wt%, recalculated to 11 oxygens. Fe^{3+} estimated following Williams and Grambling (1990).

Lithology	M	M	GM	GM	GM	GM	M	M	M	M	M	M	M	M	M
Mineral	Amph	Amph	Amph	Amph	Amph	Amph	Amph	Amph	Amph	Amph	Amph	Amph	Amph	Amph	Amph
Point	1.2	1.30	3.188	1.64	4.111	4.122	2.119	2.123	3.43	3.56	3.82	2.43	2.82	75	83
Thin section	GP96-17	GP96-17	GP96-28	GP96-28	GP96-89*	GP96-89*	GP96-107c	GP96-107c	GP97-10	GP97-10	GP97-16A	GP97-25-2	GP97-25-2	GP97-46B1	GP97-46B1
Na_2O	1.62	1.98	0.01	1.95	0.90	0.36	1.21	1.30	0.75	0.24	3.40	1.80	1.62	2.27	2.10
MgO	16.26	17.45	1.47	16.44	4.49	15.39	11.65	10.82	16.35	18.49	12.80	11.03	5.05	13.89	16.97
SiO_2	53.24	53.35	52.86	53.67	39.33	52.72	47.73	45.63	52.55	55.76	46.11	46.83	41.40	51.42	52.70
Al_2O_3	5.06	5.47	14.95	5.49	20.14	3.81	11.77	12.60	3.46	1.08	10.94	9.69	13.06	7.20	4.83
K_2O	0.08	0.11	0.00	0.11	0.52	0.31	0.31	0.55	0.30	0.10	0.64	0.57	1.44	0.12	0.12
CaO	10.86	10.09	8.28	10.11	12.03	11.47	9.72	10.54	11.94	12.66	9.78	10.25	11.51	9.29	9.96
TiO_2	0.03	0.00	0.01	0.03	0.32	0.13	0.14	0.24	0.02	0.00	0.18	0.34	0.23	0.36	0.03
FeO	9.97	6.94	17.59	9.08	17.86	12.61	14.67	14.02	11.37	8.88	11.91	15.97	23.70	11.56	8.77
MnO	0.15	0.11	0.56	0.08	0.11	0.18	0.17	0.09	0.37	0.42	0.12	0.20	0.17	0.12	0.05
Cr_2O_3	0.01	0.05	0.00	0.04	0.00	0.00	0.09	0.07	0.05	0.07	0.08	0.00	0.00	0.06	0.06
NiO					0.06	0.02	0.05	0.00							
Total	97.24	95.50	95.71	96.85	95.72	96.97	97.47	95.69	97.09	97.63	95.97	96.70	98.19	96.25	95.45
Si	7.59	7.62	7.67	7.62	6.00	7.63	6.94	6.78	7.59	7.88	6.83	6.98	6.41	7.44	7.60
Al^{IV}	0.41	0.38	0.32	0.38	1.96	0.35	1.05	1.19	0.41	0.12	1.15	0.98	1.56	0.52	0.40
Al^{VI}	0.44	0.54	2.23	0.54	1.67	0.30	0.97	1.01	0.18	0.06	0.76	0.72	0.82	0.71	0.42
Ti	0.00	0.00	0.00	0.00	0.04	0.01	0.02	0.03	0.00	0.00	0.02	0.04	0.03	0.04	0.00
Fe^{tot}	1.19	0.83	2.14	1.08	2.28	1.53	1.78	1.74	1.37	1.05	1.48	1.99	3.07	1.40	1.06
Mn	0.02	0.01	0.07	0.01	0.01	0.02	0.02	0.01	0.04	0.05	0.02	0.03	0.02	0.01	0.01
Mg	3.45	3.71	0.32	3.48	1.02	3.32	2.53	2.40	3.52	3.90	2.83	2.45	1.17	3.00	3.65
Ca	1.66	1.54	1.29	1.54	1.97	1.78	1.51	1.68	1.85	1.92	1.55	1.64	1.91	1.44	1.54
Ni		0.00			0.01	0.00	0.01	0.00							
Na	0.45	0.55	0.00	0.54	0.27	0.10	0.34	0.37	0.21	0.07	0.98	0.52	0.49	0.64	0.59
K	0.02	0.02	0.00	0.02	0.10	0.06	0.06	0.10	0.05	0.02	0.12	0.11	0.28	0.02	0.02
Cr	0.00	0.00	0.00	0.00	0.00	0.00	0.00	0.00	0.00	0.00	0.00	0.00	0.00	0.00	0.00
Cations	15.22	15.20	14.05	15.19	15.33	15.11	15.22	15.32	15.24	15.06	15.73	15.45	15.76	15.22	15.28
Fe^{3+}	0.00	0.00	0.00	0.00	0.00	0.00	0.00	0.00	0.00	0.00	0.00	0.00	0.00	0.00	0.00
Fe^{2+}	1.19	0.83	2.14	1.08	2.28	1.53	1.78	1.74	1.37	1.05	1.48	1.99	3.07	1.40	1.06

Table A3.6: Representative analyses of amphibole. Analyses in wt%, recalculated to 23 oxygens, following the method of Holland and Blundy (1994).

Lithology	GM	GM	GO	GO	M	GM	GM	M	GO	M	GO	GO	GM	M	M
Mineral	Fsp	Fsp	Fsp	Fsp	Fsp	Fsp	Fsp	Fsp	Fsp	Fsp	Fsp	Fsp	Fsp	Fsp	Fsp
Point	4.143	4.109	4.187	4.205	2.120	286	2.133	2.86	2.178	213	3.5	3.15	4.193	77	82
Sample	GP96-35c	GP96-89*	GP96-94-P	GP96-94-P	GP96-107c	GP96-126//	GP97-2-L	GP97-25-2	GP97-33	GP97-39B	GP97-44-1	GP97-44-1	GP97-45A	GP97-46B1	GP97-46B1
Na_2O	7.68	5.63	10.46	0.51	8.16	11.76	8.40	7.95	10.61	13.01	0.61	11.36	11.55	10.71	11.21
MgO	0.00	0.00	0.00	0.00	0.00	0.00	0.00	0.00	0.01	0.70	0.00	0.00	0.00	0.00	0.00
SiO_2	61.54	54.97	66.86	63.53	60.96	68.08	60.44	59.91	65.64	63.24	63.85	68.10	68.98	65.07	65.99
Al_2O_3	24.27	27.53	20.53	18.38	23.52	19.73	24.34	24.75	20.90	22.04	17.56	18.88	19.11	21.39	20.80
K_2O	0.26	0.07	0.07	16.75	0.11	0.09	0.10	0.12	0.04	0.41	16.18	0.06	0.08	0.07	0.07
CaO	5.03	10.75	0.81	0.00	5.81	0.18	5.86	6.55	2.00	0.32	0.19	0.33	0.33	2.09	1.27
TiO_2	0.00	0.00	0.00	0.00	0.00	0.00	0.00	0.12	0.01	0.03	0.00	0.00	0.00	0.00	0.00
FeO	0.04	0.08	0.02	0.01	0.09	0.02	0.00	0.42	0.91	0.44	0.00	0.02	0.16	0.38	0.34
MnO	0.00	0.01	0.06	0.00	0.00	0.02	0.08	0.05	0.10	0.00	0.01	0.00	0.01	0.00	0.06
Cr_2O_3	0.00	0.00	0.00	0.02	0.00	0.00	0.06	0.00	0.00	0.09	0.01	0.06	0.04	0.00	0.00
NiO		0.01			0.02						0.04	0.00	0.02		
Total	98.77	98.94	98.73	99.17	98.65	99.84	99.22	99.83	100.20	100.16	98.39	98.73	100.21	99.71	99.70
Si	2.78	2.50	2.98	2.95	2.75	2.97	2.70	2.68	2.90	2.74	3.00	3.02	3.02	2.87	2.90
Al	1.29	1.48	1.08	1.01	1.25	1.02	1.28	1.31	1.09	1.13	0.97	0.99	0.98	1.11	1.08
Ca	0.24	0.52	0.04	0.00	0.28	0.01	0.28	0.31	0.09	0.01	0.01	0.02	0.02	0.10	0.06
Na	0.67	0.50	0.90	0.05	0.71	1.00	0.73	0.69	0.91	1.09	0.06	0.98	0.98	0.92	0.96
K	0.01	0.00	0.00	0.99	0.01	0.01	0.01	0.01	0.00	0.02	0.97	0.00	0.00	0.00	0.00
Cations	5.00	5.00	5.00	5.00	5.00	5.00	5.00	5.00	5.00	5.00	5.00	5.00	5.00	5.00	5.00
XAb	0.72	0.48	0.96	0.04	0.71	0.99	0.72	0.68	0.90	0.97	0.05	0.98	0.98	0.90	0.94
XAn	0.26	0.51	0.04	0.00	0.28	0.01	0.28	0.31	0.09	0.01	0.01	0.02	0.02	0.10	0.06
XOr	0.02	0.00	0.00	0.96	0.01	0.01	0.01	0.01	0.00	0.02	0.94	0.00	0.00	0.00	0.00

Table A3.7: Representative analyses of plagioclase. Analyses in wt%, normalised to 5 cations.

Litholog	GO	M	GM	GM	M	GM	GM	GO	GM	GM	GO	GO	GO	GO	M	M	GO
Mineral	Chl	Chl	Chl	Chl	Chl	Chl	Chl	Chl	Chl	Chl	Chl	Chl	Chl	Chl	Chl	Chl	Chl
Point	3.309	4.21	6.3	6.23	4.57	4.116	4.119	4.256	2.120	2.140	3.138	3.147	2.268	2.275	169	205	3.14
Sample	GP96-22	GP96-26L	GP96-37A	GP96-37A	GP96-82	GP96-89*	GP96-89*	GP96-94-P	GP97-2L	GP97-2L	GP97-32P	GP97-32P	GP97-33	GP97-33	GP97-39B	GP97-39B	GP97-44-1
Na_2O	0.00	0.10	0.13	0.11	0.03	0.05	0.01	0.01	0.07	0.00	0.03	0.00	0.00	0.05	0.03	0.34	0.01
MgO	11.28	8.02	11.41	13.39	18.18	16.06	16.15	6.51	13.49	14.81	7.38	15.85	6.75	13.41	20.28	17.96	6.56
SiO_2	26.42	24.31	24.19	25.63	25.39	25.95	25.42	23.79	24.05	24.49	24.49	25.62	23.45	24.33	26.98	29.25	26.11
Al_2O_3	17.77	19.43	22.93	20.81	21.90	19.63	20.63	19.50	21.32	22.05	22.27	21.18	21.86	22.41	21.12	17.84	17.78
K_2O	0.08	0.02	0.06	0.02	0.00	0.03	0.01	0.09	0.00	0.00	0.50	0.01	0.02	0.02	0.27	2.14	0.87
CaO	0.18	0.04	0.00	0.01	0.09	0.05	0.03	0.02	0.02	0.00	0.06	0.02	0.04	0.00	0.08	0.06	0.05
TiO_2	0.00	0.13	0.03	0.09	0.05	0.00	0.07	0.01	0.03	0.01	0.00	0.04	0.00	0.07	0.09	0.19	0.21
FeO	28.25	35.16	28.91	26.65	19.55	23.36	22.83	35.02	25.48	24.21	32.61	21.88	34.30	25.37	16.82	16.94	34.70
MnO	0.25	0.70	0.00	0.06	0.11	0.16	0.20	0.52	0.43	0.31	0.81	0.08	0.27	0.13	0.34	0.22	0.66
Cr_2O_3	0.06	0.00	0.04	0.08	0.02	0.06	0.13	0.00	0.00	0.00	0.05	0.00	0.04	0.07	0.10	0.42	0.10
NiO					0.00	0.07	0.06										0.02
Total	84.23	87.88	87.62	86.71	85.27	85.30	85.45	85.42	84.83	85.87	88.11	84.61	86.69	85.74	86.08	85.37	87.05
Si	5.91	5.43	5.20	5.49	5.33	5.57	5.43	5.48	5.27	5.25	5.38	5.49	5.27	5.25	5.55	6.19	5.92
Al^{IV}	2.09	2.57	2.80	2.51	2.67	2.43	2.57	2.52	2.73	2.75	2.62	2.51	2.73	2.75	2.45	1.81	2.08
Al^{VI}	2.60	2.55	3.00	2.75	2.76	2.54	2.63	2.78	2.78	2.83	3.15	2.83	3.06	2.94	2.66	2.64	2.67
Ti	0.00	0.02	0.01	0.01	0.01	0.00	0.01	0.00	0.01	0.00	0.00	0.01	0.00	0.01	0.01	0.03	0.04
Fe^{tot}	5.29	6.57	5.19	4.78	3.43	4.19	4.08	6.75	4.67	4.34	5.99	3.92	6.45	4.57	2.89	3.00	6.58
Mn	0.05	0.13	0.00	0.01	0.02	0.03	0.04	0.10	0.08	0.06	0.15	0.01	0.05	0.02	0.06	0.04	0.13
Mg	3.76	2.67	3.65	4.28	5.69	5.14	5.15	2.23	4.41	4.73	2.42	5.06	2.26	4.31	6.21	5.66	2.22
Ca	0.04	0.01	0.00	0.00	0.02	0.01	0.01	0.00	0.00	0.00	0.01	0.00	0.01	0.00	0.02	0.01	0.01
Ni					0.00	0.01	0.01										0.00
Na	0.00	0.04	0.06	0.04	0.01	0.02	0.00	0.00	0.03	0.00	0.01	0.00	0.00	0.02	0.01	0.14	0.01
Cr	0.01	0.00	0.01	0.01	0.00	0.01	0.02	0.00	0.00	0.00	0.01	0.00	0.01	0.01	0.02	0.07	0.02
OH	16.00	16.00	16.00	16.00	16.00	16.00	16.00	16.00	16.00	16.00	16.00	16.00	16.00	16.00	16.00	16.00	16.00
Cations	35.74	36.01	35.92	35.88	35.95	35.95	35.95	35.87	35.98	35.96	35.74	35.83	35.83	35.90	35.88	35.59	35.66

Table A3.8: Representative analyses of chlorite. Analyses in wt%, recalculated to 28 oxygens and 16 OH.

Lithology	GM	GM	GM	GM	GM	GM	GM	GM	GM	GM	GM	GM	GO
Mineral	Ctd	Ctd	Ctd	Ctd	Ctd	Ctd	Ctd	Ctd	Ctd	Ctd	Ctd	Ctd	Ctd
Punt	6.4	6.5	6.25	3.85	3.88	3.92	3.98	3.100	2.54	2.58	2.63	2.64	2.154
Thin section	GP96-37A	GP96-37A	GP96-37A	GP96-44P	GP96-44P	GP96-44P	GP96-44P	GP96-44P	GP96-90L	GP96-90L	GP96-90L	GP96-90L	GP97-33
Na_2O	0.00	0.00	0.07	0.00	0.00	0.01	0.00	0.03	0.00	0.00	0.00	0.00	0.00
MgO	3.67	3.66	3.24	4.71	3.73	4.82	4.06	4.06	3.80	4.72	4.09	4.43	2.62
SiO_2	24.82	24.62	24.64	24.52	24.40	24.53	24.50	24.16	24.19	24.44	24.24	24.32	24.05
Al_2O_3	41.15	41.54	41.58	39.99	39.79	39.93	39.91	39.70	39.27	39.36	39.27	39.71	40.24
K_2O	0.02	0.00	0.00	0.00	0.00	0.01	0.01	0.00	0.02	0.02	0.05	0.00	0.00
CaO	0.01	0.00	0.00	0.02	0.00	0.00	0.00	0.01	0.02	0.00	0.00	0.00	0.03
TiO_2	0.00	0.00	0.00	0.00	0.00	0.00	0.03	0.00	0.00	0.02	0.00	0.00	0.06
FeO	22.02	22.56	23.30	21.34	22.14	20.59	22.62	21.92	21.98	20.55	20.72	21.22	23.72
MnO	0.13	0.09	0.02	0.12	0.14	0.00	0.12	0.06	0.00	0.03	0.05	0.00	0.31
Cr_2O_3	0.13	0.03	0.01	0.04	0.05	0.00	0.00	0.04	0.04	0.01	0.05	0.00	0.02
NiO				0.00	0.07	0.00	0.03	0.08	0.00	0.08	0.01	0.10	
Total	91.92	92.39	92.75	90.67	90.21	89.87	91.21	89.85	89.24	89.06	88.36	89.68	91.03
Si	2.03	2.01	2.01	2.03	2.04	2.04	2.03	2.03	2.05	2.05	2.06	2.04	2.01
Al^{IV}	3.00	3.00	3.00	3.00	3.00	3.00	3.00	3.00	3.00	3.00	3.00	3.00	3.00
Al^{VI}	0.97	0.99	1.00	0.91	0.92	0.92	0.90	0.92	0.91	0.90	0.93	0.92	0.97
Ti	0.00	0.00	0.00	0.00	0.00	0.00	0.00	0.00	0.00	0.00	0.00	0.00	0.00
Fe^{3+}	0.02	0.00	0.00	0.09	0.07	0.08	0.10	0.07	0.08	0.10	0.07	0.08	0.03
Cr	0.01	0.00	0.00	0.00	0.00	0.00	0.00	0.00	0.00	0.00	0.00	0.00	0.00
Fe^{2+}	1.49	1.53	1.58	1.39	1.47	1.35	1.47	1.46	1.47	1.34	1.40	1.41	1.63
Mn	0.01	0.01	0.00	0.01	0.01	0.00	0.01	0.00	0.00	0.00	0.00	0.00	0.02
Mg	0.45	0.45	0.39	0.58	0.46	0.60	0.50	0.51	0.48	0.59	0.52	0.55	0.33
Ca	0.00	0.00	0.00	0.00	0.00	0.00	0.00	0.00	0.00	0.00	0.00	0.00	0.00
Ni				0.00	0.00	0.00	0.00	0.01	0.00	0.01	0.00	0.01	
Na	0.00	0.00	0.01	0.00	0.00	0.00	0.00	0.00	0.00	0.00	0.00	0.00	0.00
K	0.00	0.00	0.00	0.00	0.00	0.00	0.00	0.00	0.00	0.00	0.01	0.00	0.00
OH	4.00	4.00	4.00	4.00	4.00	4.00	4.00	4.00	4.00	4.00	4.00	4.00	4.00
Cations	11.98	11.99	12.00	12.01	12.00	12.00	12.02	12.01	12.00	12.00	11.98	12.00	12.00
XFe	0.77	0.77	0.80	0.71	0.77	0.71	0.75	0.75	0.76	0.71	0.74	0.73	0.83
XMg	0.23	0.22	0.20	0.28	0.23	0.29	0.24	0.25	0.24	0.29	0.26	0.27	0.16
XMn	0.00	0.00	0.00	0.00	0.01	0.00	0.00	0.00	0.00	0.00	0.00	0.00	0.01

Table A3.9: Representative analyses of chloritoid. Analyses in wt%, recalculated to 10 oxygens and 4 OH. Fe^{3+} is estimated to be 1-(AlVI+Ti+Cr).

Appendix 4

Representative electron microprobe analyses from The Voltri mélange

SAMPLE	MAIN	INCL / EARLY	RIMS / LATE	ACCESSORIES
MEL96-1B	Grt, Omp, Gln, Plag	Ep	Amph, Czo, Chl (later)	Qtz, Rt, Op, Ttn, Py
MEL96-1E	Grt Omp, Gln, Plag	WhM, Gln, Omp	Amph, Bt, Ep	Qtz, Op, Py
MEL96-2B	Grt, Omp, Gln, Plag, WhM		Amph	Qtz, Ttn, Py
MEL96-3A	Grt, Omp, Gln, Plag		Chl, Ep	Qtz, Op, Rt, Ttn, Py
MEL96-4B	Grt, Omp, Gln, Plag	Czo, WhM, Gln	Amph, Ep, Chl	Qtz, Op, Ttn, Py
MEL96-4c	Grt, Omp, Gln, WhM, Czo, Plag		Amph, Ep, Chl	Qtz, Ttn, Op, Py
MEL96-4d	Grt, Omp, Gln, Plag	Czo, WhM, Gln	Amph, Bt, Chl	Qtz, Ttn, Op, Py
MEL96-4G	Amph, Carb, Plag, Chl, WhM			Apt, Ilm
MEL96-9A	Grt, Omp, Gln, WhM, Plag		WhM, Amph	Qtz, Carb, Ttn, Py

Table A4.1: Mineral assemblages of studied samples.

Mineral	Grt	Grt	Grt	Grt	Grt	Grt	Grt	Grt	Grt	Grt	Grt	Grt	Grt	Grt	Grt
Point	3.108	3.16	3.23	4.56	4.63	4.73	4.75	3.31	3.32	3.155	3.161	2.6	2.29	2.99	2.100
Thin section	MEL96-1B	MEL96-1E	MEL96-1E	MEL96-2B	MEL96-2B	MEL96-3A	MEL96-3A	MEL96-4B	MEL96-4B	MEL96-4c	MEL96-4c	MEL96-4d	MEL96-4d	MEL96-9A	MEL96-9A
Na_2O	0.03	0.07	0.03	0.02	0.00	0.04	0.03	0.00	0.00	0.06	0.00	0.04	0.00	0.02	0.04
MgO	2.31	2.64	0.38	3.46	3.84	2.73	4.17	0.39	1.38	0.52	2.00	0.43	1.66	1.41	1.50
SiO_2	37.45	36.82	36.28	37.25	37.48	36.90	37.34	36.72	36.67	37.19	37.23	36.41	36.43	37.32	37.14
Al_2O_3	20.14	21.03	20.11	21.16	21.06	20.68	21.03	20.49	20.87	19.93	20.31	20.25	20.77	20.33	20.13
K_2O	0.01	0.02	0.00	0.01	0.01	0.01	0.00	0.00	0.00	0.00	0.00	0.00	0.01	0.00	0.00
CaO	6.33	4.55	9.15	5.46	5.13	5.58	6.26	9.42	8.28	9.95	6.67	10.32	7.59	6.99	7.18
TiO_2	0.04	0.00	0.16	0.04	0.00	0.02	0.03	0.07	0.07	0.05	0.06	0.19	0.05	0.03	0.06
FeO	33.80	34.72	19.60	31.49	32.12	33.38	30.95	29.29	31.86	30.87	33.14	25.43	32.61	33.95	33.30
MnO	0.22	0.70	14.03	0.53	0.43	0.02	0.36	4.25	0.16	1.33	0.48	6.37	0.23	0.07	0.36
Cr_2O_3	0.00	0.03	0.05	0.00	0.00	0.00	0.00	0.09	0.06	0.05	0.00	0.07	0.01	0.00	0.07
NiO	0.00									0.00	0.00			0.01	0.00
Total	100.25	100.45	99.71	99.39	100.06	99.27	100.12	100.72	99.29	99.91	99.89	99.47	99.33	100.01	99.66
Si	3.00	2.94	2.94	2.98	2.98	2.97	2.95	2.94	2.96	3.00	2.99	2.95	2.94	3.00	3.00
Al	1.90	1.98	1.92	1.99	1.97	1.96	1.96	1.94	1.99	1.90	1.93	1.93	1.98	1.93	1.92
Ti	0.00	0.00	0.01	0.00	0.00	0.00	0.00	0.00	0.00	0.00	0.00	0.01	0.00	0.00	0.00
Fe^{tot}	2.26	2.32	1.33	2.11	2.13	2.25	2.04	1.96	2.15	2.08	2.23	1.72	2.20	2.29	2.25
Mn	0.01	0.05	0.96	0.04	0.03	0.00	0.02	0.29	0.01	0.09	0.03	0.44	0.02	0.01	0.02
Mg	0.28	0.31	0.05	0.41	0.45	0.33	0.49	0.05	0.17	0.06	0.24	0.05	0.20	0.17	0.18
Ca	0.54	0.39	0.79	0.47	0.44	0.48	0.53	0.81	0.72	0.86	0.57	0.89	0.66	0.60	0.62
Ni	0.00									0.00	0.00			0.00	0.00
Cr	0.00	0.00	0.00	0.00	0.00	0.00	0.00	0.01	0.00	0.00	0.00	0.00	0.00	0.00	0.00
Cations	8.00	8.00	8.00	8.00	8.00	8.00	8.00	8.00	8.00	8.00	8.00	8.00	8.00	8.00	8.00
Fe^{3+} (Droop)	0.10	0.13	0.18	0.04	0.08	0.08	0.14	0.16	0.08	0.09	0.08	0.14	0.13	0.06	0.07
Fe^{2+}	2.17	2.19	1.15	2.07	2.06	2.17	1.91	1.81	2.07	1.99	2.15	1.58	2.07	2.23	2.18
XPyrope	9.18	10.69	1.55	13.85	15.28	11.01	16.64	1.57	5.60	2.07	8.00	1.75	6.77	5.63	5.99
XAndradite	4.91	6.08	9.05	2.15	3.75	4.20	6.68	7.77	4.06	4.79	4.08	7.51	6.25	2.95	3.79
XAlmandine	72.24	74.48	38.88	69.26	69.10	72.77	64.59	61.20	69.87	66.26	71.74	53.27	70.40	74.14	72.50
XUvarovite	0.00	0.09	0.16	0.00	0.00	0.00	0.00	0.28	0.17	0.16	0.00	0.23	0.03	0.00	0.22
XSpessartine	0.50	1.60	32.64	1.19	0.97	0.04	0.82	9.79	0.36	3.03	1.09	14.75	0.52	0.17	0.81
XGrossular	13.17	7.07	17.71	13.55	10.91	11.99	11.27	19.39	19.94	23.69	15.08	22.49	16.03	17.10	16.69

Table A4.2: Representative analyses of garnet. Analyses in wt%, recalculated to 12 oxygens and 8 cations.

Mineral	Omp	Omp	Omp	Omp	Omp	Omp	Omp	Omp	Omp	Omp	Omp	Omp	Omp	Omp	Omp
Point	3.107	3.105	2.80	3.17	4.55	4.64	4.72	4.74	3.30	3.33	3.159	3.164	2.28	2.102	2.103
Thin section	96-1B	96-1B	96-1E	96-1E	96-2B	96-2B	96-3A	96-3A	96-4B	96-4B	96-4c	96-4c	96-4d	96-9A	96-9A
Na_2O	7.24	7.50	8.69	7.42	6.51	8.03	7.98	7.41	7.87	6.42	8.21	6.72	7.76	7.90	7.97
MgO	7.09	7.05	5.07	6.06	7.50	6.86	6.97	7.66	6.37	7.27	6.31	7.32	6.63	6.56	5.88
SiO_2	55.14	55.68	55.06	53.76	54.59	55.39	54.59	54.83	54.67	54.13	56.07	55.75	54.18	56.13	55.80
Al_2O_3	6.43	7.60	7.16	7.08	6.10	8.25	8.04	6.93	7.56	7.09	10.48	8.87	7.51	9.37	8.24
K_2O	0.00	0.00	0.00	0.00	0.00	0.00	0.02	0.03	0.00	0.00	0.00	0.00	0.02	0.00	0.01
CaO	12.00	11.94	9.08	11.48	13.37	11.00	11.16	12.43	10.98	13.92	10.90	13.30	11.75	11.44	11.15
TiO_2	0.00	0.00	0.01	0.05	0.04	0.00	0.16	0.10	0.02	0.00	0.00	0.02	0.06	0.02	0.06
FeO	11.20	9.74	13.43	12.18	11.12	9.31	9.69	10.25	10.95	9.76	7.11	7.28	11.12	7.89	10.76
MnO	0.06	0.00	0.16	0.08	0.10	0.00	0.03	0.00	0.00	0.00	0.00	0.00	0.11	0.00	0.15
NiO	0.03	0.00	0.00	0.02	0.00	0.00	0.00	0.00	0.00	0.10	0.00	0.03	0.02	0.05	0.03
Cr_2O_3	0.04	0.00	0.00								0.01	0.00		0.06	0.00
Total	99.10	99.52	98.66	98.02	99.30	98.84	98.59	99.64	98.39	98.69	99.09	99.24	99.12	99.29	99.99
Si	2.01	2.01	2.02	1.99	2.00	2.01	1.98	1.98	2.00	1.99	2.01	2.02	1.97	2.02	2.01
Al^{IV}	0.00	0.00	0.00	0.01	0.00	0.00	0.02	0.02	0.00	0.01	0.00	0.00	0.03	0.00	0.00
Al^{VI}	0.28	0.32	0.31	0.30	0.26	0.35	0.33	0.28	0.33	0.29	0.44	0.38	0.29	0.40	0.35
Ti	0.00	0.00	0.00	0.00	0.00	0.00	0.00	0.00	0.00	0.00	0.00	0.00	0.00	0.00	0.00
Cr	0.00	0.00	0.00	0.00	0.00	0.00	0.00	0.00	0.00	0.00	0.00	0.00	0.00	0.00	0.00
Fe^{tot}	0.34	0.29	0.41	0.38	0.34	0.28	0.29	0.31	0.34	0.30	0.21	0.22	0.34	0.24	0.32
Mg	0.00	0.00	0.01	0.00	0.00	0.00	0.00	0.00	0.00	0.00	0.00	0.00	0.00	0.00	0.00
Mn	0.39	0.38	0.28	0.33	0.41	0.37	0.38	0.41	0.35	0.40	0.34	0.39	0.36	0.35	0.32
Ca	0.47	0.46	0.36	0.46	0.52	0.43	0.43	0.48	0.43	0.55	0.42	0.52	0.46	0.44	0.43
Na	0.51	0.53	0.62	0.53	0.46	0.56	0.56	0.52	0.56	0.46	0.57	0.47	0.55	0.55	0.56
Ni	0.00	0.00	0.00								0.00	0.00		0.00	0.00
Cations	4.00	4.00	4.00	4.00	4.00	4.00	4.00	4.00	4.00	4.00	4.00	4.00	4.00	4.00	4.00
Fe^{3+}	0.21	0.18	0.27	0.24	0.20	0.20	0.24	0.26	0.23	0.17	0.10	0.06	0.28	0.12	0.18
Fe^{2+} (C&C 1974)	0.13	0.12	0.14	0.13	0.14	0.08	0.05	0.05	0.11	0.13	0.11	0.17	0.06	0.12	0.15
XJd (=XNa-XAcm (Fe3+))															
XJd	0.30	0.35	0.35	0.29	0.26	0.36	0.32	0.26	0.33	0.29	0.47	0.42	0.27	0.43	0.38

Table A4.3: Representative analyses of pyroxenes. Analyses in wt%, normalised to 6 oxygens and 4 cations. Sample codes all start with MEL.

Mineral	Amf	Amf	Amf	Amf	Amf	Amf	Amf	Amf	Amf	Amf	Amf	Amf	Amf	Amf	Amf	Amf
Point	3.103	3.106	4.212	4.265	4.276	4.15	2.488	1.113	3.157	3.168	4.25	4.28	4.39	4.48	2.98	2.108
Thin section	96-1B	96-1B	96-1E	96-1E	96-1E	96-3A	96-4B	96-4B	96-4c	96-4c	96-4d	96-4d	96-4G	96-4G	96-9A	96-9A
Na_2O	6.74	6.95	4.22	7.00	0.97	2.75	6.16	7.06	7.00	0.58	6.62	2.33	0.35	0.77	5.99	7.16
MgO	9.47	10.94	9.12	10.61	15.56	8.71	8.06	8.92	9.18	18.33	9.11	9.71	21.20	20.09	9.76	10.53
SiO_2	57.22	58.15	48.58	57.79	54.80	46.65	54.32	57.14	57.90	55.57	57.24	49.77	57.77	56.29	56.43	58.24
Al_2O_3	7.48	9.22	7.29	8.86	0.56	7.27	9.25	9.57	10.62	0.81	9.20	4.51	0.08	0.46	6.35	10.36
K_2O	0.03	0.03	0.30	0.01	0.02	0.21	0.08	0.02	0.01	0.04	0.02	0.11	0.02	0.07	0.07	0.01
CaO	0.62	0.45	9.06	0.52	11.37	9.63	1.48	0.36	0.19	12.42	0.67	9.39	12.94	12.37	1.67	0.26
TiO_2	0.00	0.00	0.00	0.00	0.00	0.25	0.05	0.00	0.00	0.00	0.00	0.11	0.00	0.00	0.00	0.00
FeO	14.66	10.26	18.07	11.35	13.84	21.52	15.57	13.62	11.12	9.36	13.07	20.18	5.11	6.88	15.79	10.01
MnO	0.11	0.00	0.10	0.00	0.15	0.18	0.07	0.00	0.02	0.19	0.02	0.45	0.21	0.23	0.18	0.06
Cr_2O_3	0.00	0.02	0.05	0.00	0.01	0.05	0.00	0.02	0.00	0.00	0.07	0.00	0.03	0.13	0.00	0.00
NiO	0.03	0.05	0.05	0.05	0.07	0.06		0.00	0.00	0.07	0.00	0.13	0.06	0.03	0.10	0.06
Total	96.33	95.99	96.73	96.14	97.24	97.16	94.97	96.67	96.01	97.30	95.92	96.70	97.65	97.28	96.24	96.57
Si	8.04	8.04	7.31	8.02	7.94	7.11	7.92	8.00	8.05	7.90	8.04	7.54	7.99	7.92	8.02	8.02
Al^{IV}	0.00	0.00	0.69	0.00	0.06	0.86	0.08	0.00	0.00	0.10	0.00	0.45	0.01	0.08	0.00	0.00
Al^{VI}	1.24	1.50	0.60	1.45	0.04	0.44	1.51	1.58	1.74	0.03	1.52	0.35	0.01	0.00	1.06	1.68
Ti	0.00	0.00	0.00	0.00	0.00	0.03	0.01	0.00	0.00	0.00	0.00	0.01	0.00	0.00	0.00	0.00
Fe^{tot}	1.72	1.19	2.27	1.32	1.68	2.74	1.90	1.59	1.29	1.11	1.54	2.55	0.59	0.81	1.88	1.15
Mn	0.01	0.00	0.01	0.00	0.02	0.02	0.01	0.00	0.00	0.02	0.00	0.06	0.02	0.03	0.02	0.01
Mg	1.98	2.26	2.04	2.20	3.36	1.98	1.75	1.86	1.90	3.88	1.91	2.19	4.37	4.21	2.07	2.16
Ca	0.09	0.07	1.46	0.08	1.77	1.57	0.23	0.05	0.03	1.89	0.10	1.52	1.92	1.86	0.25	0.04
Ni	0.00	0.01	0.01	0.01	0.01	0.01		0.00	0.00	0.01	0.00	0.02	0.01	0.00	0.01	0.01
Na	1.84	1.86	1.23	1.89	0.27	0.81	1.74	1.92	1.89	0.16	1.80	0.69	0.09	0.21	1.65	1.91
K	0.01	0.01	0.06	0.00	0.00	0.04	0.02	0.00	0.00	0.01	0.00	0.02	0.00	0.01	0.01	0.00
Cr	0.00	0.00	0.00	0.00	0.00	0.00	0.00	0.00	0.00	0.00	0.00	0.00	0.00	0.00	0.00	0.00
Cations	14.93	14.93	15.68	14.96	15.14	15.63	15.16	15.00	14.91	15.12	14.92	15.40	15.02	15.13	14.98	14.97
Fe^{3+}	0.66	0.42	0.00	0.47	0.00	0.00	0.00	0.33	0.23	0.00	0.34	0.00	0.06	0.00	0.61	0.26
Fe^{2+}	1.07	0.76	2.27	0.84	1.68	2.74	1.90	1.27	1.06	1.11	1.19	2.55	0.54	0.81	1.27	0.90

Table A4.4: Representative analyses of amphibole. Analyses in wt%, recalculated to 23 oxygens, following the method of Holland and Blundy (1994). Sample codes all start with MEL.

Mineral	Plag	Fspar	Plag	Plag	Plag	Fspar	Plag	Plag	Fspar	Plag	Plag
Point	3.109	2.363	4.251	4.275	4.4	2.483	1.111	1.120	2.5	4.18	4.29
Thin section	MEL96-1B	MEL96-1E	MEL96-1E	MEL96-1E	MEL96-3A	MEL96-4B	MEL96-4B	MEL96-4B	MEL96-4d	MEL96-4d	MEL96-4d
Na_2O	11.73	11.07	10.55	11.36	11.41	10.68	10.87	11.33	12.06	11.76	11.09
MgO	0.00	0.00	1.50	0.30	0.01	0.00	0.00	0.00	0.00	0.00	0.00
SiO_2	68.42	66.60	66.38	68.29	68.07	65.98	66.76	67.78	67.02	68.47	67.71
Al_2O_3	19.19	19.87	17.79	18.68	19.60	20.54	20.22	19.55	20.09	19.03	19.87
K_2O	0.02	0.10	0.06	0.05	0.02	0.04	0.02	0.02	0.06	0.06	0.25
CaO	0.17	0.85	1.96	0.37	0.62	1.45	1.11	0.59	0.83	0.24	0.83
TiO_2	0.00	0.00	0.06	0.00	0.00	0.00	0.00	0.00	0.00	0.00	0.00
FeO	0.00	0.29	1.59	0.55	0.20	0.33	0.26	0.22	0.20	0.12	0.36
MnO	0.02	0.00	0.00	0.03	0.02	0.06	0.00	0.03	0.04	0.06	0.08
Cr_2O_3	0.00	0.01	0.00	0.00	0.00	0.00	0.00	0.02	0.00	0.06	0.02
NiO	0.00		0.01	0.00	0.02		0.01	0.00		0.02	0.08
Total	99.53	98.79	99.89	99.60	99.90	99.02	99.24	99.48	100.25	99.68	100.10
Si	3.00	2.96	3.02	3.03	2.99	2.93	2.96	2.99	2.91	3.00	2.97
Al	0.99	1.04	0.95	0.98	1.01	1.08	1.06	1.02	1.03	0.98	1.03
Ca	0.01	0.04	0.10	0.02	0.03	0.07	0.05	0.03	0.04	0.01	0.04
Na	1.00	0.95	0.93	0.98	0.97	0.92	0.93	0.97	1.02	1.00	0.94
K	0.00	0.01	0.00	0.00	0.00	0.00	0.00	0.00	0.00	0.00	0.01
Cations	5.00	5.00	5.00	5.00	5.00	5.00	5.00	5.00	5.00	5.00	5.00
XAb	0.99	0.95	0.90	0.98	0.97	0.93	0.95	0.97	0.96	0.99	0.95
XAn	0.01	0.04	0.09	0.02	0.03	0.07	0.05	0.03	0.04	0.01	0.04
XOr	0.00	0.01	0.00	0.00	0.00	0.00	0.00	0.00	0.00	0.00	0.01

Table A4.5: Representative analyses of plagioclase. Analyses in wt%, normalised to 5 cations.

Mineral	Ep	Ep	Ep	Ep	Ep	Ep	Ep	Ep	Ep
Point	4.8	4.10	4.12	2.515	3.169	4.19	4.20	4.21	4.30
Thin section	MEL96-3A	MEL96-3A	MEL96-3A	MEL96-4B	MEL96-4c	MEL96-4d	MEL96-4d	MEL96-4d	MEL96-4d
Na_2O	0.00	0.01	0.00	0.06	0.03	0.04	0.01	0.01	0.00
MgO	0.04	0.00	0.00	0.06	0.01	0.05	0.05	0.07	0.02
SiO_2	38.14	37.96	38.10	38.41	36.96	38.74	38.54	38.79	37.71
Al_2O_3	26.86	24.56	25.03	28.94	20.00	26.37	28.08	28.55	24.59
K_2O	0.00	0.01	0.01	0.02	0.00	0.01	0.00	0.00	0.00
CaO	24.14	23.43	23.84	23.55	23.34	24.00	24.36	24.20	23.48
TiO_2	0.25	0.09	0.06	0.07	0.00	0.41	0.02	0.09	0.00
FeO	7.17	9.90	9.27	6.42	15.28	6.94	5.55	5.12	9.90
MnO	0.07	0.22	0.07	0.22	0.10	0.42	0.22	0.26	0.10
Cr_2O_3	0.00	0.04	0.01	0.08	0.00	0.03	0.00	0.03	0.08
NiO	0.02	0.00	0.08		0.00	0.00	0.10	0.00	0.00
Total	96.60	96.17	96.30	97.69	95.68	96.94	96.81	97.08	95.68
Si	2.99	3.02	3.02	2.97	3.00	3.03	3.00	3.01	3.01
Al^{IV}	0.01	0.00	0.00	0.03	0.00	0.00	0.00	0.00	0.00
Al^{VI}	2.48	2.30	2.34	2.60	1.92	2.43	2.58	2.61	2.31
Ti	0.01	0.01	0.00	0.00	0.00	0.02	0.00	0.01	0.00
Fe^{tot}	0.47	0.66	0.61	0.40	1.04	0.45	0.36	0.33	0.66
Mn	0.00	0.01	0.00	0.01	0.01	0.03	0.01	0.02	0.01
Mg	0.00	0.00	0.00	0.01	0.00	0.01	0.01	0.01	0.00
Ca	2.03	2.00	2.02	1.95	2.03	2.01	2.03	2.01	2.01
Na	0.00	0.00	0.00	0.01	0.01	0.01	0.00	0.00	0.00
Cr	0.00	0.00	0.00	0.00	0.00	0.00	0.00	0.00	0.00
Cations	8.00	8.00	8.00	7.98	8.00	8.00	8.00	8.00	8.00
Fe^{3+}	0.47	0.66	0.61	0.40	1.04	0.45	0.36	0.33	0.66
Fe^{2+}	0.00	0.00	0.00	0.00	0.00	0.00	0.00	0.00	0.00
$Si+Al^{IV}$	3.00	3.02	3.02	3.00	3.00	3.03	3.00	3.01	3.01
$Al^{VI}+Ti+Fe^{3+}+Cr$	2.96	2.97	2.95	3.00	2.95	2.91	2.94	2.95	2.98
Rest	2.04	2.01	2.03	1.98	2.04	2.05	2.06	2.04	2.02

Table A4.6: Representative analyses of epidote group minerals. Analyses in wt%, recalculated to 12.5 oxygens and 8 cations.

Mineral	WhM	WhM	WhM	WhM	WhM	WhM	WhM
Point	2.503	3.156	3.160	3.162	3.163	2.7	2.96
Thin section	MEL96-4B	MEL96-4c	MEL96-4c	MEL96-4c	MEL96-4c	MEL96-4d	MEL96-9A
Na_2O	0.02	0.36	0.04	0.11	0.11	0.00	0.03
MgO	5.07	2.78	5.33	5.53	5.55	5.09	5.03
SiO_2	52.43	49.54	55.63	55.77	55.67	52.25	53.84
Al_2O_3	19.80	26.93	20.15	21.15	21.03	20.01	19.92
K_2O	11.01	10.67	11.07	10.70	10.46	10.13	11.01
CaO	0.10	0.00	0.00	0.02	0.03	0.14	0.01
TiO_2	0.11	0.12	0.07	0.14	0.13	0.11	0.10
FeO	5.04	4.69	4.32	3.01	3.32	5.33	3.58
MnO	0.04	0.04	0.01	0.00	0.04	0.03	0.09
Cr_2O_3	0.04	0.01	0.06	0.00	0.00	0.00	0.07
NiO		0.00	0.00	0.02	0.00		0.00
Total	93.56	95.09	96.63	96.41	96.29	93.07	93.57
Si	3.63	3.36	3.69	3.68	3.68	3.62	3.68
Al^{IV}	0.37	0.64	0.31	0.32	0.32	0.38	0.32
Al^{VI}	1.24	1.51	1.27	1.32	1.31	1.26	1.29
Ti	0.01	0.01	0.00	0.01	0.01	0.01	0.01
Fe^{tot}	0.29	0.27	0.24	0.17	0.18	0.31	0.21
Mn	0.00	0.00	0.00	0.00	0.00	0.00	0.01
Mg	0.52	0.28	0.53	0.54	0.55	0.53	0.51
Ca	0.01	0.00	0.00	0.00	0.00	0.01	0.00
Ni		0.00	0.00	0.00	0.00		0.00
Na	0.00	0.05	0.01	0.01	0.01	0.00	0.00
K	0.97	0.92	0.94	0.90	0.88	0.90	0.96
Cr	0.00	0.00	0.00	0.00	0.00	0.00	0.00
Cations	7.05	7.04	6.99	6.95	6.95	7.00	6.99
Mg-number	64.22	51.39	68.71	76.61	74.88	62.99	71.45
Si (p.f.u.)	3.63	3.36	3.69	3.68	3.68	3.62	3.68
Oct (p.f.u.)	2.07	2.07	2.04	2.04	2.05	2.10	2.02

Table A4.7: Representative analyses of white mica. Analyses in wt%, recalculated to 11 oxygens.

Mineral	Bt	Bt	Bt	Bt	Bt	Bt
Point	2.416	2.426	2.436	1.457	1.465	1.477
Thin section	MEL96-1E	MEL96-1E	MEL96-1E	MEL96-4d	MEL96-4d	MEL96-4d
Na_2O	0.62	0.09	1.20	0.10	0.16	0.09
MgO	1.63	11.67	9.17	4.67	9.01	8.18
SiO_2	44.97	36.11	38.14	34.01	35.74	32.75
Al_2O_3	27.42	16.87	15.71	15.71	15.56	16.46
K_2O	9.28	9.61	7.75	6.33	5.19	8.23
CaO	0.35	0.06	0.16	2.51	0.51	0.33
TiO_2	0.44	0.32	0.19	0.59	0.41	0.26
FeO	7.48	19.30	17.05	29.04	25.63	25.22
MnO	0.10	0.56	0.49	0.70	0.37	0.44
Cr_2O_3	0.01	0.05	0.00	0.00	0.00	0.04
NiO						
Total	92.29	94.60	89.86	93.65	92.57	91.96
Si	3.20	2.78	3.02	2.76	2.83	2.68
Al^{IV}	0.80	1.22	0.98	1.24	1.17	1.32
Al^{VI}	1.49	0.31	0.49	0.27	0.29	0.27
Ti	0.02	0.02	0.01	0.04	0.02	0.02
Fe^{tot}	0.44	1.24	1.13	1.97	1.70	1.73
Mn	0.01	0.04	0.03	0.05	0.02	0.03
Mg	0.17	1.34	1.08	0.57	1.06	1.00
Ca	0.03	0.00	0.01	0.22	0.04	0.03
Ni						
Na	0.09	0.01	0.18	0.02	0.03	0.02
K	0.84	0.94	0.78	0.66	0.53	0.86
Cr	0.00	0.00	0.00	0.00	0.00	0.00
Cations	7.09	7.91	7.72	7.78	7.69	7.95
Fe^{3+}	0.07	0.19	0.17	0.30	0.25	0.26
Fe^{2+}	0.38	1.06	0.96	1.68	1.44	1.47
XAl	0.72	0.11	0.19	0.10	0.10	0.10
XTi	0.01	0.01	0.00	0.01	0.01	0.01

Table A4.8: Representative analyses of biotite. Analyses in wt%, recalculated to 11 oxygens. Fe^{3+} estimated following Williams and Grambling (1990).

Mineral	Chl	Chl	Chl	Chl	Chl	Chl	Chl	Chl	Chl	Chl	Chl	Chl	Chl	Chl	Chl	Chl
Point	4.70	4.7	4.9	4.14	1.110	1.112	1.119	1.460	1.466	1.467	1.472	1.475	1.488	4.24	4.41	4.47
Thin section	MEL96-3A	MEL96-3A	MEL96-3A	MEL96-3A	MEL96-4B	MEL96-4B	MEL96-4B	MEL96-4d	MEL96-4d	MEL96-4d	MEL96-4d	MEL96-4d	MEL96-4d	MEL96-4d	MEL96-4G	MEL96-4G
Na_2O	0.02	0.03	0.00	0.01	0.05	0.02	0.01	0.09	0.00	0.05	0.34	0.06	0.07	0.03	0.00	0.02
MgO	13.51	14.17	13.64	15.21	14.36	13.67	15.43	14.39	12.83	16.53	13.22	14.29	13.71	9.08	26.81	26.87
SiO_2	25.06	25.69	25.59	25.60	26.86	26.46	27.24	26.46	24.94	24.61	27.11	26.51	25.03	24.41	30.61	30.34
Al_2O_3	18.74	18.50	19.04	17.07	16.18	17.08	16.22	16.95	18.86	15.29	16.77	17.01	19.20	17.93	15.68	15.12
K_2O	0.00	0.02	0.01	0.01	0.01	0.00	0.00	0.04	0.02	0.02	0.05	0.02	0.14	0.04	0.00	0.00
CaO	0.03	0.05	0.01	0.13	0.06	0.08	0.03	0.15	0.05	0.03	0.72	0.07	0.10	0.05	0.02	0.00
TiO_2	0.00	0.02	0.04	0.04	0.00	0.00	0.00	0.33	0.09	0.04	0.05	0.05	0.06	0.00	0.00	0.00
FeO	29.09	27.36	27.29	26.14	28.48	28.99	27.22	27.08	29.53	24.85	27.41	27.86	28.55	33.53	12.23	11.20
MnO	0.16	0.28	0.28	0.19	0.23	0.21	0.09	0.39	0.39	0.31	0.37	0.44	0.38	0.41	0.12	0.21
Cr_2O_3	0.00	0.05	0.01	0.02	0.00	0.08	0.02	0.00	0.02	0.00	0.06	0.01	0.04	0.01	0.05	0.78
NiO		0.00	0.00	0.12	0.08	0.00	0.08							0.07	0.18	0.00
Total	86.59	86.05	85.85	84.46	86.17	86.49	86.14	85.88	86.70	81.66	86.04	86.23	87.16	85.43	85.62	84.52
Si	5.49	5.60	5.59	5.67	5.88	5.78	5.91	5.79	5.47	5.64	5.93	5.79	5.44	6.15	6.15	6.16
Al^{IV}	2.51	2.40	2.41	2.33	2.12	2.22	2.09	2.21	2.53	2.36	2.07	2.21	2.56	1.85	1.85	1.84
Al^{VI}	2.32	2.35	2.48	2.13	2.05	2.18	2.05	2.15	2.35	1.78	2.25	2.16	2.35	1.86	1.86	1.77
Ti	0.00	0.00	0.01	0.01	0.00	0.00	0.00	0.05	0.01	0.01	0.01	0.01	0.01	0.00	0.00	0.00
Fe^{tot}	5.33	4.99	4.98	4.84	5.21	5.30	4.94	4.95	5.42	4.77	5.01	5.08	5.18	2.05	2.05	1.90
Mn	0.03	0.05	0.05	0.04	0.04	0.04	0.02	0.07	0.07	0.06	0.07	0.08	0.07	0.02	0.02	0.04
Mg	4.41	4.60	4.44	5.02	4.68	4.45	4.99	4.69	4.20	5.65	4.31	4.65	4.44	8.02	8.02	8.13
Ca	0.01	0.01	0.00	0.03	0.01	0.02	0.01	0.04	0.01	0.01	0.17	0.02	0.02	0.00	0.00	0.00
Ni		0.00	0.00	0.02	0.01	0.00	0.01							0.03	0.03	0.00
Na	0.01	0.01	0.00	0.00	0.02	0.01	0.00	0.04	0.00	0.02	0.14	0.03	0.03	0.00	0.00	0.01
Cr	0.00	0.01	0.00	0.00	0.00	0.01	0.00	0.00	0.00	0.00	0.01	0.00	0.01	0.01	0.01	0.12
OH	16.00	16.00	16.00	16.00	16.00	16.00	16.00	16.00	16.00	16.00	16.00	16.00	16.00	16.00	16.00	16.00
Cations	36.10	36.02	35.96	36.09	36.04	36.01	36.02	35.99	36.07	36.29	35.97	36.03	36.11	35.99	35.99	35.98

Table A4.9: Representative analyses of chlorite. Analyses in wt%, recalculated to 28 oxygens and 16 OH.

Dankwoord, Acknowledgements

Zoals veel mensen in mijn directe en minder directe omgeving weten, heb ik enorm genoten van mijn promotietijd. De vrijheid om je tijd in te delen en je interesses na te jagen heb ik als een grote luxe ervaren. De combinatie van eigen onderzoek met het begeleiden van studenten tijdens practica in het veld of de collegezaal vind ik ideaal.
Net als de meeste promovendi heb ik mindere periodes gehad in de afgelopen jaren. Soms wist ik niet goed hoe ik verder moest met mijn project, of moest ik lange dagen maken om een deadline te halen die ik of anderen me gesteld hadden. In die periodes heb ik de steun van mijn vrienden en familie hard nodig gehad, terwijl ik hen door de drukte eigenlijk heb verwaarloosd. Jullie begrip, peptalks en etentjes waren geweldig!
En nu... is het af! Zonder de hulp en de steun van heel veel mensen was het nooit zo ver gekomen. Een aantal mensen wil ik hier graag specifiek noemen, wat ook betekent dat ik mensen ga vergeten. Vooraf wil ik dus al mijn familie, vrienden, collega's (die laatste twee gaan vaak samen!) en anderen bedanken voor alles.
Om te beginnen een levensgroot ¡Gracias! voor Reinoud: al in een vroeg stadium viel mijn liefde voor de veldgeologie je op, waardoor je me tijdens de rest van mijn studietijd in het oog hield. Wat ik nu van optische mineralogie en structurele geologie weet heb ik voor een groot deel van jou geleerd. Je hebt me gesteund toen ik meer wilde leren over metamorfe petrologie. Helaas was er niet altijd veel tijd om over geologie te praten, maar met name bij de laatste loodjes was je altijd snel en erg doeltreffend met je correcties. Zonder jouw hulp was het nooit zo snel af gekomen.
Rinus, als tweede promotor hield je mijn voortgang altijd in de gaten, meestal vanuit de achtergrond. Jouw bijdragen en sturing aan het modelleerwerk waren geweldig belangrijk. Jouw geofysische kijk op de geologie van de Alpen hielp mij vaak om aan de grootschalige processen te blijven denken. Je correcties in de allerlaatste stadia waren erg verhelderend en hielpen me mijn doelstellingen nauwkeuriger te formuleren.
Menno heeft de modellen voor slab detachment en TARM ontwikkeld waarop hoofdstuk zes gebaseerd is. In onze gesprekken over het modelleren werd me steeds weer duidelijk hoe belangrijk het is om aannames expliciet te noemen. Ik heb veel geleerd van onze gesprekken over de geologie van de Alpen, omdat ik opnieuw moest nadenken over dingen die ik vanzelfsprekend had gevonden. Ik wil je specifiek bedanken voor de snelheid waarmee je nog "even" een nieuw modelletje draaide, of een plotje maakte als we weer eens de modelresultaten en hun implicaties voor mijn veldgebieden hadden doorgesproken.
I would like to thank Roberto Compagnoni and Bruno Lombardo, for introducing me to Gran Paradiso, its rocks and infrastructure, and for visiting me during my field seasons in the Piantonetto Valley. It was so nice to be able to speak English and talk geology for a while.The ENTE Parco Nazionale Gran Paradiso allowed me to study and sample the rocks in the national park, and very kindly let me stay in the houses of the guards at Telessio and in Noasca. All the park guards, especially Elio Polla and Piero Contratto, are thanked for their hospitality, and for teaching me Italian. The Club

Alpinistico Pontese and especially the various gestori of Rifugio Pontese, are thanked for their hospitality, for their help in assuring my rocks made their way to the valley safely and for teaching me Italian.
Thanks to the Museo Cantonale di Storia Naturale in Lugano, for issuing me a permit to carry out fieldwork and collect rock samples in Ticino. Tijdens het veldwerk in Ticino in 1998 was Alex(-andra) een erg gezellige en toegewijde fieldy.
Will Lamb taught me a lot of metamorphic petrology; what a shame I did not realise in what field you work when you were in Utrecht. Thanks heaps for reviewing my chapters and for suggesting many points of improvement. And many thanks to both you and Julie for having me as your guest when I came to Texas; it was great to play Sinterklaas for a bit.
Thanks also to Gisella for translating the summary into Italian at very short notice, and of course, for being such a great distant friend.
Ondersteuning bij het gebruik van machines, het doorlopen van de bureaucratie en andere meer creatieve zaken is onontbeerlijk en daarom wil ik hier een heel groepje mensen bedanken. I would like to thank Stuart Kearns for his very helpful instructions on using the electron microprobe, and for (almost always) keeping it going very well, also during the evenings and weekends. I had very good times working in your lab. Herman heeft me enthousiast, snel en effectief geholpen met het kijken naar microstructuren op de SEM en het maken van mooie plaatjes. Tony was altijd bereid even snel een blik door mijn microscoop te werpen. Je hebt menig mineraal voor me ontmaskerd en je liefde voor de petrologie is aanstekelijk. Magda was altijd bereid dingetjes op te knappen als de druk te hoog werd. En altijd met belangstelling en een lach. Het is fantastisch dat we met z'n allen op je kunnen rekenen!!
De collectie en het personeel van de bibliotheek van Aardwetenschappen zijn bijzonder goed. Ik was iedere keer weer verbaasd als een obscure referentie gewoon in de kast stond. En als ik iets niet kon vinden, wist Jan, Marcel of Lidy bijna altijd waar het stond. Geweldig! Ook in de slijpkamer is veel en hard voor me gewerkt, met name Inge en Otto leverden altijd zo snel mogelijk, en vrijwel altijd erg goed werk. Zonder jullie bijdragen had ik dit proefschrift nooit kunnen schrijven. Ik wil de AV dienst bedanken voor hun altijd creatieve bijdragen: Jaco voor het harde werken en het luisteren naar mijn wensen, Fred voor het helpen bij het converteren van obscure bestanden, en Paul voor het oplossen van problemen als die waren ontstaan.
Many thanks also to professors Roberto Compagnoni (Torino), Martin Engi (Bern), Stefan Schmid (Basel) and Jacques Touret (Amsterdam) for being willing to be part of the examination committee of this thesis. And thanks for getting it done quickly as well.
Financiële steun voor mijn onderzoek kwam in de eerste plaats van NWO (GOA, en later ALW). Mijn aanvragen voor congressen, veldwerk, werkbezoek en zelfs een computer werden altijd gehonoreerd. De interactie met buitenstaanders is voor mij heel belangrijk geweest en ik hoop dat het ruimhartige beleid met betrekking tot de reisbudgetten wordt voortgezet. EU-TMR financially supported my microprobe analyses at the EU Geochemical Facility at Bristol University (UK) and is gratefully acknowledged.
I would also like to thank Stan, for his comments during the early stages of my project,

and for financial support to visit the Siena Summerschool in December 1995. De VMSG financierde de Alpenexcursie in 1998 en het was geweldig. Saskia trok de kar, waardoor het uiteindelijk allemaal gebeurde. Reinoud heeft de excursie met groot enthousiasme geleid en Rinus heeft het geheel mogelijk gemaakt. De groep was erg gezellig, en door de grote variëteit in achtergrond ontstonden vaak heel boeiende discussies (bijvoorbeeld over groen en grijs bij de Glarus overschuiving; het was voor mij een eye-opener).
Op het instituut was er bijna iedere vrijdag de broodnodige ontspanning bij de Solid Rock activiteiten. De praatjes waren boeiend, de borrels altijd gezellig en de barbecues onvergetelijk (niet in het minst door de hoofdpijn op de dag erna). Ik hoop dat de sfeer bij StG-HPT-Petro nog lang zo goed blijft als hij de afgelopen jaren is geweest. Bedankt allemaal!!
Mijn paranimf Armelle is voor mij in de afgelopen jaren heel belangrijk geweest. We kenden elkaar nauwelijks toen we op een kamer kwamen, maar ik had me geen betere kamergenoot kunnen wensen. Onze gesprekken over vragen binnen en buiten de geologie, allerlei zaken in onze levens, en soms ook gewoon het weer braken de dag en maakten onze kamer voor mij tot een thuis buitenshuis. Bedankt voor de talloze snelle en minder snelle maaltijden waarvoor jij en Rob me uitnodigden; jullie zijn geweldige vrienden. Wat is het jammer dat ik je niet mee kan nemen naar DC! Veel succes met de laatste loodjes en ik kom juichen op jouw promotie.
Bart is mijn andere paranimf en ook hij is heel belangrijk voor me geweest de laatste jaren. Eerst als gezellige huisgenoot op de Pelikaanstraat en later tijdens etentjes en Waddenweekendjes hebben we eindeloos gepraat over "life, the universe and everything". Je combinatie van zelfvertrouwen en zelfspot maakt discussiëren tot een groot plezier.
Mijn andere vrienden binnen, maar ook buiten de faculteit wil ik bedanken voor de leuke avonden en dagen die we samen hebben gehad. De afwisseling met het werk was ontzettend belangrijk. Ik heb jullie de laatste jaren te weinig gezien, en helaas zal het contact de komende paar jaar nog wat moeilijker worden. Gelukkig bestaat er zoiets als e-mail. We houden contact!
Het is al vaak geschreven, maar omdat het waar is herhaal ik het nog maar eens: de steun en het begrip van mijn familie en schoonfamilie zijn vreselijk belangrijk geweest. Marianne, Sigrid en Bas vroegen me regelmatig wat nou eigenlijk het nut was van mijn werk en hielden me met beide benen op de grond. Dank voor alle gezelligheid! Bij Arno, Wilma en Tessa was ik altijd welkom en jullie interesse en steun zijn erg waardevol geweest.
Mijn ouders hebben een heel belangrijke plaats in mijn leven. Ze hebben me altijd onvoorwaardelijk gesteund in alles. Ze hebben me aangemoedigd (en op z'n tijd vermaand) en hebben altijd op de achtergrond voor me klaargestaan. Lieve Papa en Mama, aan jullie draag ik dit proefschrift op, omdat ik dit punt zonder jullie nooit had bereikt.
En tenslotte, maar op de allereerste plaats, wil ik Wim bedanken voor zijn liefde en steun, voor het corrigeren van alle hoofdstukken zodra er een ruwe versie was, en eigenlijk gewoon voor alles!

Curriculum Vitae

Fraukje Myriam Brouwer

Born 24 May 1973, Uden, The Netherlands

1985 - 1991	Secondary education (V.W.O.) at the Kruisheren Kollege, Uden
1991 - 1995	M.Sc. (doctoraal) in Structural Geology at Utrecht University
1995 - 1996	Research assistant (toegevoegd onderzoeker) in Structural Geology and Tectonics at Utrecht University
1996 - 2000	Research and teaching assistant (O.i.O.) in Structural Geology and Tectonics at Utrecht University, funded by the Netherlands Organisation for Scientific Research (N.W.O.)